

THE ROLE OF BARYONS AND NEUTRINOS IN  
THE EVOLUTION OF LARGE-SCALE  
STRUCTURE

Benjamin Mummery

A thesis submitted in partial fulfilment of the requirements of  
Liverpool John Moores University  
for the degree of  
Doctor of Philosophy.

May 2018

# Declaration

The work presented in this thesis was carried out at the Astrophysics Research Institute, Liverpool John Moores University. Unless otherwise stated, it is the original work of the author.

While registered as a candidate for the degree of Doctor of Philosophy, for which submission is now made, the author has not been registered as a candidate for any other award. This thesis has not been submitted in whole, or in part, for any other degree.

Benjamin Mummery  
Astrophysics Research Institute  
Liverpool John Moores University  
IC2, Liverpool Science Park  
146 Brownlow Hill  
Liverpool  
L3 5RF  
UK

OCTOBER 8, 2018

# Abstract

Galaxy groups and clusters (GGCs) hold a privileged position within the cosmological hierarchy. As the most recent structures to have formed, their abundances, spatial distribution and individual properties bear the indelible imprint of the background cosmology, initial conditions and their formation history, making them valuable probes of both cosmology and astrophysics. It has, however, become increasingly clear over the past decade that making use of these probes for precision cluster cosmology requires detailed, realistic predictions for the observed properties of GGCs. Producing these necessitates the use of large cosmological hydrodynamical simulations with realistic ‘sub-grid’ prescriptions for baryonic physics. One mechanism in need of addressing is the effect of the cosmic background of massive neutrinos. As these remain relativistic to relatively late times, they will free-stream out of overdensities, altering the formation of large-scale structure (LSS). If this effect can be accurately modelled, it presents an independent method of constraining the value of the neutrino mass by means of LSS observations.

This thesis makes use of the cosmo-OWLS and BAHAMAS cosmological hydrodynamical simulation suites to explore the separate and combined effects of baryon physics (particularly feedback from active galactic nuclei, AGN) and the free-streaming of massive neutrinos on large-scale structure. I focus on five diagnostics: i) the halo mass function; ii) halo mass density profiles; iii) the halo mass–concentration relation; iv) the clustering of haloes; and v) the clustering of matter; and I explore the extent to which the effects of baryon physics and neutrino free-streaming can be treated independently.

Based on this work, I anticipate that the clustering of GGCs will be sensitive to the value chosen for the summed neutrino mass. I therefore use these simulated data in conjunction with data from the GAMA survey to compare the clustering of simulated and observed galaxy groups in the context of a selection of potential neutrino mass values. I extract simulated galaxy catalogues from lightcones constructed from the BAHAMAS runs, and apply cuts to both the GAMA and BAHAMAS catalogues to create consistent, volume-limited galaxy samples. These samples are complete down to an integrated stellar mass of  $10^{10}M_{\odot}$  out to a redshift of 0.2. In order to eliminate any methodological differences between the simulated and observed measurements, analysis of these catalogues is carried out in an exactly consistent fashion. GGCs are identified by means of a Friends-of-Friends (FoF) algorithm run on the galaxy samples. I use the multiplicity and integrated stellar mass of each group as independent tracers of the halo mass, calculating the 2-point, 3-dimensional GGC comoving auto-correlation function in equally populated bins of each. I also examine the contribution of several potential sources of uncertainty in this measurement, namely: i) the intrinsic scatter in the stellar mass - halo mass and multiplicity - halo mass relations; ii) the effect of redshift space distortions; and iii) the fragmentation problem arising from my adoption of a fixed linking length in the FoF algorithm.

Consistent with previous studies, I find that both AGN feedback and neutrino free-streaming suppress the total matter power spectrum, although their scale and redshift dependencies differ significantly. The inclusion of AGN feedback can significantly reduce the masses of groups and clusters, and increase their scale radii. These effects lead to a decrease in the amplitude of the mass–concentration relation and an increase in the halo autocorrelation function at fixed mass. Neutrinos also lower the masses of GGCs while having no significant effect on the shape of their density profiles (thus also affecting the mass–concentration relation and halo clustering in a qualitatively similar way to feedback). I show that, with only a small number of exceptions, the combined effects of baryon physics and neutrino free-streaming on all five diagnostics can be estimated to typically better than a few percent accuracy by treating these processes independently (i.e., by multiplying their separate effects).

In comparing to the GAMA observations, I find that these data provide insufficient statistical power to constrain the value of the summed neutrino mass. This is primarily due to the intrinsic scatter in the stellar mass - halo mass relation, and the strong dependence of the sensitivity on precise mass binning. As a consequence, more precise estimations of the halo mass will be required in future work seeking to utilise this metric. Finally, I find that the clustering of simulated BAHAMAS groups is remarkably consistent with that of observed GAMA groups. This lends additional weight to the argument that BAHAMAS accurately reproduces the properties of the GGC population, and supports its use as a cosmological tool.

# Publications

In the course of completing the work presented in this thesis, the following papers have been submitted for publication in a refereed journal:

**Mummery, B. O.**, I. G. McCarthy, S. Bird, and J. Schaye

2017. The separate and combined effects of baryon physics and neutrino free streaming on large-scale structure. *MNRAS*, 471:227-242

# Acknowledgements

First and foremost, I would like to extend the warmest thanks possible to my supervisor, Ian McCarthy. His no-nonsense approach, decisive insights, and patient tutelage have proven indispensable time and time again, and his willingness to take on a simulation-heavy project with a student with minimal coding experience is a testament to his longanimity. While my PhD has been comparatively devoid of serious external issues – I have suffered only one broken bone which, as I understand it, is getting off pretty lightly – Ian’s understanding, support and humour in these matters have been instrumental in overcoming them. I would also like to thank my second supervisor, Ivan Baldry, as well as Chris Collins, Simeon Bird, and Jope Schaye for their unwavering willingness to discuss any aspect of this work, however minor, and for providing the immense benefits of their knowledge and experience in innumerable aspects of this work. Furthermore, I would like to thank (in alphabetical order) Rob Crain, Jon Loveday, Alex Meade, Peder Norberg, and John Peacock for their extremely useful comments, suggestions and discussions. I owe a special debt of gratitude to Amandine le Brun for her contributions to the simulations, without which much of this work would have been impossible.

Additionally, I would like to thank Harriet Brown, Claire Burke, Danielle Coogan, Martin Coulby, Jonathan Davies, Kate Furnell, Stacey Habergham-Mawson, David Hyder, Phil James, Helen Jermak, Alison Keen, Gavin Lamb, Marie Martig, Rhana Nicholson, Andrew Newsam, Simon Prentice and Sam Walton, who have, in a thousand tiny or not so tiny ways, kept me from the brink of insanity, and also Joseph Fernandez who has done nothing but push me towards it.

Special mention must be made of Anna Hodgkinson, Danielle Coogan, Dan Harman, and Stuart Macaulay for their miraculous ability to somehow make things actually work.

Finally, I would like to extend my thanks to my family, friends and, in particular, Charlotte Donohoe-Keyes for their understanding and support during the extended periods of stress and antisociality that this work has engendered, and for sharing my view that it was all worth it in the end.

This work used the DiRAC Data Centric system at Durham University, operated by the Institute for Computational Cosmology on behalf of the STFC DiRAC HPC Facility ([www.dirac.ac.uk](http://www.dirac.ac.uk)). This equipment was funded by BIS National E-infrastructure capital grant ST/K00042X/1, STFC capital grant ST/H008519/1, and STFC DiRAC Operations grant ST/K003267/1 and Durham University. DiRAC is part of the National E-Infrastructure. This research has made use of NASA's Astrophysics Data System Bibliographic Services. Funding for this PhD was provided by a STFC PhD studentship.

*“I’m being quoted to introduce something, but I have no idea what it is and I certainly don’t endorse it.”*

- Randall Munroe, XKCD

*“The story so far:*

*In the beginning the Universe was created.*

*This has made a lot of people very angry and been widely regarded as a bad move.”*

- Douglas Adams, The Restaurant at the End of the Universe

*“So, in the face of overwhelming odds, I’m left with only one option:*

*Im going to have to science the shit out of this.”*

- Andy Weir, The Martian

# Contents

|   |            |
|---|------------|
| <b>Declaration</b>  | <b>ii</b>  |
| <b>Abstract</b>   | <b>iii</b> |
| <b>Publications</b>   | <b>vi</b>  |
| <b>Acknowledgements</b>   | <b>vii</b> |
| <b>Contents</b>   | <b>x</b>   |
| List of Tables . . . . .  | xiv        |
| List of Figures . . . . .   | xv         |
| <b>1 General Introduction</b>   | <b>1</b>   |
| 1.1 Galaxy Groups and Clusters . . . . .                                    | 1          |
| 1.2 The Current Cosmological Model . . . . .                                | 3          |
| 1.3 The Role of Galaxy Groups and Clusters as Cosmological Probes . . . . . | 9          |
| 1.4 Baryonic Physics and Cluster Formation . . . . .                        | 11         |
| 1.4.1 Self-Similarity . . . . .   | 11         |
| 1.4.2 The Overcooling Problem . . . . .                                     | 12         |

|          |   |           |
|----------|---|-----------|
| 1.4.3    | Feedback . . . . .  | 13        |
| 1.5      | Neutrinos . . . . .   | 14        |
| 1.5.1    | Observational History . . . . .   | 14        |
| 1.5.2    | The Cosmic Neutrino Background . . . . .  | 17        |
| 1.5.3    | Neutrino Damping Length . . . . .   | 20        |
| 1.5.4    | Mass Constraints . . . . .  | 21        |
| 1.5.5    | Implications for Structure Formation . . . . .  | 25        |
| 1.6      | Cosmological Hydrodynamical Simulations . . . . .   | 25        |
| 1.6.1    | Implications of Neutrino Dark Matter . . . . .  | 27        |
| 1.6.2    | OWLS, and its descendants . . . . .   | 28        |
| 1.7      | The Internal Structure of Haloes . . . . .  | 29        |
| 1.7.1    | GGC density profiles . . . . .  | 30        |
| 1.7.2    | The Mass-Concentration Relation . . . . .   | 30        |
| 1.8      | Thesis Layout . . . . .   | 31        |
| <b>2</b> | <b>The Separate and Combined Effects of Baryon Physics and Neutrino Free-streaming on Large-Scale Structure</b> | <b>34</b> |
| 2.1      | Introduction . . . . .  | 34        |
| 2.2      | Simulations . . . . .   | 37        |
| 2.2.1    | cosmo-OWLS . . . . .  | 37        |
| 2.2.2    | BAHAMAS . . . . .   | 43        |
| 2.3      | Halo Abundances . . . . .   | 46        |
| 2.3.1    | Halo Mass Functions . . . . .   | 46        |

|          |   |           |
|----------|---|-----------|
| 2.3.2    | Cluster Counts . . . . .  | 55        |
| 2.4      | Halo structure . . . . .  | 58        |
| 2.4.1    | Total Mass Density Profiles . . . . .   | 59        |
| 2.4.2    | Mass–Concentration Relation . . . . .   | 67        |
| 2.5      | Halo Clustering . . . . .   | 76        |
| 2.6      | Matter Clustering . . . . .   | 78        |
| 2.7      | Summary and Discussion . . . . .  | 81        |
| <b>3</b> | <b>The Clustering of Galaxy Groups and Clusters: Comparing the BAHAMAS Simulations with the GAMA survey</b> | <b>84</b> |
| 3.1      | Introduction . . . . .  | 84        |
| 3.2      | Datasets . . . . .  | 87        |
| 3.2.1    | BAHAMAS . . . . .   | 87        |
| 3.2.2    | GAMA . . . . .  | 90        |
| 3.3      | Galaxy Selection, Group Finding, and Clustering . . . . .   | 91        |
| 3.3.1    | Galaxy Selection . . . . .  | 91        |
| 3.3.2    | Group Finding . . . . .   | 94        |
| 3.3.3    | Clustering . . . . .  | 96        |
| 3.4      | Results . . . . .   | 99        |
| 3.4.1    | Initial WMAP-9 Comparison Between BAHAMAS and GAMA. . . . .   | 99        |
| 3.4.2    | Where has the Sensitivity to Neutrino Mass gone? . . . . .  | 104       |
| 3.4.3    | <i>Planck</i> Results . . . . .   | 124       |
| 3.5      | Conclusions and Discussion . . . . .  | 125       |

|          |   |            |
|----------|---|------------|
| <b>4</b> | <b>Summary and Future Work</b>              | <b>128</b> |
| 4.1      | Summary . . . . .                           | 128        |
| 4.2      | Future Work . . . . .                       | 132        |
| <b>A</b> | <b>Fits to mass-concentration relations</b> | <b>135</b> |
| <b>B</b> | <b>Overview of Halo samples</b>             | <b>137</b> |
| <b>C</b> | <b><i>Planck</i> cosmology</b>              | <b>144</b> |
|          | <b>Bibliography</b>                         | <b>154</b> |

# List of Tables

|     |  |     |
|-----|--|-----|
| 1.1 | Neutrino free-streaming lengths corresponding to BAHAMAS runs . . .  | 21  |
| 2.1 | Included subgrid physics and model parameter values for the cosmo-OWLS and BAHAMAS runs used here. . . . .         | 38  |
| 2.2 | Ranges of total numbers of haloes in the various mass bins used for the diagnostics in Chapter 2 . . . . .         | 42  |
| 3.1 | Overview of BAHAMAS simulation runs used in this work. . . . .   | 85  |
| 3.2 | Overview of the galaxy samples drawn from each data set after cuts in redshift and mass have been applied. . . . . | 92  |
| 3.3 | The results of $\chi^2$ tests of the simulated BAHAMAS data against GAMA data. . . . .                             | 103 |
| 3.4 | The results of $\chi^2$ tests comparing the most extreme BAHAMAS runs. . .   | 122 |
| A.1 | Best-fit values for fits to the Mass-Concentration relation. . . . .   | 136 |
| B.1 | Overview of the galaxy group samples drawn from each data set. . . .   | 138 |
| B.2 | Overview of the massive halo samples drawn from the BAHAMAS light-cones. . . . .                                   | 142 |
| B.3 | Overview of the massive halo samples drawn from the BAHAMAS light-cones. . . . .                                   | 143 |

# List of Figures

|     |   |    |
|-----|---|----|
| 2.1 | Halo Mass Functions for the different baryon physics runs (in the absence of neutrino physics) from cosmo-OWLS and the different collisionless massive neutrino runs from BAHAMAS. . . . .  | 47 |
| 2.2 | The fractional change in the halo mass, relative to the DM-only, massless neutrino case, arising from the inclusion of baryonic feedback (left panel) and neutrino free-streaming (right panel) at $z = 0$ . . . . .  | 48 |
| 2.3 | Comparison of the halo mass functions arising when simultaneously simulating baryonic feedback and neutrino free-streaming, and those calculated by multiplying the separate effects of baryonic feedback in the absence of neutrinos and the effects of neutrino free-streaming in the absence of baryons. . . . . | 51 |
| 2.4 | Tests of the separability of the effects of neutrino free-streaming and baryon physics on halo mass. . . . .  | 52 |
| 2.5 | Evolution of the comoving halo space densities above different mass thresholds for the different baryon physics runs in the absence of neutrino physics using cosmo-OWL and in the absence of baryon physics using the different collisionless massive neutrino runs from BAHAMAS. . . . .                          | 56 |

|      |  |    |
|------|--|----|
| 2.6  | Comparison of the cluster counts above $10^{12}M_{\odot}$ arising when simulating baryonic feedback and neutrino free-streaming simultaneously and those calculated by multiplying the separate effects of baryonic feedback in the absence of neutrinos, and the effects of neutrino free-streaming in the absence of baryonic physics. . . . . | 57 |
| 2.7  | Median radial total mass density profiles in 0.5 dex <i>self-consistent</i> halo mass bins for difference baryon physics models in the absence of neutrino physics at fixed cosmology. . . . .   | 60 |
| 2.8  | Median radial total mass density profiles in 0.5 dex <i>self-consistent</i> halo mass bins for different neutrino physics models in the absence of baryon physics at fixed cosmology. . . . .  | 61 |
| 2.9  | Median radial total mass density profiles in 0.5 dex bins of the mass of the “matched” DM-only, massless neutrino halo for different baryon physics models in the absence of neutrino physics at fixed cosmology.  | 62 |
| 2.10 | Median radial total mass density profiles in 0.5 dex bins of the mass of the “matched” DM-only, massless neutrino halo for different neutrino physics models in the absence of baryonic physics at fixed cosmology.  | 63 |
| 2.11 | Comparison of the median radial total mass density profiles of haloes arising when simulating baryonic feedback and neutrino free-streaming simultaneously and with that calculated by multiplying their separate effects. . . . .   | 64 |
| 2.12 | Best fit total mass $c(M)$ relations for different baryon physics models in the absence of neutrino physics in the WMAP-7 cosmology and for different $\sum M_{\nu}$ values in the absence of baryonic physics in WMAP-9 cosmology at $z = 0$ . . . . .  | 68 |

|      |   |    |
|------|---|----|
| 2.13 | Comparison of the mass–concentration relations arising when simulating baryonic feedback and neutrino free-streaming simultaneously and those calculated by multiplying the separate effects of baryonic feedback in the absence of neutrinos, and the effects of neutrino free-streaming in the absence of baryonic physics. . . . .                             | 69 |
| 2.14 | Real-space 2-point halo autocorrelation functions for the different baryonic physics runs in the absence of neutrino physics from cosmological and the different collisionless massive neutrino runs from BAHAMAS. . . . .  | 73 |
| 2.15 | Real-space 2-point halo autocorrelation functions for the different baryonic physics models in the absence of neutrino physics from cosmological and the different collisionless massive neutrino runs from BAHAMAS. . . . .  | 74 |
| 2.16 | Comparison of the real space 2-point halo autocorrelation functions ( $\xi$ ) arising when simulating baryonic feedback and neutrino free-streaming simultaneously and those calculated by multiplying the separate effects of baryonic feedback in the absence of neutrinos and the effects of neutrino free-streaming in the absence of baryon physics. . . . . | 75 |
| 2.17 | Matter power spectra for different baryon physics models in the absence of neutrino physics in the WMAP-7 cosmology and for different $\sum M_\nu$ values in the absence of baryonic physics in the WMAP-9 cosmology at $z = 0$ . . . . .   | 79 |
| 2.18 | Comparison of the matter power spectra arising when simulating baryonic feedback and neutrino free-streaming simultaneously and those calculated by multiplying the separate effects of baryonic feedback in the absence of neutrinos and the effects of neutrino free-streaming in the absence of baryon physics. . . . .  | 80 |

|     |  |     |
|-----|--|-----|
| 3.1 | Redshift-space 2-point GGC autocorrelation as a function of the intergroup separation for GAMA and BAHAMAS in equally populated bins of integrated stellar mass. . . . .   | 100 |
| 3.2 | Redshift-space 2-point GGC autocorrelation as a function of the intergroup separation for GAMA and BAHAMAS in equally populated bins of multiplicity. . . . .  | 101 |
| 3.3 | Redshift-space 2-point autocorrelation functions for BAHAMAS GGCs in equally populated bins of halo mass $M_{200,crit}$ . . . . .  | 106 |
| 3.4 | Observable - halo mass relations for the various BAHAMAS runs in bins of halo mass. . . . .  | 107 |
| 3.5 | Observable - halo mass relations for the various BAHAMAS runs in bins of the observable. . . . .   | 108 |
| 3.6 | Redshift-space 2-point autocorrelation functions for BAHAMAS haloes in equally populated bins of $M_{*halo}$ , the 'true' stellar mass contained within $M_{200,crit}$ . . . . .                                       | 111 |
| 3.7 | Redshift-space 2-point GGC autocorrelation as a function of the intergroup separation for GAMA and BAHAMAS in equally populated bins of integrated stellar mass <i>excluding the effects of peculiar motions</i> . . . | 113 |
| 3.8 | The multiplicity and stellar mass functions of GAMA and BAHAMAS GGC samples identified using a FoF algorithm with a fixed value for the linking length. . . . .  | 116 |
| 3.9 | The multiplicity and stellar mass functions of GAMA and BAHAMAS GGC samples identified using a FoF algorithm with a mass-dependent value for the linking length. . . . .   | 117 |

|      |  |     |
|------|--|-----|
| 3.10 | The redshift-space 2-point GGC autocorrelation as a function of the inter-group separation for GAMA and BAHAMAS in equally populated bins of integrated stellar mass for groups identified using a FoF algorithm with a mass-dependent linking length. . . . .   | 119 |
| 3.11 | The redshift-space 2-point GGC autocorrelation as a function of the inter-group separation for GAMA and BAHAMAS in equally populated bins of integrated stellar mass for groups identified using a FoF algorithm with a mass-dependent linking length and excluding the effects of peculiar motions. . . . . | 120 |
| 3.12 | Redshift-space 2-point GGC autocorrelation as a function of the inter-group separation for GAMA and BAHAMAS in equally populated bins of multiplicity for groups identified using a mass-dependent linking length. . . . .   | 121 |
| 3.13 | Direct comparison between the clustering of haloes in <i>Planck</i> (dashed curves) and WMAP-9 (solid curves) cosmologies. . . . .   | 123 |
| C.1  | The redshift-space 2-point galaxy group autocorrelation as a function of the inter-group separation for GAMA and BAHAMAS in equally populated bins of integrated stellar mass for a <i>Planck</i> cosmology. . . . .   | 145 |
| C.2  | The redshift-space 2-point galaxy group autocorrelation as a function of the inter-group separation for GAMA and BAHAMAS in equally populated bins of multiplicity for a <i>Planck</i> cosmology. . . . .  | 146 |
| C.3  | Redshift-space 2-point autocorrelation functions for BAHAMAS galaxy groups in equally populated bins of halo mass $M_{200,crit}$ in the <i>Planck</i> cosmology. . . . .   | 147 |
| C.4  | Redshift-space 2-point autocorrelation functions for BAHAMAS haloes in equally populated bins of $M_{*halo}$ , the 'true' stellar mass contained within $M_{200,crit}$ in the <i>Planck</i> cosmology. . . . .   | 148 |

|     |   |     |
|-----|---|-----|
| C.5 | Redshift-space 2-point GGC autocorrelation as a function of the inter-group separation for GAMA and BAHAMAS in equally populated bins of integrated stellar mass <i>excluding the effects of peculiar motions</i> . . .                                 | 149 |
| C.6 | The multiplicity and stellar mass functions of GAMA and BAHAMAS galaxy group samples identified using a FoF algorithm with a fixed value for the linking length in the context of a <i>Planck</i> cosmology. . . .                                      | 150 |
| C.7 | The multiplicity and stellar mass functions of GAMA and BAHAMAS galaxy group samples identified using a FoF algorithm with a mass-dependent value for the linking length in the context of a <i>Planck</i> cosmology. . . . .                           | 151 |
| C.8 | The redshift-space 2-point galaxy group autocorrelation as a function of the inter-group separation for GAMA and BAHAMAS in equally populated bins of integrated stellar mass for a <i>Planck</i> cosmology. . . . .                                    | 152 |
| C.9 | Redshift-space 2-point autocorrelation as a function of the inter-group separation for GAMA and BAHAMAS GGCs identified using a FoF algorithm with a <i>mass-dependent</i> linking length in equally populated bins of integrated stellar mass. . . . . | 153 |

# Chapter 1

## General Introduction

### 1.1 Galaxy Groups and Clusters

One of the cornerstones of modern cosmology is the existence of a hierarchy of gravitationally bound structures spanning a wide range of physical scales, from individual galaxies to clusters containing thousands of galaxies. Our knowledge of these larger groupings has its roots in the late 18th century with the work of Messier (1784) and Herschel (1785), who noted the presence of overdensities of ‘nebulae’ in, respectively, the constellations of Virgo and Coma Berenices. The significance of this did not become clear until several decades later, when Slipher (1914) and Hubble (1926) established that the ‘nebulae’ were in fact galaxies, and these overdensities are now known as the Coma and Virgo clusters of galaxies.

Study into these extragalactic structures rapidly bore strange fruit when the work of Zwicky (1933) (translated into English by Andernach and Zwicky (2017)) provided a measurement of the mass of the Coma cluster. Zwicky found that the member galaxies had velocities<sup>1</sup> in excess of the expected escape velocity, i.e. that required to escape the gravity well created by the mass inferred from the optical luminosity of the member galaxies. The apparent presence of a large but invisible mass component presented the

---

<sup>1</sup>Relative to the cluster centre of mass.

first evidence for the existence of dark matter. The importance of clusters, and their less massive cousins groups, to our current understanding of cosmology is indisputable.

Our modern understanding of galaxy clusters can be summarised as follows: they are large collections of (typically between  $\sim 100$  and  $\sim 1000$ ) galaxies that are *i*) gravitationally bound and *ii*) occupy a region of order a few Mpc across (Kravtsov and Borgani, 2012). The difference between group and cluster is largely semantic and lacks a physically motivated definition. For this work, I therefore adopt the acronym GGCs (galaxy groups and clusters) as a general term, relying instead on specified ranges in mass or other properties of the objects to specify their nature.

In addition to their historical significance, GGCs occupy a position of significance within the cosmological hierarchy as a result of the current model of hierarchical formation. Under this scheme, the formation of structure begins with the gravitational collapse of small objects which then merge to form ever more massive structures. GGCs, as the most massive collapsed structures in the Universe, consequently are the most recent to have formed. This makes GGCs invaluable tests of both cosmology and astrophysics. Their abundances and spatial distribution bears the indelible mark of the background cosmology and initial conditions – a dependence that grows as one examines more and more massive objects, since their formation is still ongoing and even a small change in the rate of these processes will have a significant impact on their current population. At the same time, the deep potential wells within which they form make GGCs nearly closed boxes, positioning them as excellent laboratories within which to study the processes governing galaxy formation and the impact thereof on the intracluster medium (ICM), and vice versa.

Due almost entirely to the way in which the category has been defined, GGCs have a present-day mass of between  $10^{13}$  and  $10^{15} M_{\odot}$ , of which  $\sim 80\%$  is made up of dark matter. Of the remaining mass,  $\sim 75\%$  ( $\sim 15\%$  of the total cluster mass) is contributed by the ICM, a hot gaseous plasma distributed between the member galaxies, and  $\sim 10 - 15\%$  ( $\sim 2 - 3\%$  of the total cluster mass) by stars primarily located within the member galaxies. These estimates are made possible by the fact that clusters are the *only* structures for which all of these forms of matter may be directly observed (the hot

plasma around typical individual galaxies like the Milky Way is generally too faint to be seen).

## 1.2 The Current Cosmological Model

While our understanding of GGCs was developing as discussed above, our understanding of cosmology was undergoing a parallel, and related, evolution. The modern paradigm began in earnest in 1915 with the development of General Relativity (Einstein, 1915). This led to the proposal by Lemaître in 1927 (translated into English in Lemaître 1931) on theoretical grounds of both the expansion of the Universe, and the Big Bang origin thereof (in his words; “The Cosmic Egg exploding at the moment of the creation.” (Sidharth and Joseph, 2010)); and to the derivation by Friedmann in 1922 of the isotropic and homogenous class of cosmological models. These would go on to form the basis for the currently cosmological standard model (see, for example, Lachieze-Rey 1995; Peacock 1998; Bartelmann 2010).

The discovery of dark matter by Zwicky (1933), as mentioned above, provided the first evidence for an invisible but dominant mass component existing within the Universe. Further evidence followed, with the measurement of the flat rotation curve of the Andromeda galaxy, in contravention to the expected dynamics given a mass distribution following the observed luminosity distribution (van de Hulst et al. 1957; and its companion paper Schmidt 1957), establishing the importance of DM on the scale of individual galaxies. The exact nature of this unseen mass component continues to be the subject of ongoing research, however it is well established from inferences drawn from Big Bang Nucleosynthesis that the majority of this matter must be non-baryonic (Turner, 1999).

The accidental discovery of the Cosmic Microwave Background (hereafter CMB) by Penzias and Wilson (1965) offered a hitherto unimagined window into the early universe. Analyses of this offered firm proof that the Universe began with a hot big bang (Dicke et al., 1965), the initial energy of which provided the impetus for the ongoing

expansion of the Universe as postulated by Friedmann (1922) and measured by Hubble (1926), and generally parametrised by Hubble's law.<sup>2</sup>

This model of the Universe came with one obvious consequence: after the initial kick of the big bang, the only force acting upon the expanding mass at cosmological scales would be gravity acting in opposition to the expansion. The expansion rate must therefore be decreasing with time, and the eventual fate of the Universe would depend on whether the total energy density was such that the Universe would continue expanding, albeit at an ever diminishing rate; eventually come to a stop; or ultimately reverse leading to a period of contraction<sup>3</sup>. As more precise observations became available, however, they seemed to contradict this expectation. In 1998, independent albeit parallel work by the teams of Riess et al. (1998) and Perlmutter et al. (1999) using supernovae as standard candles demonstrated that the rate of expansion was, in fact, accelerating.

This revelation resulted in yet another paradigm shift in cosmology: the introduction of Dark Energy (hereafter DE). This model explains the accelerating expansion by adapting the cosmological constant  $\Lambda$ , an element erroneously introduced by Einstein (1917), as a description of an additional energy component that acts repulsively. In order to drive the acceleration of space in the required fashion, the energy density of DE cannot behave like matter ( $\rho_{matter} \propto a^{-3}$ ) or radiation ( $\rho_{rad} \propto a^{-4}$ ), which both dilute with increasing scale factor, but must instead remain constant as the scale factor increases ( $\rho_{DE} \propto a^0$ ). Independent evidence for the expanding universe, and the first results constraining  $\Lambda$  as non-zero, were achieved by jointly analysing CMB anisotropies and the clustering of galaxies (Efstathiou et al., 2002), firmly establishing

---

<sup>2</sup>In brief, the line-of-sight recession velocity  $v$  of an object as a function of the line-of-sight distance  $d$  due to the expansion of space is given by

$$v = Hd$$

where  $H$  is the Hubble constant (although as the rate of the expansion of space is not static with time, the moniker 'constant' is erroneous). Due to the observational uncertainty of  $H$  it is common to define the reduced Hubble constant  $h$  as

$$h = \frac{H}{100 \text{ km s}^{-1} \text{ Mpc}^{-1}}. \quad (1.1)$$

to allow simple comparison between analyses that would otherwise use different values (Croton, 2013).

<sup>3</sup>These eventualities are known colloquially as the Big Rip, Big Freeze and Big Crunch scenarios respectively.

DE as an essential part of the cosmological model. This was the final piece of what is now known as the  $\Lambda$ CDM (a contraction of  $\Lambda$  + cold dark matter) cosmological model, which has since become the current favoured cosmological model.

The  $\Lambda$ CDM model describes a Universe that is:

- Spatially flat
- Expanding at an accelerating rate.
- Went through primordial nucleosynthesis and the decoupling of matter and radiation that resulted in the CMB.
- Underwent an earlier, much more rapid period of expansion known as *inflation* that resulted in quantum density fluctuations being blown up to macro scale perturbations that would go on to seed the overdensities that, by gravitational collapse, would form the presently observed large-scale structures
- Is made up of baryons, dark matter, and dark energy in the following proportions:  $\sim 5\%$  baryonic matter;  $\sim 20\%$  dark matter; and  $\sim 75\%$  dark energy.

Despite its agreement with an ever increasing set of ever more precise cosmological measurements, this model continues to raise profound questions, not least among which are the origins of expansion itself and the true nature of dark matter and energy.

Mathematically, any expression of the Universe must be compatible with the field equations of General Relativity:

$$R_{\mu\nu} - \frac{1}{2}g_{\mu\nu}R \equiv G_{\mu\nu} = 8\pi GT_{\mu\nu} - \Lambda g_{\mu\nu}, \quad (1.2)$$

where  $R_{\mu\nu}$  is the Ricci curvature tensor,  $g_{\mu\nu}$  is the metric tensor,  $R$  is the scalar curvature,  $G_{\mu\nu}$  is the Einstein tensor,  $G$  is Newton's gravitational constant, and  $T_{\mu\nu}$  is the stress-energy tensor (Einstein, 1915).

The framework of general relativity can be used to describe an expanding universe using the Friedmann, Lemaître, Robertson, Walker (hereafter FLRW) metric. We define

the following parameters:

$(r, \theta, \phi)$  are the *comoving coordinates*. This is the coordinate system that ‘factors out’ the expansion of space, meaning that the coordinate system expands at the same rate as the space it describes. The relative comoving distance between two objects is constant if the relative motion of the two is due exclusively to the expansion of the space between them.

$a(t)$  is the *growth* or *scale factor*, which expresses the size evolution of the background universe. This is closely related to the comoving coordinates as the scale factor expresses the ratio between the physical and comoving coordinates.

$k$  is the *curvature* of the Universe, defined such that  $k > 0$  corresponds to a positive curvature (resulting in a closed, spatially finite universe);  $k = 0$  corresponds to no curvature (resulting in a spatially flat universe); and  $k < 1$  corresponds to a negative curvature (resulting in an *open* Universe).

$z$  is the *redshift*, defined as the fractional Doppler shift of light emitted by an object due to its line-of-sight velocity:

$$1 + z \equiv \frac{\lambda_{observed}}{\lambda_{emitted}} = \frac{a(t_0)}{a(t_1)} \quad (1.3)$$

where  $\lambda_{observed}$  and  $\lambda_{emitted}$  are the observed and emitted wavelengths respectively, and  $a(t_0)$  and  $a(t_1)$  are the scale factors at  $t_0$  (the time of emission) and  $t_1$  (the time of observation) respectively. The first equality corresponds to the observational definition of redshift, the second to the cosmological definition. Note that although any line-of-sight velocity contributes to the Doppler shift, this definition of redshift refers exclusively not to the intrinsic motion of the source through space, but rather to the expansion of the space between the source and the observer.

According to Kolb and Turner (1990), the FLRW metric can then be expressed as:

$$\begin{aligned} ds^2 &= c^2 dt^2 - a^2(t) \left( \frac{dr^2}{1 - kr^2} + r^2 d\theta^2 + r^2 \sin^2 \theta d\phi^2 \right) \\ &= g_{\mu\nu} dx^\mu dx^\nu, \end{aligned} \quad (1.4)$$

where  $g_{\mu\nu}$  is the metric tensor.

Combining the FLRW metric (Equation. 1.4) with Einstein's field equations (Equation. 1.2), the Friedmann energy and force equations, respectively, are obtained:

$$\left( \frac{\dot{a}}{a} \right)^2 + \frac{kc^2}{a^2} = \frac{8\pi G}{3} \rho + \frac{\Lambda}{3} \quad (1.5)$$

and

$$2\frac{\ddot{a}}{a} + \left( \frac{\dot{a}}{a} \right)^2 + \frac{kc^2}{a^2} = -8\pi G p, \quad (1.6)$$

where  $\Lambda$  is the aforementioned cosmological constant and can be written as a pressure or a density of the vacuum:

$$\Lambda \equiv 8\pi G \rho_\Lambda c^2 = -8\pi G p_\Lambda. \quad (1.7)$$

The Hubble parameter can be expressed as the ratio of the rate of change of the expansion factor to its present value,  $H \equiv \frac{\dot{a}}{a}$ . Doing so allows the Friedmann equations (Equations 1.5 and 1.6) to be written as:

$$H^2 = \frac{8\pi G}{3} \rho - \frac{kc^2}{a^2} + \frac{\Lambda}{3} \quad (1.8)$$

and

$$\frac{\ddot{a}}{a} = -\frac{4\pi G}{3} \left( \rho + \frac{3p}{c^2} \right) + \frac{\Lambda}{3}. \quad (1.9)$$

The present-day matter density that would result in a spatially flat ( $k = 0$ ) universe is referred to as the *critical density*,  $\rho_{crit} = \rho(z = 0, k = 0) \equiv \frac{3H_0^2}{8\pi G}$ . This quantity is commonly used to normalise the other cosmic densities, defining  $\Omega_i(z) \equiv \frac{\rho_i(z)}{\rho_{crit}(z)}$ .

These are the most commonly used forms of the three densities that serve as half of the six cosmological parameters that describe the flat  $\Lambda$ CDM model. The full list is:

$\Omega_m$  the total matter content (i.e the combined contribution of baryonic matter and DM)

$\Omega_b$  the total baryonic content.

$\Omega_\Lambda$  the total contribution of DE.

$h$  the reduced Hubble constant, as defined in equation 1.1

$\sigma_8$  the amplitude of the power spectrum of density fluctuations at the scale of  $8 h^{-1}$  Mpc.

$n_s$  the spectral index of the power spectrum of the density fluctuations.

The parameters  $\sigma_8$  and  $n_s$  are defined by the equality:

$$\sigma_8^2 = \frac{1}{2\pi} \int T(k)P(k)W(kR)k^2 \cdot dk, \quad (1.10)$$

where  $k$  is the comoving wavenumber;  $P(k)$  is the primordial matter power spectrum expressed as a function of  $k$  and also satisfies  $P(k) \propto k^{n_s}$ ;  $T(k)$  is the transfer function which relates the present day ‘processed’ power spectrum to the primordial power spectrum<sup>4</sup>, and  $w$  is the Fourier transform of a top-hat window function of real-space radius  $R = 8 h^{-1}$  Mpc.

While this approach treats DM as a single ‘cold’ species (CDM), i.e. a monolithic population of particles with velocities well below  $c$ , we know that some small fraction of the mass considered as such is contributed by neutrinos (see Section 1.5 below). Due

---

<sup>4</sup>We do not observe the initial power-spectrum except on the largest physical scales. The transfer function  $T(k)$  describes how the shape of the initial power-spectrum  $\Delta k(z)$  in the dark matter is modified by different physical processes through the relation

$$\Delta k(z=0) = T(k)f(z)\Delta k(z) \quad (1.11)$$

$\Delta k(z=0)$  is the power spectrum at the present epoch and  $f(z) \propto a \propto t^{2/3}$  is the linear growth factor between the scale factor at redshift  $z$  and the present epoch in the matter dominated era. The form of the transfer function is largely determined by the fact that there is a delay in the growth of the perturbations between the time when they came through the horizon and began to grow again. In the standard cold dark matter picture, this is associated with the fact that before the epoch of equality of matter and radiation, the oscillations in the photon-baryon plasma were dynamically more important than those in the dark matter.

to their small mass and high initial energy, neutrinos are relativistic at decoupling and remain so to relatively late times, and therefore act as a small ‘hot’ dark matter (HDM) component. Part of the aim of this thesis is to explore the effects of such ‘mixed’ DM models on large-scale structure formation.

For the purposes of describing the evolution of cosmological properties, particularly distances, it is convenient to follow Peebles (1993) and define the function:

$$E(z) = \sqrt{\Omega_M(1+z)^3 + \Omega_k(1+z)^2 + \Omega_\Lambda}, \quad (1.12)$$

commonly referred to as the *Peebles function*, where  $\Omega_k$  is the “spatial curvature density” defined by:

$$\Omega_M + \Omega_\Lambda + \Omega_k = 1. \quad (1.13)$$

The Peebles function is proportional to  $\dot{a}(t)/a(t)$  and consequently expresses the ratio between the present-day Hubble constant  $H_0$  and that measured by an observer at redshift  $z$ , such that:

$$H(z) = H_0 E(z). \quad (1.14)$$

### 1.3 The Role of Galaxy Groups and Clusters as Cosmological Probes

As previously mentioned, the privileged position of GGCs in the hierarchy of cosmological structure makes them invaluable probes of both cosmology and astrophysics (for recent reviews, see Voit 2005; Borgani and Kravtsov 2011; Allen et al. 2011; Kravtsov and Borgani 2012; and Weinberg et al. 2013).

For example, as the largest, gravitationally bound, virialized objects in existence, the evolution of the GGC halo mass function  $dn/dM$  is a key cosmological probe. At a fixed mass and redshift, the abundance of haloes is strongly dependent on the growth rate of structure as their ongoing development means that a small advance or delay in their formation can drastically alter the mass function. Consequently,  $dn/dM$  inherits

the same sensitivities to cosmological parameters as the structure growth rate, most directly  $\sigma_8$  and  $\Omega_M$ .

Similar dependences are found in other GGC population properties, both of the population as a whole and of individual clusters. Of particular interest in this thesis, primarily in Chapter 3 is the spatial clustering of GGCs. Estimators of the clustering of matter such as the two-point autocorrelation function, which measures the excess probability over that of a random distribution of observing a pair of objects separated by a characteristic distance as a function of that distance, can be related to the underlying matter power spectrum, assuming that sufficiently precise constraints can be placed on the observable-mass relationships employed.

Making use of these dependences is not trivial, however. Doing so requires that we

- i)* infer halo masses accurately and reliably from the observed GGC properties such as X-ray luminosity or temperature, Sunyaev-Zel'dovich effect intensity, or weak lensing shear,
- ii)* account for scatter and covariance in whichever mass-observable and observable-observable relationships are being used in the cosmological modelling
- iii)* possess a detailed knowledge of the survey selection function, and
- iv)* have a robust theoretical prediction for whatever cosmological test is being undertaken.

It is therefore vital that we have accurate, highly detailed theoretical models in order to make any cosmological inference from GGC observations. Doing so, however, is not trivial. The aforementioned sensitivity of GGC properties to both cosmology and astrophysics (1.1) that makes them such useful tests also means that accurately modelling their properties requires a detailed understanding of a wide variety of physical processes operating at a wide range of scales. Of particular interest are the roles played by the baryonic content of GGC haloes, and by the neutrino HDM component of the underlying cosmology. In the following sections (1.4 and 1.5), I will provide a brief theoretical background to the impact of these factors on GGC properties. The measurement of GGC properties is discussed in more detail in Chapter 2.

## 1.4 Baryonic Physics and Cluster Formation

### 1.4.1 Self-Similarity

Early simple models of formation assumed clusters to be virialized, and the properties of clusters, and the correlations between them, to be dependent solely on gravity. The scale-independence of gravity naturally leads to an expectation that clusters should be self-similar, i.e. all clusters should exhibit the same relations and properties, with those of more massive clusters scaled by a simple factor dependent only on the mass ratio (White and Rees, 1978; Kaiser, 1986; Voit, 2005; Borgani and Kravtsov, 2011; Kravtsov and Borgani, 2012).

As GGCs do not have sharply delineated edges, it is customary to define masses and radii in terms of the density contrast of their underlying mass overdensity. We define a radius  $r_\Delta$  as the radius from the halo centre of mass within which the density is  $\Delta$  times greater than either the universal mean density or the critical density ( $\rho_{mean}$  and  $\rho_{crit}$  respectively). This naturally leads to a mass definition  $M_\Delta$  being the mass contained within  $r_\Delta$ .

Under the assumption of self similarity, it is relatively easy to predict the evolution of a given mass-observable relation for clusters. The dependence of the critical density on the expansion rate means that its evolution can be expressed with the Peebles function as described in Section 1.2:

$$\rho_{crit}(z) = E(z)^2 \rho_{crit,0}, \quad (1.15)$$

(where  $\rho_{crit,0} \equiv \rho_{crit}(z = 0)$  is the present-day critical density). Since our definitions for mass and size can explicitly depend on  $\rho_{crit}$ , including the redshift evolution in our modelled observables is trivial. For example, since

$$M_\Delta \propto \rho_{crit}(z) r_\Delta^3 \quad (1.16)$$

then the cluster size  $r_\Delta$  by definition must scale with mass as

$$r_\Delta \propto M_\Delta^{1/3} E(z)^{-2/3}, \quad (1.17)$$

meaning that the mass density profiles  $\rho(r)$  will be identical for all haloes, independent of mass and redshift, when the radius is scaled by  $M_\Delta^{1/3} E(z)^{-2/3}$ .

### 1.4.2 The Overcooling Problem

In the early 1980s and 90s, the advent of the *Einstein Observatory*, *EXOSAT* and *ROSAT* provided the first X-ray observations of large large numbers of galaxy clusters. These data quickly showed the self-similar model to be inconsistent with a number of observational parameters, such as the observed X-ray luminosity evolution (e.g. Evrard and Henry 1991; Kaiser 1991).

This indicated that the underlying assumption of the self-similar model, that the only relevant processes are gravitational, was incorrect. In particular, low-mass clusters are observed to exhibit lower densities than more massive clusters, indicating a dependence of the mass density profile on the system total mass.

Similar solutions were presented by Kaiser (1991) and Evrard and Henry (1991) in the form of an unspecified process that imposes a minimum gas entropy. Physically, this process is modelled as heating the gas prior to it falling into the collapsing halo. This is referred to as the pre-heating model.

Another possibility was offered by radiative cooling of the baryonic content (see, for example, Bryan 2000; Dav et al. 2002; Voit and Ponman 2003). Although it seems obvious that this should be a factor given that GGCs are known to contain galaxies, its importance was bolstered by the realisation that gas in the centres of galaxies is able to cool rapidly by means of line emission and thermal bremsstrahlung (e.g. White and Rees 1978; White and Frenk 1991).

In the late 1990s, comparisons of models incorporating radiative cooling and star for-

mation (hereafter SF) to increasingly precise observational constraints revealed that the predicted galaxies and clusters exhibited stellar fractions in excess of the observational upper limits, as well as unrealistic ICM properties (e.g. Balogh et al. 2001; McCarthy et al. 2004). This became known as the *overcooling problem*, making it clear that cooling alone was not a valid solution to the self-similarity breaking. Accurate modelling of galaxy formation therefore requires the inclusion of some form of feedback process(es).

### 1.4.3 Feedback

Star formation itself offers an obvious source of feedback in the form of supernovae (SNe). These dramatic expulsions of energy can drive interstellar winds and heat the ISM, delaying further star formation (Larson, 1974; White and Frenk, 1991; Ponman et al., 1999; Voit, 2005). While a necessary inclusion, SN feedback fails to fully resolve the overcooling problem at group and cluster scales (Borgani et al., 2004; Kay et al., 2004; Borgani et al., 2005, 2006; Davé et al., 2008). Additional form(s) of feedback are therefore necessitated.

It is now commonly accepted that the centres of galaxies are host to supermassive black holes (SMBHs), giving rise to active galactic nuclei (AGN) (King, 2003). Mounting observational evidence over the past two decades has supported the theory that the growth of the SMBHs is closely tied to the growth of their host galaxies, and has gone so far as demonstrating close correlations between AGN *feedback* and the properties of massive galaxies, groups, and clusters (Benson et al., 2003; Bower et al., 2006; De Lucia and Blaizot, 2007; McNamara and Nulsen, 2007; McCarthy et al., 2010, 2011; Fabian, 2012). As an example, where the pre-heating model would dictate that non-gravitational processes should heat low-entropy gas in the high-redshift progenitors of groups, McCarthy et al. (2011) found that AGN feedback has the effect of ejecting such gas from the progenitor.

In addition, baryonic physics has importance well beyond its effect on the properties of GGCs. The work of van Daalen et al., for example, has demonstrated that the physics

of galaxy formation has a significant effect on the clustering of matter, both in terms of the matter power spectrum (van Daalen et al., 2011) and the 2-point autocorrelation function of galaxies and subhaloes (van Daalen et al., 2014). These results indicate that constraints drawn from cosmological data are dependent on the baryon physics model even where those data are not directly related to the baryonic content of the Universe.

## 1.5 Neutrinos

As mentioned in Section 1.2, the presence of neutrinos contributes a small HDM component to the cosmology. This modifies the processes of structure formation (see Section 1.5.5 below), necessitating the inclusion of neutrino physics in LSS models. In this section, I provide a brief overview of our current observational and theoretical understanding of the Universe’s neutrino content, before discussing in general terms the mechanics of its effect on the GGC population.

### 1.5.1 Observational History

The existence of the neutrino (specifically the electron neutrino  $\nu_e$ ) was first postulated in 1930 by Wolfgang Pauli<sup>5</sup> (Pauli, 1994) to explain the apparent breaking of energy, momentum and angular momentum conservation in beta decay. Over the next two and a half decades, indirect observational evidence for the neutrino continued to mount, culminating with the first *direct* detection by Cowan et al. (1956). Detections of the muon neutrino ( $\nu_\mu$ ) and tau neutrino ( $\nu_\tau$ ) followed in 1962 and 2000 (Danby et al., 1962; DONUT Collaboration et al., 2001), although the existence of the latter had been strongly indicated since the discovery of the Tau particle by Perl et al. (1975).

Detections of neutrinos have primarily focussed on solar neutrinos produced as electron neutrinos via the proton-proton chain reaction, as these are vastly more abundant on earth than those from any other sources. Early detections of these, specifically the

---

<sup>5</sup>Although the *neutrino* name was not attached to the particle until 1932.

Homestake Experiment in the late 1960s, found a flux of electron neutrinos between one half and one third of the expected value (Cleveland et al., 1998). This discrepancy, dubbed the ‘solar neutrino problem’, posed a significant challenge for neutrino physics for the next 4 decades. Although multiple explanations were proposed, data from the Super-Kamiokande (Fukuda et al., 1998) experiment provided a positive detection of neutrino oscillations.

The ability of neutrinos to oscillate between flavours was first proposed by Bruno Pontecorvo in 1957 (Cohen et al., 2009). In brief, this posits that the three active neutrino flavours are in fact each a different superposition of three neutrino states of different masses. This emerges as a natural outcome of gauge theories with massive neutrinos, where the neutrino flavour  $\Delta \in \{e, \mu, \tau\}$  and mass eigenbasis  $i \in \{1, 2, 3\}$  can be written as:

$$\begin{aligned} |\nu_\Delta\rangle &= \sum_i U_{\Delta i}^* |\nu_i\rangle \\ |\nu_i\rangle &= \sum_\Delta U_{\Delta i} |\nu_\Delta\rangle \end{aligned} \quad (1.18)$$

where  $X^*$  is the complex conjugate of  $X$ , and  $U_{\Delta i}$  is the Pontecorve-Maki-Nakagawa-Sakata (PMNS) matrix, an analogue for the CKM matrix that describes the mixing of quarks.<sup>6</sup>

The propagation of the mass eigenstates  $|\nu_i\rangle$  can be described with a plane wave solution. In natural units with  $c = 1$ ,  $\hbar = 1$ , such a solution can be expressed as a function of the time  $t$  from the start of propagation as:

$$|\nu_i(t)\rangle = e^{-i(E_i - \vec{p}_i \cdot \vec{x})} |\nu_i(t_0)\rangle \quad (1.19)$$

---

<sup>6</sup>This applies explicitly for neutrinos. For antineutrinos, the complex conjugate should appear in the second expression rather than the first, such that:

$$\begin{aligned} |\nu_\Delta\rangle &= \sum_i U_{\Delta i} |\nu_i\rangle \\ |\nu_i\rangle &= \sum_\Delta U_{\Delta i}^* |\nu_\Delta\rangle \end{aligned}$$

where  $E_i$  is the energy of the relevant mass eigenstate  $i$ ,  $\vec{p}_i$  is the three-dimensional momentum, and  $\vec{x}$  is the particle's current position relative to its initial ( $t_0$ ) position.

As all currently observable neutrinos are ultra-relativistic, the approximations  $|\vec{p}_i| = p_i \gg m_i$  and  $t \approx L$ , where  $L$  is the travel distance, may be applied. Doing so permits the total energy  $E$  of a particle to be related to its mass eigenstate by the relation

$$E_i = \sqrt{p_i^2 + m_i^2} \approx E + \frac{m_i^2}{2E}, \quad (1.20)$$

and thus the wavefunction (Equation 1.19) may be written as:

$$|\nu_i(L)\rangle = e^{-im_i^2 \frac{L}{2E}} |\nu_i(L_0)\rangle. \quad (1.21)$$

The dependence of the exponent on the mass  $m_i$  means that eigenstates with differing masses will oscillate at different frequencies, heavier ones oscillating with greater frequencies. As the measured flavour at a point in time  $t$  (or distance  $L$ ) from the beginning of the neutrino's propagation is a combination of these eigenstates, then a neutrino emitted with flavour  $a$  has a probability of being measured as having flavour  $b$ ,  $P_{a \rightarrow b}$ , that varies as a function of  $t$  ( $L$ ). Specifically:

$$P_{a \rightarrow b} = |\langle \nu_b(t) | \nu_a \rangle|^2 = \left| \sum_i U_{ai}^* U_{bi} e^{-im_i^2 \frac{L}{2E}} \right|^2. \quad (1.22)$$

As this model explicitly depends upon different mass values  $m_i$  for the three active neutrino species, its confirmation as the solution of the solar neutrino problem firmly establishes that at least two of these species are massive.

Oscillation experiments such as Super-Kamiokande are sensitive to the differences of the squared neutrino masses. Observations of solar neutrinos constrain  $\Delta m_{2,1}^2 = m_2^2 - m_1^2$ , while experiments observing atmospheric neutrinos, those produced by cosmic rays colliding with nuclei in the upper atmosphere, are sensitive to  $\Delta m_{3,1}^2 = m_3^2 - m_1^2$ . The current values of these constraints are approximately  $\Delta m_{2,1}^2 \approx 2.5 \times 10^{-5} \text{eV}^2$ ,  $\Delta m_{3,1}^2 \approx 7.5 \times 10^{-5} \text{eV}^2$  (Qian and Vogel, 2015). However, because these

experiments are not sensitive to an absolute mass scale, the hierarchy of masses remains unclear. Specifically, it is not yet known whether  $m_3$  is greater or lesser than  $m_1$  and  $m_2$ . The former case is referred to the ‘normal’ hierarchy, and the latter as the ‘inverted’ hierarchy.

While a fascinating problem and focus of ongoing research, the specific nature of the neutrino mass hierarchy is not directly relevant to this work. What is of relevance, for reasons discussed below (Section 1.5.5), is the sum of the masses of the three active neutrino species  $\Sigma m_\nu = \sum_i \nu_i = m_1 + m_2 + m_3$ . The above values of  $\Delta m_{2,1}^2$  and  $\Delta m_{3,1}^2$  impose a strong lower limit on  $\Sigma m_\nu$  of 0.056(0.095) eV for a normal (inverted) mass hierarchy.

## 1.5.2 The Cosmic Neutrino Background

The existence of neutrinos has interesting implications for cosmology. In particular, the frequent weak interactions occurring at high temperatures in the early Universe (such conditions being required by the standard hot big bang model) would produce a large number of neutrinos. As the Universe cools, the weak interaction rate falls below the expansion rate and the neutrinos decouple from the rest of the matter, forming the cosmic neutrino background (C $\nu$ B). This occurs at  $t \sim 1$ s, meaning that the C $\nu$ B in principal carries information about the Universe pre-dating the surface of last scattering, although direct detection remains a distant possibility.

Prior to decoupling, weak interactions are sufficiently rapid to maintain thermal equilibrium at a single temperature between the neutrinos and the “thermal bath” of matter and radiation. As spin 1/2 particles, the distribution of energies among neutrinos obeys the relativistic Fermi-Dirac distribution. After decoupling, the neutrinos that now constitute the C $\nu$ B evolve largely independently of the physics of the rest of the universe, retaining a close approximation of their equilibrium distribution:

$$f(\epsilon) = \frac{g_s}{h_p^3} \frac{1}{\epsilon/k_B T_\nu + 1} \quad (1.23)$$

where  $\epsilon = a(p^2 + m_\nu^2)^{1/2}$  is the comoving energy,  $T_{\nu,0}$  is the neutrino temperature,  $g_s$  is the number of spin degrees of freedom, and  $h_p$  and  $k_B$  are the Planck and Boltzmann constants respectively. (Ma, 2000).

Although neutrino decoupling does not occur instantaneously at a fixed  $T_{\nu,dec}$  as the precise temperature at which decoupling occurs is dependent on the neutrino flavour, the instantaneous approximation is reasonably accurate. Under this assumption, since the momenta and temperature are affected identically by the expansion of the Universe, the CνB retains both the comoving number density and the momentum spectrum of the coupled neutrinos, i.e.:

$$f_{eq}(p) = \left[ \exp\left(\frac{p}{T} - \frac{\mu_\nu}{T}\right) + 1 \right]^{-1}, \quad (1.24)$$

where  $T$  is the temperature, and  $\frac{\mu_\nu}{T} \equiv \xi_\nu$ , the ratio of the neutrino chemical potential to the temperature, is the neutrino degeneracy parameter.

The value of  $T_{\nu,dec}$  can be approximated by equating the weak interaction rate

$$\Gamma_\nu = \langle \sigma_\nu n_\nu \rangle \sim G_F^2 T^5, \quad (1.25)$$

where  $G_F$  is Fermi's Constant, with the expansion rate

$$H = \sqrt{\frac{8\pi}{3M_p^2} \rho} \sim \frac{T^2}{M_p}, \quad (1.26)$$

where  $M_p$  is the planck mass and  $\rho$  is the total energy density which is dominated by radiation so that  $\rho \propto T^4$ . Equating these gives:

$$T \sim (M_p G_F^2)^{-1/3} \sim 1\text{MeV} \quad (1.27)$$

putting the time of neutrino decoupling at approximately 1 second after the big bang.

Shortly after this point, pair production of electron-antielectron pairs becomes inefficient, heating the photons by  $e^\pm$  annihilations. If it is assumed that having already decoupled the neutrinos are unaffected in this entropy transfer, the entropy of the elec-

tromagnetic plasma is conserved. Consequently, the change in the photon temperature before and after this point can be calculated. As their evolution will be identical with the exception of this discontinuity, we can equate the photon temperature before this point with the neutrino temperature:  $T_\gamma^{before} = T_\nu^{before}$ . Therefore:

$$\frac{T_\gamma}{T_\nu} = \frac{T_\gamma^{after}}{T_\gamma^{before}} = \left(\frac{11}{4}\right)^{\frac{1}{3}} \approx 1.40102 \quad (1.28)$$

according to Lesgourgues and Pastor (2012). The combination of this with the momentum spectrum presented in Equation 1.24 allows present-day properties of the CνB to be conveniently calculated. As the neutrinos are governed by Fermi-Dirac statistics, their number density per flavour may be calculated as:

$$n_\nu = \frac{3}{11}n_\gamma = \frac{6\zeta\{3\}}{11\pi^2}T_\gamma^3 \quad (1.29)$$

where  $\zeta\{X\}$  is the zeta function of  $X$ , leading to a present day value of approximately  $113 \text{ cm}^{-3}$  per flavour or  $339 \text{ cm}^{-3}$  in total in the standard case of 3 neutrino species. The total energy density of neutrinos, must be calculated numerically, however the extreme limits are well defined analytically as:

$$\begin{aligned} \rho_\nu(m_\nu \ll T_\nu) &= \frac{7\pi^2}{120} \left(\frac{4}{11}\right)^{\frac{4}{3}} T_\nu^4 \\ \rho_\nu(m_\nu \gg T_\nu) &= m_\nu n_\nu. \end{aligned} \quad (1.30)$$

Consequently, in the non-relativistic limit the contribution of the massive neutrinos to the energy density, and consequently their effect on cosmology, is a function of the sum of their masses. Current constraints on the values of  $\sqrt{\Delta m_{3,1}^2}$  and  $\sqrt{\Delta m_{2,1}^2}$  both exceed the present day value of  $T_\nu$ , therefore at least two of the neutrino species must be non-relativistic today. If the third species is sufficiently light to have remained relativistic, its relative contribution to  $\rho_\nu$  will consequently be negligible. In the more commonly used cosmological units of the ratio to the universal critical density, this can be expressed as:

$$\Omega_\nu = \frac{\rho_\nu}{\rho_{crit}} = \frac{\sum_i m_i}{93.14h^2 \text{ eV}} \quad (1.31)$$

### 1.5.3 Neutrino Damping Length

Following their decoupling from matter and radiation, neutrinos can be described as a collisionless fluid, the constituent particles of which free-stream with a characteristic velocity equal to their thermal velocity  $v_{th}$  (at least on average). As a consequence, over a given time interval they will move out of overdensities whose physical size is smaller than the distance they can travel in that time. In other words, density perturbations will be damped on scales smaller than the free-streaming length.

One can define the free-streaming wavenumber as:

$$k_{FS} = \left( \frac{4\pi G \bar{\rho}(t) a^2(t)}{v_{th}^2(t)} \right)^{1/2}. \quad (1.32)$$

Neutrinos become relativistic at time  $t_{NR}$ , the point at which their kinetic energy  $3k_B T_\gamma$  is comparable to their rest mass energy  $m_\nu c^2$ . While the neutrinos are relativistic  $v_{th}$  is approximately  $c$  and the free-streaming length is approximately equal to the Hubble radius. After becoming non-relativistic, the thermal velocity decays like

$$\begin{aligned} v_{th} &= \frac{\langle p \rangle}{m_\nu} \\ &\approx 158(1+z) \left( \frac{m_\nu}{\text{eV}} \right)^{-1} \text{ kms}^{-1} \end{aligned} \quad (1.33)$$

such that the non-relativistic free streaming wavenumber is given by:

$$k_{fs}(t) = 0.8 \frac{\sqrt{\Omega_\Lambda + \Omega_m(1+z)^3}}{(1+z)^2} \left( \frac{m}{\text{eV}} \right) h\text{Mpc}^{-1}. \quad (1.34)$$

The free streaming length continues to increase after the neutrinos become non-relativistic, but does so more slowly than the scale factor. The comoving free streaming length therefore actually reaches a maximum at  $t_{NR}$ . The comoving wavenumber for this point can be calculated as

$$k_{NR} = 0.018 \Omega_m^{1/2} \left( \frac{m_\nu}{\text{eV}} \right)^{1/2} h\text{Mpc}^{-1} \quad (1.35)$$

Table 1.1: Neutrino free-streaming lengths corresponding to BAHAMAS runs with massive neutrinos. The columns are: (1) The simulation run considered; (2) The comoving free-streaming wave number at  $t_{NR}$ ; and (3) The comoving free-streaming length at  $t_{NR}$ . The values given in columns (2) and (3) are calculated using Eqn. 1.35 with values from Table 3.1

| (1)<br>BAHAMAS run | (2)<br>$\log(k_{NR})$<br>[ $\log(h\text{Mpc}^{-1})$ ] | (3)<br>$\lambda_{NR}$<br>[ $h^{-1}\text{Mpc}$ ] |       |
|--------------------|---|---|-------|
| WMAP-7             | NU 0.06   | -2.633  | 429.2 |
|                    | NU 0.12   | -2.482  | 303.5 |
|                    | NU 0.24   | -2.332  | 214.6 |
|                    | NU 0.48   | -2.181  | 151.7 |
| <i>Planck</i>      | NU 0.06   | -2.612  | 409.5 |
|                    | NU 0.12   | -2.460  | 288.5 |
|                    | NU 0.24   | -2.307  | 202.7 |
|                    | NU 0.48   | -2.152  | 141.8 |

(Lesgourgues and Pastor, 2014).

In Table. 1.1 I present values of the comoving free streaming length  $\lambda_{NR}$  and wavenumber  $k_{NR}$  calculated using Eqn. 1.35 for the various neutrino models used in this Thesis. These simulations comprise a  $400 h^{-1}$  Mpc comoving periodic box. As can be seen from the Table,  $\lambda_{NR}$  is comparable with the box size in all cases, with only the lowest mass neutrino realisation,  $m_\nu = 0.06$  eV, exceeding the box size. Consequently, the simulation runs used in this Thesis cover (almost or entirely) the full range of scales at which neutrino free-streaming is expected to impact on large-scale structure (LSS) formation.

#### 1.5.4 Mass Constraints

Current observations are consistent with a flat universe, i.e.  $\Omega_{total} = \Omega_m + \Omega_\nu + \Omega_\Lambda \approx 1$ , with the contribution of non-relativistic matter  $\Omega_m$  approximately equal to 0.3. By application of equation 1.31, this places a hard upper limit on the summed neutrino mass of:

$$\Sigma m_\nu \lesssim 27.9 h^2 \text{ eV} \quad (13.7 \text{ eV for } h = 0.7) \quad (1.36)$$

in the extreme case where  $\Omega_m = \Omega_\nu$ .

More reasonable constraints can be obtained by careful analysis of cosmological data. In brief, the presence of massive neutrinos that are relativistic at decoupling alters the CMB temperature anisotropy spectrum  $C_l^T$  and matter power spectrum  $P(k)$ : delaying the time of equality, enhancing small scale perturbations and expanding the size of the sound horizon at equality; and reducing the growth of CDM fluctuations. This effect can be seen as a slight enhancement and shift to lower  $l$  of the acoustic peaks in  $C_l^T$ , and a concomitant attenuation in  $P(k)$  at high  $k$ . Mass constraints derived from these effects depend on the cosmological observations included in the analysis.

Briefly, CMB data alone is able to set a limit of  $\sum M_\nu < 1.31.4$  eV depending on whether the dark energy component is a cosmological constant or not. Introducing observations sensitive to the background cosmological evolution can greatly improve this boundary, for example the inclusion of direct  $H_0$  measurements as well as BAO scale observations reduces this limit to  $\sum M_\nu < 0.48$  eV.

In addition to the CMB, LSS measurements can provide useful constraints on  $P(k)$  at a range of scales and redshifts. The most applicable observations are:

**Galaxy or GGC clustering.** The use of the spatial distribution of objects to constrain cosmological parameters is one of the more venerable techniques on this list, dating back to the work of Rubin (1954) and Limber (1954), at which stage its calculation comprised predominantly of manually counting galaxies in specified cells on photographic plates. The advent of reliable redshift measurements to provide line-of-sight distance information and computers with which to analyse the ever larger catalogues becoming available has only increased the applicability of this measurement (see, for example, Peebles (1980)). Relating the power spectrum of galaxies or groups to  $P(k)$  is made difficult at small scales where the corrections are non-linear and redshift-space distortions and light-to-mass bias would need to be accurately constrained. In the linear regime, this can constrain the shape of  $P(k, z)$ , but the inclusion of the bias as a (admittedly well motivated) free parameter makes it impossible to constrain the amplitude. More

recent work by (amongst others) Thomas et al. (2010) and Reid et al. (2010a) using the Sloan Digital Sky Survey (SDSS) and Riemer-Sørensen et al. (2012) using data from the Dark Energy Survey (DES) have placed valuable constraints on the halo power spectrum. For sufficiently deep data sets, there is also the option of performing tomography, as has been done with the Sloan Digital Sky Survey (SDSS) data by Xia et al. (2012).

**Cluster mass function.** As their formation depends on the growth of initial density perturbations, the distribution of the masses of haloes that make up LSS, and therefore that of the GGCs that form within them, may be related to the properties of the initial perturbation field. Specifically, the mass function of GGCs  $dn(M, z)/dM$  within a mass and redshift bin is related to the quantity  $\sigma^2(M, z)$ , the variance in density found within a sphere containing mass  $M$ . This can be derived from the convolution of an appropriate window function with  $P(k, z)$ . Seminal work with N-body simulations by Press and Schechter (1974) established a useful theoretical framework by which the mass function could be studied. Subsequent extensions and alternative derivations have followed, notably Jenkins et al. (2001), predominantly motivated by the results of ever more detailed numerical simulations. Despite the difficulties entailed in observationally determining GGC or halo masses, observational constraints on  $dn(M, z)/dM$  and therefore  $\sigma_8$  are provided by (amongst others) Mantz et al. (2010) and Reid et al. (2010b), the former using X-ray observations from ROSAT, the latter the MaxBCG catalogue.

**Galaxy weak lensing.** The effects of foreground mass concentrations on the light of background sources were first detected by Lynds and Petrosian (1986), who observed a ring-like distributions of light in surveys of GGCs, although it the gravitational mechanism by which they arise was not proposed until Soucail et al. conducted further analysis of one such ring in 1987. While such examples of strong lensing are too rare and limited to exceptionally high mass foreground lenses to be of much assistance when studying *populations* of GGCs, the potential of “weak” lensing effects to carry information about GGC masses has been

well established since its first observational detection by Tyson et al. (1990). Briefly: as the image of a background galaxy passing through an overdensity becomes extended tangential to the centre of mass ('sheared'), a statistical analysis of the alignments of galaxies can map the foreground lensing potential. This can be related to  $P(k, z)$  via the Poisson equation. As with galaxy clustering, it is possible to capture redshift evolution by splitting a sufficiently deep catalogue into redshift bins and performing shear tomography. More recent cosmic shear surveys (see, for example, Tereno et al. (2009)) have achieved sufficient precision to provide bounds on neutrino parameters.

***Lyman-alpha forest.*** The light emitted from distant quasars is depleted at wavelengths corresponding to the Lyman alpha series of hydrogen transitions as photons are absorbed by foreground neutral hydrogen in the interstellar galactic medium (IGM). As photons are continuously redshifted, the *observed* wavelength at which light from a given source is affected depends on the line-of-sight distance from the observer to the absorbing IGM. The fraction of photons of that wavelength that were absorbed at that point is proportional to its local density of neutral hydrogen. Hence, within a limited wavelength range referred to as the *Lyman alpha forest*, the variation of quasar spectra with wavelength traces the variation in hydrogen density along the line of sight. This mechanism was first proposed by Lynds (1971) to explain the absorption spectrum of quasar 4C 05.34, and linked to the distribution of intergalactic gas along the line-of-sight (as opposed to interactions within the quasar sources themselves) by Oort (1981).

The Fourier expansion of the spectrum (averaged over sufficiently many spectra) provides an estimate of the flux power spectrum that can then be related to  $P(k)$ . This is complicated somewhat by the fact that the scales probed by this technique are mildly non-linear, typically  $0.3 < k < 3h\text{Mpc}^{-1}$ , and therefore require numerical techniques including hydrodynamical treatment of baryonic physics in order to model accurately. Nonetheless, analyses of Lyman alpha data alone place a bound of  $\sum M_\nu < 0.9eV$ . Work by Viel et al. (2010), for example, has succeeded in inferring neutrino mass bounds by these means.

Better results can be achieved by combining the data listed above, allowing the models to be constrained over a wider range in  $k$  and  $z$ . The results arrived at depend somewhat on which data are used, and I refer the reader to Lesgourgues and Pastor (2012) for a detailed overview. However, taken as a whole, the combinations of all of the data sets described above consistently indicate an upper bound of  $\Sigma m_\nu < 0.3$  eV at a 95% confidence level for the standard  $\Lambda$ CDM model, or  $\Sigma m_\nu < 0.5$  eV for DE with an arbitrary equation of state.

### 1.5.5 Implications for Structure Formation

Due to their small mass and thermal decoupling, the neutrinos constituting the  $C\nu B$  remain relativistic up to relatively late times. As a result, they are less susceptible to gravitational collapse than the rest of the matter content of the Universe. Neutrinos tend to free-stream out of overdensities. Consequently, whatever portion of the mass content of the Universe is contributed by the neutrinos is functionally unavailable for structure formation. This is highly significant as it means that knowledge of the neutrino physics may be necessary for accurate predictions of large-scale structure or, inversely, if the other factors can be constrained, observations of large-scale structure can be used to place constraints on the neutrino mass.

## 1.6 Cosmological Hydrodynamical Simulations

The highly non-linear nature of the processes governing galaxy formation, and therefore the overall growth of structure, require that numerical techniques be used to accurately model them. While these have the advantage of allowing simultaneous treatment of gravitational and hydrodynamical processes, limitations are imposed by the finite spatial and mass resolutions.

The current highly advanced crop of numerical simulations have humble roots. The very first gravitational simulation considered only 37 particles, and predated the widespread

use of digital technology by almost 2 decades. Instead, particles were represented by light bulbs, and the gravitational force between them approximated by the resultant flux (Holmberg, 1941).

The advent of digital computing made carrying out these sorts of calculations significantly easier, and collisionless “N-body” gravitational simulations of roughly 100 particles were being produced by the early 1960s (von Hoerner, 1960, 1963; Aarseth, 1963). Simulations incorporating gas dynamics closely followed, with seminal 1-dimensional work carried out by Larson (1969), as the scale and detail of simulations continued to increase.

The application of these tools to the study of the growth of cosmological structure has its roots in the work of Press and Schechter (1974) who used N-body simulations to study the mass distribution of haloes arising from hierarchical structure formation. This development took place alongside a number of milestones in cosmological theory, notably the development of plausible dark matter models (Cowsik and McClelland, 1972; Bond et al., 1980) and Gaussian random field theory (Bardeen et al., 1986), that spurred an increased interest in cosmological simulation.

Gravitational N-body simulations provided invaluable insights into the behaviour of DM, for example the halo density profile determined by Navarro et al. (1996), and the numerous successes of the Millennium Simulation (Springel et al., 2005b) and its successors in describing the distribution of matter on extremely large scales. However, for the study of GGCs and smaller scales, such as the formation or dynamics of individual galaxies, it has become increasingly apparent that non-gravitational physics must be taken into account. This has necessitated the development of hydrodynamical simulations that incorporate prescriptions for baryonic physics alongside the gravitational calculations. While such projects inevitably lag behind their N-body counterparts in terms of resolution due to the increased number of calculations required per-particle, they are more successful at reproducing galaxy- and GGC-scale observations. For example, Metzler and Evrard (1994) demonstrated that the inclusion of stellar feedback in the form of galactic winds produced more realistic galaxy cluster properties. As available computational power continued to increase, such ‘hydrodynamical’ simula-

tions were able to probe increasing scales in increasing detail, with Pearce et al. (1999) presenting the first successful effort to simulate galaxy formation at sufficiently large scales that the *clustering* of the resultant galaxies could be studied.

An ongoing challenge of these programs has been the calibration of the descriptions for physical effects that fall below the spatial or mass resolution of the simulation, for example radiative cooling and feedback from star formation, supernovae and AGN heating. These ‘sub-grid’ prescriptions must be put in by hand to approximate the larger-scale effects of these processes, and can therefore require careful tuning in order to match observations.

### 1.6.1 Implications of Neutrino Dark Matter

As an example of the power of cosmological simulation, consider the following case. In the 1980s the presence of the  $C\nu B$  posed a potential solution to the ongoing question regarding the exact nature of DM. For a neutrino mass of  $\sim 30$  eV, the neutrino density  $\Omega_\nu$  would be sufficient to match observations consistent with a flat universe without invoking DM beyond the standard model. However, this gives a characteristic damping length on the scale of tens of megaparsecs. With the neutrino mass component dominating the gravitational behaviour of the Universe, this would prevent the collapse of overdensities smaller than this scale. Analogously to the calculation of the Jeans mass, one can calculate the minimum mass for an overdensity to undergo collapse under these conditions. For these assumptions, this mass is of order  $10^{15}M_\odot$ , i.e. the mass of a supercluster. Hot dark matter-dominated universes therefore undergo top-down structure formation, with the most massive objects forming first. For a full derivation and discussion of this calculation, see Bond and Efstathiou (1984).

While initially promising, this model was proven to be inconsistent with the observed Universe through the application of two separate simulation approaches. Firstly, simulations of nonlinear collapse taking into account the dissipation of baryonic matter carried out by, for example, Bond et al. (1984); Shapiro et al. (1983) showed that the shock of gravitational collapse on this scale heats the baryonic content to the point

where 85% remains unable to condense. The absence of X-rays from shock-heated gas and the obvious inconsistency of the observed “cooled” mass contributing only 15% of the total baryonic matter when primordial nucleosynthesis constrains  $\Omega_b \approx 0.1$  strongly disfavour this model (White, 1986).

Meanwhile, N-body simulations by (amongst others) Frenk et al. (1983) demonstrated that the observed distribution of superclusters restricted their formation time to  $z_{sc} < 2$  and favoured  $z_{sc} \leq 0.5$ .

Cosmological simulations are therefore responsible for ruling out neutrinos as the dominant component of DM, and place a strong upper limit on their mass.

### 1.6.2 OWLS, and its descendants

The OverWhelming Large Simulations (hereafter OWLS) project presented in Schaye et al. (2010) represented an important development in the field of cosmological modelling. This was the first time that simulations succeeded in simultaneously matching the observed present-day properties of the hot plasma and stellar populations within galaxy groups, the former only made possible by the inclusion of ‘sub-grid’ prescriptions for AGN feedback.

However, computational limitations restrict not only the minimum mass and spatial resolution, but also the total number of particles that can be followed, and by extension places an upper limit on the volume that can be considered for a given resolution. While successful in reproducing the properties of individual groups and clusters, the 100 Mpc on a side cube OWLS volume did not contain enough of these massive (and therefore rare) systems to allow the study of their population properties. In order to facilitate this, Le Brun et al. (2014) produced the cosmo-OWLS extension, expanding the volume to 400 Mpc on a side. In terms of its simulation strategy, cosmo-OWLS aimed to explore the parameter space associated with the modelling of AGN feedback at fixed cosmology.

The latest addition to this is the BAryons and HAloes of MAssive Systems (BAHAMAS,

McCarthy et al. 2018). While mechanically closely related to the cosmo-OWLS project, with which it shares code, total volume, (some) subgrid prescriptions and resolution, BAHAMAS differs markedly in two significant factors. First, it includes a prescription for the presence of a cosmic background of massive neutrinos. Second, BAHAMAS has an almost perfectly opposed simulation strategy to cosmo-OWLS, adopting a fixed subgrid model for baryonic physics while varying the background cosmology, specifically the value chosen for the summed mass of the three active neutrino species. It is these two complementary simulation suites, cosmo-OWLS and BAHAMAS, that are used within this thesis.<sup>7</sup>

## 1.7 The Internal Structure of Haloes

Both neutrino free-streaming and baryonic feedback, as discussed above, act to oppose the formation of structure, and are therefore expected to exhibit qualitatively broadly similar effects on the *abundances* of haloes. It is, however, less evident in what way the *internal* properties of individual haloes are impacted. Two diagnostics of particular interest are the radial mass profiles and mass–concentration relations. I briefly summarise these measurements below.

---

<sup>7</sup>BAHAMAS and cosmo-OWLS are part of an ongoing effort by the community to produce cosmological simulations of very high accuracy. Notable other projects include the EAGLE (Evolution and Assembly of GaLaxies and their Environments) and Illustris simulation sets. Briefly, EAGLE, like cosmo-OWLS, is a successor to the OWLS project and uses much of the same simulation framework. It differs primarily in volume and resolution – whereas cosmo-OWLS aimed to simulate a significantly larger volume, EAGLE retains the same box size as OWLS, but simulates it at much higher resolution. This reflects the EAGLE project’s focus on the physics of galaxy formation and evolution.

The Illustris project is similar in focus and scope to EAGLE, however it utilises a novel adaptive mesh refinement (AMR) realisation in which cells can move with time, as opposed to the smoothed particle hydrodynamics (SPH) of EAGLE. Significantly, it shares EAGLE’s focus on galaxies and their formation, and is of comparable volume and resolution (although a direct resolution comparison between SPH and AMR is impossible).

In both cases, the simulations are engineered to produce reasonably accurate reproductions of the properties of the observed galaxy population. EAGLE, for example, calibrates the subgrid model directly on the  $z \sim 0$  galaxy stellar mass function. While they exhibit remarkable success in the galaxy regime, these projects are ill suited to studies of GGCs due to their comparatively limited volume. Additionally, they lack the prescription for a massive neutrino background available in BAHAMAS.

I refer the reader to Schaye et al. (2015) and Crain et al. (2015) for further information on EAGLE; and to Vogelsberger et al. (2014) for Illustris.

### 1.7.1 GGC density profiles

As mentioned above, one of the early successes of cosmological simulations was the discovery by Navarro et al. (1996) of the universality of the spherically-averaged 1-dimensional radial density profiles of DM haloes. Later work has shown that this degree of self-similarity does not exactly mirror reality due to the scale-dependent nature of the non-gravitational physical effects that govern galaxy formation (see Sections 1.4.1 - 1.4.3, and the references therein). Nonetheless, the Navarro-Frenk-White (NFW) profile remains a good approximation outside the central (i.e. galaxy-dominated) regions.

Measuring the density profile observationally presents a number of challenges as the dark matter mass in radial bins is difficult to measure directly. However, spectrographic X-ray data in radial annuli, for example, can be used with careful deprojection to infer the dynamical properties of the hot gas component including its mass profile (Voigt and Fabian, 2006; Newman et al., 2013). On smaller scales, stellar dynamics of galaxies can be used similarly to constrain the overall mass distribution.

A full discussion of the observational techniques involved in measuring the GGC density profile is beyond the scope of this work, however in the context of perfectly constrained simulation data it presents a useful and informative diagnostic.

### 1.7.2 The Mass-Concentration Relation

Closely related to the density profile is the mass-concentration relation. This arises from the fact that the scaling parameters that define the Navarro-Frenk-White (NFW) profile may be expressed in terms of the halo mass  $M_\Delta$  and a dimensionless “concentration” parameter  $c$ , this latter being the ratio of the radius within which the aforementioned mass is measured,  $r_\Delta$  to the “scale radius”  $r_s$ , the point where the gradient of the density profile is equal to the isothermal value of  $r^{-2}$ .<sup>8</sup> This is a convenient way to

---

<sup>8</sup>In most cases,  $r_\Delta$  is chosen to approximate the virial radius of the halo, so the concentration parameter may be conceptualised as the ratio of virial and scale radii.

generalise the internal structures of the halo population in the form of the relationship  $c(M)$  between the concentration and halo mass.

In gravitational simulations, the characteristic concentration of a halo depends solely on the critical density of the universe at the time of its collapse. As a consequence, at fixed redshift  $c$  increases monotonically with halo mass as the more massive haloes formed at earlier times when the value of  $\rho_{crit}$  was higher. A degree of scatter is introduced by the dependence of the subsequent evolution of  $c$  on the halo mass, with evolution happening faster in lower mass haloes. The inclusion in simulations of baryonic feedback and other non-gravitational effects that modify the density profiles has a concomitant impact on  $c(M)$ .

Observationally,  $c(M)$  suffers the same difficulties as the density profile, compounded by its own intrinsic scatter. Nonetheless it remains a useful tool for constraining the internal properties of GGCs as a population. (Ludlow et al., 2014)

## 1.8 Thesis Layout

This thesis is organised as follows:

In Chapter 2 I explore the effects of baryon physics (particularly feedback from active galactic nuclei, AGN) and the free streaming of massive neutrinos on LSS formation and the properties of GGCs, in the context of simulated haloes drawn from the cosmo-OWLS and BAHAMAS simulation suites. In particular, I examine the effects both in isolation, and when included self-consistently, investigating in detail the extent to which the two may be addressed independently. I focus on five diagnostics: i) the halo mass function; ii) halo mass density profiles; iii) the halo mass–concentration relation; iv) the clustering of haloes; and v) the clustering of matter.

Consistent with previous studies, I find that both AGN feedback and neutrino free-streaming suppress the total matter power spectrum, although their scale and redshift dependencies differ significantly. The inclusion of AGN feedback can significantly

reduce the masses of GGCs, and increase their scale radii. These effects lead to a decrease in the amplitude of the mass–concentration relation and an increase in the halo autocorrelation function at fixed mass. Neutrinos also lower the masses of GGCs while having no significant effect on the shape of their density profiles (thus also affecting the mass–concentration relation and halo clustering in a qualitatively similar way to feedback). I show that, with only a small number of exceptions, the combined effects of baryon physics and neutrino free-streaming on all five diagnostics can be estimated to typically better than a few percent accuracy by treating these processes independently (i.e., by multiplying their separate effects).

As part of this investigation, I establish that the amplitude of the real-space, 3D, 2-point autocorrelation function of GGC haloes is sensitive to the summed value of the neutrino masses  $\sum M_\nu$ . I pursue this further in Chapter 3, exploring the possibility of using the observed clustering of GGCs to constrain the neutrino mass. I use galaxy catalogues drawn from the GAMA survey, and compare to equivalent catalogues taken from simulated observations constructed from lightcones of the BAHAMAS simulations with a range of values of  $\sum M_\nu$ . In order to ensure the maximum methodological consistency, I treat the simulated and observed data identically at each stage. From these, I construct GGC catalogues, assigning galaxies on the basis of a Friends-of-Friends (FoF) algorithm, then estimate the 2-point 3D redshift space autocorrelation function of GGCs in observable bins (specifically the GGC richness and integrated stellar mass).

I conclude that these measurements have insufficient statistical power to constrain the neutrino mass. By comparison with a parallel analysis making use of the ‘true’ properties of the simulated GGCs (i.e. those perfectly constrained by the detailed knowledge of the simulation space), I determine that this is primarily the result of scatter in the observable–halo mass relations ‘smearing out’ the heavily mass-dependent effect of neutrino free-streaming. Significantly, however, I find by direct comparison between the BAHAMAS and GAMA results that the simulations reproduce the observed GGC clustering to remarkable precision.

Finally, in Chapter 4 I provide a summary of these results, along with a discussion of

future work that will build on this work.

## **Chapter 2**

# **The Separate and Combined Effects of Baryon Physics and Neutrino Free-streaming on Large-Scale Structure**

The majority of the work presented in this chapter and Appendix A was published in a peer reviewed journal:

Mummery, B. O., I. G. McCarthy, S. Bird, and J. Schaye

2017. The separate and combined effects of baryon physics and neutrino free streaming on large-scale structure. *MNRAS*, 471:227-242

### **2.1 Introduction**

Recent simulation-based work has shown that various physical processes associated with galaxy formation (e.g., radiative cooling, star formation, and feedback processes) can significantly affect not only the predicted distribution of baryons, but also that of the underlying dark matter component. For example, it has been shown that both the

total matter power spectrum (e.g., van Daalen et al. 2011; Schneider and Teysier 2015) and the halo mass function (e.g., Sawala et al. 2013; Cui et al. 2014; Velliscig et al. 2014; Cusworth et al. 2014; Schaller et al. 2015) can be affected at the tens of percent level relative to that predicted by a standard gravity-only dark matter simulation. If these effects are ignored, they are expected to lead to significant biases in cosmological parameters inferred by comparing predicted and observed aspects of large-scale structure (LSS) (e.g., Semboloni et al. 2011; Eifler et al. 2015; Harnois-Déraps et al. 2015).

However, galaxy formation is not the only process that affects the resultant distribution of LSS. Recently, there has been a resurgence in interest in the effects of massive neutrinos. This resurgence has been driven by the apparent tension in the observed abundance of massive GGCs compared to that predicted when a *Planck* cosmology based on the primary CMB is adopted (e.g., Planck Collaboration et al. 2014, 2016b), in conjunction with similar tensions between the *Planck* primary CMB constraints and those derived from tomographic analysis of cosmic shear data (Heymans et al., 2013; Hildebrandt et al., 2017). It has been argued that massive neutrinos can potentially reconcile this tension (e.g., Wyman et al. 2014; Battye and Moss 2014), although this remains controversial (e.g., MacCrann et al. 2015). Regardless of whether neutrinos resolve the tension, atmospheric and solar oscillation experiments have found that the three active species of neutrinos have a summed mass of at least 0.06 eV (0.1 eV) when adopting a normal (inverted) hierarchy (Lesgourgues and Pastor, 2006). The fact that neutrinos have appreciable mass and will act as a form of hot dark matter that will resist significant gravitational collapse (due to free streaming motion), implies that they will affect the predicted LSS. Whether these effects are minor or dominant in comparison to those due to galaxy formation is presently unclear and depends on the (relatively poorly constrained) absolute mass scale of the neutrinos and the efficiencies of relevant feedback processes.

Given that both baryon physics and massive neutrinos likely play a role in the formation of LSS in the Universe, it is important to consider their combined effect and whether it amounts to more (or less) than ‘the sum of its parts’. That is, to what ex-

tent is there cross-talk between the baryon physics and neutrinos? Do they suppress or enhance each other's effects on LSS, or can they be treated separately?

The work presented in this chapter aims to address these questions by means of direct numerical simulation. The effects of baryon physics and massive neutrinos are considered separately and in combination, using the recent cosmo-OWLS (Le Brun et al., 2014; McCarthy et al., 2014) and BAHAMAS (McCarthy et al., 2018) suites of cosmological hydrodynamical simulations. The two suites are complementary, in that cosmo-OWLS varies the implemented subgrid physics for stellar and AGN feedback at fixed cosmology (with massless neutrinos), while BAHAMAS varies the neutrino mass for a fixed (calibrated) feedback model. I further complement these simulations with reference dark matter-only simulations (both with massless and massive neutrinos). This combination of complementary simulations provides an unprecedented opportunity to examine the effects of both baryon feedback and the free-streaming of massive neutrinos not simply in isolation, but also capturing their combined effects on large-scale structure.

In this chapter I examine five different ways of characterising LSS:

1. The halo mass function;
2. The total mass density profiles in bins of halo mass;
3. The mass–concentration relation;
4. The spatial clustering of haloes (characterised by the 3D 2-point autocorrelation function); and
5. The clustering of matter (characterised by the total matter power spectrum)

I demonstrate that both feedback and neutrino free-streaming can have considerable effects on these aspects of LSS and that, to typically better than a few percent accuracy, their combined effects can be estimated by treating these processes independently (i.e., by multiplying their separate effects).

This chapter is organised as follows. In Section 2.2 I present a brief summary of the cosmo-OWLS and BAHAMAS simulations. In Section 2.3 I examine the effects of baryon physics and neutrinos on the abundance of haloes. In Section 2.4 I examine

their effects on the total mass density profiles (2.4.1) and the mass–concentration relation (2.4.2). In Sections 2.5 and 2.6 I explore how the spatial clustering of haloes and matter (respectively) are affected. Finally, in Section 2.7 I summarize and discuss my findings.

## 2.2 Simulations

I use the cosmo-OWLS (Le Brun et al., 2014; McCarthy et al., 2014) and BAHAMAS (McCarthy et al., 2017) suites of cosmological hydrodynamical simulations, both of which are descendants of the Overwhelmingly Large Simulations (OWLS) project detailed in Schaye et al. (2010). As already noted in Section 2.1, the two suites are predicated on different investigation strategies. Cosmo-OWLS varies the implemented subgrid physics for stellar and AGN feedback at fixed cosmology. In contrast, BAHAMAS implements a fixed, calibrated feedback model while varying the cosmology. These approaches are complimentary, allowing the two effects to be examined independently as well as in conjunction. Below I provide a brief overview of the simulations, but I refer the reader to Le Brun et al. (2014) and McCarthy et al. (2018) for further details of the simulations and comparisons with the observed properties of present-day GGCs.

Table 2.1 provides a summary of the included subgrid physics and the model parameter values for the various cosmo-OWLS and BAHAMAS runs I have used in this chapter.

### 2.2.1 cosmo-OWLS

The cosmo-OWLS suite of cosmological hydrodynamical simulations consists of 400  $\text{Mpc}/h$  comoving on a side, periodic box simulations containing  $2 \times 10^4$  particles. The simulations adopt a cosmology based on the maximum likelihood parameter values obtained from the analysis of WMAP-7 data (Komatsu et al., 2011); i.e.,  $\{\Omega_m, \Omega_b, \Omega_\Lambda, \sigma_8, n_s, h\} = \{0.272, 0.0455, 0.728, 0.81, 0.967, 0.704\}$ . The algorithm of Eisenstein and Hu (1999) was used to compute the transfer function and N-GenIC (de-

Table 2.1: Included subgrid physics and model parameter values for the cosmo-OWLS and BAHAMAS runs used here. (1) Simulation name; (2) inclusion of photoionizing ultra-violet and X-ray backgrounds according to Haardt and Madau (2001); (3) inclusion of radiative cooling and star formation; (4) for runs with star formation,  $V_w$  is the velocity kick (in km/s) adopted in the stellar feedback (with a fixed mass-loading of 2); (5) inclusion of AGN feedback; (6)  $\Delta T_{\text{heat}}$  is the temperature by which gas is heated by AGN feedback; (7)  $n_{\text{heat}}$  is the number of gas particles heated by AGN feedback; (8) inclusion of massive neutrinos; (9) the summed mass of neutrinos (assuming a normal hierarchy of neutrino masses); (10) dark matter particle mass; (11) initial baryon particle mass. A more detailed discussion of these parameters can be found in Section 2.2.

| (1)<br>Simulation | (2)<br>UV/X-ray<br>background | (3)<br>Cooling and<br>star formation | (4)<br>$V_w$<br>[km/s] | (5)<br>AGN<br>feedback | (6)<br>$\Delta T_{\text{heat}}$<br>[K] | (7)<br>$n_{\text{heat}}$ | (8)<br>$\nu$ | (9)<br>$M_\nu$<br>[eV] | (10)<br>$M_{DM}$<br>[ $10^9 M_\odot/h$ ] | (11)<br>$M_{\text{bar},\text{init}}$<br>[ $10^8 M_\odot/h$ ] |
|-------------------|-------------------------------|--------------------------------------|------------------------|------------------------|--|--------------------------|--------------|------------------------|--|--|
| <b>cosmo-OWLS</b> |                               |                                      |                        |                        |  |                          |              |                        |  |  |
| NOCOOL            | Yes                           | No                                   | -                      | No                     | -                                      | -                        | No           | -                      | 3.75                                     | 7.54   |
| REF               | Yes                           | Yes                                  | -                      | No                     | -                                      | -                        | No           | -                      | 3.75                                     | 7.54   |
| AGN 8.0           | Yes                           | Yes                                  | 600                    | Yes                    | $10^{8.0}$                             | 1                        | No           | -                      | 3.75                                     | 7.54   |
| AGN 8.5           | Yes                           | Yes                                  | 600                    | Yes                    | $10^{8.5}$                             | 1                        | No           | -                      | 3.75                                     | 7.54   |
| AGN 8.7           | Yes                           | Yes                                  | 600                    | Yes                    | $10^{8.7}$                             | 1                        | No           | -                      | 3.75                                     | 7.54   |
| DMONLY            | No                            | No                                   | -                      | No                     | -                                      | -                        | No           | -                      | 4.50                                     | -  |
| <b>BAHAMAS</b>    |                               |                                      |                        |                        |  |                          |              |                        |  |  |
| NU 0.00           | Yes                           | Yes                                  | 300                    | Yes                    | $10^{7.8}$                             | 20                       | Yes          | massless               | 3.85                                     | 7.66   |
| NU 0.06           | Yes                           | Yes                                  | 300                    | Yes                    | $10^{7.8}$                             | 20                       | Yes          | 0.06                   | 3.83                                     | 7.66   |
| NU 0.12           | Yes                           | Yes                                  | 300                    | Yes                    | $10^{7.8}$                             | 20                       | Yes          | 0.12                   | 3.81                                     | 7.66   |
| NU 0.24           | Yes                           | Yes                                  | 300                    | Yes                    | $10^{7.8}$                             | 20                       | Yes          | 0.24                   | 3.77                                     | 7.66   |
| NU 0.48           | Yes                           | Yes                                  | 300                    | Yes                    | $10^{7.8}$                             | 20                       | Yes          | 0.48                   | 3.68                                     | 7.66   |
| NU 0.00 DM        | No                            | No                                   | -                      | No                     | -                                      | -                        | Yes          | massless               | 4.62                                     | -  |
| NU 0.06 DM        | No                            | No                                   | -                      | No                     | -                                      | -                        | Yes          | 0.06                   | 4.61                                     | -  |
| NU 0.12 DM        | No                            | No                                   | -                      | No                     | -                                      | -                        | Yes          | 0.12                   | 4.58                                     | -  |
| NU 0.24 DM        | No                            | No                                   | -                      | No                     | -                                      | -                        | Yes          | 0.24                   | 4.53                                     | -  |
| NU 0.48 DM        | No                            | No                                   | -                      | No                     | -                                      | -                        | Yes          | 0.48                   | 4.44                                     | -  |

veloped by V. Springel)<sup>1</sup> was used to make the initial conditions, at a starting redshift of  $z = 127$ . The dark matter and (initial) baryon particle masses are  $\approx 3.75 \times 10^9 h^{-1} M_\odot$  and  $\approx 7.54 \times 10^8 h^{-1} M_\odot$ , respectively. The gravitational softening is fixed to  $4 h^{-1}$  kpc (in physical coordinates below  $z = 3$  and in comoving coordinates at higher redshifts).<sup>2</sup>

The simulations were carried out with a version of the Lagrangian TreePM-SPH code GADGET3 (last described in Springel, 2005), which was modified to include new subgrid physics as part of the OWLS project. Le Brun et al. (2014) presented a set of five baryon physics models along with a corresponding dark matter only run, all of which adopted identical initial conditions. I make use of each of these for this investigation. These models are:

- DMONLY: A dissipationless “dark matter-only” simulation.
- NOCOOL: A standard non-radiative model; i.e., inclusion of baryons and hydrodynamics but no subgrid modules for radiative cooling, star formation, etc.
- REF: In addition to the inclusion of baryons and hydrodynamics, this model includes prescriptions for element-by-element radiative cooling (Wiersma et al., 2009a), star formation (Schaye and Dalla Vecchia, 2008a), stellar evolution,

<sup>1</sup><http://www.mpa-garching.mpg.de/gadget/>

<sup>2</sup>In principal, the gravitational forces between two simulation particles  $i$  and  $j$  may be calculated by simple Newtonian mechanics as:

$$\mathbf{F}_{i,j} = Gm_i m_j \frac{\mathbf{r}_j - \mathbf{r}_i}{|\mathbf{r}_j - \mathbf{r}_i|^3}. \quad (2.1)$$

However, problems arise at short distances for two reasons. First, simulation particles typically represent masses far in excess of the typical mass of a star ( $\sim 10^9 M_\odot$  in the case of BAHAMAS and cosmo-OWLS) and therefore represent systems the mass of which is distributed over some region. At a sufficiently close approach, therefore, the point mass approximation of the simulation particle is no longer a good description for the physical mass distribution it represents. Secondly, the increasingly rapid dynamics that result from close encounters between mass distributions means that at some limit the chosen timestep will fail to adequately capture their resulting motions.

These difficulties are typically addressed by smoothing the pointwise gravitational potential, modifying the gravitational law at small distances, for example as:

$$\mathbf{F}_{i,j}^{softened} = Gm_i m_j \frac{\mathbf{r}_j - \mathbf{r}_i}{(|\mathbf{r}_j - \mathbf{r}_i|^2 + \epsilon^2)^{3/2}} \quad (2.2)$$

where  $\epsilon$ , which determines the degree to which the potential is smoothed, is the softening length. This replaces the point mass with an extended mass distribution at sufficiently close approach (i.e.  $|\mathbf{r}_j - \mathbf{r}_i| \sim \epsilon$ ) and reduces to the point mass case in 2.1 for  $|\mathbf{r}_j - \mathbf{r}_i| \gg \epsilon$  Rodionov and Sotnikova (2005)

mass loss and chemical enrichment (Wiersma et al., 2009b) from Type II and Ia supernovae and Asymptotic Giant Branch stars, and kinetic stellar feedback (Dalla Vecchia and Schaye, 2008).

- AGN 8.0, AGN 8.5, and AGN 8.7: In addition to the physics included in the REF model, these models include a prescription for supermassive black hole (BH) growth and AGN feedback (Springel et al., 2005a; Booth and Schaye, 2009).

A full discussion of the black hole physics included in the AGN 8.0, AGN 8.5, and AGN 8.7 runs can be found in Springel et al. (2005a) and Booth and Schaye (2009), but I include an overview of them here. In brief, an on-the-fly friends-of-friends (FoF) algorithm, with a linking length of 0.2 times the mean interparticle separation, is run during the simulation and any FoF haloes identified with at least 100 dark matter particles that do not already contain a BH ‘sink’ particle are seeded with one, with an initial mass of 0.001 times the initial gas particle mass. BH particles then grow in mass via mergers with other BH particles and through gas accretion, as described in Booth and Schaye (2009). In terms of feedback, the BHs accumulate the feedback energy in a reservoir until they are able to heat neighbouring gas particles by a pre-determined amount  $\Delta T_{\text{heat}}$ . cosmo-OWLS uses 1.5 per cent of the rest-mass energy of the gas which is accreted on to the supermassive black holes for the AGN feedback, which results in a good match to the normalisation of the black hole scaling relations (Booth and Schaye 2009; Le Brun et al. 2014), independently of the exact value of  $\Delta T_{\text{heat}}$ . The three AGN models differ only by their value of  $\Delta T_{\text{heat}}$ , which is the most important parameter of the feedback model in terms of the gas-phase properties of the resulting GGC population (Le Brun et al. 2014; McCarthy et al. 2018). It is set to  $\Delta T_{\text{heat}} = 10^{8.0}$  K for AGN 8.0,  $\Delta T_{\text{heat}} = 10^{8.5}$  K for AGN 8.5, and  $\Delta T_{\text{heat}} = 10^{8.7}$  K for AGN 8.7. Note that since the same quantity of gas is being heated in these models, more time is required for the black holes to accrete a sufficient amount of gas to heat the adjacent gas to a higher temperature. Therefore, increased heating temperatures lead to more episodic and violent feedback events.

The range of cosmo-OWLS models considered here is notably somewhat extreme. While the AGN 8.0 and AGN 8.5 models skirt the upper and lower bounds of the observed trend between hot gas mass and halo mass for X-ray-bright galaxy groups (see Le Brun et al. 2014), the third AGN model, AGN 8.7, featuring the most extreme feedback, yields GGCs with gas fractions that are considerably lower than those observed. At the other end of the scale, the REF and NOCOOL models which neglect AGN feedback have significantly higher total baryon fractions than observed for local X-ray-bright galaxy groups (e.g., Sun et al. 2009). While this range of models is clearly somewhat extreme, there are three important caveats to consider:

- i)* since the role of observational selection effects is not well understood for GGCs, current observations cannot rule out the existence of a population of virialized groups which are X-ray faint and may have lower gas fractions, therefore the AGN 8.7 model cannot be necessarily excluded on this bases;
- ii)* there are too few observational constraints on high-redshift systems to judge whether or not the various models are realistic at earlier times; and
- iii)* for the purposes of this chapter, accurately reproducing the observed Universe is of secondary importance to my primary goal of investigating the underlying trends and interactions of these two mechanisms: baryonic feedback and neutrino free-streaming.

Bearing these caveats in mind, I elected to explore the trends using the full ensemble of cosmo-OWLS models discussed.

A resolution study for cosmo-OWLS can be found in Appendix A of Le Brun et al. (2014), where it is demonstrated that the gas and stellar mass fractions of the simulated GGCs are reasonably well converged. Specifically, these metrics change by only a few percent over an increase in mass resolution of a factor of 8.

Table 2.2: Ranges of total numbers of haloes in the various mass bins used for the diagnostics in this Chapter. The columns are: (1) The diagnostic for which the specified range is used; (2) Boundaries of the specified bin in units of  $\log(M_{\odot})$ ; (3) The redshift value of the simulation snapshot from which haloes are sourced; and (4) The minimum and maximum number of haloes found in the specified bin across the various BAHAMAS and cosmo-OWLS runs examined.

| (1)<br><b>Diagnostic</b> | (2)<br><b>Mass range</b> $\left[ M = \log \left( \frac{M_{200}}{M_{\odot}} \right) \right]$ | (3)<br><b><math>z</math></b> | (4)<br>$N_{haloes}^{min}$ | (5)<br>$N_{haloes}^{max}$ |
|--------------------------|---|------------------------------|---------------------------|---------------------------|
| Halo Mass Functions      | $2 \times 10^{12} \leq M < 10^{15}$   | 0                            | 114,920                   | - 134,152                 |
|                          |   | 1                            | 83,441                    | - 116,923                 |
|                          |   | 2                            | 34,606                    | - 61,474                  |
| Cluster Counts           | $M \geq 10^{12}$  | 0                            | 231,603                   | - 261,120                 |
|                          |   | 1                            | 198,028                   | - 239,211                 |
|                          |   | 2                            | 101,358                   | - 149,565                 |
|                          | $M \geq 10^{13}$  | 0                            | 19,011                    | - 28,115                  |
|                          |   | 1                            | 9,292                     | - 17,472                  |
|                          |   | 2                            | 1,810                     | - 4,979                   |
|                          | $M \geq 10^{14}$  | 0                            | 646                       | - 1,675                   |
|                          |   | 1                            | 101                       | - 337                     |
|                          |   | 2                            | 2                         | - 9                       |
| Density Profiles         | $12.0 \leq M < 12.5$  |                              | 153,581                   | - 18,2687                 |
|                          | $12.5 \leq M < 13.0$  |                              | 50,152                    | - 59,366                  |
|                          | $13.0 \leq M < 13.5$  |                              | 14,176                    | - 20,303                  |
|                          | $13.5 \leq M < 14.0$  | 0                            | 3,889                     | - 6,137                   |
|                          | $14.0 \leq M < 14.5$  |                              | 856                       | - 1,460                   |
|                          | $14.5 \leq M < 15.0$  |                              | 83                        | - 206                     |
|                          | $15.0 \leq M < 15.5$  |                              | 7                         | - 10                      |
| Mass-Concentration       | $13 \leq M < 15.5$  | 0                            | 19,011                    | - 28,115                  |
|                          |   | 1                            | 9,292                     | - 17,472                  |
|                          |   | 2                            | 1,810                     | - 4,970                   |
| Halo CLustering          | $12 \leq M < 13$  |                              | 208,218                   | - 237,768                 |
|                          | $13 \leq M < 14$  | 0                            | 18,065                    | - 26,440                  |
|                          | $14 \leq M < 15$  |                              | 939                       | - 1,666                   |

### 2.2.2 BAHAMAS

In common with cosmo-OWLS, the BAHAMAS suite presented in McCarthy et al. (2017) consists of 400  $\text{Mpc}/h$  comoving on a side, periodic box simulations containing  $2 \times 1024^3$  particles. In this chapter, I use a subset of the BAHAMAS suite whose initial conditions are based on the updated maximum-likelihood cosmological parameters derived from the WMAP-9 data (Hinshaw et al., 2013); i.e.,  $\{\Omega_m, \Omega_b, \Omega_\Lambda, \sigma_8, n_s, h\} = \{0.2793, 0.0463, 0.7207, 0.821, 0.972, 0.700\}$ .

I also use a massive neutrino extension of BAHAMAS recently completed by McCarthy et al. (2018). Specifically, using the semi-linear algorithm of Ali-Haïmoud and Bird (2013), McCarthy et al. have run massive neutrino versions of the WMAP-9 cosmology for several different choices of the total summed neutrino mass,  $M_\nu$ , ranging from the minimum mass implied by neutrino oscillation experiments of  $\approx 0.06$  eV (Lesgourgues and Pastor, 2006) up to 0.48 eV, in factors of two. When implementing massive neutrinos, all other cosmological parameters are held fixed apart from  $\sigma_8$  and the matter density in cold dark matter, which was decreased slightly to maintain a flat model (i.e., so that  $\Omega_b + \Omega_{\text{cdm}} + \Omega_\nu + \Omega_\Lambda = 1$ ). The parameter  $\sigma_8$  characterises the amplitude of linear theory  $z = 0$  matter density fluctuations on  $8h^{-1}$  Mpc scales. Instead of holding this number fixed, the amplitude,  $A_s$ , of the density fluctuations at the epoch of recombination (as inferred by WMAP-9 data assuming massless neutrinos) is held fixed, in order to retain agreement with the observed CMB angular power spectrum. Other strategies for implementing neutrinos are also possible (e.g., decreasing  $\Omega_\Lambda$  instead of  $\Omega_{\text{cdm}}$ ) but McCarthy et al. have found with small test simulations that the precise choice of what is held fixed (apart from the power spectrum amplitude) does not have a large effect on the local GGC population. Most important is the value of  $\Omega_\nu$ , which is related to  $M_\nu$  via  $\Omega_\nu = M_\nu / (93.14 \text{ eV } h^2)$  (Lesgourgues and Pastor, 2006) and ranges from 0.0013 to 0.0105 for our choices of summed neutrino mass. For completeness, the runs with  $M_\nu = 0.0, 0.06, 0.12, 0.24, \text{ and } 0.48$  eV have  $\sigma_8 = 0.821, 0.813, 0.799, 0.766, \text{ and } 0.705$ , respectively.

For both the runs with and without massive neutrinos, the Boltzmann code CAMB<sup>3</sup> (Lewis et al. 2000; April 2014 version) was used to compute the transfer functions and a modified version of N-GenIC to create the initial conditions, at a starting redshift of  $z = 127$ . N-GenIC has been modified by S. Bird to include second-order Lagrangian Perturbation Theory corrections and support for massive neutrinos<sup>4</sup>. Note that in producing the initial conditions for BAHAMAS, the separate transfer functions computed by CAMB for each individual component (baryons, neutrinos, and CDM) are used, whereas in cosmo-OWLS (and indeed in most existing cosmological hydro simulations) the baryons and CDM adopt the same transfer function, corresponding to the total mass-weighted function. Note also that McCarthy et al. use the same random phases for each of the simulations, implying that intercomparisons between the different runs are not subject to cosmic variance complications.

The BAHAMAS runs used in this chapter have dark matter and (initial) baryon particle masses for a WMAP-9 massless neutrino cosmology of  $\approx 3.85 \times 10^9 h^{-1} M_{\odot}$  and  $\approx 7.66 \times 10^8 h^{-1} M_{\odot}$ , respectively. The particle masses differ only slightly from this when massive neutrinos are included. These alterations are detailed in Table 2.1. The gravitational softening of the runs presented is fixed to  $4 h^{-1} \text{ kpc}$ , as in cosmo-OWLS.

The BAHAMAS runs were carried out with the same version of the GADGET3 code that was used in (cosmo-)OWLS. As noted above, to perform runs with massive neutrinos included, McCarthy et al. used the semi-linear algorithm developed by Ali-Haïmoud and Bird (2013) (see also Bond et al. 1980; Ma and Bertschinger 1995; Brandbyge et al. 2008; Brandbyge and Hannestad 2009; Bird et al. 2012), implemented in the GADGET3 code. Schematically, the semi-linear code computes neutrino perturbations on the fly at every time step using a linear perturbation integrator *sourced from the non-linear baryons+CDM potential*, adding the result to the total gravitational force. Because the neutrino power is calculated at every time step, the dynamical responses of the neutrinos to the baryons+CDM and of the baryons+CDM to the neutrinos are mutually and self-consistently included. Because the integrator uses perturbation theory,

<sup>3</sup><http://camb.info/>

<sup>4</sup><https://github.com/sbird/S-GenIC>

this method does not account for the non-linear response of the neutrino component to itself. However, this limitation has negligible consequences for my purposes, and indeed most analyses of BAHAMAS, as only a very small fraction of the neutrinos (with lower velocities than are typical) are expected to collapse and the neutrinos as a whole constitute only a small fraction of the total matter density. This has been explicitly tested by comparing the predicted mass density profiles of simulated GGCs using the semi-linear algorithm with that predicted using a particle-based treatment of the massive neutrinos (e.g., Viel et al. 2010; Bird et al. 2012), for simulations with CDM and neutrinos but no baryons. The resulting mass profiles typically agree to better than two percent accuracy over the full range of radii resolved in the simulations.

In addition to neutrinos, the various BAHAMAS runs (with or without massive neutrinos) also include the effects of radiation when computing the background expansion rate. This leads to a few percent reduction in the amplitude of the present-day linear matter power spectrum compared to a simulation that only considers the evolution of dark matter and dark energy in the background expansion rate.

As touched on above, BAHAMAS differs significantly from cosmo-OWLS in terms of its approach to the choice of parameter values for the subgrid feedback. In particular, McCarthy et al. (2017) explicitly calibrated the stellar and AGN feedback models to reproduce the observed present-day galaxy stellar mass function and the amplitude of the hot gas mass–halo mass relation of GGCs respectively, as determined by X-ray observations. By calibrating to these observables, the simulated GGCs are guaranteed to have the correct baryon content in a global sense. The associated back reaction of the baryons on the total matter distribution should therefore also be broadly correct. McCarthy et al. (2017) have shown that the BAHAMAS simulations reproduce an unprecedentedly wide range of properties of massive systems, including the various observed mappings between galaxies, hot gas, total mass, and black holes.

A resolution study for BAHAMAS is presented in Appendix C of McCarthy et al. (2017), where it is demonstrated that the gas and stellar mass fractions are reasonably well converged (to better than  $\approx 10\%$  in the case of a strong test, and to  $\approx 2\%$  in the case of a weak test, using the terminology of Schaye et al. 2015) over the range of

halo masses that I consider in this work.

In Table 2.2 I present an overview of the various mass bins used for the diagnostics throughout this Chapter. In each bin, I specify the minimum and maximum number of haloes found to occupy it across the various cosmo-OWLS and BAHAMAS simulation runs examined.

## 2.3 Halo Abundances

### 2.3.1 Halo Mass Functions

I begin by examining the effects of baryonic physics and the inclusion of massive neutrinos, both separately and in combination, on the halo mass function (HMF). I define the halo mass function,  $\Phi$ , as the number of haloes with mass  $M_{200,\text{crit}}$  per comoving cubic Mpc per logarithmic unit mass. In other words,

$$\Phi \equiv \frac{dn}{d \log_{10}(M_{200,\text{crit}})}, \quad (2.3)$$

where  $M_{200,\text{crit}}$  is the mass contained within a radius that encloses a mean density of 200 times the universal critical density at that redshift. Haloes are identified using a standard FoF algorithm run on the dark matter distribution, with a linking length of 0.2 in units of the mean interparticle separation. The SUBFIND algorithm (Springel et al., 2001; Dolag et al., 2009) is used to calculate the spherical overdensity mass  $M_{200,\text{crit}}$  (i.e., the mass contained within the radius that encloses a mean density that is  $200 \times$  the critical density at that redshift). These spheres are centred on the position of the main subhalo's particle with the minimum gravitational potential.

In the left panel of Figure 2.1 I plot the HMFs for the various baryon physics runs (without neutrinos) from cosmo-OWLS. For runs that lack feedback from AGN, the HMF, as expected, largely follows that of the DMONLY case, at least for the range of halo mass in which I am interested for the purposes of this chapter. However, when one includes feedback from AGN the situation changes significantly – gas is ejected

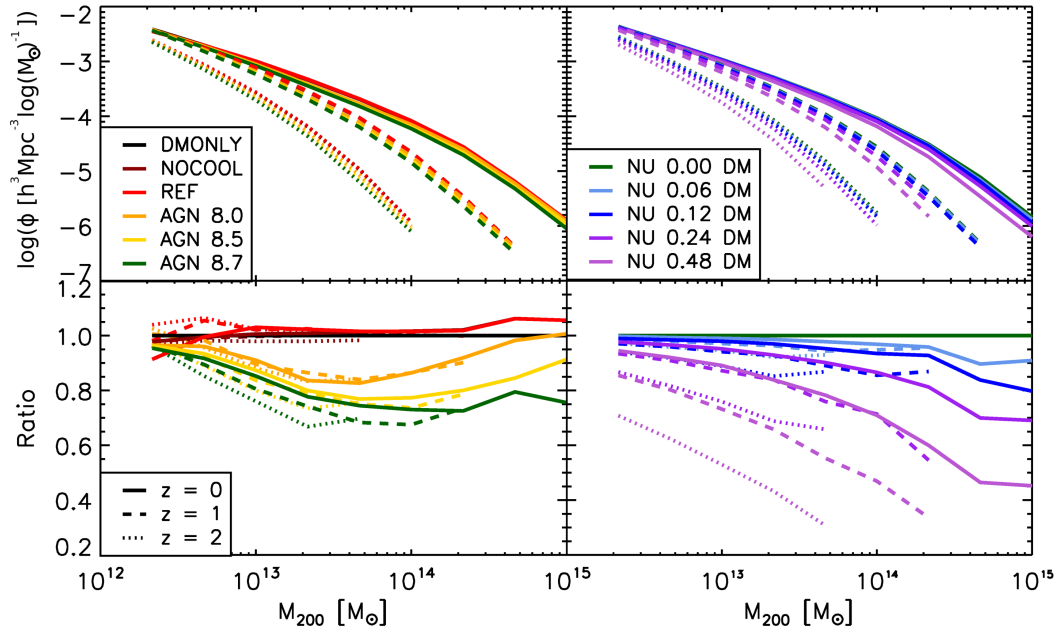


Figure 2.1: Halo mass functions (HMFs) for the different baryon physics runs (in the absence of neutrino physics) and the different massive neutrino runs in the absence of baryon physics. *Top Left*: HMFs for the different baryon physics runs (in the absence of neutrino physics) from cosmo-OWLS. *Bottom Left*: The cosmo-OWLS HMFs normalised by the DMONLY case. *Top Right*: HMFs for the different collisionless massive neutrino runs from BAHAMAS. *Bottom Right*: The BAHAMAS HMFs normalised by the massless neutrino case. Suppression of the HMF due to AGN feedback (orange, yellow and green, left) is important at intermediate (group) masses but becomes less important at high halo masses, where it begins to converge towards the DMONLY case (with the mass scale where the convergence occurs depending on the AGN heating temperature  $\Delta T_{\text{heat}}$ ). The suppression due to feedback is only a weak function of redshift. In the collisionless neutrino simulations (right panel), the suppression is strongest for the highest mass haloes and, in contrast to the effects of feedback, exhibits a strong redshift dependence.

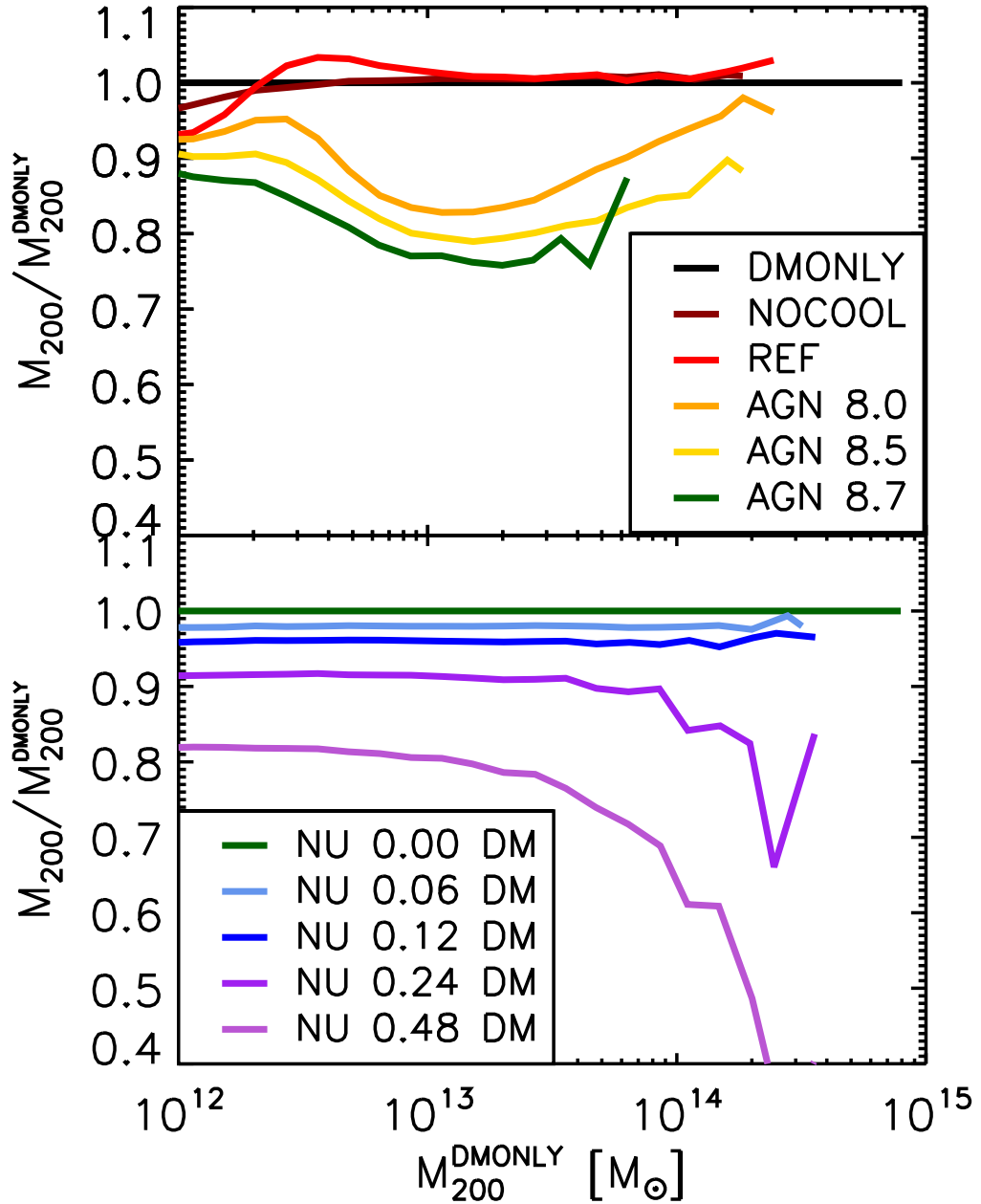


Figure 2.2: The fractional change in the halo mass, relative to the DM-only, massless neutrino case, arising from the inclusion of baryonic feedback (left panel) and neutrino free-streaming (right panel) at  $z = 0$ . As in Figure 2.1, colours denote the various BAHAMAS and cosmo-OWLS runs as detailed in Table 2.1. *Top:* AGN feedback can reduce the mass of a halo by up to  $\approx 20\%$  at group masses, but tends towards the DMONLY case at higher masses with the mass scale for convergence depending on the choice of AGN heating temperature  $\Delta T_{\text{heat}}$ . *Bottom:* The free-streaming of massive neutrinos in collisionless simulations reduces halo masses to a similar degree at group masses, but is of increasing importance at higher masses. These effects drive those seen in the HMFs (Figure 2.1).

from the high-redshift progenitors of GGCs (McCarthy et al., 2011) leading to a significant suppression (of up to  $\approx 20 - 30\%$ ) of the HMF at masses of  $\sim 10^{13-14}M_{\odot}$  in  $M_{200,\text{crit}}$ , in agreement with that previously reported by Velliscig et al. (2014), who analysed a subset of the cosmo-OWLS runs (see also Cui et al. 2014; Cusworth et al. 2014). The reduction in the baryonic mass also leads to a shallowing of the gravitational potential well. This causes the dark matter distribution to expand outwards becoming less densely concentrated, and also results in a reduction in the accretion rate onto the main progenitor (e.g., Sawala et al. 2013; Velliscig et al. 2014), which is why the  $M_{200,\text{crit}}$  masses of individual haloes can be reduced by somewhat more than the universal baryon fraction of  $\Omega_b/\Omega_m$ .

The deeper potential wells of higher-mass ( $M_{200,\text{crit}} > 10^{14}M_{\odot}$ ) systems are able to retain a larger fraction of their baryons. Consequently, the behaviour in the HMF tends back towards the DMONLY case at the highest masses. The precise mass scale where the AGN runs converge towards the DMONLY case depends on the adopted heating temperature, with higher heating temperatures increasing this mass scale, as one would anticipate based on the strong dependence of the baryon fraction on the AGN heating temperature reported previously by Le Brun et al. (2014) and McCarthy et al. (2017). At lower masses (below  $10^{13}M_{\odot}$ ), the trends for the AGN cases also tend back towards the DMONLY case. This is due to inefficient accretion onto the black holes. The precise location of this convergence in the simulations, however, is sensitive both to the initial mass of black hole sink particles and the halo mass at which they are seeded.

In contrast, neutrino free-streaming, as shown in the right panels of Figure 2.1, preferentially suppresses the high-mass end of the HMF (see also Costanzi et al. 2013). This is due to the fact that the effect of the free-streaming of massive neutrinos on the linear matter power spectrum grows with time, and appears in the clustering statistics from the collapse redshift of the halo. Consequently, more massive objects, which collapse later in CDM-based cosmologies, are more strongly affected by neutrino free-streaming. The strength of this suppression also varies strongly as a function of the summed neutrino mass, with higher values leading to a stronger reduction of the HMF. Interestingly, while the suppression due to baryonic feedback (left panels of Figure 2.1)

is only weakly dependent on redshift, the massive neutrino runs show stronger evolution with redshift.

While Figure 2.1 shows the change in number density at fixed halo mass, I also want to explicitly examine the change in halo mass at fixed number density. This is a more physical measurement, since baryonic feedback and neutrino free-streaming do not directly affect the *abundance* of haloes, rather they alter distribution of the *masses* of the haloes.

In order to determine the effects of baryonic feedback and neutrino free-streaming on individual haloes, I construct a matched set of haloes across all simulation runs. Haloes are matched using the unique particle IDs for the dark matter particles. For each particle assigned to a halo in the DM-only, massless neutrino case, the particle with the matching ID is identified in each of the other simulations. In each case, the halo containing the highest number of identified particles is selected as the match. This method finds matches for  $\approx 83\%$  and  $\approx 90\%$  of haloes in the cosmo-OWLS and BAHAMAS cases respectively, for haloes in the range  $12 \leq \log(M_{200,\text{crit}}^{\text{DMONLY}}/M_{\odot}) \leq 15$  where the  $M_{200,\text{crit}}^{\text{DMONLY}}$  value under consideration is that of the halo in the DM-only, massless neutrino case.

I show in Figure 2.2 the fractional change in halo mass as a function of the mass in the dark matter only, massless neutrino case. Unsurprisingly, the behaviour of the alteration to halo mass arising from baryonic feedback and neutrino free-streaming is almost identical to their effects on the HMF (Figure 2.1).

Henceforth, when using the matched sample of haloes I use for each halo the values of  $M_{200}$  and  $r_{200}$  that correspond to the matching halo in the dark matter-only, massless neutrino case.

### Separability

While the effects of baryon physics and neutrino free-streaming have individually been investigated in a number of previous studies (although generally with much poorer

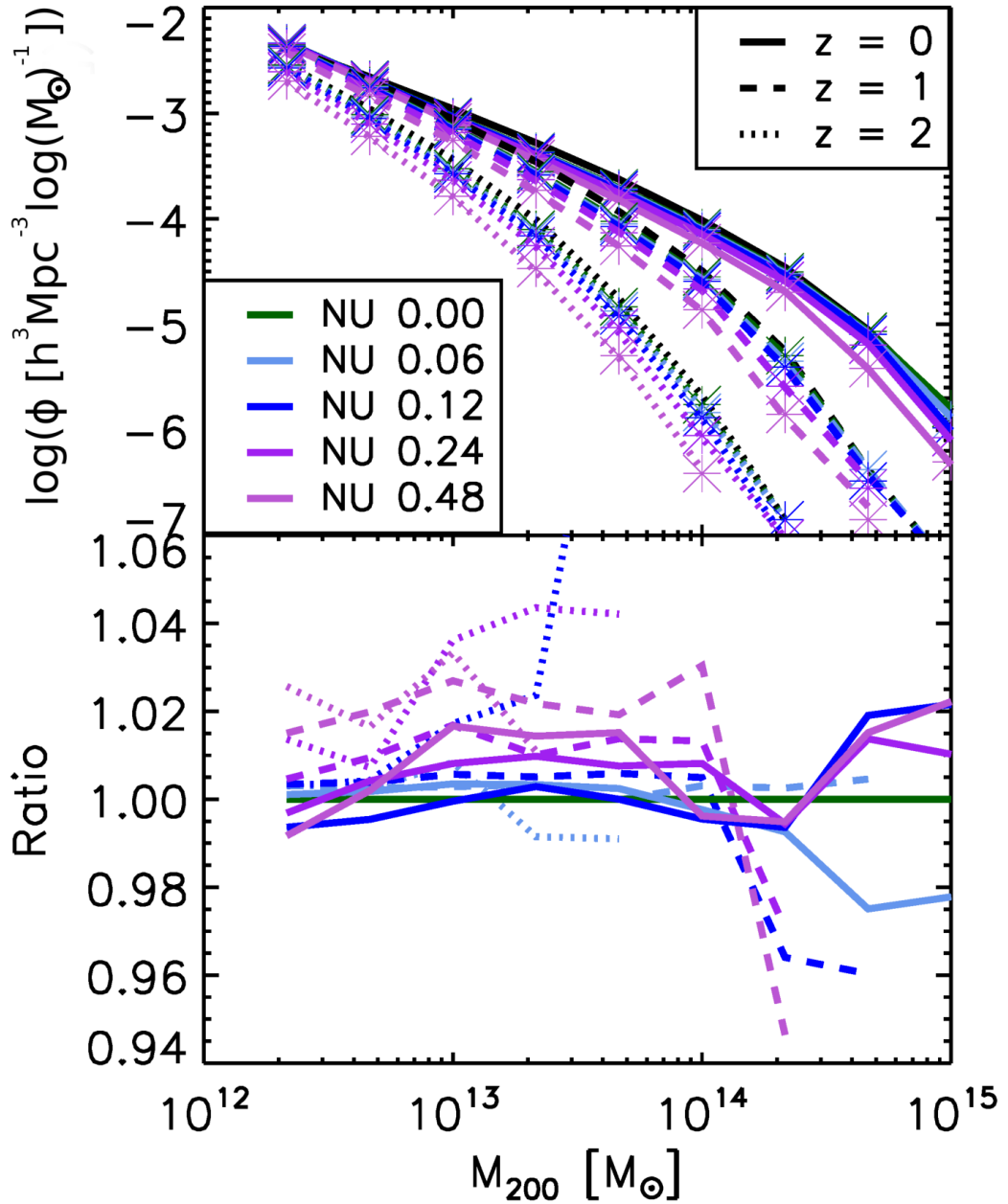


Figure 2.3: Comparison of the halo mass functions arising when simultaneously simulating baryonic feedback and neutrino free-streaming, and those calculated by multiplying the separate effects of baryonic feedback in the absence of neutrinos and the effects of neutrino free-streaming in the absence of baryons. *Top:* Curves display the HMFs arising when simultaneously simulating neutrino free-streaming and baryonic feedback. The multiplicative calculations are displayed by crosses. In both cases, colours correspond to different values for the summed neutrino mass while solid, dashed and dotted curves display the results at redshifts of 0, 1 and 2 respectively. *Bottom:* The ratio of each simultaneous simulation to the corresponding multiplicative prediction. The two cases agree to within a few percent accuracy over the full range of halo masses and redshifts that I have examined.

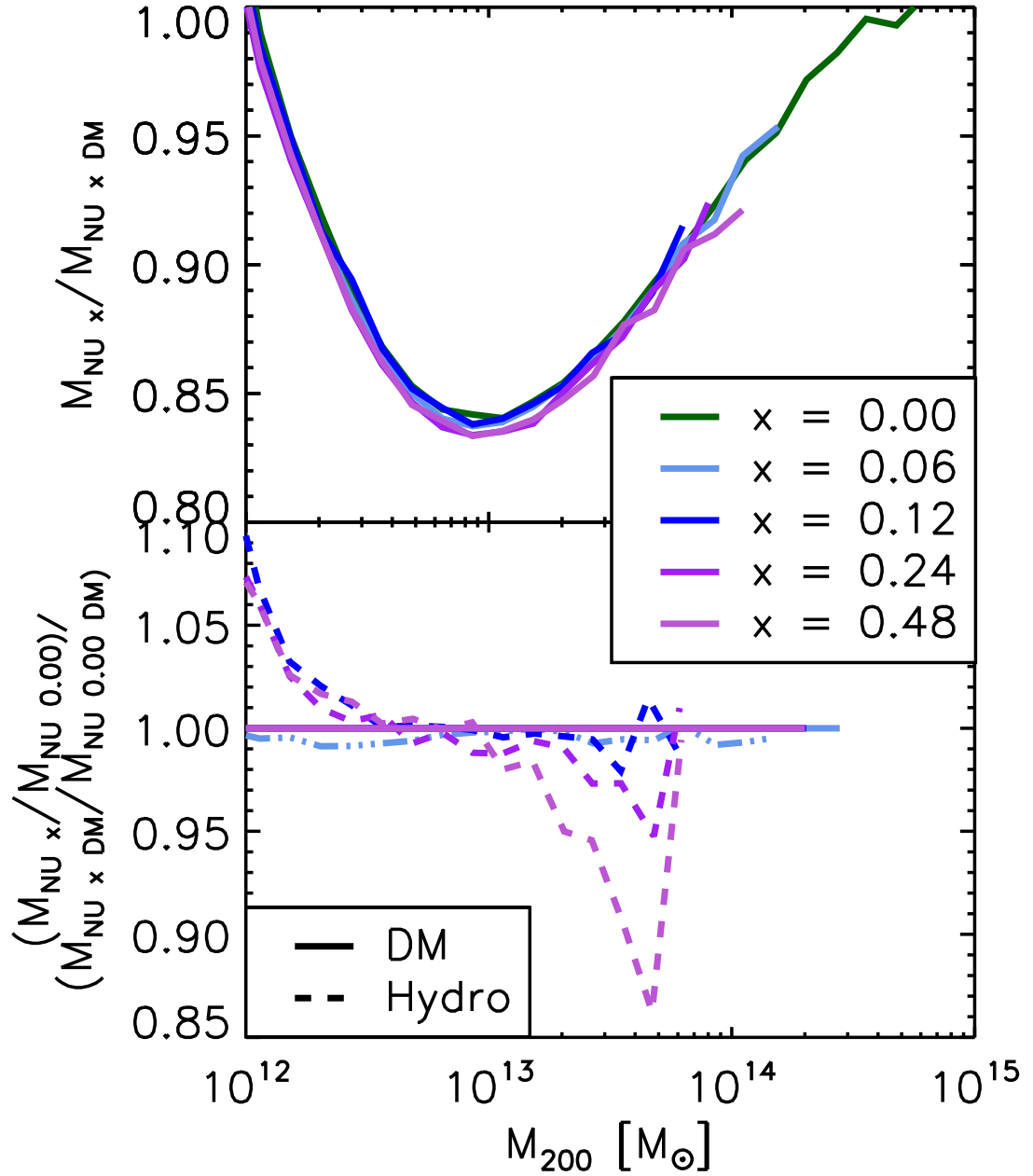


Figure 2.4: Two tests of the separability of the effects of neutrino free-streaming and baryon physics on halo mass. *Top:* The effect on the halo mass due to baryon physics at different fixed values of the summed neutrino mass for a matched set of haloes. Colours correspond to the different values for the summed neutrino mass. The effect of baryon physics on the halo mass is independent of the choice of summed neutrino mass to approximately 1% accuracy. *Bottom:* The effect on the halo mass due to neutrino free-streaming for different physics models, normalised to the collisionless case. Solid and dashed lines correspond to the dark matter-only results and those of the BAHAMAS feedback model respectively. The effect of neutrino free-streaming is independent of the implemented baryon physics.

statistics), their combined effect has not been examined. In particular, it is unclear to what extent the baryonic effects (particularly gas expulsion from AGN feedback) and neutrino free-streaming can be treated independently, or whether they amplify (or perhaps suppress) each other.

To answer this question, I compare the HMFs of the BAHAMAS runs that include both baryon physics and massive neutrinos (curves) with that expected if the feedback and free-streaming are treated separately (crosses) in the top panel of Figure 2.3. Specifically, I characterise the effect of the HMF due to AGN feedback alone as the ratio of the HMF of the BAHAMAS hydro run with massless neutrinos (NU 0.00) to that of the BAHAMAS DMONLY run with massless neutrinos (NU 0.00 DM), and I characterise the effect due to neutrino free-streaming alone as the ratios of the various BAHAMAS DMONLY runs with massive neutrinos (NU 0.06 DM, NU 0.12 DM, NU 0.24 DM, and NU 0.48 DM) to the BAHAMAS DMONLY run with massless neutrinos (NU 0.00 DM). I then multiply these separate suppression factors to obtain the combined suppression, such that the multiplicative prediction for the HMF is given by:

$$\begin{aligned}\Phi_{NU X}^{Mult} &= \Phi_{NU 0 DM} \cdot \left( \frac{\Phi_{NU X DM}}{\Phi_{NU 0 DM}} \right) \cdot \left( \frac{\Phi_{NU 0}}{\Phi_{NU 0 DM}} \right) \\ &= \frac{\Phi_{NU X DM} \cdot \Phi_{NU 0}}{\Phi_{NU 0 DM}},\end{aligned}\tag{2.4}$$

where  $NU X DM$  is the chosen collisionless (i.e. excluding baryonic physics) run with massive neutrinos, i.e.  $X \in \{0.06, 0.12, 0.48\}$ .<sup>5</sup>

In the lower panel of Figure 2.3 I show the ratio of the HMF of the self-consistent

---

<sup>5</sup>I have also experimented with combining the separate effects of neutrinos in *additive* fashion, by adding the mass loss due to baryons alone to that from neutrino free-streaming alone and comparing the resulting halo mass function with that derived from the self-consistent simulations with both effects present simultaneously. Explicitly, for a measurement  $f$  I define the additive prediction in the case with  $\sum M_\nu = X$  eV,  $f_{NU X}^{Add}$ , as:

$$\begin{aligned}f_{NU X}^{Add} &= f_{NU 0 DM} + (f_{NU X DM} - f_{NU 0 DM}) + (f_{NU 0} - f_{NU 0 DM}) \\ &= f_{NU X DM} + f_{NU 0} - f_{NU 0 DM}\end{aligned}\tag{2.5}$$

I find, however, that this generally results in a poorer reproduction of the HMF predicted by the self-consistent simulations, whereas the multiplicative treatment works very well over all mass ranges. I therefore proceed with the multiplicative approach.

simulations (i.e., with both baryons and neutrinos present together) to that predicted by the treating the baryons and neutrinos separately. In other words, I take the ratio of the lines and crosses in the top panel of Figure 2.3. As can be seen, multiplying the separate effects of baryon physics and neutrino free-streaming reproduces their combined effect obtained when both are included simultaneously remarkably well. The self-consistent HMFs are reproduced to a few percent accuracy by combining the separate effects of neutrinos and baryons in a multiplicative fashion over the full range of halo masses, summed neutrino masses, and redshifts that I consider.

It is perhaps somewhat surprising that the effects of baryon physics and neutrinos can be treated independently in this way. For example, an implication of Equation 2.4 is that a halo whose mass has been reduced (relative to a dark matter-only sim) by neutrino free-streaming is not any more susceptible to gas expulsion by AGN feedback than a halo of the same mass in a massless neutrino case. In other words, the effects of baryon physics or neutrino free-streaming in a simulation with both present are almost of the same magnitude as when one of these processes is omitted.

To further explore the separability of baryon physics and neutrino free-streaming, I perform two further tests. Firstly, I examine the amplitude of the isolated effect of baryon physics on the halo mass in the context of the various neutrino masses, i.e. is the amplitude of the change in the halo mass due to baryon physics sensitive to the choice of neutrino physics? For each chosen neutrino mass  $X \in \{0.06, 0.12, 0.24, 0.42\}$ , I compare the mass of each matched halo in the DM-only dissipationless run incorporating the selected neutrino mass,  $M_{NU X DM}$ , to its mass in the hydrodynamical run with that neutrino mass,  $M_{NU X}$ . To directly compare between the different neutrino runs, I plot the median ratio of these masses  $M_{NU X}/M_{NU X DM}$  in the top panel of figure 2.4 in bins of the mass of the matching halo in the DM-only case with massless neutrinos.

To an accuracy of approximately 1 per cent, the effect on the median halo mass due to baryon physics is independent of the choice of summed neutrino mass.

In the bottom panel of Figure 2.4, I show the effect on the halo mass due to neutrino

free-streaming for two different physics models: the dark matter-only case (characterised as  $M_{NUX}/M_{NU0.00}$ ) and the BAHAMAS calibrated feedback model (characterised as  $M_{NUXDM}/M_{NU0.00DM}$ ). Here one can again see that the effects of neutrino free-streaming are nearly independent of the included baryon physics. Thus, the level of accuracy with which the simple separability assumption reproduces the self-consistent neutrinos+baryon physics simulations in Figure 2.3 is no coincidence, it reflects the fact that these processes truly are approximately independent of one another.

### 2.3.2 Cluster Counts

In Figure 2.5 I show the effects of baryon physics and neutrino free-streaming on the halo space density for haloes with masses exceeding different threshold values of  $10^{12} M_{\odot}$ ,  $10^{13} M_{\odot}$ , and  $10^{14} M_{\odot}$ . At a given redshift, I compute the space density by simply integrating the HMF above a given mass threshold<sup>6</sup>. The halo space density, or ‘number count’, is more closely linked to what is typically measured observationally, as many surveys do not have a sufficiently large volume to robustly measure the HMF, particularly at high masses.

The results presented in the top panels of Figure 2.5 demonstrate that the evolution of the halo space density is sensitive to baryon physics and the presence of massive neutrinos, although the dependencies on halo mass and redshift are clearly stronger. In the bottom panels of Figure 2.5, I effectively remove the halo mass dependence by showing the ratio of the halo space density with respect to that predicted by the DMONLY case (left) or with respect to the NU 0.00 DM case (right) for the different mass thresholds. The bottom left panel of Figure 2.5 shows that AGN feedback reduces the abundance of haloes of fixed mass (as shown previously, e.g., Cusworth et al. 2014; Velliscig et al. 2014). I find that the suppression does not evolve significantly with redshift. By contrast, the abundance of haloes above a fixed mass threshold becomes increasingly suppressed at high redshift by neutrino free-streaming, particu-

<sup>6</sup>Note that because of the steepness of the HMF, the total halo space density is dominated by haloes with masses near the chosen threshold value.

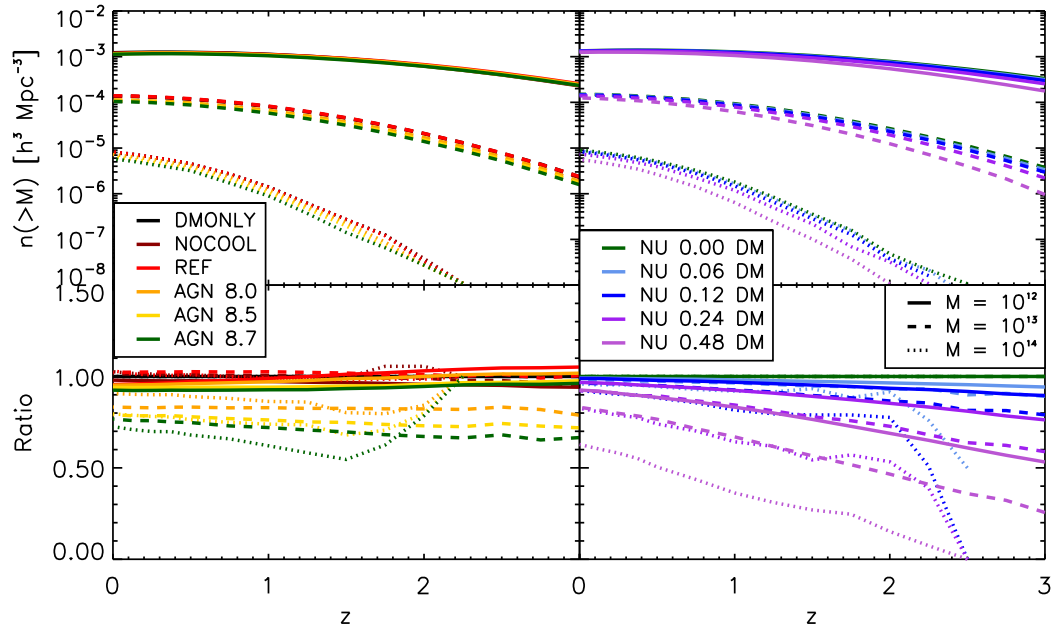


Figure 2.5: Evolution of the comoving halo space densities above different mass thresholds [i.e.,  $n(M_{200,\text{crit}} > M_{\text{threshold}}, z)$ ] for the different baryon physics runs in the absence of neutrino physics using cosmo-OWLS and for the different neutrino physics runs in the absence of baryon physics using the different massive neutrino runs from BAHAMAS. *Top Left:* Comoving halo space densities for the different baryon physics runs in the absence of neutrino physics from cosmo-OWLS. *Bottom Left:* The halo space densities for the baryon physics models normalised to the DMONLY case. *Top Right:* Comoving halo space densities for the different collisionless neutrino physics runs from BAHAMAS. *Bottom Right:* The halo space densities for the massive neutrino models normalised to the dark matter-only, massless neutrino (NU 0.00 DM) case. Solid, dashed, and dotted curves correspond to threshold masses of  $10^{12} M_{\odot}$ ,  $10^{13} M_{\odot}$ , and  $10^{14} M_{\odot}$ , respectively. The introduction of AGN feedback results in a suppression of the halo space density that is nearly independent of redshift, while the suppression above a fixed mass threshold due to neutrino free-streaming increases strongly with increasing redshift, particularly for models with high values of the summed neutrino mass.

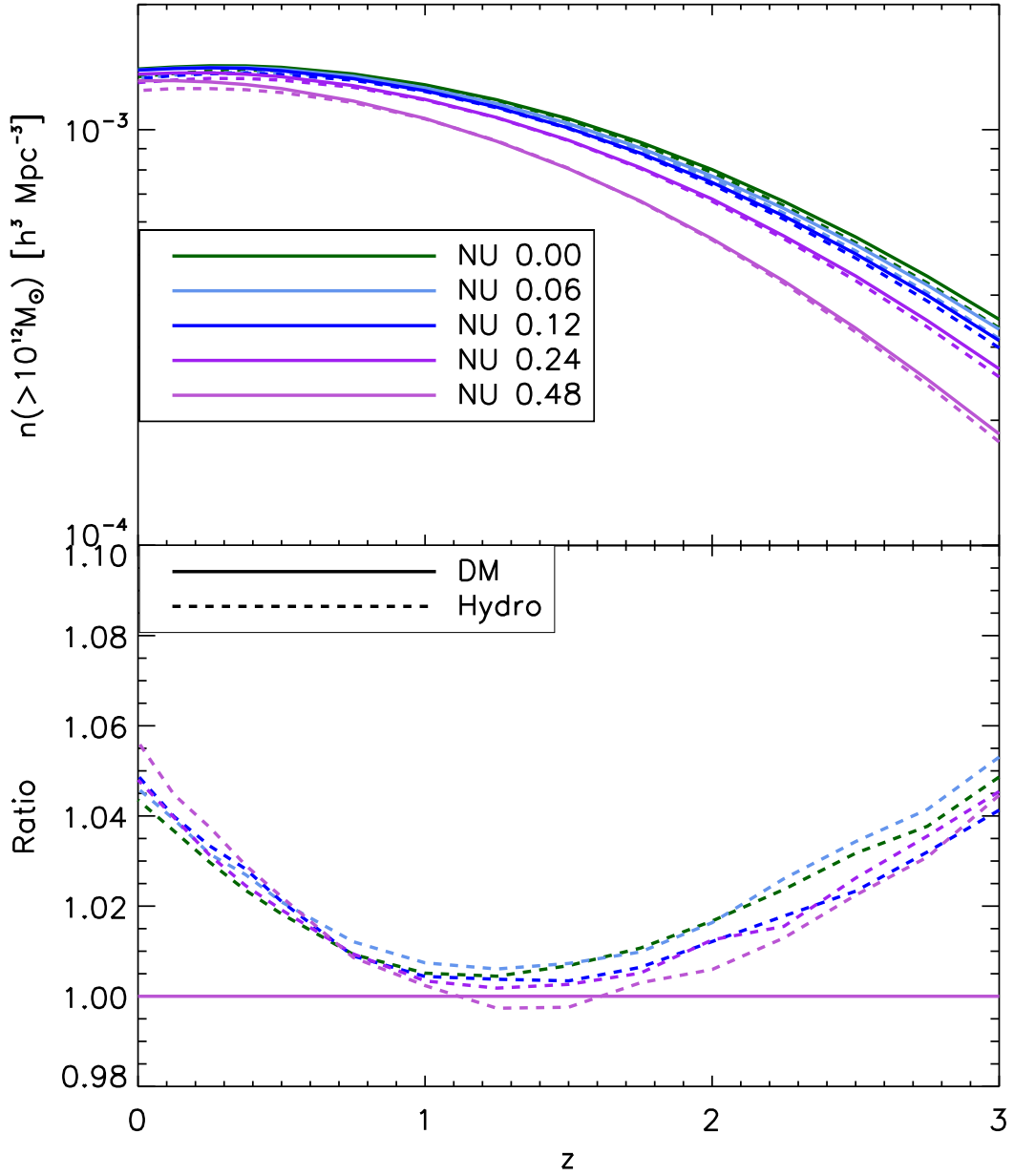


Figure 2.6: Comparison of the cluster counts above  $10^{12}M_{\odot}$  arising when simulating baryonic feedback and neutrino free-streaming self-consistently (solid lines) and those calculated by multiplying the separate effects of baryonic feedback in the absence of neutrinos, and the effects of neutrino free-streaming in the absence of baryonic physics (dashed lines). *Bottom:* each of the multiplicative models normalised by the corresponding self-consistent case. In general, treating these effects separately reproduces the combined result to a few percent accuracy across the range of redshifts considered here.

larly for high mass thresholds and high summed neutrino masses (bottom right panel of Figure 2.5). The latter result can be understood by recognizing that by considering haloes above a fixed mass threshold, we are considering increasingly rare systems with lower initial overdensities when moving to higher redshift (e.g., a  $10^{13} M_{\odot}$  at  $z = 2$  will correspond to a massive cluster today).

### Separability

I now examine the separability of the two effects. I follow the technique laid out in Section 2.3.1, wherein the combined effect is predicted by multiplying together the fractional effect due to each of the mechanisms in isolation. As I adopt this approach for each of the tests going forward, I here generalise Equation 2.4 so that the multiplicative prediction for an arbitrary measurement  $f$  in the context of a cosmology with a summed neutrino mass  $\sum M_{\nu}/\text{eV} = X$  is given by:

$$\begin{aligned} f_{NUX}^{Mult} &= f_{NU0DM} \cdot \left( \frac{f_{NUXDM}}{f_{NU0DM}} \right) \cdot \left( \frac{f_{NU0}}{f_{NU)DM}} \right) \\ &= \frac{f_{NUXDM} \cdot f_{NU0}}{n_{NU0DM}} \end{aligned} \quad (2.6)$$

In Figure 2.6 I present the results of this investigation. As was the case for the HMF, I find that the combined effects of baryon physics and neutrino free-streaming on the integrated halo space density can be recovered to a few percent accuracy by treating the baryon physics and neutrino effects separately.

## 2.4 Halo structure

Having explored the separate and combined effects of feedback and massive neutrinos on the overall abundance of haloes, I now examine their effects on the internal structure of haloes. In particular, I examine the spherically-averaged density profiles in bins of halo mass, and the halo mass–concentration relation.

### 2.4.1 Total Mass Density Profiles

In Figures 2.7 and 2.8, I plot the median total mass density profiles in bins of the total halo mass. Each panel corresponds to a different halo mass range (each 0.5 dex in width), ranging from  $\log(M_{200,\text{crit}}/M_{\odot}) = 13$  to 15.5 (top left to bottom right). Note that ‘total mass’ here includes only DM in collisionless runs (i.e. Figure 2.8 and subsequently Figure 2.10), while additionally including the contributions of stars and gas in hydrodynamical runs (i.e. Figure 2.7 and subsequently Figures 2.9 and 2.11). Despite the differences in composition, these measures are directly equivalent as the DM content in collisionless runs is increased to represent the ‘missing’ baryonic mass. Despite this, I never directly compare results from these two sets of simulation runs, only comparing the relative *change* in the profiles.

Figure 2.7 shows the effects of baryon physics in the absence of massive neutrinos on the total mass density profiles, while Figure 2.8 shows the effects of neutrino free-streaming in the absence of baryon physics. To reduce the dynamic range of the plots, I have scaled the mass density by  $r^2$  (i.e. so that an isothermal distribution would correspond to a horizontal line). The subpanels display the ratio of the each profile to the median profile in the relevant DM-only, massless neutrino case (i.e. DMONLY in Figures 2.7 and 2.9; NU 0.00 DM in Figures 2.8 and 2.10). The oscillatory features visible at low radii in Figure 2.10 are the result of radial bin edge effects. As  $r/r_{200}$  in the matched case is defined in terms of the  $r_{200}$  value of the matched halo in the DMONLY case, radial bins in a given mass bin have the same *physical* sizes across all simulation runs. As neutrino free-streaming lowers the overall density while leaving the shape of the profile unchanged, this means that local random deviations from a smooth density distribution are found in the same bin in all cases, leading to the noise in low radii (and therefore narrow and less populated) bins being highly correlated between simulation runs. Note that this effect is not present in the matched cases presented in Figures 2.9 and 2.11, as inclusion or otherwise of baryonic physics, and the relative strength thereof, alter the dynamics of the central regions, fundamentally changing the mass distribution.

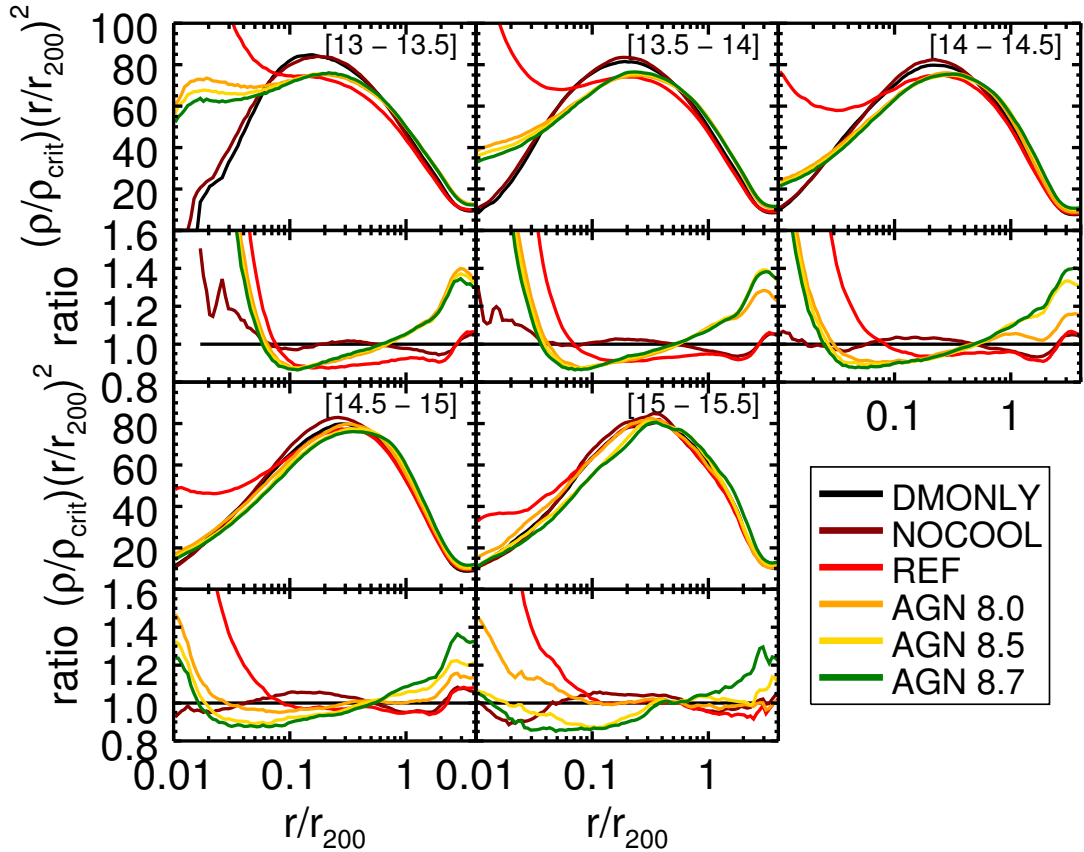


Figure 2.7: Median radial total mass density profiles in 0.5 dex mass bins for different baryon physics models in the absence of neutrino physics at fixed cosmology. The panels correspond to different mass bins with the stated ranges in  $\log(M_{200,\text{crit}}/M_{\odot})$ . The upper section of each panel displays the median profiles scaled by  $r^2$ ; the lower section of each panel displays the ratio of each of the radial density profiles to that of the DM-only, massless neutrino case (DMONLY) in the selected mass bin. Haloes are binned on their own, present-day mass (i.e. not using the matched halo mass). Different baryon physics runs are denoted by colour as in Figures 2.1 and 2.5. Baryon physics significantly alter the overall shape of the radial density profile. Turning on cooling (i.e. going from NOCOOL to REF) significantly increases the density at small radii ( $r \lesssim 0.1 R_{200}$ ). AGN feedback reduces the central densities, increasing the density at higher ( $r > 1 R_{200}$ ) radii. The strength of these effects increases with the AGN heating temperature (e.g. going from AGN 8.0 to AGN 8.7).

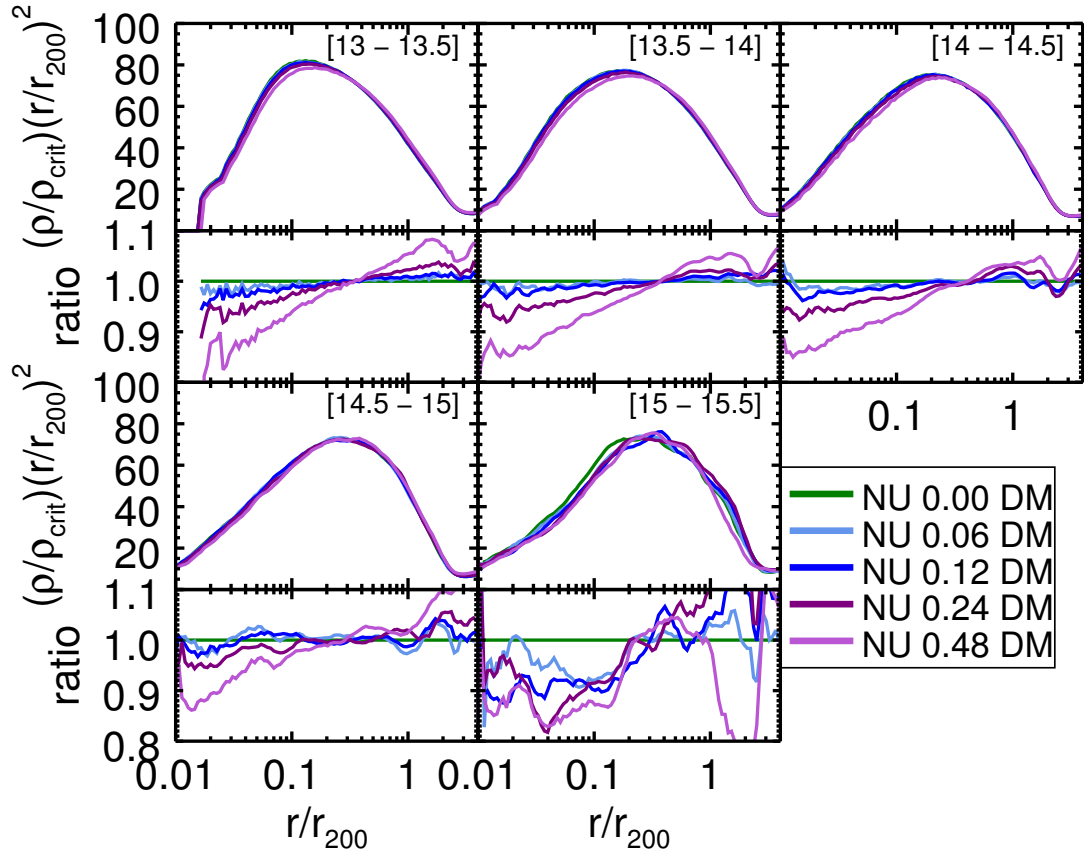


Figure 2.8: Median radial total mass density profiles in 0.5 dex mass bins for different neutrino physics models in the absence of baryonic physics at fixed cosmology. The panels correspond to different mass bins with the stated ranges in  $\log(M_{200,\text{crit}}/M_{\odot})$ . The upper section of each panel displays the median profiles scaled by  $r^2$ ; the lower section of each panel displays the ratio of each of the radial density profiles to that of the DM-only, massless neutrino case (NU 0.00 DM) in the selected mass bin. Haloes are binned on their own, present-day mass (i.e. not using the matched halo mass). Different neutrino masses are denoted by colour as in Figures 2.1 and 2.5. Increased values of  $\sum M_{\nu}$  result in a 'tilt' of the radial density profile - lowering the densities within  $\approx 0.4 R_{200}$  and increasing it above this radius.

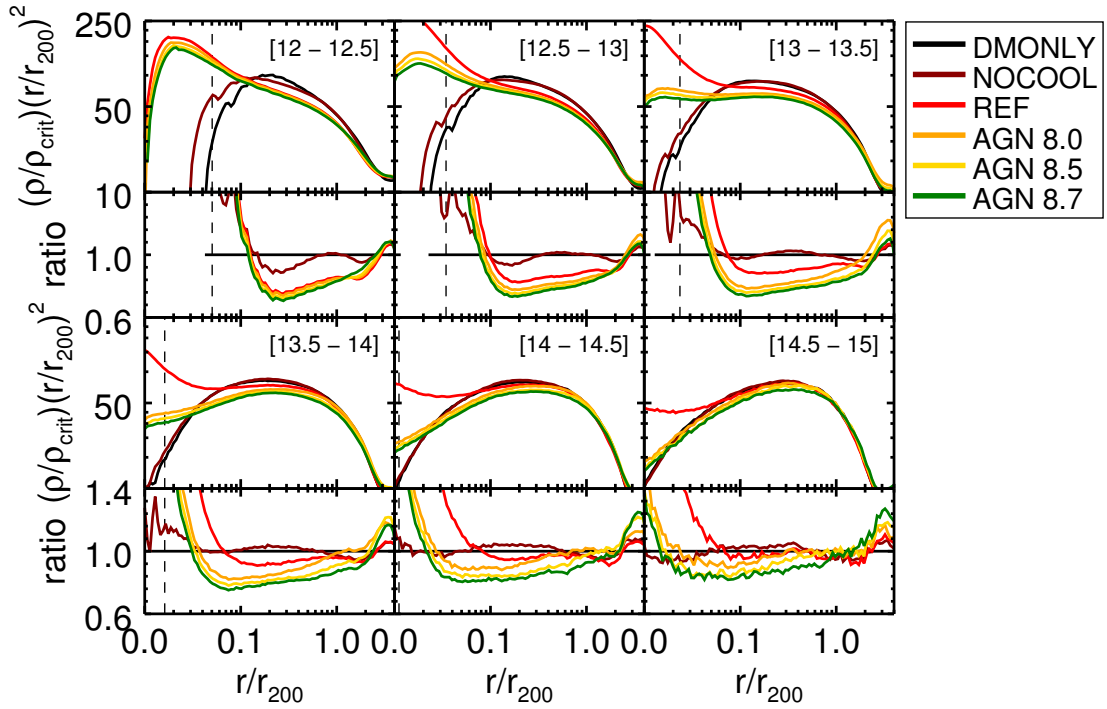


Figure 2.9: Median radial total mass density profiles in 0.5 dex mass bins for different baryon physics models in the absence of neutrino physics at fixed cosmology. Individual panels correspond to mass bins in the dark matter-only, massless neutrino simulation with the stated ranges of  $\log(M_{200,\text{crit}}^{\text{DMONLY}}/M_{\odot})$ . Within each of the 6 panels, the upper section displays the median profiles scaled by  $r^2$ , while the lower section displays the ratio of each density profile to that of the DM-only, massless neutrino case (DMONLY) in that bin. Haloes in other simulations were binned using the mass of their matched DM only, massless neutrino equivalent and  $r_{200}$  corresponds to that from the DM-only, massless neutrino run. Line colours correspond to runs with different subgrid prescriptions for baryon physics as in Figures 2.1 and 2.5. The vertical dashed line marks the location of three times the gravitational softening length from the halo center.

The inclusion of baryonic cooling results in much higher central densities while leaving the outskirts largely untouched compared to the NOCOOL case. The introduction of AGN heating redistributes material from the central regions ( $r/r_{200} < 0.1$ ) to the outskirts ( $r/r_{200} > 0.5$ ). This effect is greatest at low halo masses.

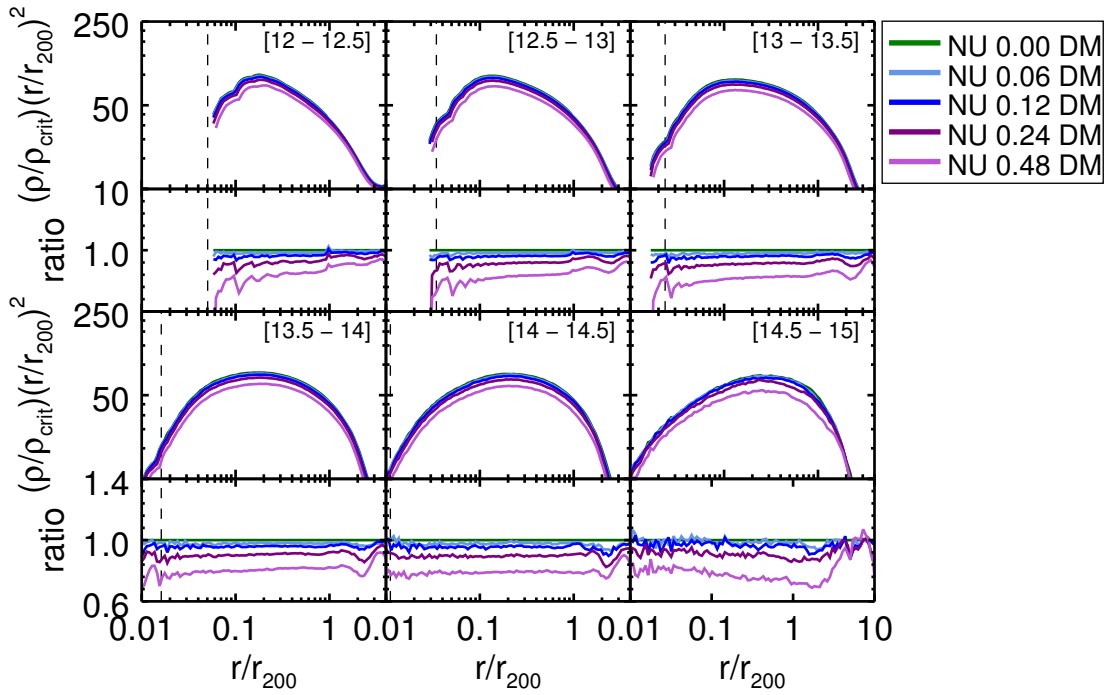


Figure 2.10: Median radial total mass density profiles in 0.5 dex mass bins for different neutrino physics models in the absence of baryonic physics at fixed cosmology. As in Figure 2.9 the panels correspond to different mass bins with the stated ranges in  $\log(M_{200,\text{crit}}^{\text{DMONLY}}/M_{\odot})$ . The upper section displays the median profiles scaled by  $r^2$ , while the lower section of each panel displays the ratio of each of the radial density profiles to that of the DM-only, massless neutrino case (NU 0.00 DM) in the selected mass bin; and haloes are binned on the mass of the matched DM-only, massless neutrino halo. Different neutrino masses are denoted by colour as in Figures 2.1 and 2.5. The vertical dashed line marks the location of three times the gravitational softening length from the halo center.

Neutrino free-streaming lowers the amplitude of the mass density profiles while approximately preserving their NFW-like shape (within the virial radius).

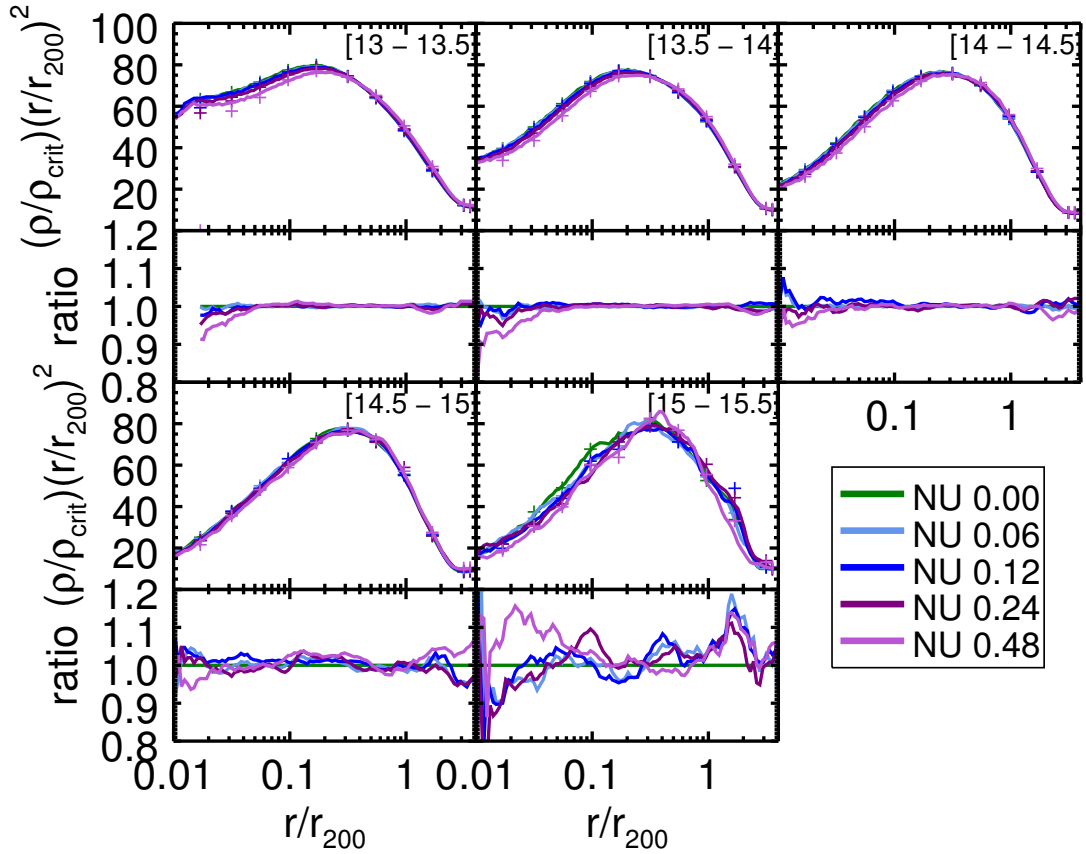


Figure 2.11: Comparison of the median radial total mass density profiles of haloes arising when simulating baryonic feedback and neutrino free-streaming simultaneously (curves) and with that calculated by multiplying their separate effects (crosses). Haloes are binned using their self-consistent masses from each of the simulations, with the mass ranges for each bin stated in units of  $\log(M_{200,\text{crit}}/M_{\odot})$ . Line colours correspond to runs with different neutrino masses as in Figs 2.3 and 2.4. The upper section in each panel displays the median profiles scaled by  $r^2$ , while the lower panel shows the ratio of each of the multiplicatively predicted profiles to the corresponding self-consistent profile. The two cases agree to within a few percent at  $r > 0.05r_{200}$ , with the exception of the highest mass bin where there are relatively poor statistics.

It is clear from Figure 2.7 that the baryonic processes, as expected, result in marked alterations to the density profile. Most notably, the inclusion of radiative cooling (i.e. moving from NOCOOL to REF) increases the density at small radii  $r < 0.1 R_{200}$  as particles can sink lower into the gravity well. Activating AGN feedback opposes this process, heating the central regions and lowering their density. This also results in increased densities at higher radii,  $r > 1 R_{200}$ , an effect that can be understood as a side effect of imposing a fixed mass bin. Altering the feedback processes alters the shape of the radial density profile, but the binning scheme ensures that the median mass contained be identical in each case.

This effect can also be seen in the neutrino mass case displayed in Figure 2.8. Higher values of  $\sum M_\nu$  lower the density at small radii and increase it at higher radii, with the inflection point lying at about  $0.4 R_{200}$ . In contrast to Figure 2.7 however, this is clearly the result of a change in the 'tilt' of the profile.

As above, while this information is useful from an observational point of view, my aim is to understand the effect of these physics on a halo-by-halo basis. I therefore construct a new selection of haloes for each bin, binning first the haloes in the relevant DM-only, massless neutrino case by their total mass, then selecting these same objects in the other simulation runs using the unique particle ID matching scheme described in Section 2.3.1. These results are displayed in Figures. 2.9 and 2.10.

As seen in Figure 2.7, Figure 2.9 shows that the inclusion of baryonic physics can significantly alter the radial total density profile away from the standard Navarro-Frenk-White (NFW) shape. In the absence of radiative cooling and AGN feedback, the baryons closely trace the dark matter resulting in minimal alteration to the profile (e.g., Lin et al. 2006). However, the activation of radiative cooling, star formation and stellar feedback causes much higher central densities. In contrast to Figure 2.7, there is a corresponding reduction in the density between  $0.08$  and  $1 r_{200}$  of  $\approx 10\%$ , as seen by comparing the REF and NOCOOL cases. AGN heating somewhat counteracts this effect, reducing central densities while redistributing material to the outer regions of the halo. While the density profiles of all three AGN models examined here are similar between  $0.08$  and  $1 r_{200}$ , higher values for AGN heating result in higher densities beyond  $r_{200}$

and lower densities in the central regions of the halo. The redistribution of material causes the scale radius to increase relative to the DMONLY case. This makes intuitive sense as the more energetic (albeit comparatively infrequent) outbursts of AGN with higher heating temperatures will eject more mass from the progenitors of the halo and cause a greater degree of expansion of the dark matter. The effects of baryonic physics become less important in higher mass bins, due to the deeper potential wells of these systems.

Figure 2.10 shows that, to a first approximation, the impact of neutrino free-streaming alone (i.e., with no baryons present) is to produce haloes with a lower overall amplitude of the mass density profiles within  $r_{200}$  while approximately preserving the Navarro-Frenk-White (NFW)-like shape. In effect, the free-streaming of massive neutrinos acts primarily to reduce the mass of a given halo relative to the mass it would achieve in the absence of neutrino physics. Beyond  $\sim r_{200}$ , however, there is also a change in shape, as is evident from the ‘oscillatory’ feature in the subpanels that show the ratio of the profiles with respect to that of the massless neutrino case. Physically, I interpret this feature as being due to the less evolved state of collapse of GGCs in the simulations with massive neutrinos. In the language of clustering, the scale that marks the transition from the ‘1 halo’ term (i.e., the profile of the central halo) to the ‘2 halo’ term (the clustering of other nearby systems), as well as its amplitude, is altered by neutrino free-streaming. I plan to explore the use of this feature as a constraint on the summed neutrino mass in a future study.

This effect is responsible for the changing ‘tilt’ observed in Figure 2.8. Haloes selected at fixed *self-consistent* halo mass in runs with higher values of  $\sum M_\nu$  correspond to higher mass bins in terms of their *matched* halo mass. Since neutrino free-streaming acts to lower the amplitude of the density profile without changing its shape, these objects transition through  $\rho \propto r^{-2}$  at higher values of  $\frac{r}{R_{200}}$  (i.e. are less concentrated). At the same *self-consistent* mass, they therefore have lower densities in the central regions and higher densities at higher radii. It is this effect that dominates Figure 2.8.

### Separability

As in Section 2.3, I investigate to what degree the two processes may be treated independently. In Figure 2.11, I compare the results of simulation runs combining baryon physics and neutrino free-streaming (curves) with those obtained by multiplying together the strengths of the two effects in isolation, this time for the radial density profiles (crosses). My formalism for this is identical in form to that shown in eq. (2.4), with the HMF exchanged for the radial density profile. As can be seen, the combined effects are reproduced to an accuracy of a few percent in all but the very central regions of the halo ( $r < 0.05 r_{200}$ ), with the exception of the highest mass bin where we have comparatively poor statistics.

It is important to note here that in Figure 2.11 I have reverted back to an unmatched set of haloes. That is, I have used the self-consistent masses from each of the simulations for this test.

### 2.4.2 Mass—Concentration Relation

The internal structure of CDM haloes in cosmological simulations is known to depend on their formation history, in that systems that collapsed earlier tend to have higher present-day concentrations on average than those that collapsed later on (e.g., Wechsler et al. 2002). This sensitivity is linked to the evolution of the (background) density of matter in the Universe, such that systems that collapsed earlier on had to have a higher physical density (in an absolute sense) to be overdense with respect to the background density, which was higher at earlier times. In CDM models, low-mass haloes typically collapse before high-mass haloes and, when combined with the evolution of the background density, this gives rise to the expectation that low-mass systems ought to be more concentrated than high-mass haloes, a result which is borne out in high resolution cosmological simulations (e.g., Bullock et al. 2001; Eke et al. 2001; Neto et al. 2007).

As I have demonstrated in Section 2.4.1, non-gravitational processes (e.g., feedback)

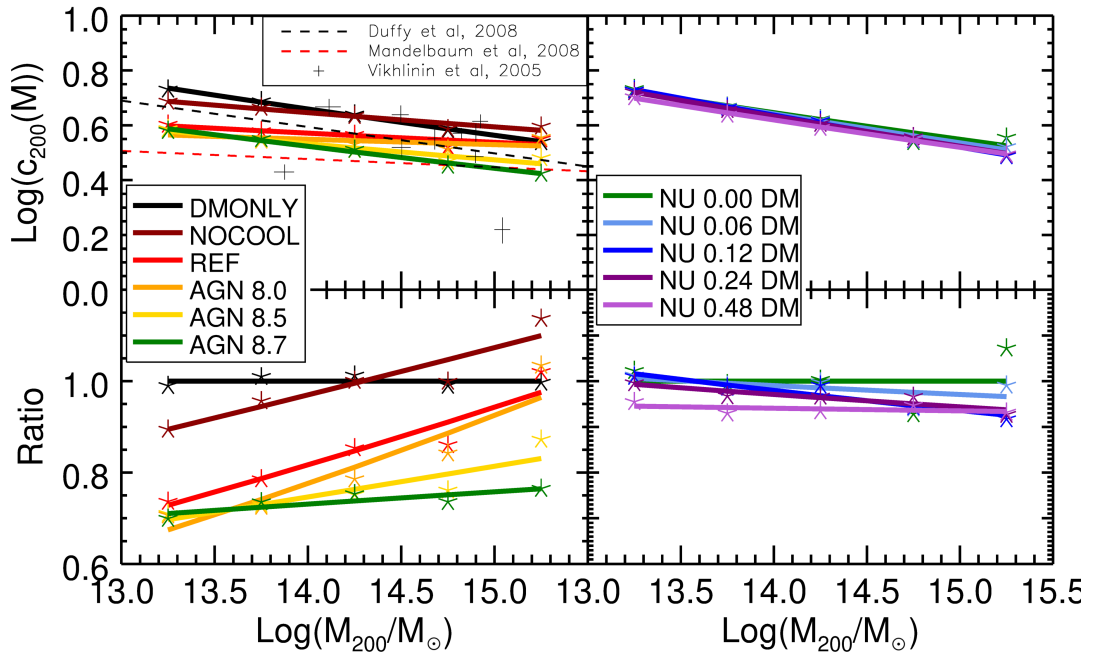


Figure 2.12: Best fit total mass  $c(M)$  relations for different baryon physics models in the absence of neutrino physics in the WMAP-7 cosmology (left) and for different  $\sum M_\nu$  values in the absence of baryonic physics in WMAP-9 cosmology (right) at  $z = 0$ . Halo masses are those from each of the individual simulations (i.e., not the matched DM-only masses). Stars mark the locations of the mean concentration value in each 0.5 dex mass bin, solid lines display the best-fit power laws to these means with the functional form of equation 2.8. The upper panel displays these in  $\log(c) - \log(M)$  space, while the lower panel displays the same data normalised to the best fit for the the relevant DM only model. In the top left panel I additionally plot the results of Duffy et al. (2008), Mandelbaum et al. (2008), and Vikhlinin et al. (2005) for comparison. Increasing  $\sum M_\nu$  results primarily in a reduction of the amplitude of  $c(M)$  with respect to the DMONLY NU 0.00 DM model with minimal alteration to the gradient. Conversely, baryonic feedback alters both the amplitude and the gradient. The amplitudes of both effects are comparable to, or less than, the scatter in observational data.

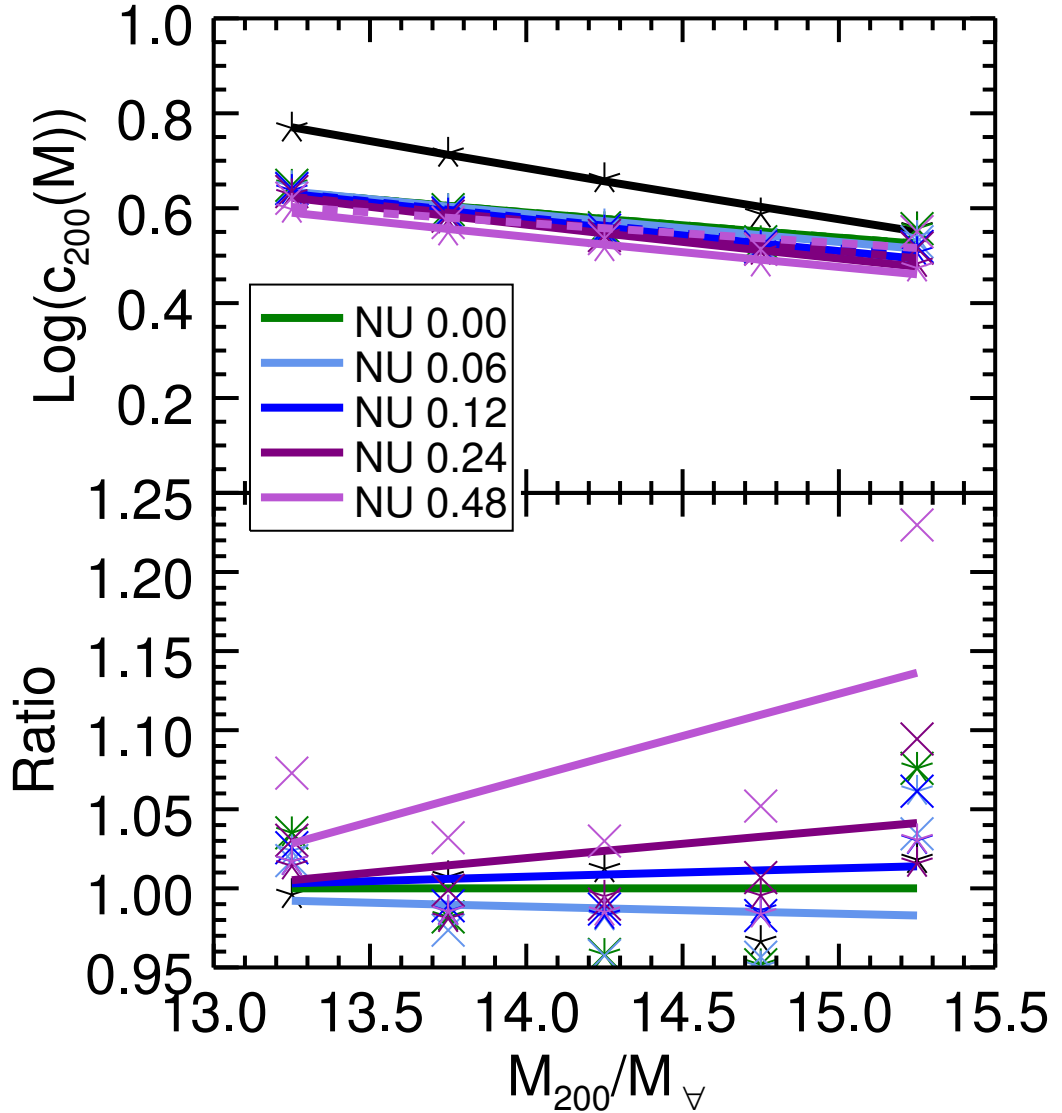


Figure 2.13: *Top:* Comparison of the mass–concentration relations arising when simulating baryonic feedback and neutrino free-streaming simultaneously (stars) and those calculated by multiplying the separate effects of baryonic feedback in the absence of neutrinos, and the effects of neutrino free-streaming in the absence of baryonic physics (crosses). As in Figure 2.12, lines display the best fit total mass  $c(M)$  relationship to these data, solid lines corresponding to the self-consistent case, dashed lines to the multiplicative prediction. *Bottom:* each of the multiplicative models normalised by the best fit relation of the corresponding self-consistent case. In general, treating these effects separately reproduces the combined result to a few percent accuracy.

and neutrino free-streaming also alter the internal structure of collapsed haloes, and therefore ought to modify the mass–concentration relation. Here I examine the separate and combined effects that these processes have on this relation.

As is customary, I define the concentration parameter,  $c_\Delta$ , as the ratio of the radius enclosing an overdensity of  $\Delta$  times the critical density,  $r_\Delta$  to the Navarro-Frenk-White (NFW) scale radius,  $r_s$ , i.e.:

$$c_\Delta \equiv \frac{r_\Delta}{r_s}. \quad (2.7)$$

I derive two estimates of the scale radius (and therefore the concentration), by fitting Navarro-Frenk-White (NFW) profiles to the total and dark matter mass density profiles, respectively. Below I present results for the case of  $\Delta = 200$ . When deriving estimates of the scale radius, I fit the Navarro-Frenk-White (NFW) profile over the radial range  $0.1 \leq r/r_{200} \leq 1.0$  for halo masses of  $\log(M_{200,\text{crit}}/M_\odot) \geq 13$ , noting that by adopting a minimum radius of  $0.1 r_{200}$  I am largely avoiding the region dominated by stars that is typically not well fit by the Navarro-Frenk-White (NFW) form for these haloes. I exclude haloes below this mass as the star dominated region approaches the scale radius (see Figure 2.9).<sup>7</sup> To give approximate equal weighting to the different radial bins over the range that I consider, I actually fit to the quantity  $\rho r^2$ , as done in several previous studies (e.g., Neto et al. 2007). I derive concentration estimates for each individual halo satisfying  $M_{200,\text{crit}} > 10^{13}M_\odot$  in all of the simulations.

I bin the resulting  $c_{200}$  values into equally-spaced logarithmic mass bins (0.5 dex width) between 13.0 and 15.0 in  $\log(M_{200,\text{crit}}/M_\odot)$ . In each bin, I calculate the mean concentration value,  $\langle c_{200} \rangle$ , the standard deviation ( $\sigma_{\ln(c_{200})}$ ) of the intrinsic scatter around  $\langle c_{200} \rangle$ , and the mean halo mass,  $\langle M_{200,\text{crit}} \rangle$ . As the scatter in  $c_{200}$  is approximately log normal,  $\langle c_{200} \rangle$  and  $\sigma_{\ln(c_{200})}$  were computed by fitting a Gaussian distribution to the histogram of the  $c_{200}$  values in 100 equally-spaced logarithmic bins spanning 3 dex centred on an estimate for the mean value.

Previous studies found that the distribution of mass and concentration values for DMONLY

<sup>7</sup>Note that  $r_s > 0.1 r_{200}$  for the halo mass ranges under consideration.

haloes in N-body simulations at  $z = 0$  was well fitted by a power law of the form

$$c_{\Delta}(M_{\Delta}) = A \cdot \left( \frac{M_{\Delta}}{M_{Fiducial}} \right)^B . \quad (2.8)$$

Gao et al. (2008) demonstrated that a power law of this form continued to be a good fit to samples of haloes in N-body simulations out to redshifts of 2, although the value of the parameter  $A$  varied as a function of  $z$ . I follow Duffy et al. (2008) and parametrise this redshift dependence by expanding Eqn. 2.8 to the form

$$c_{\Delta}(M_{\Delta}) = A \cdot \left( \frac{M_{\Delta}}{M_{Fiducial}} \right)^B \cdot (1 + z)^C . \quad (2.9)$$

Note that at fixed redshift, the  $A$  and  $C$  parameters in Eqn. 2.9 are degenerate. Therefore, when I present the results of my analysis below at  $z = 0$  I present fits to Eqn. 2.8. However, I include the results of fitting Eqn. 2.9 over the redshift range  $0 \leq z \leq 2$  in Table A.1 in Appendix A.

In Figure 2.12 I display the best-fit  $z = 0$  total mass–concentration relations from equation 2.8 for different baryon physics models in the absence of neutrino physics in the WMAP-7 cosmology (left panel), and for the different  $\sum M_{\nu}$  values in the absence of baryonic physics in the WMAP-9 cosmology (right panel), using the self-consistent masses from each simulation (i.e., for an unmatched set of haloes). In the upper-left panel of this plot I additionally display best fitting relationships derived by Duffy et al. (2008) and Mandelbaum et al. (2008), the former of which is fitted to DM haloes in a WMAP-5 cosmology (taken from the *millenium* simulations), while the latter made use of observed clusters with weak-lensing masses identified in the Sloan Digital Sky Survey (SDSS). Finally, I have also overplotted the hydrostatic mass and concentration values, and their associated errors, of low-redshift relaxed clusters measured by Vikhlinin et al. (2005) using *Chandra* data. Note that the values of these last data are not directly comparable with the results presented in the rest of the plot as they display  $c_{500}$  and  $M_{500}$ , however the magnitude of the measurement errors and the extent of scatter may be compared qualitatively.

Consistent with previous studies (e.g., Duffy et al. 2010), I find that the inclusion of efficient feedback results in a lowering of the amplitude of the mass–concentration relation (left panel of Figure 2.12). There is also a slight shallowing of the relation with respect to the DMONLY case, driven by the increasing importance of feedback with decreasing halo mass. Note that the mass–concentration relation is altered in two ways: the profile shapes (and therefore the scale radius) are altered by feedback (Figure 2.9) and the overall halo mass is also affected.

It can be seen from the right panel of Figure 2.12 that neutrino free-streaming lowers the amplitude of the mass–concentration relation and also has a slight effect on its shape. As in the case of feedback, this is due both to a (slight) change in the shapes of the profiles (an increase in the scale radius) and to a lowering of the overall halo mass. By analysing the mass–concentration relation for a matched set of haloes, I deduce that the change in the halo mass is more important than the change in the scale radius for halo masses above  $\sim 14.5$  in  $\log(M_{200,\text{crit}}/M_{\odot})$ , while the reverse is true at lower masses. The overall amplitude and slope of the relations measured here are broadly consistent with those measured in previous work, in the context of both simulated and observed haloes (see also the direct comparison with the best-fit parameters of Duffy et al. (2008) in Appendix A). However, the magnitude of the effect is small, with even the most extreme AGN case (AGN 8.7) sitting within the scatter of observed haloes.

In analogy to my exploration of the halo masses, I have examined to what extent the effects of baryon physics and neutrino free-streaming on the mass–concentration relation can be treated separately (i.e., does it reproduce the combined effect, when both baryons and massive neutrinos are present). I find that in a relative sense treating these effects separately reproduces the combined result to a few percent accuracy, as would be expected from the similar success in recovering the density profiles (see Figure 2.11). These results are displayed in Figure 2.13.

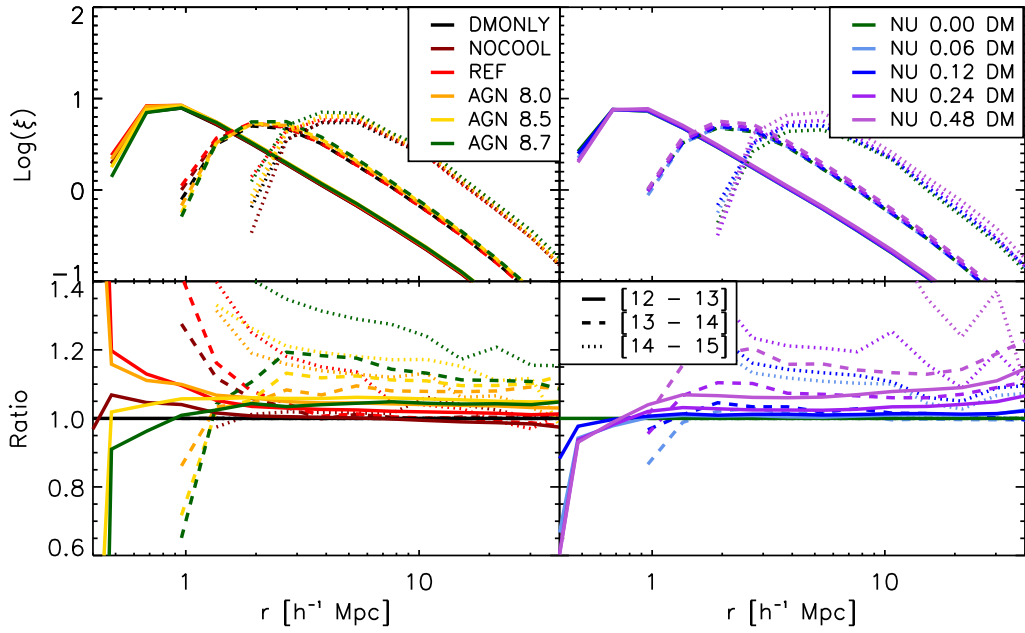


Figure 2.14: Real-space 2-point halo autocorrelation functions ( $\xi$ ) for the different baryonic physics runs in the absence of neutrino physics from cosmo-OWLS (left) and the different collisionless massive neutrino runs from BAHAMAS (right). Solid, dashed and dotted curves correspond to  $\xi$  for haloes in mass bins of  $10^{12} - 10^{13}M_{\odot}$ ,  $10^{13} - 10^{14}M_{\odot}$  and  $10^{14} - 10^{15}M_{\odot}$  in  $M_{200,\text{crit}}$  respectively. The bottom left panel shows  $\xi$  for each of the baryonic physics models normalised to the DMONLY case, while the bottom right panel shows the massive neutrino models normalised to the dark matter-only massless neutrino (NU 0.00 DM) case. The introduction of AGN feedback results in a  $\sim 10\%$  increase in the amplitude of the autocorrelation function, with the precise shift depending on the halo mass range and AGN heating temperature under consideration. Neutrino free-streaming also increases the amplitude, with the strength of the effect depending sensitively on the precise value of the summed neutrino mass.

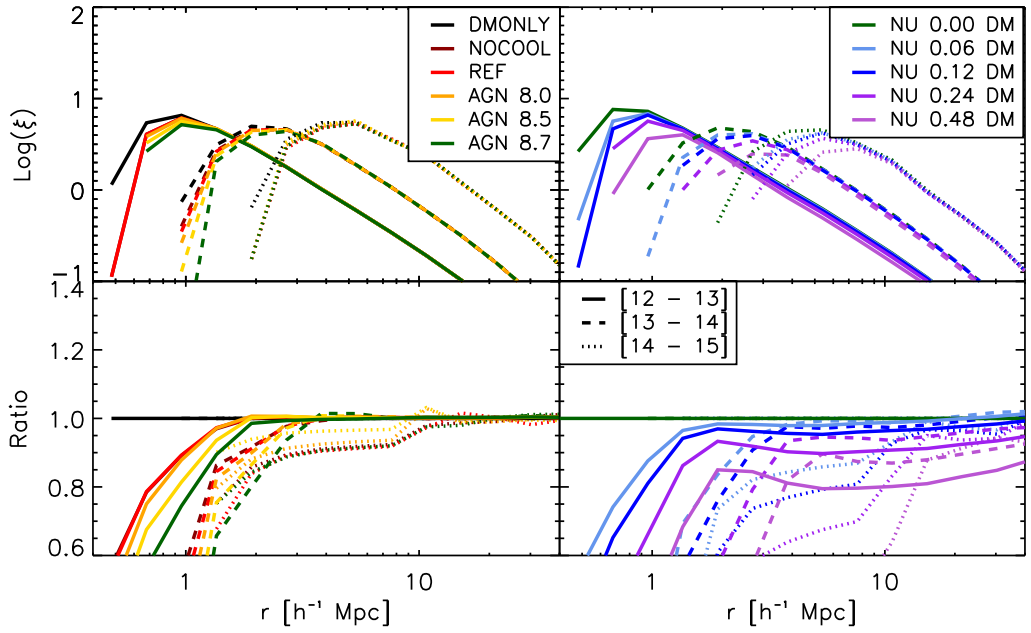


Figure 2.15: Real-space 2-point halo autocorrelation functions ( $\xi$ ) for the different baryonic physics models in the absence of neutrino physics from cosmo-OWLS (left) and the different collisionless massive neutrino runs from BAHAMAS (right). The bottom left panel shows  $\xi$  for each of the baryonic physics models normalised to the DMONLY case, while the bottom right panel shows the massive neutrino models normalised to the dark matter-only massless neutrino (NU 0.00 DM) case. In contrast to Figure 2.14, solid, dashed and dotted curves correspond to  $\xi$  for matched haloes in mass bins of  $10^{12} - 10^{13}M_{\odot}$ ,  $10^{13} - 10^{14}M_{\odot}$  and  $10^{14} - 10^{15}M_{\odot}$  in  $M_{200,\text{crit}}^{\text{DMONLY}}$  respectively, i.e. selecting the same set of haloes in each simulation. As can be clearly seen from the bottom-left panel, the large-scale clustering of a chosen set of haloes is, to a very high level of accuracy, unaffected by baryon physics. Conversely, neutrino free-streaming can suppress the amplitude of the halo autocorrelation function by  $\sim 10\%$ .

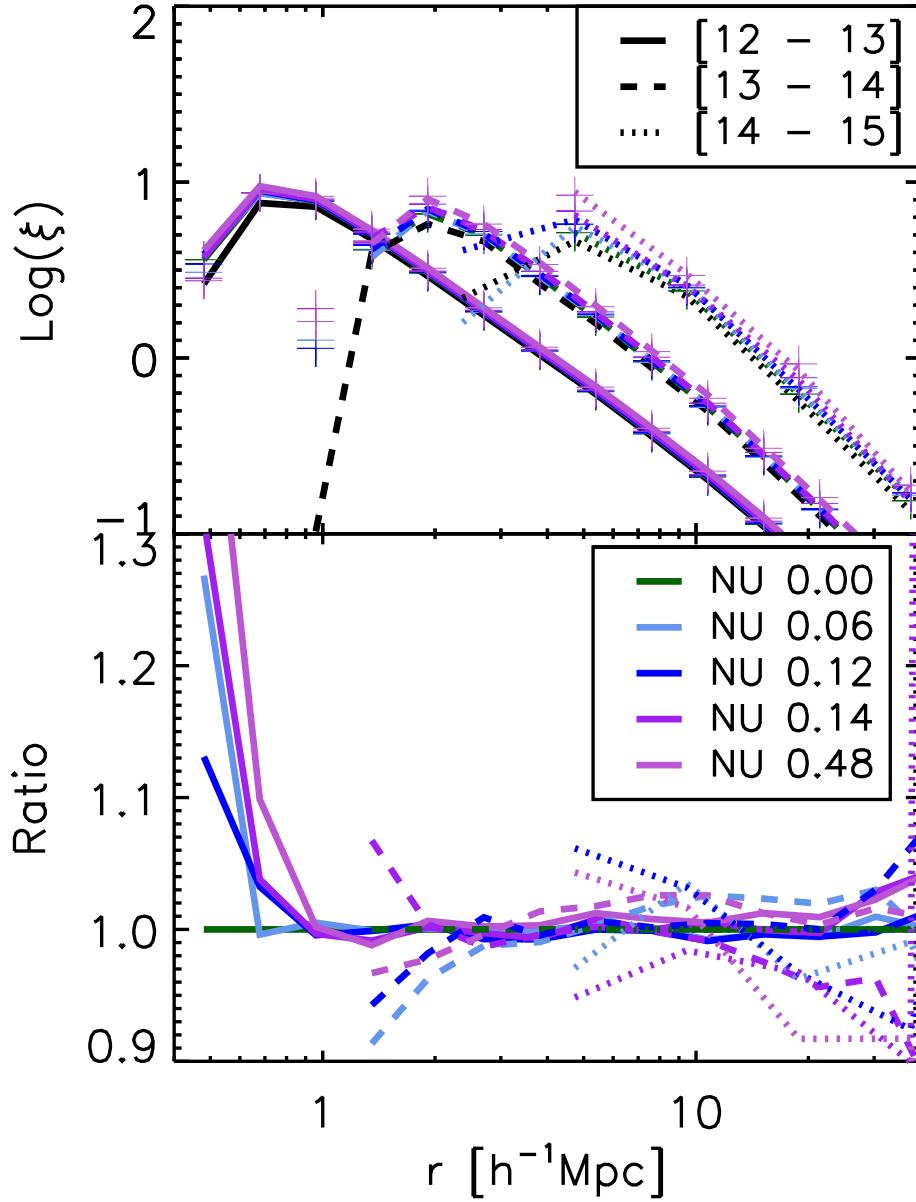


Figure 2.16: Comparison of the real space 2-point halo autocorrelation functions ( $\xi$ ) arising when simulating baryonic feedback and neutrino free-streaming simultaneously (curves) and those calculated by multiplying the separate effects of baryonic feedback in the absence of neutrinos and the effects of neutrino free-streaming in the absence of baryon physics (crosses). Solid, dashed and dotted lines correspond to  $\xi$  for haloes in mass bins of  $10^{12} - 10^{13}M_{\odot}$ ,  $10^{13} - 10^{14}M_{\odot}$  and  $10^{14} - 10^{15}M_{\odot}$  in  $M_{200,\text{crit}}$  respectively. The bottom panel shows each of the multiplicative models normalised by the corresponding combined case. The multiplicative treatment recovers the combined result with a few percent accuracy for  $r > 1h^{-1}\text{Mpc}$  independent of the chosen summed neutrino mass in all but the highest mass bin.

## 2.5 Halo Clustering

Having quantified the effects of feedback and neutrino free-streaming on the masses and internal structure of haloes, I now proceed to examine their separate and combined effects on the spatial distribution of haloes. Specifically, I focus here on the clustering of FoF haloes in bins of halo mass, as characterised by the 3D two-point autocorrelation function. I examine the clustering of matter in general in Section 2.6.

I compute the autocorrelation function,  $\xi$ , of FoF groups as the excess probability (with respect to a random distribution) of having another FoF group present at a particular distance; i.e.,

$$\xi(r) = \frac{DD(r)}{RR(r)} - 1, \quad (2.10)$$

where  $DD(r)$  and  $RR(r)$  are the ‘data’ and ‘random’ pair counts in radial bins. I compute  $RR(r)$  analytically, assuming the FoF groups are spread homogeneously throughout the simulation volume at the mean density of haloes of the particular mass range under consideration. I compute  $\xi$  in 20 logarithmic radial bins between 0.1 and 100  $h^{-1}$  comoving Mpc.

In Figure 2.14 I show the separate effects of baryon physics (left panel) and neutrino free-streaming (right panel) on the autocorrelation function in three different halo mass bins. Consistent with the results of van Daalen et al. (2014), I find that AGN feedback *increases* the amplitude of the autocorrelation by  $\sim 10\%$ , with the precise shift depending on the halo mass range and the AGN heating temperature. Neutrino free-streaming has a qualitatively similar effect, with the shift depending sensitively on the adopted mass range and the summed mass of neutrinos,  $M_\nu$ .

At first sight it is odd that the inclusion of massive neutrinos leads to an increase in the amplitude of the halo clustering signal, given that it is well known that neutrinos suppress the matter power spectrum (e.g., Bond et al. 1980, see also Section 2.6). The origin of this apparent inconsistency lies in the fact that I am plotting the clustering signal in bins of halo mass in Figure 2.14 and that I am using the self-consistent masses from each of the simulations when placing the FoF groups into halo mass bins. Since

feedback and neutrino free-streaming affect the halo masses (they generally lower them with respect to the DMONLY case with massless neutrinos), the clustering signal will be different for different simulations simply because I am considering a different set of systems for each simulation. Indeed, van Daalen et al. (2014) have shown that, in the case of massless neutrino simulations, the increased amplitude of the large-scale autocorrelation in hydrodynamical simulations with respect to the DMONLY case can be entirely accounted for by the change in halo mass.

I confirm the findings of van Daalen et al. (2014) in the left panel of Figure 2.15, where I use my halo matching technique to identify a common set of haloes for the different simulations. Specifically, I bin haloes by their corresponding masses in the DMONLY case. To a high level of accuracy, I find that on scales  $r \gg r_{200}$  the clustering is unaffected by baryon physics when considering a common set of haloes (i.e., feedback does not push haloes around).

The situation is different in the case of neutrino free-streaming, however, which I consider in the right panel of Figure 2.15. In particular, when I account for the effects of changes in the halo mass, by adopting a common set of haloes, I find that the large-scale clustering signal is now suppressed by  $\sim 10\%$ . Physically this makes sense, since the free-streaming of the neutrino background acts to delay the growth of fluctuations (i.e., it suppresses the matter power spectrum). This result is useful for galaxy surveys that compare with semi-empirical models such as SHAM, or with SA models, which are based on the masses of haloes in DMONLY simulations. However, it is important to note that for observational surveys that use directly measured masses, e.g. by combining with galaxy-galaxy lensing, it is Figure 2.14 that is most directly relevant.

In Figure 2.16 I test how well treating the effects of baryon physics and neutrino free-streaming separately (i.e., multiplicatively) reproduces their combined effects on the clustering of massive haloes. For this test, I use the self-consistent halo masses from each simulation, rather than identifying a common set of haloes and binning using masses from the massless DMONLY run. In the top panel of Figure 2.16 I compare the clustering signal measured directly from the hydrodynamics+neutrino simulations (curves) to that predicted by treating these two processes separately (crosses). So,

for example, the prediction for the NU 0.24 case would be to multiply the clustering signal of the massless DMONLY run, NU 0.00 DM, by the ratio of the hydrodynamics to DMONLY case with massless neutrinos (i.e., NU 0.00/NU 0.00 DM) and by the ratio of the massive to massless neutrino cases in the absence of baryon physics (i.e., NU 0.24 DM/NU 0.00 DM). The bottom panel of Figure 2.16 shows the ratio of the prediction arising from the multiplicative approach to the self-consistent calculation.

I find that for  $r > 1h^{-1}\text{Mpc}$  and  $12 \leq \log(M_{200,\text{crit}}/M_{\odot}) \leq 14$ , the combined effects of neutrino free-streaming and baryon physics can be reproduced extremely well (1-2% accuracy), by considering these effects separately, independently of the choice of summed neutrino mass,  $M_{\nu}$ . This agreement worsens slightly in the highest mass bin, where the two cases deviate by  $\approx 10\%$  at large radii for the highest summed neutrino mass.

## 2.6 Matter Clustering

As a final LSS diagnostic, I now consider the effects of baryon physics and massive neutrinos on the total matter power spectrum. I compute the matter power spectra using the GenPK code<sup>8</sup>.

In Figure 2.17 I show the separate effects of baryon physics (left panel) and neutrino free-streaming (right panel) on the matter power spectrum at three different redshifts. Consistent with the previous findings of van Daalen et al. (2011), I find that AGN feedback suppressed the matter power spectrum on small scales ( $k > 1 \text{ h/Mpc}$ ), at levels of up to 10-20%. Neutrino free-streaming also suppresses the matter power spectrum, but over a wider range of scales (up to the free-streaming scale  $\sim 100 \text{ Mpc}$ , Ali-Haïmoud and Bird 2013). While the suppression due to neutrino free-streaming is largely insensitive to the redshift, that due to baryonic feedback grows by a factor of  $\sim 2$  between  $z = 2$  and  $z = 0$

In Figure 2.18 I show the combined effects of baryon physics and neutrino free-

<sup>8</sup><https://github.com/sbird/GenPK>

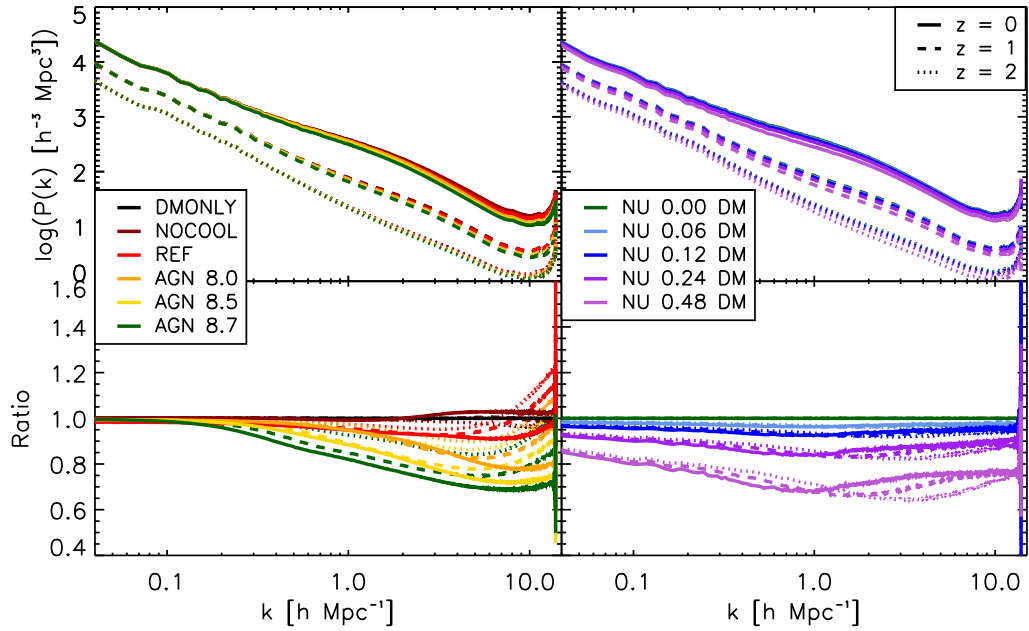


Figure 2.17: Matter power spectra for different baryon physics models in the absence of neutrino physics in the WMAP-7 cosmology (left) and for different  $\sum M_\nu$  values in the absence of baryonic physics in the WMAP-9 cosmology (right) at  $z = 0$ . As in Figure 2.1, colours denote the various runs (see the legend and Table 2.1), while the different linestyles denote different redshifts. The bottom left panel shows matter power spectra for the cosmo-OWLS runs normalised to the DMONLY case, whereas in the bottom right panel the collisionless BAHAMAS runs have been normalised by the massless neutrino case. Baryonic feedback suppresses the matter power spectrum by 10-20% on small scales ( $k > 1$  h/Mpc). In contrast, the suppression due to neutrino free-streaming depends strongly on the choice of summed neutrino mass and has an effect over a much wider range of scales. The suppression due to baryonic feedback grows by a factor of  $\sim 2$  between  $z = 2$  and  $z = 0$ , whereas the level of suppression resulting from neutrino free-streaming is only weakly dependent on redshift.

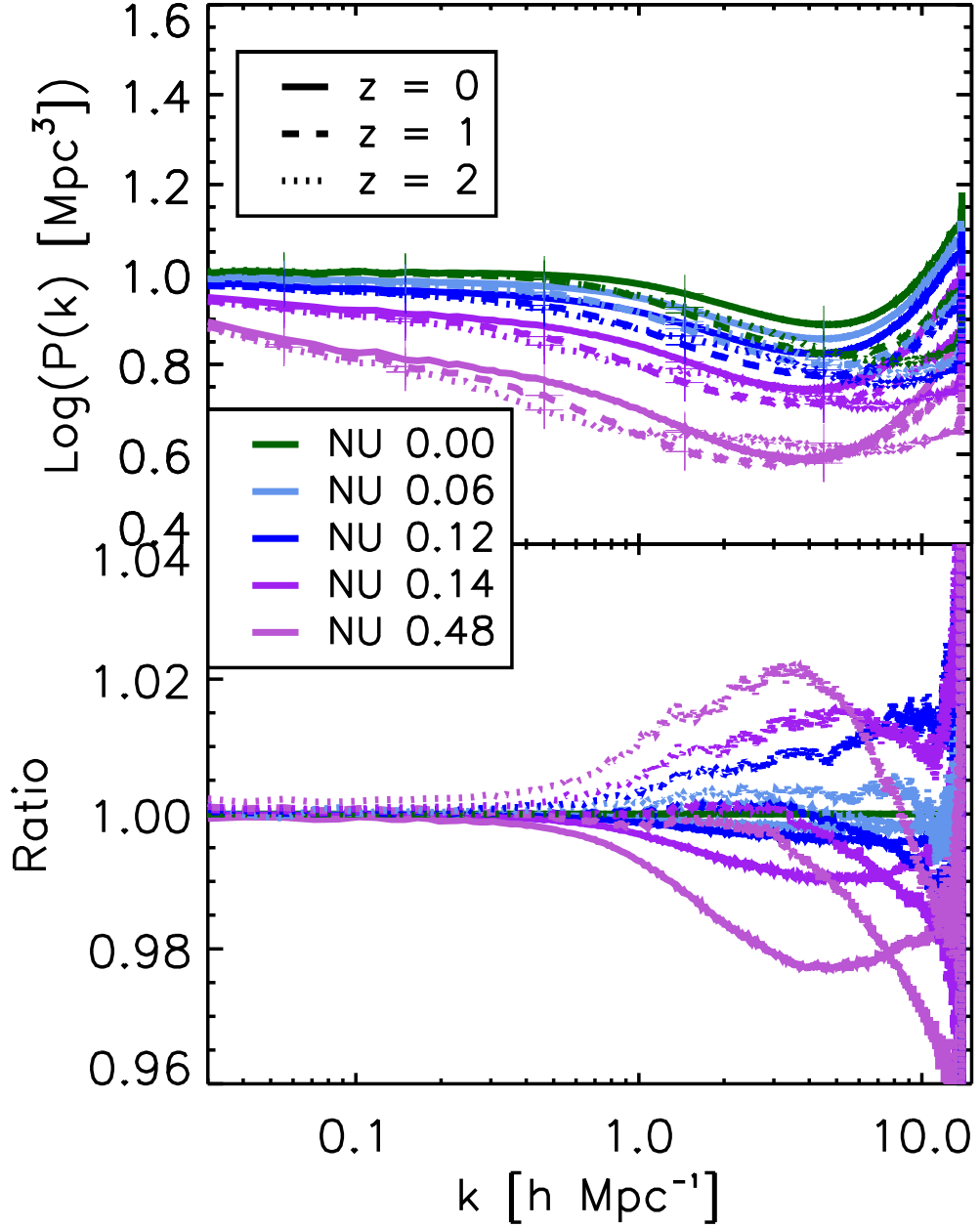


Figure 2.18: Comparison of the matter power spectra ( $P(k)$ ) arising when simulating baryonic feedback and neutrino free-streaming simultaneously (curves) and those calculated by multiplying the separate effects of baryonic feedback in the absence of neutrinos and the effects of neutrino free-streaming in the absence of baryon physics (crosses). Solid, dashed and dotted lines correspond to  $P(k)$  at redshifts of 0, 1 and 2 respectively. The bottom panel shows each of the multiplicative models normalised by the corresponding combined case. As in Figure 2.16, the multiplicative treatment recovers the combined result to better than 3% accuracy independent of the chosen summed neutrino mass for  $0.04 \leq k[\text{h}/\text{Mpc}] \leq 10$ .

streaming (curves) and compare this with the predicted power spectra when these effects are treated separately and then multiplied (crosses). The predictions reproduce the power spectra from the self-consistent simulations to typically better than 2% accuracy over the full range of redshifts and summed neutrino masses I have considered for wavenumbers of  $k < 10$  h/Mpc. This result provides some reassurance for existing studies that have treated these processes independently (e.g., Harnois-Déraps et al. 2015).

## 2.7 Summary and Discussion

I have used the cosmo-OWLS and BAHAMAS suites of cosmological hydrodynamical simulations to explore the separate and combined effects of baryon physics (particularly AGN feedback) and neutrino free-streaming on different aspects of large-scale structure (LSS), including the halo mass function and halo number counts, the spherically-averaged density profiles and mass–concentration relation, and the clustering (autocorrelations) of haloes and matter.

From this investigation I conclude the following:

- AGN feedback can suppress the halo mass function by  $\approx 20 - 30\%$  relative to the DMONLY case on the scale of GGCs, a result which is largely insensitive to redshift (Figure 2.1, left panels), as also found by Velliscig et al. (2014). Neutrino free-streaming preferentially suppresses the high-mass (cluster) end of the HMF, with a strong dependence on redshift and the choice of summed neutrino mass (Figure 2.1, right panels).
- In terms of mass density profiles, the inclusion of baryonic physics, and in particular radiative cooling and AGN heating, produces higher central (due to cooling) and peripheral densities (due to gas ejection), with lower densities at intermediate radii (due to gas ejection), relative to the DMONLY case. The gas expulsion leads to an expansion of the dark matter, such that the Navarro-Frenk-White (NFW) scale radius increases (Figure 2.9). To a first approximation, the

free-streaming of massive neutrinos reduces the amplitude of the mass density profiles while approximately preserving their shape within the virial radius (Figure 2.10). However, there is a change in the shape of the profile just beyond the virial radius, such that the radius that marks the transition from the ‘1 halo’ to the ‘2 halo’ term decreases with increasing summed neutrino mass.

- The free-streaming of massive neutrinos results in a reduction in the amplitude of the mass–concentration relation by  $\sim 10\%$  (depending on the summed neutrino mass) with only minimal alteration to its slope (Figure 2.12, right panels). This is due both to a lowering of the overall halo mass and a slight increase of the scale radius. By contrast, AGN feedback alters both the amplitude and the slope of the mass–concentration relation (Figure 2.12, left panels), as also found by Duffy et al. (2010). The amplitude shift here is due mainly to an increase in the scale radius, driven by the expansion of the dark matter halo due to gas expulsion from feedback. The change in slope reflects the increased importance of feedback for groups relative to clusters.
- In bins of halo mass, both AGN feedback and neutrino free-streaming result in an apparent enhancement of the amplitude of the 2-point halo correlation function on large scales ( $r \gg r_{200}$ ), by  $\sim 10\%$  with respect to the DMONLY case with massless neutrinos at  $z = 0$  (Figure 2.14). In the case of simulations with baryons and massless neutrinos, this is due entirely to the effect on the halo mass (so that the mass bins contain different systems in different simulations) rather than a true alteration of the spatial distribution of haloes (Figure 2.15, left panels), consistent with the findings of van Daalen et al. (2014). In the case of simulations with massive neutrinos, when the change in halo mass is accounted for, I find that the large-scale clustering of haloes is actually *suppressed* relative to a massless neutrino case (Figure 2.15, right panels), as expected.
- On small scales ( $k > 1 \text{ h/Mpc}$ ) the matter power spectrum can be suppressed by AGN feedback by up to 10-20% at  $z = 0$ , consistent with the previous findings of van Daalen et al. (2011). This factor increases by a factor of  $\approx 2$  between  $z = 2$  and  $z = 0$  (Figure 2.17, left panels). Neutrino free-streaming also sup-

presses the matter power spectrum, but over a much wider range of scales (see also Semboloni et al. 2011). This suppression is nearly insensitive to redshift but depends strongly on the adopted summed neutrino mass (Figure 2.17, right panels).

- I have investigated the extent to which the effects of baryon physics and neutrino free-streaming can be treated independently. The procedure of multiplying together the magnitudes of the two effects when taken in isolation reproduces their combined effects to typically a few percent accuracy for the halo mass function (Figure 2.3), the mass density profiles (Figure 2.11), the mass–concentration relation (Figure 2.13), and the clustering of haloes (Figure 2.16) and matter (Figure 2.18) over ranges of  $12 \leq M_{200,\text{crit}}/M_{\odot} \leq 15$ ,  $12 \leq M_{200,\text{crit}}/M_{\odot} \leq 14.5$ ,  $12 \leq M_{200,\text{crit}}/M_{\odot} \leq 14$  and  $0.04 \leq k \text{ [h/Mpc]} \leq 10$ , respectively. My simulation-based matter power spectrum findings are therefore consistent with those of Mead et al. (2016), who explored the degeneracies between feedback, massive neutrinos, and modified gravity in the context of a modified ‘halo model’ formalism (see Mead et al. 2015 for further details).

My work has demonstrated that both AGN feedback and neutrino free-streaming can have a considerable impact on LSS. They should therefore both be included in cosmological analyses. Through the use of self-consistent cosmological simulations I have shown that, to a high degree of accuracy, these processes are separable (i.e., can be treated independently), which should considerably simplify the inclusion of their effects in cosmological studies that adopt, for example, the halo model formalism or the linear matter power spectrum (e.g., from CAMB).

# Chapter 3

## The Clustering of Galaxy Groups and Clusters: Comparing the BAHAMAS Simulations with the GAMA survey

### 3.1 Introduction

Recent years have seen a resurgence of interest in the effects of massive neutrinos on LSS which has been driven primarily by a number of apparent tensions between the *Planck* primary CMB cosmological constraints and constraints coming from, for example, the observed abundances of massive clusters (Planck Collaboration et al., 2014, 2016b) and constraints from tomographic analysis of cosmic shear data (Heymans et al., 2013; Hildebrandt et al., 2017).

While the invocation of massive neutrinos to reconcile these tensions (e.g., Wyman et al. 2014; Battye and Moss 2014; McCarthy et al. 2018) remains controversial (e.g., MacCrann et al. 2015), their inclusion in cosmological models is a necessity for precise LSS predictions. This is because solar oscillation experiments have found that the three active neutrino species have a summed mass  $M_\nu$  of at least 0.06 eV (0.1 eV) when adopting a normal (inverted) hierarchy (Lesgourgues and Pastor, 2006). Since

Table 3.1: Overview of BAHAMAS simulation runs used in this work. The columns are: (1) The label assigned to the cosmology in which the run has been carried out; (2) The label assigned to the individual run; (3) The summed mass of the three active neutrino species; (4) Hubble’s constant; (5) The present-day matter density (in units of the critical density); (6) The present-day baryon density; (7) The present-day dark matter density; (8) The present-day neutrino density (computed as  $\Omega_\nu = \frac{M_\nu}{93.14 h^{-1} \text{eV}}$ ); (9) The spectral index of the initial power spectrum; (10) The amplitude of the initial matter power spectrum at a CAMB pivot  $k$  of  $2 \times 10^{-3} \text{ Mpc}^{-1}$ ; (11) The present-day linearly evolved amplitude of the initial matter power spectrum on a scale of  $8 h^{-1} \text{ Mpc}$ ; (12) The dark matter particle mass; (13) The initial baryon particle mass.

| Cosmology     | run     | $\sum M_\nu$<br>[eV] | $H_0$<br>[kms $^{-1}$ Mpc $^{-1}$ ] | $\Omega_m$ | $\Omega_b$ | $\Omega_{cdm}$ | $\Omega_\nu$ | $n_s$  | $A_s$<br>[ $10^{-9}$ ] | $\sigma_8$ | $M_{DM}$<br>[ $10^9 h^{-1} M_\odot$ ] | $M_{bar,init}$<br>[ $10^8 h^{-1} M_\odot$ ] |
|---------------|---------|----------------------|-------------------------------------|------------|------------|----------------|--------------|--------|------------------------|------------|---------------------------------------|---|
| (1)           | (2)     | (3)                  | (4)                                 | (5)        | (6)        | (7)            | (8)          | (9)    | (10)                   | (11)       | (12)                                  | (13)  |
|               | NU 0.00 | 0                    |                                     |            |            | 0.2330         | 0.0          |        |                        | 0.8211     | 3.85                                  |   |
|               | NU 0.06 | 0.06                 |                                     |            |            | 0.2317         | 0.0013       |        |                        | 0.8069     | 3.83                                  |   |
| WMAP-9        | NU 0.12 | 0.12                 | 70.00                               | 0.2793     | 0.0463     | 0.2304         | 0.0026       | 0.9720 | 2.392                  | 0.7924     | 3.81                                  | 7.66  |
|               | NU 0.24 | 0.24                 |                                     |            |            | 0.2277         | 0.0053       |        |                        | 0.7600     | 3.77                                  |   |
|               | NU 0.48 | 0.48                 |                                     |            |            | 0.225          | 0.0105       |        |                        | 0.7001     | 3.68                                  |   |
|               | NU 0.06 | 0.06                 | 67.87                               | 0.3067     | 0.0482     | 0.2571         | 0.0014       | 0.9701 | 2.309                  | 0.8085     | 4.25                                  | 7.97  |
|               | NU 0.12 | 0.12                 | 67.68                               | 0.3091     | 0.0488     | 0.2574         | 0.0029       | 0.9693 | 2.326                  | 0.7943     | 4.26                                  | 8.07  |
| <i>Planck</i> | NU 0.24 | 0.24                 | 67.23                               | 0.3129     | 0.0496     | 0.2576         | 0.0057       | 0.9733 | 2.315                  | 0.7664     | 4.26                                  | 8.21  |
|               | NU 0.48 | 0.48                 | 66.43                               | 0.3197     | 0.0513     | 0.2567         | 0.0117       | 0.9811 | 2.253                  | 0.7030     | 4.25                                  | 8.49  |

cosmological relic neutrinos will remain relativistic until relatively late times, a non-zero neutrino mass will result in them acting as a form of hot dark matter. This leads to a portion of the total mass budget available for the formation of structure acting to resist significant gravitational collapse due to free-streaming motion, and therefore to an effect on the overall LSS. Precise predictions of LSS therefore require the inclusion of massive neutrinos.

The BAHAMAS project, a suite of cosmological hydrodynamical simulations including prescriptions for the effects of massive neutrinos, was enacted in part to address this necessity. BAHAMAS provides a selection of runs wherein the value of  $M_\nu$  is dialled in the context of a fixed feedback model calibrated to reproduce observed baryon fractions of massive galaxies and GGCs, and with the remaining cosmological parameters based on either the WMAP-9 or *Planck* best fit parameters (see McCarthy et al. 2018 for further details).

Work by Jakobs et al. (2017) has demonstrated that BAHAMAS reproduces the observed stacked weak lensing and thermal Sunyaev-Zel'dovich effect signals as a function of GGC richness or integrated stellar mass. This supports the use of BAHAMAS not simply as a tool for investigating the qualitative behaviour of LSS as a function of various cosmological models, but as a way to make quantitative predictions of LSS observations. On this basis, the present study aims to compare predictions of the clustering of GGCs (as characterised by the GGC 2-point autocorrelation function) from BAHAMAS with observations from the GAMA survey.

This chapter is organised as follows: In Section 3.2 I discuss the simulated (Section 3.2.1) and observational (Section 3.2.2) datasets used. Section 3.3 describes my treatment of these datasets, specifically the construction of consistent, volume-limited galaxy catalogues for both the simulated and observed datasets (Section 3.3.1); the assignment of these galaxies to FoF groups (Section 3.3.2); and the methodology by which I estimate the GGC clustering (Section 3.3.3). The results of this investigation are presented in Section 3.4, first the comparison of the GAMA and BAHAMAS results in Section 3.4.1; then an examination of potential sources of uncertainty in these data in Section 3.4.2. Finally in Section 3.5 I present my conclusions and a summary of this

work.

## 3.2 Datasets

### 3.2.1 BAHAMAS

I use the BARYons and HALoes of MAssive Systems (BAHAMAS) suite of cosmological hydrodynamical simulations to make predictions for the GAMA observations. I provide a brief summary of the simulations here, and refer the reader to McCarthy et al. (2017) and McCarthy et al. (2018) where they are discussed in further detail.

The BAHAMAS suite comprises a selection of  $400 h^{-1}$  Mpc comoving box simulations, each containing  $2 \times 1024^3$  particles. Transfer functions were computed with the Boltzmann code CAMB<sup>1</sup> and the initial conditions were created using a version of N-GenIC that has been modified to include support for massive neutrinos and second-order Lagrangian Perturbation Theory corrections<sup>2</sup>. A version of the Lagrangian TreePM-SPH code GADGET3 (last described in Springel 2005), modified as part of the OWLS project to include new subgrid physics as described in Schaye et al. (2010), was used to run the simulations. This version has been further modified to implement the semi-linear algorithm developed by Ali-Haïmoud and Bird (2013) to include the effects of massive neutrinos on both the background expansion rate and the growth of density fluctuations. At each timestep, the algorithm uses a linear perturbation integrator sourced from the non-linear baryons+CMD potential to compute neutrino perturbations on the fly which are added to the total gravitational force. This allows for the self-consistent inclusion of the mutual responses of the neutrinos to the baryons+CDM and of the baryons+CDM to the neutrinos at each time step.

In addition to the effects of massive neutrinos (where applicable), the computation of the background expansion rate includes the effects of radiation. SPH smoothing is carried out using the nearest 48 neighbours, and the gravitational softening is fixed to

---

<sup>1</sup><http://camb.info>

<sup>2</sup><https://github.com/sbird/S-GenIC>

$4h^{-1}$  Mpc comoving at  $z > 3$ , and  $4h^{-1}$  Mpc in physical units below this.

Subgrid prescriptions are included for metal-dependent radiative cooling (Wiersma et al., 2009a), star formation (Schaye and Dalla Vecchia, 2008b), stellar evolution, mass loss and chemical enrichment from Type II and Ia supernovae and asymptotic giant branch stars (Wiersma et al., 2009b). Also incorporated into the simulations are stellar feedback (Dalla Vecchia and Schaye, 2008) and the prescription for AGN feedback and black hole growth detailed in Booth and Schaye (2009).

In order to ensure that collapsed structures arising in the simulations have the correct global baryon content, the parameters governing the efficiencies of the stellar and AGN feedback mechanisms have been adjusted so that the simulations produce present-day NFW and gas mass fraction - halo mass relations of GGCs that are consistent with those inferred from high-resolution X-ray observations. This ensures that the associated back reaction of baryons on the total matter distribution should be broadly correct. McCarthy et al. (2017) demonstrated that this approach accurately reproduces an unprecedented range of massive system properties, including the observed mappings between galaxies, hot gas, total mass and black holes. Note that the feedback efficiency parameters used are identical across the varying cosmological parameters of the different BAHAMAS runs. While the calibration was explicitly carried out in the context of the fiducial WMAP 9-year cosmology with massless neutrinos, McCarthy et al. (2018) demonstrated that the internal properties of collapsed structures are largely insensitive to the variations in cosmology considered by BAHAMAS, and I am therefore confident in the continued validity of this calibration over different runs.

I use a total of 10 runs from the BAHAMAS suite for this work. These runs span five different values for the summed neutrino mass between 0 and 0.48 eV. For each value, runs have been carried out with initial conditions based on the WMAP-9 and *Planck* cosmological constraints. As discussed in McCarthy et al. (2018), two subtly different approaches have been taken when selecting the values of the other cosmological parameters for the WMAP-9 and *Planck* cases. For runs using the WMAP-9-based cosmological constraints, the value of  $\Omega_{cdm}$  in each case is reduced in order to maintain a flat geometry, i.e.  $\Omega_m = \Omega_{cdm} + \Omega_b + \Omega_\nu + \Omega_\Lambda = 1$ , while the remaining parameters

are held constant. For runs based on the *Planck* cosmological parameters, the Markov chains of Planck Collaboration et al. (2016a) have been used to select best fitting parameters when the selected massive neutrino realisation is included. The advantages of this approach is that the adopted cosmological model retains a virtually identical match to the primary CMB angular power spectrum, whereas adjusting only  $\Omega_{cdm}$  (in the case of the WMAP-9-based simulations) does not precisely preserve the CMB TT power spectrum. However, the differences in these approaches are negligibly small for my purposes.

### Light cones

In order to facilitate direct comparisons between the simulations and observations, ‘synthetic observations’ of the simulations have been produced. Specifically, light cones are first created by randomly translating and rotating simulation snapshots, which are stacked along the line of site between  $z = 0$  and  $z = 0.5$  (McCarthy et al., 2014, 2018). Given the size of the simulation box, the largest opening angle that can be adopted (i.e., without replicating across the field of view) is just larger than 15 degrees. Catalogues are therefore produced spanning an area of  $15 \text{ deg} \times 15 \text{ deg}$  back to  $z = 0.5$ . Ten quasi-independent light cones per simulation are produced by using different random transformations of the simulation snapshots along the line of sight. To more closely match the geometry of the GAMA survey, each field is separated into three 5 by 12 degree fields matching the angular sizes of the three equatorial GAMA fields. From these fields are drawn the galaxy catalogues which I use to make direct comparisons with GAMA observations.

Galaxy stellar masses are calculated as the sum of the masses of all star particles belonging to the FoF subhalo within a spherical 3d aperture of 30 kpc radius centered on the location of the subhalo particle with the lowest gravitational potential. Schaye et al. (2015) and McCarthy et al. (2017) have shown that this measurement agrees well with the Petrosian stellar mass estimate.

In addition to the synthetic datasets, I also make use of the full halo and simulated

galaxy catalogues drawn from the light cones. This gives me an additional population with which to compare in the case of each BAHAMAS run. Haloes are identified by using a standard 3D Friends-of-Friends (FoF) algorithm run on the particles in the simulation snapshots, adopting a linking length of 0.2 times the mean interparticle separation. These catalogues provide me with a ‘true’<sup>3</sup>, spatially-complete sample of overdense regions for which the ‘true’ values of important parameters, such as the 3D spherical overdensity mass, the number of luminous galaxies they contain within some 3D aperture, and positions and peculiar velocities, are known. Comparison between analyses of these ‘true’ samples and the corresponding synthetic samples permits me to determine the impact of effects such as scatter in  $M_* - M_{halo}$  relation of GGCs and the impact of peculiar velocities on FoF group finding.

I present a summary of the cosmological parameters and mass resolution of simulations used in Table 3.1.

### 3.2.2 GAMA

For comparison with BAHAMAS I use galaxy catalogues from the GAMA survey data release 3 (Baldry et al., 2018). GAMA is a spectroscopic survey covering  $\sim 286$  degrees<sup>2</sup> split across five fields. In total, it has observed nearly 300,000 galaxies and is highly complete down to a limiting magnitude of  $r < 19.8$ . I make use of the G09, G12 and G15 equatorial fields, comprising a total of 180 degrees<sup>2</sup>. This choice is motivated by the uniform target selection adopted in these fields (Kuijken et al., 2015).

An important advantage of spectroscopic surveys is that they allow one, at least in principle, to robustly distinguish systems which are collapsed/collapsing from collections of galaxies that are grouped purely in projection, which happens in the absence of redshift information or with uncertain photometric redshift estimates.

The masses of galaxies in the GAMA catalogues used here are derived by stellar population synthesis (SPS) fitting. Briefly, stellar evolution models are used with an assumed

---

<sup>3</sup>i.e. perfectly capturing the simulated reality of the BAHAMAS runs

initial mass function to produce models that describe the spectral evolution of single-age, or ‘simple’, stellar populations (SSPs). These SSPs are then combined according to some an assumed galaxy star formation history in order to construct composite stellar populations (CSPs) that describe the spectral characteristics of a galaxy. These synthesised CSPs can then be used to produce predicted spectral energy distributions (SEDs) that can be compared with spectrographic observations of real galaxies. Fitting to the observational SED data allows constraints to be placed on the stellar population parameters, most notably, at least for my purposes here, the stellar mass. For a full discussion of this technique and its specifics with regards to GAMA I refer the reader to Taylor et al. (2011).

The work carried out by Jakobs et al. (2017) confirmed the validity of using GAMA stellar mass estimates derived by this method alongside the measurements made within BAHAMAS and described in Section 3.2.1 above. Specifically, for an approximately volume limited sample created with identical mass and redshift cuts as those used for this work, the NFWs are in good agreement (See Figure. 2 of that paper). This is largely unsurprising as the BAHAMAS simulations were explicitly calibrated to reproduce the observed present-day NFW derived from SDSS data, against which mass estimates the GAMA galaxy stellar masses were shown to be in agreement by Taylor et al. (2011).

## 3.3 Galaxy Selection, Group Finding, and Clustering

### 3.3.1 Galaxy Selection

Following McCarthy et al. (2017), I limit my analysis of BAHAMAS simulated galaxies to systems with stellar masses of  $M_* \geq 10^{10} M_\odot$ , where  $M_*$  is measured within a 3D 30 kpc (physical) aperture. Schaye et al. (2015) (see also McCarthy et al. 2017) have shown that this aperture choice results in stellar mass estimates that are a good approximation to more observationally-oriented estimates, such as those based on Petrosian fluxes. Note that this stellar limit was adopted in McCarthy et al. based on the results

Table 3.2: Overview of the galaxy samples drawn from each data set after cuts in redshift and mass have been applied. The columns are: (1) the data set from which the galaxy sample is drawn; (2) the total number of galaxies in the sample; (3) the angular density of galaxies in the sample. Note that the values quoted for the BAHAMAS WMAP-9 data sets are aggregated over 30 5 by 12 degree fields for , while those for BAHAMAS *Planck* are aggregated over ten 15 by 15 degree fields.

| Sample                |         | $N_{gal}$ | $n_{gal}$<br>[ $10^6 \text{Gpc}^{-3}$ ] |
|-----------------------|---------|-----------|---|
| (1)                   |         | (2)       | (3)                                     |
| GAMA WMAP-9           | G09     | 12,329    | 3.681                                   |
|                       | G12     | 15,770    | 4.708                                   |
|                       | G15     | 15,901    | 4.747                                   |
| GAMA <i>Planck</i>    | G09     | 12,329    | 3.396                                   |
|                       | G12     | 15,770    | 4.344                                   |
|                       | G15     | 15,901    | 4.380                                   |
| BAHAMAS WMAP-9        | NU 0.00 | 528,459   | 5.259                                   |
|                       | NU 0.06 | 525,801   | 5.232                                   |
|                       | NU 0.12 | 526,519   | 5.240                                   |
|                       | NU 0.24 | 514,595   | 5.240                                   |
|                       | NU 0.48 | 495,086   | 4.927                                   |
| BAHAMAS <i>Planck</i> | NU 0.06 | 673,135   | 4.944                                   |
|                       | NU 0.12 | 676,885   | 4.935                                   |
|                       | NU 0.24 | 684,364   | 4.900                                   |
|                       | NU 0.48 | 683,389   | 4.734                                   |

of a resolution study of the BAHAMAS simulations (see the appendix of that study).

As I want to make a like-with-like comparison between the simulations and observations, I impose the same lower stellar mass limit when selecting galaxies from the GAMA survey. GAMA is a spectroscopic survey of galaxies identified in the SDSS and is, like SDSS, an inherently flux-limited survey. As a consequence, GAMA is only (approximately) spectroscopically complete to galaxies with  $M_* \geq 10^{10} M_\odot$  out to  $z \approx 0.2$ . While I could in principle adopt the same flux limit for BAHAMAS as in GAMA and proceed out to higher redshifts (i.e., with both the simulated and observed galaxy samples probing progressively more massive systems beyond  $z \approx 0.2$ ), for the present study I instead limit my analysis to  $z \leq 0.2$ , constructing effectively volume-limited samples for both BAHAMAS and GAMA. This approach was also adopted by Jakobs et al. (2017). One advantage of using volume-limited samples is that it results in a consistent definition for GGCs that is independent of redshift. Additionally, quantities such as the multiplicity (richness) and integrated GGC stellar mass, which are often used to track halo mass, are also implicitly independent of redshift, as they are derived by integrating galaxies down to the same stellar mass limit independent of distance.

I therefore apply these two cuts, i.e.,  $M_* \geq 10^{10} M_\odot$  and  $z \leq 0.2$ , to both the GAMA and BAHAMAS galaxy catalogues, resulting in approximately volume-limited galaxy samples of equal angular size, total volume and depth. All subsequent treatment of these catalogues is carried out consistently between the simulated and observed data.

The total number of galaxies in these samples are presented in Table 3.2. As I combine the 30 fields for each BAHAMAS WMAP-9 run I quote the total number of galaxies across these fields. Similarly, for the *Planck* runs the quoted values are totals across the ten 15 by 15 degree fields for each run. To facilitate qualitative comparisons between these samples, in column (3) of table 3.2 I include the comoving number density of galaxies (in  $(Gpc/h)^{-3}$ ) in each sample, although these values do not account for the reduction in the effective area of the GAMA fields due to the masking of foreground sources. This leads to an apparent overestimation of the galaxy number density within

BAHAMAS. Full-sky comoving volumes for each cosmology were computed using the Cosmology calculator developed by Wright (2006). The comoving volume contained within the footprint of each survey was computed by:

$$V_{survey} = V_{fullsky} \frac{A_{survey}}{A_{fullsky}} = V_{fullsky} \frac{\pi \Delta RA \cdot \Delta Dec}{360^2} \quad (3.1)$$

where  $\Delta RA$  and  $\Delta Dec$  are the RA and Dec range of the survey footprint respectively.

### 3.3.2 Group Finding

I identify GGCs by means of a 2D FoF algorithm following the scheme of Robotham et al. (2011), albeit in the context of a volume-limited galaxy sample.

Two galaxies are linked together if their angular (transverse) and line-of-sight distances are smaller than the predefined ‘linking lengths’. The transverse and line-of-sight linking lengths are defined based on (fractions of) the mean comoving separation(s) of objects in the sample. Two galaxies  $i$  and  $j$  are linked if:

$$\begin{aligned} \tan \theta_{i,j} \cdot \frac{d_{com,i} + d_{com,j}}{2} &\leq b \cdot \langle sep_i \rangle, \\ |d_{com,i} - d_{com,j}| &\leq b \cdot R \cdot \langle sep_i \rangle \end{aligned} \quad (3.2)$$

where  $\theta_{ij}$  is the angle between the galaxies,  $d_{com,k}$  is the line-of-sight comoving distance to galaxy  $k$  (derived from the redshift),  $\langle sep_i \rangle$  is the mean comoving separation, and  $b$  and  $R$  are multiplicative coefficients. These expressions are equivalent to equations (1) and (4) of Robotham et al. (2011).

I compute the mean separation  $\langle sep_i \rangle$  by first rank ordering the galaxies by stellar mass and then computing the space density per comoving volume,  $n$ , of galaxies with mass  $> M_*$ . The separation as a function of stellar mass is then just  $\langle sep_i \rangle \equiv n_i^{-1/3}$ .

Note that, in general, adopting a scheme where the linking lengths are determined by (a fraction of) the mean space density of objects can lead to different linking lengths being adopted for the simulations and the observations, or even between different sim-

ulations. This is just because the space density of galaxies of a given stellar mass can be different between the simulations and the observations (i.e., there can be differences in the galaxy stellar mass functions). If this is the case, the grouping of galaxies could differ in a systematic way between the simulations and observations and complicate comparisons between them. However, I point out that, in the present case, the galaxy stellar mass functions agree very well between the different simulations (see figure 4 of McCarthy et al. 2018) and between the simulations and GAMA (see figure 2 of Jakobs et al. 2017). The latter is a direct result of the feedback calibration strategy of BAHAMAS (McCarthy et al., 2017). As a consequence, the adopted linking lengths agree very well between the different simulations and GAMA. Furthermore, I have explicitly checked that adopting precisely the same linking lengths (derived from the BAHAMAS NU 0.00 simulation) for all the datasets yields virtually identical results and my conclusions remain the same.

In order to fully specify the linking lengths, I also require values for the multiplicative coefficients,  $b$  and  $R$ . These values cannot be derived from first principles and are therefore somewhat arbitrary, but a common strategy to specify them is to use synthetic (or ‘mock’) galaxy catalogues and compare the resulting GGC catalogues with the ‘true’ one as the values of  $b$  and  $R$  are systematically varied. Robotham et al. (2011) followed this strategy using synthetic catalogues generated from a semi-analytic model of galaxy formation. By comparing the resultant FoF groups and their galaxy membership to the ‘true’ galaxy groups in the model, they found that  $b = 0.06$  and  $R = 18$  are good choices for robustly linking galaxies to groups within their virial radii. Note that  $R$  needs to be significantly larger than  $b$  in order to account for the peculiar motions of galaxies (which leads to the so-called ‘Finger of God’ effect in redshift space). I follow Robotham et al. (2011) and adopt the same values for  $b$  and  $R$  in my analysis.

My initial analysis follows Jakobs et al. (2017) in adopting fixed linking lengths for the entire selection, where  $\langle sep_i \rangle = \langle sep_{all} \rangle$  is the mean separation for all galaxies in my sample. Note that this mean separation is effectively set by the space density of the lowest-mass galaxies (with  $M_* \approx 10^{10} M_\odot$ ), since they are the most abundant. However, adopting a fixed linking length is not necessarily the optimal strategy. In-

deed, Jakobs et al. (2017) have found that adopting a fixed linking length results in a degree of spurious fragmentation of high-mass GGCs compared to the ‘true’ catalogue (see also Section 3.4.2 below). While in principle this should not impede my ability to compare the observed and simulated GGCs (since I have consistently applied the same linking strategy for both), I nevertheless explore how my results are affected by the linking strategy later (see Section 3.4.2).

Finally, I note that when applying the FoF algorithm, a reference cosmology must be adopted in order to convert redshifts and angular separations into comoving distance separations. Consequently, it is necessary to re-analyse the observational data when comparing to synthetic observations based on simulations with different cosmologies. Note, however, that most of the effects of varying the background cosmology are implicitly removed as I use comoving distances in units of  $\text{Mpc}/h$  and my analysis is restricted to relatively low redshifts. Nevertheless, when performing quantitative comparisons between GAMA and BAHAMAS I consistently adopt the given simulation’s cosmology (either WMAP-9 or *Planck*) when analysing the GAMA data.

### 3.3.3 Clustering

#### Clustering Estimator

The spatial clustering of a population of objects, such as GGCs, can be characterised by its two-point autocorrelation function. Here I employ the two-point function  $w(\theta)$  introduced by Landy and Szalay (1993). While the overall amplitude and shape of the autocorrelation function is somewhat sensitive to the estimator used, my interest is in relative differences between identically calculated autocorrelation functions and my results are therefore insensitive to the precise estimator that is used.

I have performed the initial clustering analysis in the context of both the 3D redshift space autocorrelation function,  $\xi(r)$ , and the projected angular autocorrelation function,  $w(\theta)$ . While the results in both cases are qualitatively similar (as would be expected), projection effects in the latter mean that the former is better constrained. I

therefore adopt  $\xi(r)$  as my clustering estimator throughout this study.

For a distribution of objects and a suitably normalised random distribution of identical mean density and sampling geometry, the Landy and Szalay (1993) estimator is given by:

$$\xi(r_{3D}) = \frac{DD(r_{3D}) - 2DR(r_{3D}) + RR(r_{3D})}{RR(r_{3D})}, \quad (3.3)$$

where  $DD(r)$  and  $RR(r)$  are the pair counts as a function of the 3D radial separation between the data and random distributions, respectively, and  $DR(r)$  is the cross-correlated pair counts of the data and random datasets. The pair counts are calculated as:

$$\begin{aligned} DD(r_{3D}) &= \sum_i^{N_D} \sum_j^{N_D} P(|\mathbf{p}_{D,i} - \mathbf{p}_{D,j}|, r_{3D}) \\ DR(r_{3D}) &= \sum_i^{N_D} \sum_j^{N_R} P(|\mathbf{p}_{D,i} - \mathbf{p}_{R,j}|, r_{3D}) \\ RR(r_{3D}) &= \sum_i^{N_R} \sum_j^{N_R} P(|\mathbf{p}_{R,i} - \mathbf{p}_{R,j}|, r_{3D}), \end{aligned} \quad (3.4)$$

where  $N_D$  and  $N_R$  are the total number of points in the data and random sets, respectively, and  $\mathbf{p}_{X,n}$  is the position vector of the  $n^{\text{th}}$  point in dataset  $X$ . This estimator has been shown to be less affected by bias and variance than similar estimators (Kerscher et al., 2000).

In order to reduce Poisson noise, I scale  $N_R$  up by a factor  $F$  relative to  $N_D$ , normalising the resulting pair counts by the relevant factor ( $F$  in the case of  $DR$  and  $F^2$  in the case of  $RR$ ) before calculating  $\xi$ . I adopt  $F = 10$  as a good trade-off between minimising the statistical noise and computational expense.

I generate random distributions of galaxies to which to compare by drawing random values of RA, Dec and  $z$  within the limits set by the maximum and minimum values in the observed and simulated datasets after normalising the RA and Dec values to the central values in each field.

RA and Dec values are drawn from a uniform distribution. In order to reproduce

the redshift distribution in the data sample, I draw random redshift values from the cumulative distribution function of data redshifts, smoothed with a Gaussian kernel to remove local overdensities in  $z$ . I follow Collins et al. (2000) in using a standard deviation for the gaussian of  $5600 \text{ km s}^{-1}$ .

For each of the GGC catalogues described above (whether derived from GAMA or the synthetic or ‘true’ BAHAMAS datasets), I calculate 2-point GGC autocorrelation functions as a function of the comoving radial distance  $r_{3D}$  using the techniques discussed above in three bins of both integrated stellar mass  $M_*$  and multiplicity  $N$ . Note that the integrated stellar mass is just the sum of the stellar masses of the individual galaxies belonging to a GGC, so it is integrated down to a stellar mass limit of  $10^{10} M_{\odot}$ . Note also that in order to accurately estimate the real stellar mass of a GGC it is necessary to apply a correction to account for low mass galaxies that are not reliably detected. For the purposes of this comparison, since my primary interest is the *relative* differences between the clustering signals, such an adjustment is unnecessary. The construction of consistent galaxy samples and identical treatment of the observed and simulated data sets ensures that the mass binning is consistent. For comparison, I also compute the clustering for the ‘true’ BAHAMAS datasets; i.e., I use the ‘true’ halo catalogues from the simulation and bin in ‘true’ halo stellar mass  $M_{*,halo}$  (using the all of the associated galaxies above the minimum mass within  $r_{200,crit}$ ) and ‘true’ multiplicity  $N_{halo}$ , as well as the total halo mass  $M_{200,crit}$ .

I choose bin edges such that the three bins are approximately equally populated in the case of the GAMA dataset for  $M_*$  and  $N$  bins, or in the NU 0.00 BAHAMAS case for the  $N_{halo}$  bins. Autocorrelation functions for each individual field are averaged in each comoving radial bin, and the standard error on the mean calculated. Due to my selection of light cones, I am also able to estimate the cosmic variance errors on the BAHAMAS data by rank ordering values in each comoving radial bin for each BAHAMAS run and selecting the central 60% of values.

Note that the factor of 10 increase in survey area between the GAMA and BAHAMAS datasets means that the simulated BAHAMAS result is much better constrained than the observational GAMA result.

## 3.4 Results

In this section, I present a comparison of the two-point autocorrelation functions of GGCs from BAHAMAS and GAMA. I will conclude that the simulations reproduce the observed clustering of GGCs in GAMA very well, but that this comparison does not strongly constrain the summed mass of neutrinos, as might have been expected given the theoretical results of Mummery et al. (2017), presented in Chapter 2. In Section 3.4.2, I explore four possible causes for why the clustering of optically-identified GGCs is not as sensitive to the summed neutrino mass as the clustering of dark matter haloes, concluding that the main culprit is the scatter in the GGC observable-halo mass relations.

### 3.4.1 Initial WMAP-9 Comparison Between BAHAMAS and GAMA.

In the top rows of Figures 3.1 and 3.2 I display the redshift-space 2-point autocorrelation functions for GAMA and BAHAMAS in equally populated bins of integrated stellar mass and multiplicity, respectively. A WMAP-9 cosmology is adopted for both the simulations and observations, while the summed neutrino mass is varied between  $M_\nu = 0$  and 0.48 eV. The middle rows display the same data normalised to the BAHAMAS massless neutrino case, while the bottom rows display them normalised to the mean of the three GAMA fields. In all panels, thick error bars correspond to the error on the mean in each comoving radial bin, while the thin error bars show the 60% confidence interval of the cosmic variance between BAHAMAS light cones, as described in the previous section.

Whether binned by integrated stellar mass (Fig. 3.1) or multiplicity (Fig. 3.2), the simulations reproduce the observed clustering of GAMA GGCs remarkably well. A slight offset is present at the very largest scales ( $r > 10h^{-1}$  Mpc), which is due to the finite box size of the simulations (e.g., Tormen and Bertschinger 1996; Bagla and Ray 2005).

Note that in order to accurately reproduce the observed clustering of the GGCs, a num-

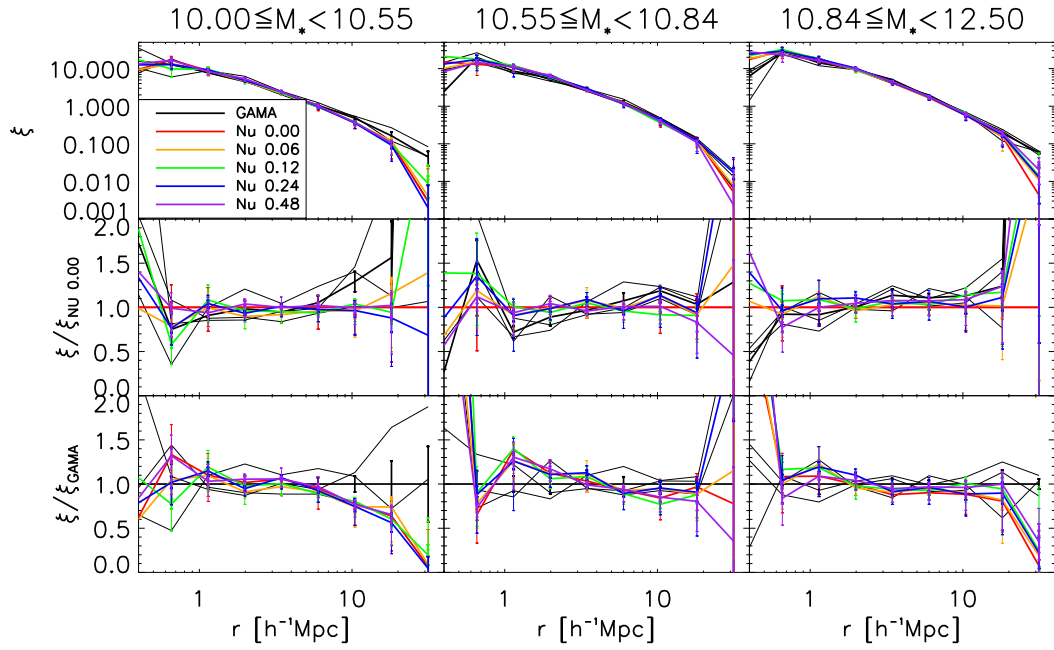


Figure 3.1: *Top*: Redshift-space 2-point GGC autocorrelation as a function of the inter-group separation for GAMA (black curve) and BAHAMAS (coloured curves) in equally populated bins of integrated stellar mass. For the BAHAMAS curves, thick error bars display the standard error on the mean and thin error bars show the 60th percentile of the cosmic variance. In the GAMA case, error bars show the standard error on the mean. *Middle*: The ratio of the autocorrelation function in each case to the BAHAMAS massless neutrino (“nu 0.00”) case. *Bottom*: The ratio of the autocorrelation function in each case to the GAMA case. There is remarkably good agreement between the BAHAMAS and GAMA cases in all three bins. However, there is no evidence for a systematic offset between the BAHAMAS neutrino cases.

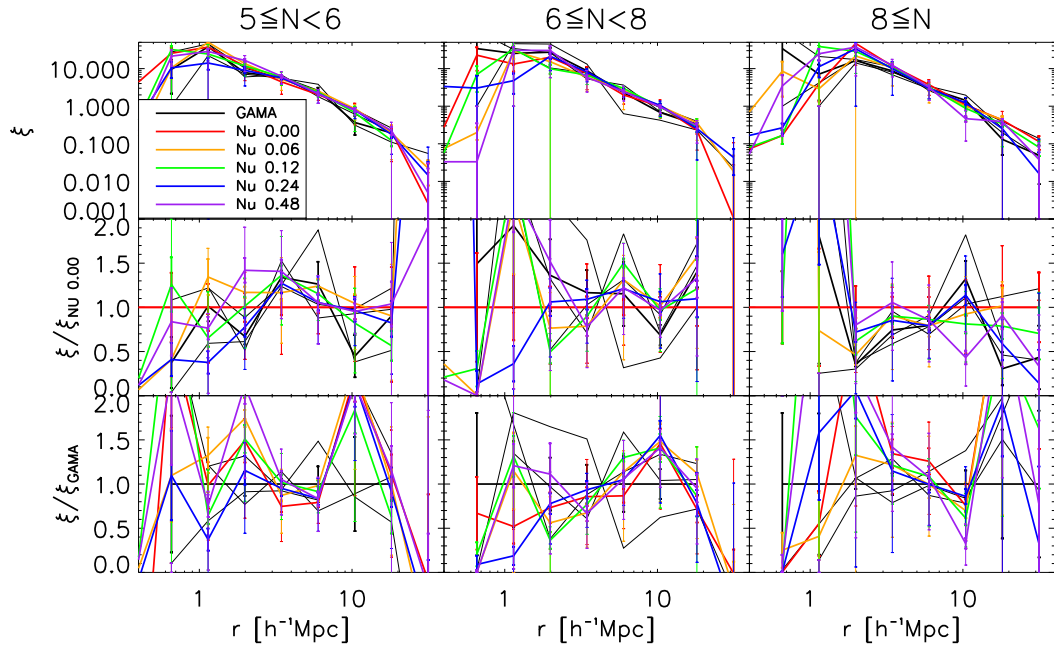


Figure 3.2: *Top*: redshift-space 2-point GGC autocorrelation as a function of the inter-group separation for GAMA (black curve) and BAHAMAS (coloured curves) in equally populated bins of multiplicity. For the BAHAMAS curves, thick error bars display the standard error on the mean and thin error bars show the 60th percentile of the cosmic variance. In the GAMA case, error bars show the standard error on the mean. *Middle*: The ratio of the autocorrelation function in each case to the BAHAMAS massless neutrino (“ $\nu$  0.00”) case. *Bottom*: The ratio of the autocorrelation function in each case to the GAMA case. There is remarkably good agreement between the BAHAMAS and GAMA cases in all three bins. However, there is no evidence for a systematic offset between the BAHAMAS neutrino cases.

ber of non-trivial conditions should be met by the simulations. These include having approximately the correct cosmology (as this sets the abundance of host dark matter haloes), the simulated stellar mass–halo mass relation should be correct for the selected galaxy sample (required so as to select the same types of systems in the simulations and observations, prior to group finding), and the distribution and abundance of satellites should be correct (otherwise the richness and integrated stellar mass would be incorrect). Of these, it is only the second condition (i.e., the match in the stellar mass–halo mass relation of galaxies) that was achieved via calibration. Otherwise, no aspect of the simulations was calibrated to reproduce the optical properties of GGCs or how such systems cluster in space.

While overall the simulations agree well with the GAMA observations, it is evident from the middle plots that any offset between the various neutrino realisations in the BAHAMAS runs is small compared to the errors on the autocorrelation function. In order to make a statistical statement about the fits, I calculate reduced  $\chi^2$  values for each BAHAMAS run as a model for the GAMA data. These values are calculated from the standard error on the means, and are displayed in Table 3.3.

It can be seen from the results displayed in Table 3.3 and Figures 3.1 and 3.2 that, while the BAHAMAS simulations provide a very good fit to the GAMA GGC autocorrelation functions, no strong statistical argument can be made for the data favouring any one neutrino case. I therefore turn my attention to determining the primary issues in detecting the effect of massive neutrinos in the GGC autocorrelation function, and determining what schemes may be most effective for future work.

Several possible mechanisms exist to explain the non-detection of the expected neutrino signal in GAMA-equivalent simulated BAHAMAS observations. I know from the work presented in Chapter 2, specifically the left panel of Figure 2.14, that the neutrinos affect the 3D 2-point halo autocorrelation function in bins of *halo* mass by upwards of 10%. The issue, therefore, must lie in the translation between the 3D clustering of haloes at a fixed redshift and binned on halo mass and the observationally-determined redshift-space clustering of identified GGCs within a redshift range and binned in some tracer of halo mass, i.e. stellar mass or multiplicity.

Table 3.3: The results of  $\chi^2$  tests of the simulated BAHAMAS data against GAMA data, and between the most extreme BAHAMAS runs. The columns are: (1) The variable and range for the specified bin; (2-6) The  $\chi^2/NDF$  value for each simulation run with respect to the GAMA data.

|   | Bin<br>(1)               | $\chi^2$ w.r.t. GAMA |                |                |                |                |
|---|--------------------------|----------------------|----------------|----------------|----------------|----------------|
|   |                          | NU 0.00<br>(2)       | NU 0.06<br>(3) | NU 0.12<br>(4) | NU 0.24<br>(5) | NU 0.48<br>(6) |
| <b>WMAP-9<br/>fixed linking length</b>                    | $10.00 \leq M_* < 10.55$ | 10.5                 | 5.41           | 1.40           | 1.40           | 3.69           |
|   | $10.55 \leq M_* < 10.84$ | 0.962                | 1.02           | 1.65           | 0.820          | 1.15           |
|   | $10.84 \leq M_* < 12.50$ | 5.06                 | 9.72           | 2.19           | 0.980          | 0.947          |
|   | $5 \leq N < 6$           | 1.10                 | 1.23           | 1.05           | 1.35           | 0.899          |
|   | $6 \leq N < 8$           | 0.514                | 0.418          | 0.540          | 0.434          | 0.426          |
|   | $8 \leq N$               | 0.198                | 0.321          | 0.288          | 0.443          | 0.299          |
| <b>WMAP-9<br/>mass-dependent<br/>linking length</b>       | $10.00 \leq M_* < 10.55$ | 1.32                 | 1.95           | 0.728          | 1.94           | 1.15           |
|   | $10.55 \leq M_* < 10.84$ | 0.843                | 0.966          | 1.08           | 0.645          | 0.838          |
|   | $10.84 \leq M_* < 12.50$ | 3.98                 | 2.59           | 1.53           | 1.74           | 3.00           |
|   | $5 \leq N < 6$           | 0.748                | 0.779          | 0.39           | 0.667          | 0.565          |
|   | $6 \leq N < 8$           | 0.480                | 0.585          | 0.372          | 0.488          | 0.409          |
|   | $8 \leq N$               | 0.737                | 0.699          | 0.379          | 0.517          | 0.477          |
| <i>Planck</i><br><b>fixed linking length</b>              | $10.00 \leq M_* < 10.55$ |                      | 0.541          | 0.901          | 0.485          | 1.78           |
|   | $10.55 \leq M_* < 10.84$ |                      | 1.36           | 0.735          | 1.29           | 0.951          |
|   | $10.84 \leq M_* < 12.50$ |                      | 0.695          | 0.558          | 0.715          | 0.609          |
|   | $5 \leq N < 6$           | -                    | 1.15           | 1.47           | 1.24           | 1.01           |
|   | $6 \leq N < 8$           |                      | 1.34           | 1.55           | 2.40           | 1.61           |
|   | $8 \leq N$               |                      | 0.874          | 1.38           | 0.914          | 0.757          |
| <i>Planck</i><br><b>mass-dependent<br/>linking length</b> | $10.00 \leq M_* < 10.55$ |                      | 0.753          | 0.67           | 0.962          | 1.24           |
|   | $10.55 \leq M_* < 10.84$ |                      | 0.953          | 1.87           | 2.44           | 0.775          |
|   | $10.84 \leq M_* < 12.50$ |                      | 1.22           | 1.34           | 1.37           | 1.49           |
|   | $5 \leq N < 6$           | -                    | 1.65           | 1.24           | 3.53           | 1.60           |
|   | $6 \leq N < 8$           |                      | 1.19           | 1.33           | 1.25           | 0.877          |
|   | $8 \leq N$               |                      | 1.24           | 1.31           | 16.7           | 2.09           |

Below, I explore a number of potential causes for decreased sensitivity to neutrino mass, namely:

- Contributions from GGCs over a redshift range with evolving clustering.
- Cosmology dependence of, and scatter in, the relations between GGC observable (e.g., multiplicity) and halo mass.
- The impact of peculiar velocities on group finding.
- The fragmentation of more massive GGCs resulting from the use of a fixed FoF linking length.

### 3.4.2 Where has the Sensitivity to Neutrino Mass gone?

#### Evolution of Clustering Over a Range of Redshifts

The GGCs I have selected from GAMA and BAHAMAS span a range of redshifts,  $0 < z < 0.2$ . Evolution of the clustering even over this relatively modest range of redshifts could potentially ‘smear out’ the cosmological signal I am looking for. In order to test this, I make use of the ‘true’ halo catalogues from the BAHAMAS light cones. As discussed in Section 3.2.1, these catalogues are produced by first running a standard 3D FoF algorithm on the particles in the full simulation box at each snapshot. The ‘true’ FoF groups are then distributed in light cones in precisely the same manner as done for the simulated galaxies (i.e., stacking the FoF catalogues from each snapshot along the line of sight, using the same random rotations/translations as for the galaxy catalogues). The ‘true’ halo catalogue therefore provides access to perfectly constrained values for GGC properties, such as  $M_{*200,crit}$  (the integrated stellar mass within  $r_{200,crit}$ ), as well as the corresponding halo properties, in particular  $M_{200,crit}$ .

In order to deduce the impact of moving from a fixed-redshift halo sample as in Section 2.5 to a sample spanning a range of redshifts, I investigate the halo autocorrelation function in bins of  $M_{200,crit}$  from the light cones. My results can then be compared

with Figure 2.14, in which I also examined the clustering in bins of halo mass but at a fixed epoch (i.e., not from light cones). Aside from the selection of sources, the technique employed to compute the halo clustering is identical to that utilised to compute the GGC clustering in Section 3.4.1.

In Figure 3.3 I show the redshift-space 2-point GGC autocorrelation function for the full BAHAMAS light cones in bins of  $M_{200,crit}$  for the WMAP-9 cosmology. The lower panels display the fractional differences between the different neutrino mass implementations. As can be seen in these plots, higher values of the summed neutrino mass systemically prefer a higher amplitude for the autocorrelation function. This effect is strongest in my highest mass bin ( $12.77 \leq \log\left(\frac{M_{200}}{M_{\odot}}\right) < 15.5$ ), where I observe a  $\sim 15\%$  offset between the most extreme case ( $\sum M_{\nu} = 0.48$  eV) and the massless case. This is consistent with my expectations from Mummery et al. (2017). Note that the reported errors are somewhat larger here compared with Mummery et al. (2017), as they used the full BAHAMAS simulation volumes rather than light cones, which necessarily sample only a fraction of the total simulation volume.

In order to quantify the contribution of each effect I investigate in this section, I perform statistical tests to determine whether different neutrino runs may be distinguished. Specifically, I attempt to rule out the null hypothesis of there being no difference between the neutrino runs. To do so, I treat the NU 0.48 data, the most extreme neutrino case, as the prediction of a model describing NU 0.00, the case with massless neutrinos, and calculate the reduced  $\chi^2$  value. I do this jointly across all three bins in each case, as well as computing individual values for each bin. The results of these tests for each effect investigated are presented in Table 3.4. The high values of  $\chi^2/NDF$  in the top row demonstrate that the effects of neutrinos can be statistically differentiated in the BAHAMAS lightcones when using ‘true’ halo properties. I can therefore exclude the evolution of clustering as the dominant contributor to the non-detection of the effects of massive neutrinos in Figures 3.1 and 3.2.

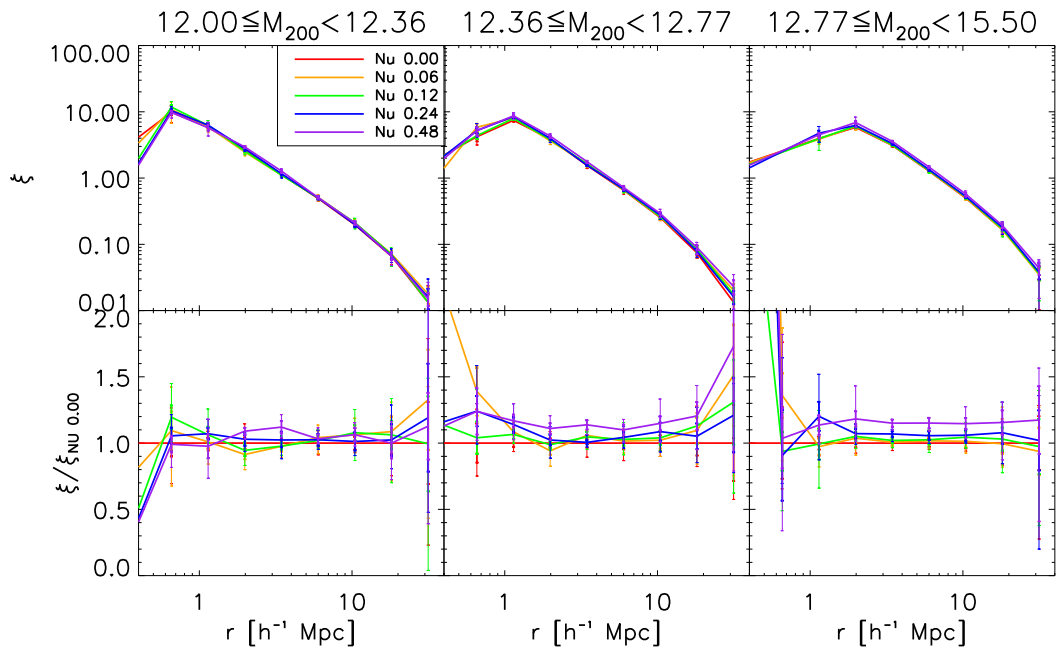


Figure 3.3: *Top:* redshift-space 2-point autocorrelation functions for BAHAMAS GGCs in equally populated bins of halo mass  $M_{200,crit}$ . As above, thick error bars display the standard error on the mean while thin error bars show the 60th percentile of the cosmic variance. *Bottom:* The autocorrelation function in each case normalised to the massless neutrino case. BAHAMAS runs with higher values for the summed neutrino mass show a higher amplitude for the GGC clustering than those with lower values. This effect is greatest in bins with higher halo mass.

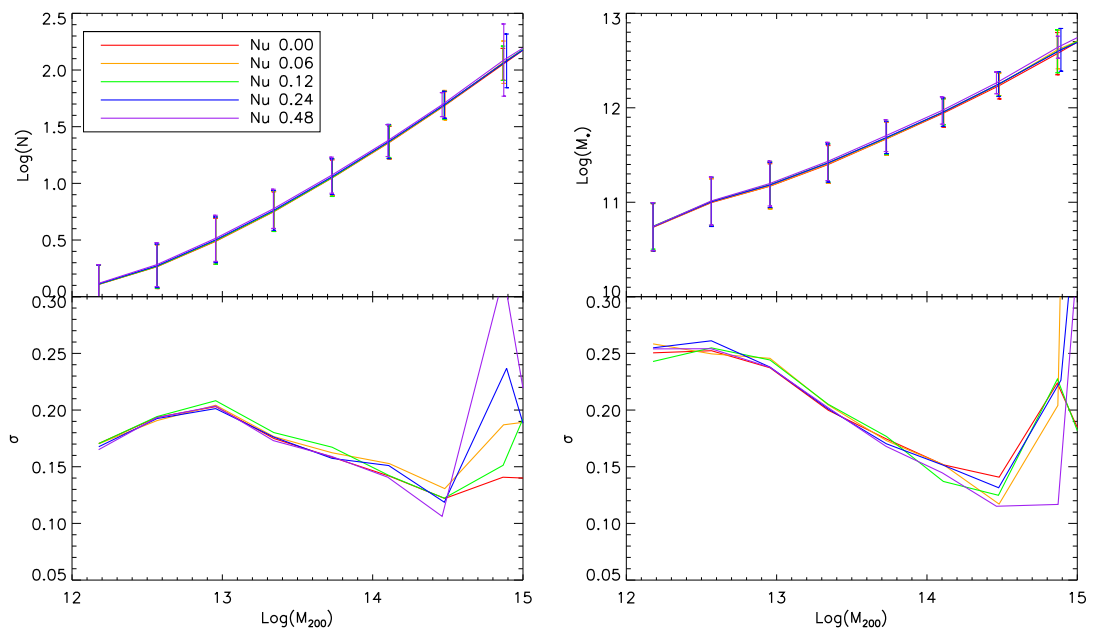


Figure 3.4: Multiplicity - halo mass and stellar mass - halo mass relations for the various BAHAMAS runs in the context of the WMAP-9 cosmology. *Top Left:* Multiplicity - halo mass relations. *Bottom Left:* RMS of the  $\log_{10}$  scatter in the Multiplicity - halo mass relations in bins of halo mass. *Top Right:* Stellar mass - halo mass relations. *Bottom Right:* RMS of the  $\log_{10}$  scatter in the Stellar mass - halo mass relations in bins of halo mass. Note that while the lower panels share a y scale, the upper panels do not.

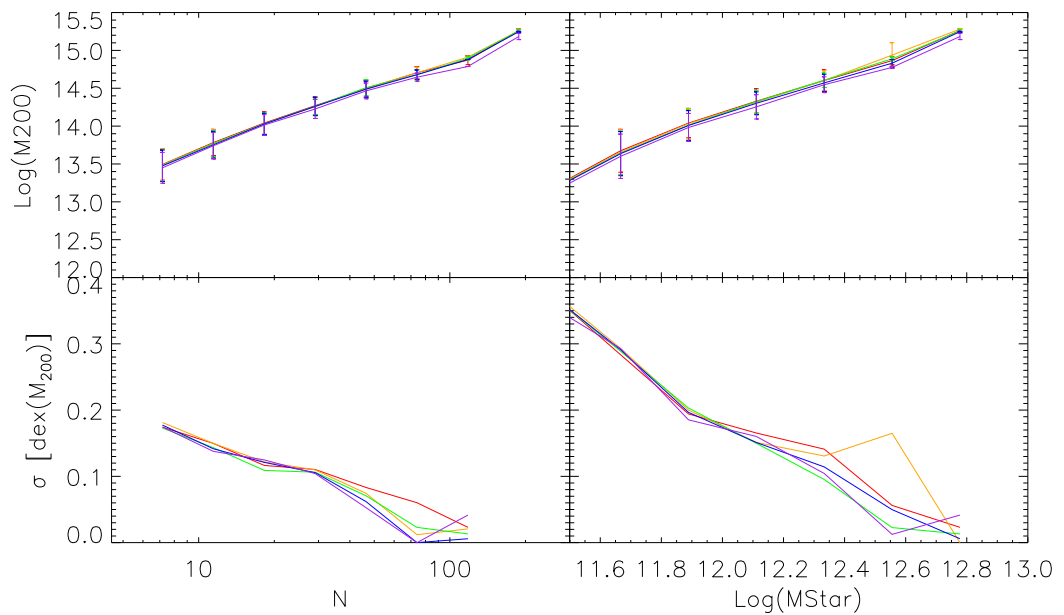


Figure 3.5: Multiplicity - halo mass and stellar mass - halo mass relations for the various BAHAMAS runs in the context of the WMAP-9 cosmology. In contrast to Figure 3.4, the relations are binned on the observable rather than the halo mass. *Top Left*: Multiplicity - halo mass relations. *Bottom Left*: RMS of the  $\log_{10}$  scatter in the Multiplicity - halo mass relations in bins of multiplicity. *Top Right*: Stellar mass - halo mass relations. *Bottom Right*: RMS of the  $\log_{10}$  scatter in the Stellar mass - halo mass relations in bins of multiplicity.

### GGC Observable–Halo Mass Relations: Cosmology Dependence and Scatter

I now turn my attention to potential issues associated with the GGC observable–halo mass relations. The first potential issue is that these relations could differ between the simulations (i.e., they depend on neutrino mass). This would imply that, when computing the clustering of GGCs in bins of some observable (e.g., multiplicity), the halo mass distribution within a given observable bin could vary with the simulation. As a consequence, I would therefore be comparing the clustering of objects of different halo masses when comparing different simulations. A second issue is the potential impact of intrinsic scatter in the GGC observable–halo relations. Intrinsic scatter will affect the measured clustering, as its presence implies that bins of fixed observable can contain a potentially wide range of halo masses (depending on the amount of scatter and the bin widths). This, in turn, will tend to smear out the effects of massive neutrinos, as their impact on the clustering of haloes is an increasing function of halo mass (see, e.g., Figure 2.14). Here I examine the nature of the observable–halo mass relations in BAHAMAS simulations.

In the upper panels of Figure 3.4 I display multiplicity–halo mass (left) and stellar mass–halo mass (right) relations for each of the BAHAMAS runs used. This I calculate as the mean multiplicity (stellar mass) value in logarithmic bins of halo mass for the full GGC catalogue generated in Section 3.3.2, with error bars corresponding to the  $\log_{10}$  RMS (i.e., scatter) about the mean. The absolute RMS of the scatter is displayed in the lower panels. While this shows the intrinsic scatter in the observable quantities in bins of the halo mass, I also include the scatter in halo mass in bins of the observable quantities in Figure 3.5.

In both cases I find that the observable is, as expected, an almost linear tracer of the underlying halo mass. I also note that there is almost no variation in the amplitude, form or intrinsic scatter of the relation between neutrino models. Naively, this is somewhat surprising, as I know from Chapter 2 that the inclusion of massive neutrinos leads to a not insignificant alteration (a reduction) to the halo mass. The lack of a visible difference here between the different simulations indicates that the values of  $N$  and  $M_*$

are sensitive to this change and adjust accordingly. This makes intuitive sense, as the alteration to the growth of structure arising from the inclusion of massive neutrinos is present from their inception, and therefore the causal relationships between the halo mass and these parameters will still hold. In other words, the haloes do not know that they are ‘supposed’ to be more massive (i.e., they evolve *along* these relations as the neutrino mass is dialled).

The low scatter in high mass (both stellar and halo) and multiplicity bins found here is in agreement with that measured by Farahi et al. (2018). This is a logical consequence of growth of structure - as hierarchical clustering causes the potential wells of haloes to grow ever larger, both in physical size and in depth, the region within which the baryonic processes have a significant effect becomes more restricted to the centre of the halo. Beyond this, gravitational forces dominate and the self-similar scalings predicted for collisionless haloes reappear.

Significantly for this work, the consistency of the mean stellar mass– and multiplicity–halo mass relations indicates that the scaling relations are virtually independent of cosmology, implying that (at least in the absence of scatter) the clustering observable bins should have approximately the same cosmology dependence as clustering in halo mass bins.

Moving on to the impact of intrinsic scatter, I investigate this by examining the (‘true’) halo autocorrelation functions in bins of ‘true’ stellar mass and multiplicity. By focusing on the clustering of bins of (‘true’) observable for the ‘true’ halo catalogue, I am able to isolate the impact of binning on an observable (and therefore the effect of scatter in the observable–halo mass relation) as opposed to halo mass. The results for the clustering in bins of ‘true’ integrated stellar mass are displayed in the upper panels of Figure 3.6. As in Figure 3.3, the lower panels display the ratio of each case to the massless neutrino run. The results of  $\chi^2$  tests comparing NU 0.00 and NU 0.48 are given in Table 3.4.

A comparison between Figures 3.6 and 3.3 shows that the scatter in the stellar mass–halo mass relation causes a notable increase in the noise of this measurement. Fur-

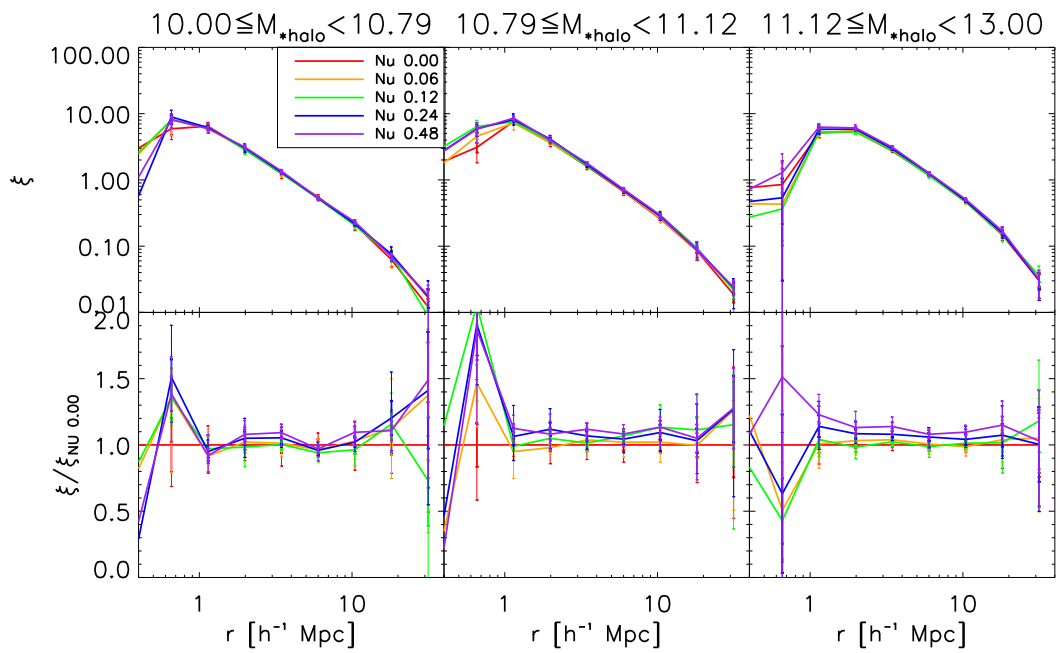


Figure 3.6: *Top:* redshift-space 2-point autocorrelation functions for BAHAMAS haloes in equally populated bins of  $M_{*halo}$ , the 'true' stellar mass contained within  $M_{200,crit}$ . Halo samples were identified by means of an on-the-fly FoF algorithm run on the BAHAMAS simulation particles. As above, thick error bars display the standard error on the mean while thin error bars show the 60th percentile of the cosmic variance. *Bottom:* The autocorrelation function in each case normalised to the massless neutrino case. BAHAMAS runs with higher values for the summed neutrino mass show a higher amplitude for the GGC clustering than those with lower values. This effect is greatest in bins with higher stellar mass.

thermore, in the highest mass bin ( $11.12 \leq \log \left( \frac{M_{*halo}}{M_{\odot}} \right) < 13.00$ ) one can see that the offset between the various BAHAMAS runs is no longer clearly monotonic as it was for objects binned on their halo mass. While some small difference is still discernible for the highest neutrino mass case, it is clearly much less dramatic than for the case where the correlation functions were computed in bins of halo mass. Note that as in Figure 3.3, the mass bins in Figure 3.6 have been chosen such that the numbers of objects per bin in the GAMA dataset are approximately equal. This is confirmed by the sharp decrease in  $\chi^2$  when changing from binning on the true halo mass to observable mass tracers.

This result indicates that while highest mass objects are the most affected by neutrino free-streaming, their scarcity and the strong dependence of this effect on mass binning means that even the remarkably small scatter in the observable–halo mass relationships for these objects is sufficient to significantly reduce the measured amplitude of this effect.

### **The Impact of Peculiar Velocities**

The peculiar motions of galaxies can potentially affect the clustering results in two ways. First, galaxies that are near GGCs, but not actually physically associated with them, can be assigned to the group in redshift space by the FoF algorithm, purely as a result of the observable redshift not reflecting the ‘true’ Hubble redshift (i.e., the distance). This, in turn, will affect the GGC observable–halo mass relations, adding both bias and scatter to them. Second, in terms of the GGCs themselves, their peculiar velocities will affect the derived 3D distances between GGCs, particularly at small separations. I examine the impact of the latter below. In terms of the former, the addition of scatter to the GGC observable–halo mass relations will impact the clustering results as described in Section 3.4.2. This scatter, however, is in addition to the intrinsic scatter in the ‘true’ scaling relations explored there, implying that my conclusions about the significant impact of scatter in the observable–mass relations on the clustering are conservative.

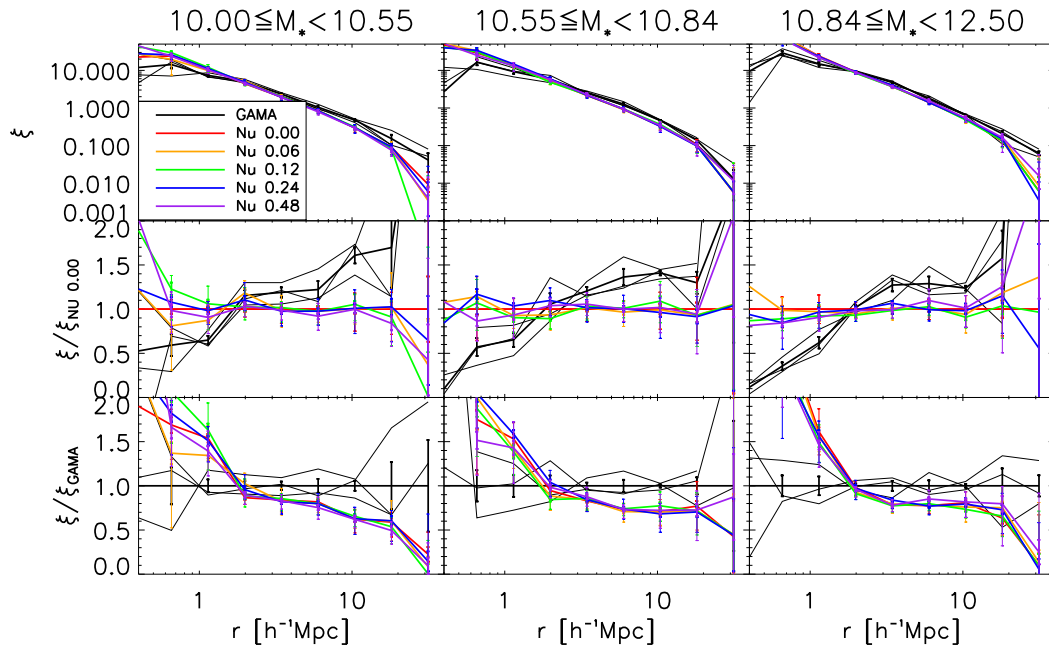


Figure 3.7: *Top:* Redshift-space 2-point GGC autocorrelation as a function of the inter-group separation for GAMA (black curve) and BAHAMAS (coloured curves) in equally populated bins of integrated stellar mass. In contrast to Figure 3.1, the redshift values used in the construction of these results for the simulated data do not include the contribution of the peculiar motions of galaxies and GGCs, i.e. only the Hubble redshift is considered. For the BAHAMAS curves, thick error bars display the standard error on the mean and thin error bars show the 60th percentile of the cosmic variance. In the GAMA case, error bars show the standard error on the mean. *Middle:* The ratio of the autocorrelation function in each case to the BAHAMAS massless neutrino (“ $\nu$  0.00”) case. *Bottom:* The ratio of the autocorrelation function in each case to the GAMA case. Since the peculiar motions cannot be excluded in the GAMA data, the agreement between GAMA and BAHAMAS is somewhat worsened in comparison to Figure 3.1. The exclusion of peculiar motions does not improve the sensitivity of this diagnostic to the neutrino mass.

In order to assess the impact that peculiar velocities have on the 3D clustering, I repeat my calculation of the 3D comoving autocorrelation function of BAHAMAS GGCs (see Figures 3.1 and 3.2) but have altered the redshift calculation to exclude the contribution from peculiar motions (i.e. the Hubble redshift only). I present the results of this analysis in Figure 3.7

I find that peculiar motions are responsible for a small increase in noise at lower values of the comoving 3D radius and for lower values of GGC stellar mass or multiplicity. These trends make intuitive sense. First, as the peculiar motions of the galaxies are expected to be approximately randomly distributed, in more populated GGCs the mean observable redshift will tend toward the Hubble redshift. Furthermore, the impact of residual peculiar motions on the inferred separation between GGCs will be a decreasing function of group separation. This is simply because the peculiar redshift becomes small in comparison to redshift difference between GGCs at large physical separations.

Additionally, removing peculiar motions from the analysis results in a small apparent decrease in the clustering amplitude at all radii. As noted above, their peculiar motions change which galaxies are assigned to FoF groups. Consequently, the fixed stellar mass and multiplicity ranges select slightly different GGC populations which cluster at slightly different characteristic distances, resulting in an apparent shift in the amplitude.

Thus, I find that peculiar GGC motions do not significantly impact upon the cosmological sensitivity of their clustering, particularly since it is the more populated GGCs which are the most sensitive to cosmology and the least affected by peculiar motions.

It is worth pointing out that in my main analysis I have focused on the 3D correlation functions, as opposed to the projected (2D) correlation functions. Projected correlation functions are insensitive to peculiar motions, so long as they are integrated over a sufficiently large line of sight distance. That there is no statistically significant difference between the BAHAMAS neutrino realisations in the projected clustering precludes peculiar motions as an important mechanism by which the underlying dependence on the neutrino mass is obscured. However, as noted above, the peculiar motions do add scat-

ter to the GGC observable–mass relations, which can affect the clustering (as described in Section 3.4.2).

### **Varying the Galaxy Linking Strategy**

As described in Section 3.3.2, I have until this point assigned galaxies to groups by means of a FoF algorithm with a fixed linking length based on the mean separation of galaxies within the survey volume. Due to the slope of the NFW, less massive galaxies are the most numerous and therefore dominate the calculation of the mean separation. As more massive GGCs tend to consist of characteristically more massive galaxies, and these galaxies cluster at greater characteristic distances than their less massive counterparts, this leads to the most massive FoF groups being fragmented into smaller groups (see Jakobs et al. 2017). As can be seen in Figures 3.3 and 3.6, it is the most massive GGCs that have the greatest sensitivity to the neutrino mass. The fragmentation problem may therefore be a potential contributor to the non-detection of the neutrino signal in my predictions for GAMA clustering.

In order to examine the impact of linking strategy, I re-analyse each dataset using a galaxy stellar mass-dependent linking length. As discussed in Section 3.3.2, this modifies the FoF algorithm such that the mean separation is calculated not based on the number density of all galaxies in the sample, but rather on that of all galaxies of greater or equal stellar mass to the galaxy for whose friends I am searching. This results in longer linking lengths for more massive galaxies and effectively prevents the fragmentation of FoF groups.

This impact of varying the linking strategy can be seen by comparing Figures 3.8 and 3.9, which display the stellar mass and multiplicity functions of FoF identified GGCs in GAMA and BAHAMAS in the case of fixed and mass-dependent linking lengths, respectively. In each case, the upper panels display the multiplicity function (left) and stellar mass function (right) of the three GAMA fields and various BAHAMAS runs, while the lower panels show the ratio of these data to the GAMA result.

Note that the apparent turnover in the GGC stellar mass function is not physical, but

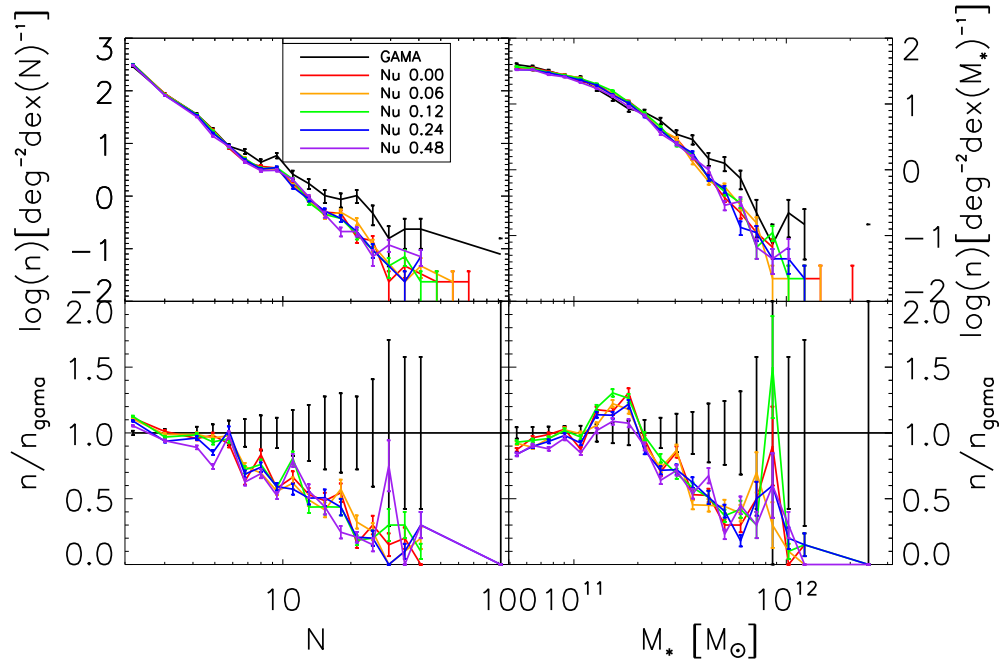


Figure 3.8: The multiplicity and stellar mass functions of GAMA and BAHAMAS GGC samples identified using a FoF algorithm with a fixed value for the linking length. *Top Left*: the multiplicity functions of the GAMA fields and BAHAMAS runs. The black curve shows the stacked function for the G09, G12 and G15 GAMA fields. Coloured lines show the functions for the various BAHAMAS neutrino mass cases, stacked over all cones and cuts. Error bars are the poisson error on the count in each integrated stellar mass bin. *Bottom Left*: the ratio of the multiplicity function in each BAHAMAS case to the GAMA result. *Top Right*: the integrated stellar mass functions of the GAMA fields and BAHAMAS runs. The black curve shows the stacked function for the G09, G12 and G15 GAMA fields. Coloured lines show the functions for the various BAHAMAS neutrino mass cases, stacked over all cones and cuts. Error bars are the poisson error on the count in each integrated stellar mass bin. *Bottom Right*: the ratio of the stellar mass function in each BAHAMAS case to the GAMA result. BAHAMAS is reasonably successful at reproducing the GAMA integrated stellar mass function at low masses ( $M_* < 10^{11.7}$ ), but shows more significant deviation at higher masses. There is a clear difference in gradient between the BAHAMAS and GAMA multiplicity functions.

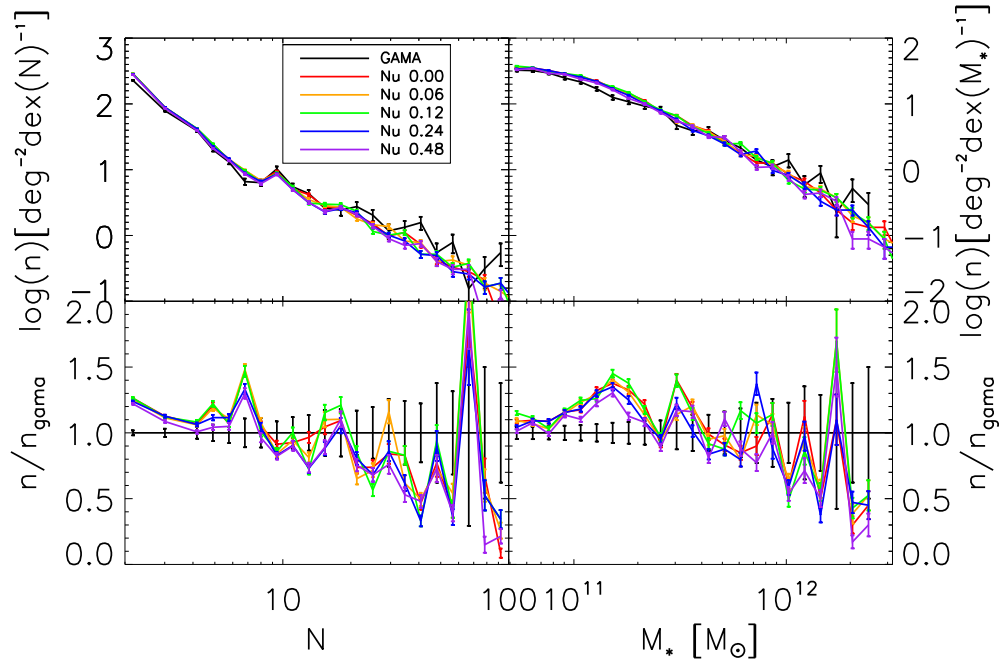


Figure 3.9: The multiplicity and stellar mass functions of GAMA and BAHAMAS GGC samples. In contrast to figure 3.8, GGC samples in this case are identified by means of a FoF algorithm with a *mass dependent* value for the linking length. *Top Left*: the multiplicity functions of the GAMA fields and BAHAMAS runs. The black curve shows the stacked function for the G09, G12 and G15 GAMA fields. Coloured lines show the functions for the various BAHAMAS neutrino mass cases, stacked over all cones and cuts. Error bars are the poisson error on the count in each integrated stellar mass bin. *Bottom Left*: the ratio of the multiplicity function in each BAHAMAS case to the GAMA result. *Top Right*: the integrated stellar mass functions of the GAMA fields and BAHAMAS runs. The black curve shows the stacked function for the G09, G12 and G15 GAMA fields. Coloured lines show the functions for the various BAHAMAS neutrino mass cases, stacked over all cones and cuts. Error bars are the poisson error on the count in each integrated stellar mass bin. *Bottom Right*: the ratio of the stellar mass function in each BAHAMAS case to the GAMA result. The use of a mass dependent linking length increases the relative abundance of high stellar mass / multiplicity groups compared to a fixed linking length for both BAHAMAS and GAMA. It also results in notable better agreement in this region, albeit with slightly worse agreement at lower masses / multiplicities.

rather arises due to the missing stellar mass of galaxies that fall below my galaxy mass cut. As lower mass GGCs consist preferentially of comparatively lower-mass galaxies, a greater proportion of the stellar mass of these objects is contained within galaxies that I am not counting towards their total stellar mass.

Figures 3.10 and 3.12 are updates of Figures 3.1 and 3.2 using the mass-dependent linking length GGC sample. The results of  $\chi^2$  tests on the calculated autocorrelation functions are given in Tables 3.3 and 3.4. As can be seen from these, the updated GGC sample offers minimal improvement over the fixed linking length case. My results remain consistent with the null hypothesis of there being no difference between the clustering of GGCs as a function of the summed neutrino mass.

For completeness, in Figure 3.11 I display the results of repeating this analysis while excluding peculiar motions as described above. Unsurprisingly, removing peculiar velocities in this context has an almost identical effect as doing so in the context of GGCs identified using a fixed linking length.

### Summary

Of the four potential causes I have explored for the reduction in the sensitivity of the GGC autocorrelation to cosmology (specifically neutrino mass), the largest effect I have identified is that of scatter in the GGC observable–halo mass relations. Even just the intrinsic scatter in the true 3D ‘observables’ is sufficient to remove most of the sensitivity, without including other relevant sources of observational scatter (e.g., incomplete or inaccurate FoF group membership assignment). Scatter affects the measured clustering, as it implies that bins of fixed observable can contain a potentially wide range of halo masses. This smears out the effects of massive neutrinos, as their impact on the clustering of haloes is an increasing function of halo mass.

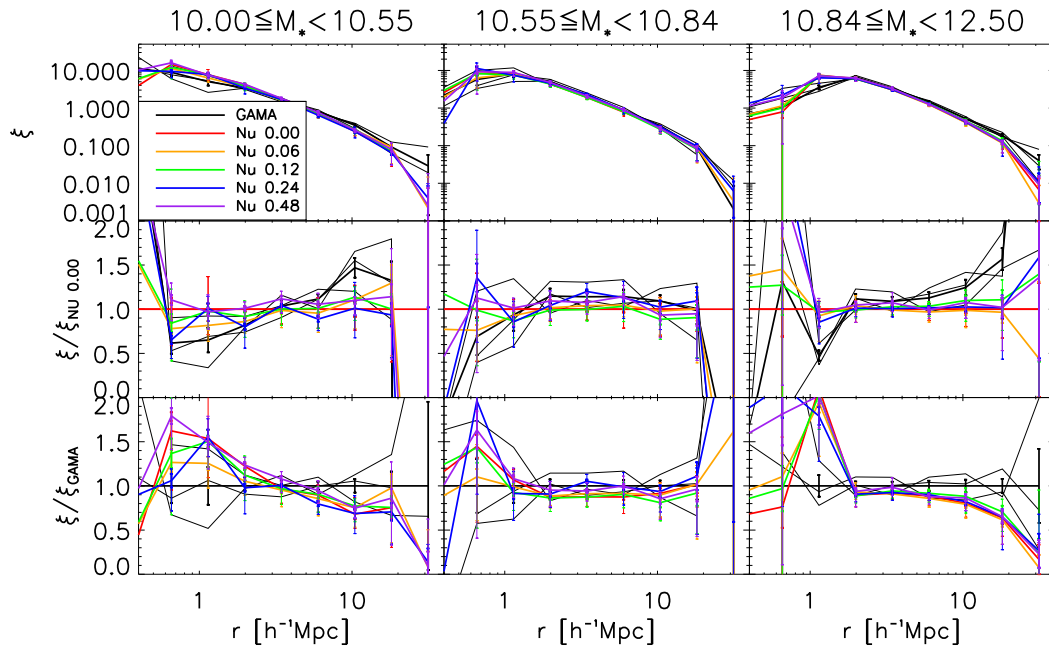


Figure 3.10: *Top:* The redshift-space 2-point GGC autocorrelation as a function of the inter-group separation for GAMA (black curve) and BAHAMAS (coloured curves) in equally populated bins of integrated stellar mass for a WMAP-9 cosmology. In contrast to figure 3.1, groups have been identified by means of a FoF algorithm with a *mass dependent* linking length as described in section 3.3.2. For the BAHAMAS curves, thick error bars display the standard error on the mean and thin error bars show the 60th percentile of the cosmic variance. In the GAMA case, error bars show the standard error on the mean. *Middle:* The ratio of the autocorrelation function in each case to the BAHAMAS massless neutrino (“nu 0.00”) case. *Bottom:* The ratio of the autocorrelation function in each case to the GAMA case. There is remarkably good agreement between the BAHAMAS and GAMA cases in all three bins. However, there is no evidence for a systematic offset between the BAHAMAS neutrino cases.

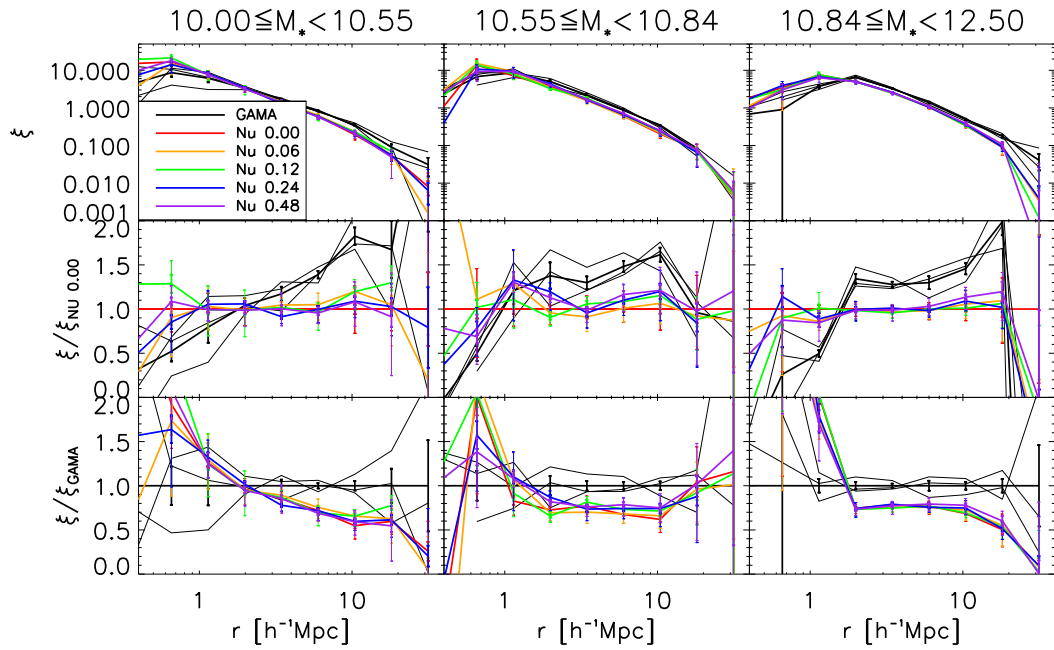


Figure 3.11: *Top:* The redshift-space 2-point GGC autocorrelation as a function of the inter-group separation for GAMA (black curve) and BAHAMAS (coloured curves) in equally populated bins of integrated stellar mass for groups identified using a FoF algorithm with a mass-dependent linking length and excluding the effects of peculiar motions for a WMAP-9 cosmology. As in Figure 3.10, groups have been identified by means of a FoF algorithm with a *mass dependent* linking length as described in section 3.3.2. In contrast to that Figure, only the Hubble redshift has been considered. For the BAHAMAS curves, thick error bars display the standard error on the mean and thin error bars show the 60th percentile of the cosmic variance. In the GAMA case, error bars show the standard error on the mean. *Middle:* The ratio of the autocorrelation function in each case to the BAHAMAS massless neutrino (“nu 0.00”) case. *Bottom:* The ratio of the autocorrelation function in each case to the GAMA case. As in Figure 3.7, the exclusion of peculiar motions results in a small However, there is no evidence for a systematic offset between the BAHAMAS neutrino cases.

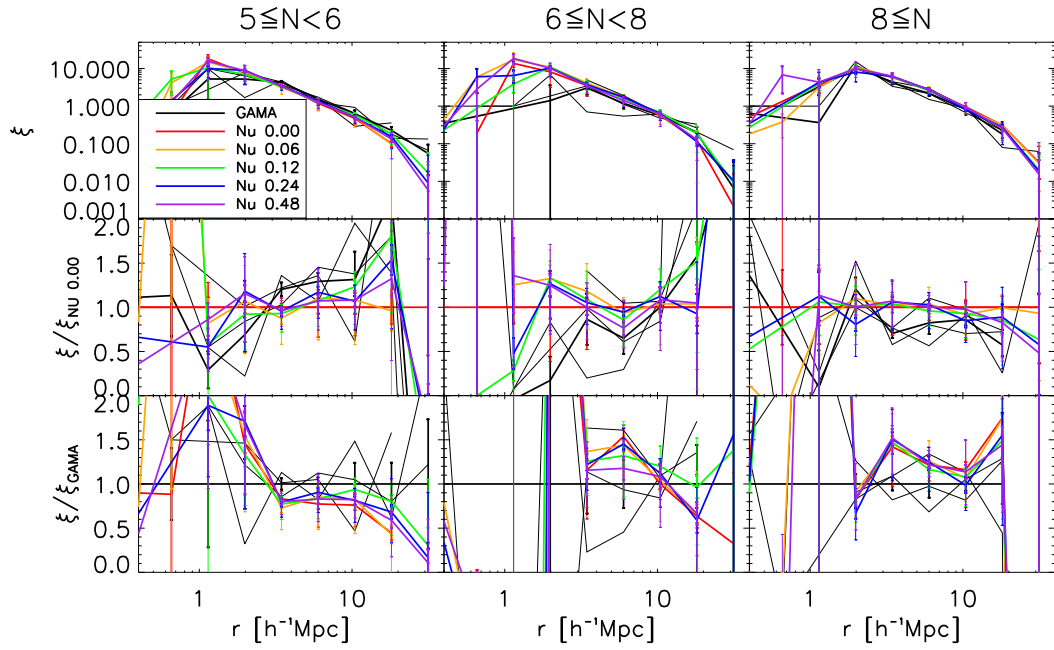


Figure 3.12: *Top*: redshift-space 2-point GGC autocorrelation as a function of the inter-group separation for GAMA (black curve) and BAHAMAS (coloured curves) in equally populated bins of multiplicity. In contrast to Figure. 3.2, groups were identified by means of a FoF algorithm with a *mass-dependent* linking length. For the BAHAMAS curves, thick error bars display the standard error on the mean and thin error bars show the 60th percentile of the cosmic variance. In the GAMA case, error bars show the standard error on the mean. *Middle*: The ratio of the autocorrelation function in each case to the BAHAMAS massless neutrino (“nu 0.00”) case. *Bottom*: The ratio of the autocorrelation function in each case to the GAMA case. There is remarkably good agreement between the BAHAMAS and GAMA cases in all three bins. However, there is no evidence for a systematic offset between the BAHAMAS neutrino cases.

Table 3.4: The results of  $\chi^2$  tests determining how well the various neutrino runs can be distinguished in the different data sets and binning strategies constructed in this section. For each of the data the reduced  $\chi^2$  value is calculated as the goodness of fit between the NU 0.00 and NU 0.48 BAHAMAS runs. This is done individually in each bin, as well as jointly across all three bins considered. The columns are: (1) The dataset in question. Sets denoted  $X^{halo}$  refer to the ‘true’ halo properties determined from the BAHAMAS FoF groupfinder run on the full particle distribution. Sets denoted  $X - z_{pec}$  do not include peculiar velocities in the calculation of the line-of-site distance, i.e. the 3-dimensional distribution within the cone is recovered perfectly. (2) The FoF linking strategy used to identify GGCs. (3) The reduced  $\chi^2$  between NU 0.00 and NU 0.48 in each individual bin (see Table 3.3 for the bin edges) . (4) The reduced  $\chi^2$  between NU 0.00 and NU 0.48 calculated jointly across all three bins.

| (1)<br><b>Data</b> | (2)<br>FoF linking strategy      | (3)<br>Bins |       |       | (4)<br><b>Total</b> |
|--------------------|----------------------------------|-------------|-------|-------|---------------------|
| $M_{200}^{halo}$   | BAHAMAS particle<br>groupfinder  | 1.19        | 3.42  | 4.92  | 3.17                |
| $M_*^{halo}$       |                                  | 1.33        | 1.95  | 2.14  | 1.71                |
| $N^{halo}$         |                                  | 0.957       | 0.428 | 3.11  | 1.45                |
| $M_* - z_{pec}$    | fixed linking<br>length          | 1.76        | 0.862 | 2.82  | 1.21                |
| $N - z_{pec}$      |                                  | 1.21        | 1.19  | 2.02  | 1.48                |
| $M_*$              |                                  | 0.519       | 0.974 | 1.85  | 1.14                |
| $N$                |                                  | 1.27        | 1.97  | 2.49  | 1.21                |
| $M_* - z_{pec}$    | mass-dependent<br>linking length | 0.981       | 1.06  | 2.73  | 1.86                |
| $N - z_{pec}$      |                                  | 1.88        | 1.56  | 2.30  | 1.63                |
| $M_*$              |                                  | 1.41        | 1.22  | 1.90  | 1.83                |
| $N$                |                                  | 1.30        | 1.31  | 0.463 | 0.969               |

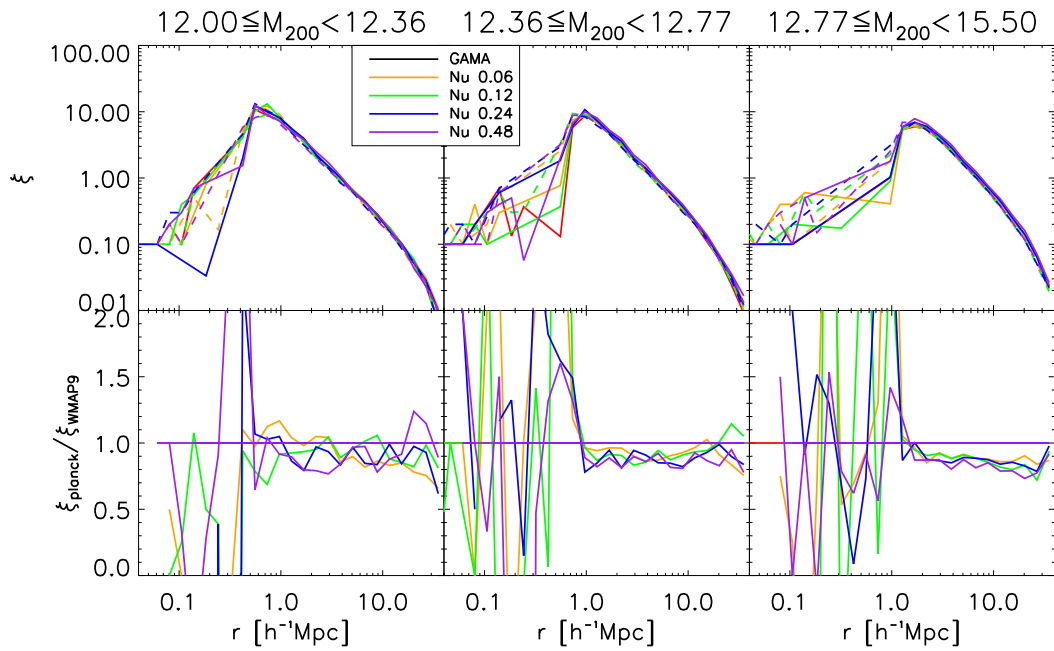


Figure 3.13: Direct comparison between the clustering of haloes in *Planck* and WMAP-9 cosmologies. *Top*: The redshift-space 2-point GGC autocorrelation as a function of the inter-group separation for objects identified from the full BAHAMAS catalogue in the context of WMAP-9 (solid curves) and *Planck* (dashed curves) in bins of the ‘true’ halo mass  $M_{200}$ . Bin limits are quoted in units of  $M_{200}/M_{\odot}$ . *Bottom*: The ratio of each of the *Planck* functions to the corresponding WMAP-9 function. In all cases, the amplitude of clustering in the *Planck* case is lower than that of the equivalent WMAP-9 case by  $\sim 20\%$ .

### 3.4.3 *Planck* Results

All of the results discussed above have been arrived at in the context of a WMAP-9 cosmology, this being the primary cosmology adopted by the BAHAMAS simulations. In parallel to this investigation, however, I have replicated each of the tests performed utilising data drawn from BAHAMAS runs based on the *Planck* cosmology, as detailed in Section 3.2. Since deriving redshift-space distances requires that a cosmology be assumed, I have re-analysed the GAMA data in the context of the *Planck* cosmology in order to facilitate direct comparisons in the same manner as the WMAP-9 comparisons presented in Section 3.4.1.

The results of this investigation are not substantively different to those arising in the context of the WMAP-9 cosmology. In both cases, the sensitivity of the GGC clustering to the choice of value for the summed neutrino mass is insufficiently large to be distinguished. This loss of sensitivity results primarily from intrinsic scatter in the observable–halo relationships. The GGC clustering prediction from *Planck* BAHAMAS runs exhibits remarkably good agreement with that observed from GAMA data analysed in the context of the *Planck* cosmology.

The *Planck* versions of WMAP-9-specific figures displayed throughout this chapter are included in Appendix C.

Additionally, in Figure 3.13 I present the results of a direct comparison between the BAHAMAS WMAP-9 and *Planck* predictions for the GGC clustering. The lower panels display the ratio of each *Planck* prediction to that of the WMAP-9 run with the matching choice of neutrino mass.

Since the value of  $\sigma_8$  is higher in *Planck* than in WMAP-9, one might naively expect that the *Planck* clustering result should have a higher amplitude than that of the WMAP-9 result. While this is indeed the case for a fixed set of haloes, at fixed *mass range*, the situation is somewhat more complex. The lower  $\sigma_8$  in WMAP-9 means that a given initial overdensity evolves into a less massive halo in WMAP-9 than in *Planck*. Thus a fixed halo mass range selects an intrinsically different population of haloes –

the haloes found in *Planck* would more accurately correspond to a higher mass range in WMAP-9 haloes.

Because more rarefied objects cluster at larger characteristic distances, they exhibit higher clustering amplitudes at fixed  $r$ . Consequently, at fixed halo mass range the difference in selected halo population results in apparently lower clustering amplitudes for *Planck* than for WMAP-9. This is the same effect that results in the dependence on halo clustering amplitude found in Chapter 2 (specifically Figure 2.14).

### 3.5 Conclusions and Discussion

I have made a careful and consistent comparison of the GGC 3D redshift-space auto-correlation functions derived from the GAMA survey and from the BAHAMAS suite of cosmological simulations (McCarthy et al., 2018). In particular, I use identical methods for selecting galaxies, assigning them to FoF groups, and computing the two-point correlation functions of the simulated and observed GGCs.

I find that the simulated clustering agrees remarkably well with the observations (see Section 3.4.1).

In Chapter 2, I demonstrated that the amplitude of the dark matter halo autocorrelation function in BAHAMAS is dependent on the value of the summed neutrino mass (due mainly to its effect on  $\sigma_8$ ). Note that this statement is not just true for the most massive clusters, but also for group- and galaxy-mass dark matter haloes. The naive expectation was, therefore, that a sample of robustly-identified GGCs (i.e., from a spectroscopic survey, such as GAMA) could be used to place constraints on cosmology when compared to the predictions of simulations.

Although the BAHAMAS simulations reproduce the observed clustering of GAMA GGCs remarkably well, the anticipated sensitivity to cosmology was not realized when the simulations were analysed in a consistent observational manner. I examined four possible mechanisms that could be responsible for the reduced sensitivity to cosmology

(see Section 3.4.2), namely:

- i)* evolution of clustering over a range of redshifts;
- ii)* cosmology dependence of and intrinsic scatter in the GGC observable–halo mass relations;
- iii)* peculiar motions of galaxies and GGCs; and
- iv)* galaxy linking strategy.

While all of these impact the results at some level, the most dominant effect is intrinsic scatter in the GGC observable–halo mass relations.

The fact that the simulated clustering agrees so well with observations in the context of *both* the WMAP-9 and *Planck* cosmologies should not be particularly surprising. It is clear from the results of this investigation that the 2-point autocorrelation function of GGCs alone is insufficient to place constraints on the background cosmology.

My findings demonstrate the importance of producing synthetic observations and performing like-with-like comparisons between theory and observations. Although it proved impractical to constrain the neutrino mass based on the GGC clustering in observable bins in a GAMA - scale survey, this remains an intriguing line of evidence. As stated previously, the dominant effect preventing such constraints being placed in this case is the intrinsic scatter in the GGC observable–halo mass relations. This suggests that significant improvements could be made by employing methods that reduce the extent of this scatter.

However, even with the intrinsic scatter removed the various neutrino cases are only just distinguishable in the higher mass bins, and remain consistent with each other in the lowest (see Figure 3.3). Given that the BAHAMAS group catalogue is larger than that of GAMA by a factor of  $\sim 10$ , the size of the observational catalogues would need to be increased by this factor in order to achieve comparable results even if the scatter were completely removed (i.e.  $\approx 5^5$  or roughly 1,800 square degrees, the equivalent of 30 of the 12 by 5 degree fields used here). An additional issue is that of cosmic variance. While the variation between BAHAMAS fields is a useful indication of the variance, it must be borne in mind that the BAHAMAS fields are stacks of projections of

the same  $400 h^{-1}\text{Mpc}$  simulation volume, and are not truly independent. The extent of the cosmic variance error bars used here are therefore conservative estimates of the true value. The expected variance between observational fields would therefore be expected to be somewhat larger than this, necessitating an even greater increase in effective area in order to achieve the same statistical power. Finally, extending the survey area to greater line-of-sight distance as a way to increase the probed volume would also bring with it an additional (although small, at least at first) reduction in the overall signal. This is because fixed mass bins extending to higher redshift begin to include objects whose present-day properties would place them in higher mass bins. This effectively blurs the mass boundary. Given that the neutrino mass-dependent amplitude shift in the clustering signal arises due to the transition of a comparatively small number of objects over this boundary, this presents an additional challenge. Nonetheless, these requirements are not unassailable barriers. the Sloan Digital Sky Survey (SDSS), for example, currently covers 14,555 square degrees and has spectroscopic data on  $\sim 10^9$  galaxies.

Despite this setback, the close agreement between the predicted clustering of BAHAMAS GGCs and that measured from GAMA remains highly significant. The use of clusters to perform cosmology requires that accurate and self-consistent predictions can be made of their properties. The success of BAHAMAS in matching so precisely the observed clustering *without direct tuning*, as well as its other comparable successes already reported (see, for example, McCarthy et al. 2018) presents an increasingly strong case for the viability of using simulations for cluster cosmology.

# Chapter 4

## Summary and Future Work

### 4.1 Summary

In Chapter 2 I presented the results of my investigation into the separate and combined effects of baryon physics (particularly AGN feedback) and neutrino free-streaming on different aspects of large scale structure: the halo mass function and number counts; the spherically-averaged density profiles; the mass–concentration relation; and the autocorrelation functions of haloes themselves as well as matter in general.

Analysis of these measures led to the following conclusions:

#### **The Halo Mass Function**

- AGN feedback can suppress the HMF by  $\approx 20 - 30\%$  relative to the DMONLY case on the scale of galaxy groups and clusters as AGN heating acts against gravitational collapse. This effect is largely insensitive to redshift.
- Neutrino free-streaming preferentially suppresses the cluster end of the HMF, exhibiting a strong dependence on redshift and the choice of neutrino mass. This is due to the formation of the most massive structures continuing to late times, causing their abundance to be more sensitive to slight changes in their formation

timescale.

### Radial Density Profiles

- The inclusion of baryonic physics results in higher central densities due to cooling, and higher peripheral densities due to gas ejection relative to the DMONLY case. Expelling gas leads to an expansion of the DM, causing the NFW scale radius to increase.
- The free-streaming of massive neutrinos reduces the present-day amplitude of the mass density profile of a given halo while leaving their shape approximately unchanged within the virial radius. The radius at which the profile transitions from the ‘1 halo’ to the ‘2 halo’ term decreases with increasing  $\sum M_\nu$ .

### The Mass–Concentration Relation

- The amplitude of the mass–concentration relation is reduced by neutrino free-streaming by up to  $\sim 10\%$  for the most extreme ( $\sum M_\nu=0.48$ ) case considered here, with only minimal alteration to its slope. This is due both to a lowering of the overall halo mass and a slight increase of the scale radius.
- AGN feedback alters both the amplitude and the slope of the mass–concentration relation. The amplitude shift is the result of an increase in the scale radius as observed in the context of the radial density profiles, while the change in slope reflects the increased efficacy of AGN feedback in altering the structure of group scale haloes as opposed to cluster scale.

### Halo Clustering

- In bins of the *self consistent* halo mass, both AGN feedback and neutrino free-streaming result in an apparent enhancement of the amplitude of the 2-point halo correlation function on large scales ( $r \gg r_{200}$ ), by  $\sim 10\%$  with respect to the DMONLY case with massless neutrinos at  $z = 0$ . In the case of simulations with

baryons and massless neutrinos, this is due entirely to the effect on the halo mass (so that the mass bins contain different systems in different simulations) rather than a true alteration of the spatial distribution of haloes.

- In the case of simulations with massive neutrinos, when the change in halo mass is accounted for, I find that the large-scale clustering of haloes is actually *suppressed* relative to a massless neutrino case as expected, due to the reduction in accretion rate for these systems.

### Matter Clustering

- On small scales ( $k > 1$  h/Mpc) the matter power spectrum can be suppressed by AGN feedback by up to 10-20% at  $z = 0$ . This factor increases by a factor of  $\approx 2$  between  $z = 2$  and  $z = 0$
- Neutrino free-streaming also suppresses the matter power spectrum, but over a much wider range of scales. This suppression is nearly insensitive to redshift but depends strongly on the adopted summed neutrino mass. This result formed part of the motivation for the work presented in Chapter 3.

### Separability

- I have investigated the extent to which the effects of baryon physics and neutrino free-streaming can be treated independently. The procedure of multiplying together the magnitudes of the two effects when taken in isolation reproduces their combined effects to typically a few percent accuracy for the halo mass function, the mass density profiles, the mass–concentration relation, and the clustering of haloes and matter over ranges of  $12 \leq M_{200,\text{crit}}/M_{\odot} \leq 15$ ,  $12 \leq M_{200,\text{crit}}/M_{\odot} \leq 14.5$ ,  $12 \leq M_{200,\text{crit}}/M_{\odot} \leq 14$  and  $0.04 \leq k$  [h/Mpc]  $\leq 10$ , respectively.

My work has demonstrated that both AGN feedback and neutrino free-streaming can have a considerable impact on LSS. They should therefore both be included in cosmological analyses. Through the use of self-consistent cosmological simulations I have

shown that, to a high degree of accuracy, these processes are separable (i.e., can be treated independently), which should considerably simplify the inclusion of their effects in cosmological studies that adopt, for example, the halo model formalism or the linear matter power spectrum (e.g., from CAMB).

In Chapter 3 I explored the possibility of constraining the value of  $\sum M_\nu$  by means of direct comparison between simulated and observed GGC clustering. Data from the BAHAMAS suite was used to construct simulated observations in the form of light cones. Catalogues of galaxies were drawn from these, then cuts in stellar mass and redshift applied both to these simulated galaxy catalogues, and the observed galaxy catalogues from the GAMA survey data release 3 in order to ensure that the selection functions of the two data sets were identical.

To ensure that no uncertainty could be introduced by methodological differences, I then treated these catalogues consistently throughout. I assigned galaxies to groups based on a FoF algorithm, then computed the 3D, redshift-space 2-point autocorrelation function of GGCs in equally populated bins of observable mass tracers, specifically the integrated stellar mass and richness.

Despite the promising result of Figure 2.14, I found that the statistical power of GAMA-equivalent observations is insufficient to detect the alteration to the clustering resulting from changing the neutrino mass, even when considering the most extreme case covered by BAHAMAS ( $\sum M_\nu = 0.48$  eV) and a survey area ten times larger than the actual GAMA fields used in this study.

I then explored in detail the potential causes of this loss of precision. Returning to the BAHAMAS light cones in their unprocessed form, I was able to investigate the impact on the sensitivity of the clustering signal of:

- i)* considering a redshift range, however small, as opposed to measuring the clustering at a fixed redshift value;
- ii)* the cosmology dependence of, and intrinsic scatter in, the group observable–halo mass relations;
- iii)* the peculiar motions of galaxies and groups; and

iv) the galaxy linking strategy.

While each of these effects serves to decrease the sensitivity of the GGC clustering to the neutrino mass, I found that the largest contributor was the intrinsic scatter in the group observable–halo mass relations. This leads me to the conclusion that it is not viable to perform cosmology with these data alone. Having identified the largest effect diminishing the sensitivity it is relatively easy to foresee methods by which this may be mitigated, however even with this effect removed entirely placing constraints on the neutrino mass requires an increase in the size of the observational catalogue by at least an order of magnitude over that used here.

A more heartening result arises from the comparison of the simulated data not to other simulations but to the *observations*. The agreement between the observed GGC clustering in GAMA, and that predicted by the BAHAMAS simulations is remarkably close. This stands with similar successes in reproducing other cluster properties (see, for example, McCarthy et al. 2018) in presenting an increasingly strong case for the viability of simulations in the pursuit of cluster cosmology.

## 4.2 Future Work

This thesis utilised the unique opportunity presented by the BAHAMAS and cosmo-OWLS simulation suites to study in detail the effects of baryon physics and the free streaming of massive neutrinos and large-scale structure formation in the context of self-consistent, hydrodynamical cosmological simulations. The findings presented in Chapter 2 demonstrated that these effects are necessary inclusions in models of LSS formation, while also establishing that, over the range of masses and redshifts considered, the two effects can be considered independently to high accuracy. This should simplify considerably their implementation as corrective terms in theoretical models. However, further work should be undertaken to establish how far beyond the regime considered here the multiplicative approximation remains valid.

Although placing constraints on the neutrino mass from GGC clustering proved non-

viable with the GAMA data set alone analysed in this way, this work identified the intrinsic scatter in the observable–halo mass relations as the primary factor in reducing the sensitivity of the clustering signal to this cosmology. An obvious route for future study, therefore, is the utilisation of techniques that reduce or eliminate the effect of this scatter. One possible avenue is exemplified in the work of Farahi et al. (2018), who found that the scatter in the stellar mass–halo mass and gas mass–halo mass relations of GGCs in BAHAMAS is anti-correlated, implying that one can potentially combine optical and X-ray observations to construct a better estimator of halo mass. Use of such observables would significantly improve the sensitivity of the clustering measurement to the cosmology. An alternative approach would be the combined analysis of GGC clustering with independent methods of determining the halo mass. For example, weak lensing is (in theory) directly sensitive to the true halo mass and would therefore bypass the scatter introduced by the stellar- and richness-halo mass relations. However, weak lensing itself introduces a number of additional sources of uncertainty such as additive and multiplicative biases, the choice of PSF model, and, significantly, intrinsic alignments. As a result, the scatter between weak lensing mass and true halo mass is significant. This scatter is less problematic at high masses where the effect of neutrinos is strongest, but is nonetheless sufficient to reduce the immediate applicability of weak lensing as a workaround in this specific case. However, since this scatter is predominately independent of the scatter in the mass-observable relationships discussed above, joint analysis of multiple independent mass measurement techniques could serve to provide a more beneficial estimator (Mandelbaum, 2017).

As discussed in Section 2.4.1 and shown most clearly in Figure 2.10, the influence of neutrino free-streaming on the radial total mass density of a consistent set of haloes is to reduce the amplitude without altering the shape. However, beyond the virial radius can be seen an ‘oscillatory’ feature in ratios between the different neutrino cases. This I interpret as the transition between the one-halo term, where the radial density profile is dominated by the halo upon which it is centred; and the two-halo term, where the contribution of nearby systems becomes significant. This sensitivity offers an additional potential route by which constraints may be placed on the neutrino mass by

observations of GGCs.

Finally, while it represents an important step forward in the use of simulations for cluster cosmology, the BAHAMAS project in its current state remains limited to investigating the effects of varying a single cosmological parameter. This work therefore ignores a potentially large degree of uncertainty in its results – since the other cosmological parameters are fixed to their best-fit values (or adjusted only in reaction to the changing  $\Omega_\nu$ , see Section 3.2.1), the contribution of the uncertainty in their values goes unaddressed. Estimating the true uncertainty is not trivial, however, as the parameters affect the observables and one another in complex ways. The eventual goal of the BAHAMAS project is to capture the entire parameter space of the cosmological parameters. However, it is computationally expensive to run even a single realisation, let alone the large number required for such a probe. Further development of BAHAMAS, therefore, will focus on developing an interpolation system, allowing the prediction of observable properties as a function of any combination of cosmological parameters by interpolating between the outputs of simulations run on a carefully sampled grid within the parameter space.

# Appendix A

## Fits to mass-concentration relations

In Table A.1 I provide the best fit power law parameter values to the mass–concentration relations of the various cosmo-OWLS and BAHAMAS runs. The listed values correspond to the coefficients of Equation 2.9. I provide these values both for the total mass density profiles, and the DM density profiles.

For comparison, I also include the values found by Duffy et al. (2008).

Table A.1: Best-fit values for the coefficients of eq. (2.9) for  $z = 0 - 2$  and  $M_{Fiducial} = 10^{14}M_{\odot}$ , and the  $1 - \sigma$  log-normal scatter of concentration values around the best fit relation. The columns are: (1): The simulation run and background cosmology of the run under consideration. (2-4): The best-fit values of the coefficients of Equation 2.9 found when considering the DM-content of the haloes alone. (5): The  $1-\sigma$  extent of scatter around the best-fit relationship described by (2-4). (6-9): As (2-5), but considering the total mass content of the haloes.

| (1)                 | DM      |       |        |             | Tot   |        |        |             |       |
|---------------------|---------|-------|--------|-------------|-------|--------|--------|-------------|-------|
|                     | A (2)   | B (3) | C (4)  | scatter (5) | A (6) | B (7)  | C (8)  | scatter (9) |       |
| WMAP-7              | NOCOOL  | 4.878 | -0.099 | -0.507      | 0.340 | 4.720  | -0.062 | -0.457      | 0.339 |
|                     | REF     | 4.650 | -0.112 | -0.360      | 0.353 | 4.124  | -0.111 | -0.327      | 0.353 |
|                     | AGN 8.0 | 4.105 | -0.061 | -0.391      | 0.363 | 3.614  | -0.105 | -0.424      | 0.363 |
|                     | AGN 8.5 | 3.917 | -0.073 | -0.432      | 0.364 | 3.599  | -0.108 | -0.462      | 0.364 |
|                     | AGN 8.7 | 3.842 | -0.071 | -0.461      | 0.369 | 3.640  | -0.094 | -0.485      | 0.369 |
| WMAP-9              | NU 0.00 | 4.553 | -0.072 | -0.467      | 0.373 | 4.099  | -0.114 | -0.515      | 0.373 |
|                     | NU 0.06 | 4.498 | -0.070 | -0.458      | 0.374 | 4.053  | -0.112 | -0.511      | 0.375 |
|                     | NU 0.12 | 4.411 | -0.074 | -0.449      | 0.373 | 3.985  | -0.114 | -0.504      | 0.375 |
|                     | NU 0.24 | 4.329 | -0.070 | -0.446      | 0.374 | 3.901  | -0.111 | -0.499      | 0.376 |
|                     | NU 0.48 | 4.055 | -0.068 | -0.402      | 0.385 | 3.646  | -0.108 | -0.450      | 0.386 |
| Duffy et al. (2008) |         |       |        |             | 4.11  | -0.084 | -0.47  |             |       |

# Appendix B

## Overview of Halo samples

The total number of GGCs in each bin for the various binning schemes used within this Thesis. The numbers identified by the various FoF strategies run on GAMA data and the equivalent BAHAMAS synthetic observations are given in Table B.1. For the full BAHAMAS catalogues contained within the lightcones, the appropriate numbers of objects are given in Table B.2 for WMAP-9 data and Table B.3 for *Planck*.

Table B.1: Overview of the galaxy group samples drawn from each data set. For the GAMA data sets, I quote the values for each of the G09, G12 and G15 fields independently, as well as the aggregate across all three fields. In order that values from different data sets may be directly compared, I include in square brackets in each case the comoving number density in units of  $10^3 \text{ Gpc}^{-3}$ . The columns are: (1): The label assigned to the data set from which the sample is drawn; (2): The total number of identified galaxy groups with two or more members; (3): The total number of identified galaxy groups with five or more members; (4-6): The number of identified galaxy groups that fall within the stellar mass bins defined in Section 3.4.1; (7-9): The number of identified galaxy groups that fall within the multiplicity bins defined in section Section 3.4.1. The sections are: (A): The total number in each bin of galaxy groups identified from the GAMA galaxy catalogues using a fixed FoF linking length; (B): The total number in each bin of galaxy groups identified from the BAHAMAS galaxy catalogues using a fixed FoF linking length; (C): The total number in each bin of galaxy groups identified from the GAMA galaxy catalogues using a mass-dependent FoF linking length; (D): The total number in each bin of galaxy groups identified from the BAHAMAS galaxy catalogues using a mass-dependent FoF linking length. In each of these sections, we present the results arising in the context of both the *Planck* and WMAP-9 cosmologies, as described in Section 3.2.1. Note that for the GAMA data set, results in different cosmologies arise from re-analysing the GAMA fields with different sets of cosmological parameters, whereas BAHAMAS has separate runs and therefore separate data sets for each cosmology.

| Sample  | N        |          | $M_*$        |                 |                 | N       |         |          |
|---|----------|----------|--------------|-----------------|-----------------|---------|---------|----------|
|   | $\geq 2$ | $\geq 5$ | 10-<br>10.55 | 10.55-<br>10.84 | $\geq$<br>10.84 | 5-6     | 6-8     | $\geq 8$ |
| (1)   | (2)      | (3)      | (4)          | (5)             | (6)             | (7)     | (8)     | (9)      |
| <b>(A) GAMA fixed linking length - WMAP-9</b> |          |          |              |                 |                 |         |         |          |
| G09   | 1,628    | 195      | 524          | 540             | 564             | 63      | 63      | 69       |
|   | [486.0]  | [58.22]  | [156.4]      | [161.2]         | [168.4]         | [18.80] | [18.80] | [20.60]  |
| G12   | 2,148    | 238      | 692          | 749             | 707             | 84      | 73      | 81       |
|   | [641.3]  | [71.05]  | [193.8]      | [223.6]         | [211.1]         | [25.08] | [21.79] | [24.18]  |
| G15   | 2,133    | 243      | 745          | 683             | 705             | 88      | 67      | 88       |
|   | [636.8]  | [72.55]  | [222.4]      | [203.9]         | [210.5]         | [26.27] | [20.00] | [26.27]  |
| Total   | 5,909    | 676      | 1,961        | 1,972           | 1,976           | 232     | 203     | 238      |
|   | [588.0]  | [67.27]  | [190.9]      | [196.2]         | [196.7]         | [23.38] | [20.20] | [23.68]  |
| <i>Planck</i>                                 |          |          |              |                 |                 |         |         |          |
| G09   | 1,628    | 235      | 524          | 540             | 564             | 63      | 84      | 88       |
|   | [541.8]  | [65.22]  | [144.3]      | [148.8]         | [155.4]         | [17.35] | [23.14] | [24.24]  |
| G12   | 2,085    | 203      | 629          | 749             | 707             | 63      | 73      | 67       |

---

|       |         |         |         |         |         |         |         |         |
|-------|---------|---------|---------|---------|---------|---------|---------|---------|
|       | [578.7] | [56.34] | [17.35] | [206.3] | [194.7] | [17.35] | [20.11] | [18.46] |
| G15   | 2,133   | 238     | 745     | 683     | 705     | 69      | 81      | 88      |
|       | [592.0] | [66.06] | [205.2] | [188.1] | [194.2] | [19.01] | [22.31] | [24.24] |
| Total | 5,846   | 676     | 1,898   | 1,972   | 1,976   | 195     | 238     | 243     |
|       | [579.4] | [67.00] | [174.3] | [181.1] | [181.4] | [18.29] | [21.85] | [22.31] |

---

**(B) BAHAMAS fixed linking length - WMAP-9**

|               |         |         |         |         |         |         |         |         |
|---------------|---------|---------|---------|---------|---------|---------|---------|---------|
| NU 0.0061,728 | 5,334   | 22,902  | 19,215  | 19,608  | 2,307   | 1,608   | 1,419   |         |
|               | [614.2] | [53.08] | [227.9] | [191.2] | [195.1] | [22.96] | [16.00] | [14.12] |
| NU 0.0661,377 | 5,340   | 22,974  | 18,960  | 19,440  | 2,259   | 1,776   | 1,305   |         |
|               | [610.8] | [53.14] | [228.6] | [188.7] | [193.5] | [22.48] | [17.67] | [12.99] |
| NU 0.1261,833 | 5,310   | 22,488  | 19,377  | 19,968  | 2,190   | 1,728   | 1,392   |         |
|               | [615.3] | [52.84] | [223.8] | [192.8] | [198.7] | [21.79] | [17.20] | [13.85] |
| NU 0.2459,871 | 5,094   | 22,941  | 17,952  | 18,975  | 2,001   | 1,770   | 1,323   |         |
|               | [595.8] | [50.69] | [228.3] | [178.6] | [188.8] | [19.91] | [17.61] | [13.17] |
| NU 0.4857,888 | 4,731   | 22,044  | 18,003  | 17,841  | 1,749   | 1,674   | 1,308   |         |
|               | [576.1] | [47.08] | [219.4] | [179.2] | [177.5] | [17.40] | [16.66] | [13.02] |

*Planck*

|               |         |         |         |         |         |         |         |         |
|---------------|---------|---------|---------|---------|---------|---------|---------|---------|
| NU 0.0679,988 | 6,673   | 31,466  | 24,937  | 23,469  | 2,647   | 2,284   | 1,742   |         |
|               | [587.5] | [49.02] | [231.1] | [183.2] | [172.4] | [19.44] | [16.78] | [12.80] |
| NU 0.1280,188 | 6,681   | 31,554  | 25,050  | 23,470  | 2,637   | 2,260   | 1,784   |         |
|               | [531.4] | [44.28] | [209.1] | [166.0] | [155.5] | [17.48] | [14.98] | [11.82] |
| NU 0.2481,304 | 6,924   | 31,291  | 25,366  | 24,542  | 2,720   | 2,302   | 1,902   |         |
|               | [485.0] | [41.31] | [186.7] | [151.3] | [146.4] | [16.23] | [13.73] | [11.35] |
| NU 0.4880,869 | 6,885   | 31,014  | 24,879  | 24,840  | 2,747   | 2,360   | 1,778   |         |
|               | [680.9] | [57.97] | [261.1] | [209.5] | [209.1] | [23.13] | [19.87] | [14.97] |

---

**(C) GAMA mass-dependent linking length - WMAP-9**

|     |         |         |         |         |         |         |         |         |
|-----|---------|---------|---------|---------|---------|---------|---------|---------|
| G09 | 1,580   | 304     | 445     | 503     | 632     | 69      | 89      | 146     |
|     | [471.7] | [907.6] | [132.9] | [150.2] | [188.7] | [20.60] | [26.57] | [43.59] |
| G12 | 1,946   | 391     | 541     | 629     | 773     | 96      | 90      | 205     |
|     | [581.0] | [116.7] | [161.5] | [187.8] | [230.8] | [28.66] | [26.87] | [61.20] |

|               |         |         |         |         |         |         |         |         |
|---------------|---------|---------|---------|---------|---------|---------|---------|---------|
| G15           | 1,935   | 362     | 590     | 602     | 742     | 92      | 72      | 198     |
|               | [577.7] | [108.1] | [176.1] | [179.7] | [221.5] | [27.47] | [21.50] | [59.11] |
| Total         | 5,461   | 1,057   | 1,576   | 1,734   | 2,147   | 257     | 251     | 549     |
|               | [543.5] | [105.2] | [156.8] | [172.6] | [213.7] | [25.58] | [24.98] | [54.63] |
| <i>Planck</i> |         |         |         |         |         |         |         |         |
| G09           | 1,579   | 304     | 444     | 502     | 633     | 69      | 89      | 146     |
|               | [250.5] | [482.3] | [122.3] | [138.3] | [174.4] | [19.01] | [24.52] | [40.22] |
| G12           | 1,943   | 391     | 540     | 630     | 773     | 96      | 93      | 202     |
|               | [539.3] | [108.5] | [148.7] | [173.5] | [212.9] | [26.44] | [25.62] | [55.64] |
| G15           | 1,934   | 362     | 589     | 603     | 742     | 92      | 72      | 198     |
|               | [536.8] | [100.5] | [162.2] | [166.1] | [204.4] | [25.34] | [19.83] | [54.54] |
| Total         | 5,456   | 1,057   | 1,573   | 1,735   | 2,148   | 257     | 254     | 546     |
|               | [540.8] | [104.8] | [144.4] | [159.3] | [197.2] | [23.60] | [23.32] | [50.13] |

**(D) BAHAMAS mass-dependent linking length - WMAP-9**

|               |         |         |         |         |         |         |         |         |
|---------------|---------|---------|---------|---------|---------|---------|---------|---------|
| NU 0.0064,359 | 11,064  | 20,373  | 18,822  | 25,143  | 3,108   | 3,024   | 4,932   |         |
|               | [640.5] | [110.1] | [202.7] | [187.3] | [250.2] | [30.93] | [30.09] | [49.08] |
| NU 0.0663,807 | 10,956  | 20,247  | 18,750  | 24,792  | 3,054   | 3,093   | 4,809   |         |
|               | [635.0] | [109.0] | [201.5] | [186.6] | [246.7] | [30.39] | [30.78] | [47.56] |
| NU 0.1264,275 | 10,962  | 19,983  | 19,050  | 25,224  | 3,138   | 3,018   | 4,806   |         |
|               | [639.6] | [109.1] | [198.9] | [189.6] | [251.0] | [31.23] | [30.03] | [47.83] |
| NU 0.2462,976 | 10,407  | 20,229  | 18,279  | 24,438  | 2,868   | 2,982   | 4,557   |         |
|               | [626.7] | [103.6] | [201.3] | [181.9] | [243.2] | [28.54] | [29.67] | [45.35] |
| NU 0.4861,317 | 9,963   | 19,956  | 18,018  | 23,328  | 2,679   | 2,844   | 4,440   |         |
|               | [610.2] | [99.14] | [198.6] | [179.3] | [232.1] | [26.66] | [28.30] | [44.18] |
| <i>Planck</i> |         |         |         |         |         |         |         |         |
| NU 0.0682,695 | 13,869  | 25,406  | 24,686  | 32,553  | 3,715   | 3,861   | 6,293   |         |
|               | [607.4] | [101.9] | [186.6] | [181.3] | [239.1] | [27.29] | [28.36] | [46.22] |
| NU 0.1283,649 | 14,021  | 25,569  | 25,078  | 32,953  | 3,715   | 3,957   | 6,349   |         |
|               | [554.4] | [92.92] | [169.5] | [166.2] | [218.4] | [24.62] | [26.22] | [42.08] |

---

|               |         |         |         |         |         |         |         |
|---------------|---------|---------|---------|---------|---------|---------|---------|
| NU 0.2484,615 | 14,297  | 25,545  | 25,089  | 33,942  | 3,885   | 4,003   | 6,409   |
| [504.8]       | [85.29] | [152.4] | [149.7] | [202.5] | [23.18] | [23.88] | [38.24] |
| NU 0.4884,828 | 14,070  | 25,275  | 25,115  | 34,397  | 3,725   | 4,183   | 6,162   |
| [714.2]       | [118.5] | [212.8] | [211.5] | [289.6] | [31.36] | [35.22] | [51.88] |

---

---

Table B.2: densities in  $10^6$  per  $Gpc^3$  Overview of the massive halo samples drawn from the BAHAMAS lightcones in the WMAP-9 cosmology. The columns are: (1): The total number of haloes in the sample with true multiplicity  $N_{halo}$  of at least 2; (2): The total number of haloes in the sample with true multiplicity  $N_{halo}$  of at least 5; (3): The total number of haloes in the sample with total mass  $M_{200}$  of at least  $10^{12}M_{\odot}$ ; (4-6): The number of haloes that fall within each of the chosen true multiplicity bins; (7-9): The number of haloes that fall within each of the chosen true stellar mass bins; (10-12): The number of haloes that fall within each of the chosen true total halo mass bins. In each case, I include in square brackets the comoving number density of haloes in each bin in units of  $10^6 Gpc^{-3}$ .

| Totals            |                   |                        | $N_{halo}$     |                |            | $log(M_*)$             |                            |                   | $M_{200}$                 |                              |                   |
|-------------------|-------------------|------------------------|----------------|----------------|------------|------------------------|----------------------------|-------------------|---------------------------|------------------------------|-------------------|
| $N_{halo} \geq 2$ | $N_{halo} \geq 5$ | $M_{200} \geq 10^{12}$ | $5 \leq N < 6$ | $6 \leq N < 8$ | $N \leq 8$ | $10 \leq M_* < 10.647$ | $10.647 \leq M_* < 10.940$ | $M_* \leq 10.940$ | $12 \leq M_{200} < 12.36$ | $12.36 \leq M_{200} < 12.77$ | $M_{200} < 12.77$ |
| (1)               | (2)               | (3)                    | (4)            | (5)            | (6)        | (7)                    | (8)                        | (9)               | (10)                      | (11)                         | (12)              |
| NU 0.00           |                   |                        |                |                |            |                        |                            |                   |                           |                              |                   |
| 935,717           | 125,927           | 2,224,003              | 37,854         | 37,406         | 50,667     | 784,474                | 676,794                    | 733,215           | 1,313,030                 | 588,947                      | 322,026           |
| [7.45]            | [1.00]            | [17.7]                 | [0.301]        | [0.298]        | [0.403]    | [6.25]                 | [5.39]                     | [5.84]            | [10.5]                    | [4.69]                       | [2.56]            |
| NU 0.06           |                   |                        |                |                |            |                        |                            |                   |                           |                              |                   |
| 930,997           | 124,564           | 2,203,453              | 38,319         | 36,631         | 49,614     | 773,057                | 669,265                    | 731,955           | 1,304,938                 | 583,413                      | 315,102           |
| [7.41]            | [0.992]           | [17.5]                 | [0.305]        | [0.292]        | [0.395]    | [6.15]                 | [5.33]                     | [5.83]            | [10.4]                    | [4.64]                       | [2.51]            |
| NU 0.12           |                   |                        |                |                |            |                        |                            |                   |                           |                              |                   |
| 925,840           | 122,848           | 2,192,201              | 38,104         | 36,573         | 48,171     | 746,305                | 676,166                    | 745,002           | 1,303,345                 | 579,320                      | 309,536           |
| [7.37]            | [0.978]           | [17.5]                 | [0.303]        | [0.291]        | [0.383]    | [5.94]                 | [5.38]                     | [5.93]            | [10.4]                    | [4.61]                       | [2.46]            |
| NU 0.24           |                   |                        |                |                |            |                        |                            |                   |                           |                              |                   |
| 907,379           | 117,121           | 2,124,026              | 36,373         | 35,186         | 45,562     | 746,152                | 643,494                    | 707,849           | 1,270,547                 | 56,0988                      | 292,491           |
| [7.22]            | [0.932]           | [16.9]                 | [0.290]        | [0.280]        | [0.363]    | [5.94]                 | [5.12]                     | [5.64]            | [10.1]                    | [4.47]                       | [2.33]            |
| NU 0.48           |                   |                        |                |                |            |                        |                            |                   |                           |                              |                   |
| 86,8761           | 106,443           | 2,005,103              | 34,907         | 32,279         | 39,257     | 702,685                | 614,006                    | 664,054           | 1,222,684                 | 524,498                      | 257,921           |
| [6.92]            | [0.847]           | [16.0]                 | [0.278]        | [0.257]        | [0.313]    | [5.59]                 | [4.89]                     | [5.29]            | [9.73]                    | [4.18]                       | [2.05]            |

Table B.3: densities in  $10^6$  per  $Gpc^3$  Overview of the massive halo samples drawn from the BAHAMAS lightcones in the *Planck* cosmology. The columns are: (1): The total number of haloes in the sample with true multiplicity  $N_{halo}$  of at least 2; (2): The total number of haloes in the sample with true multiplicity  $N_{halo}$  of at least 5; (3): The total number of haloes in the sample with total mass  $M_{200}$  of at least  $10^{12}M_{\odot}$ ; (4-6): The number of haloes that fall within each of the chosen true multiplicity bins; (7-9): The number of haloes that fall within each of the chosen true stellar mass bins; (10-12): The number of haloes that fall within each of the chosen true total halo mass bins. In each case, I include in square brackets the comoving number density of haloes in each bin in units of  $10^6 Gpc^{-3}$ .

| Totals            |                   |                        | $N_{halo}$     |                |            | $log(M_*)$             |                            |                   | $M_{200}$                 |                              |                   |
|-------------------|-------------------|------------------------|----------------|----------------|------------|------------------------|----------------------------|-------------------|---------------------------|------------------------------|-------------------|
| $N_{halo} \geq 2$ | $N_{halo} \geq 5$ | $M_{200} \geq 10^{12}$ | $5 \leq N < 6$ | $6 \leq N < 8$ | $N \leq 8$ | $10 \leq M_* < 10.647$ | $10.647 \leq M_* < 10.940$ | $M_* \leq 10.940$ | $12 \leq M_{200} < 12.36$ | $12.36 \leq M_{200} < 12.77$ | $M_{200} < 12.77$ |
| (1)               | (2)               | (3)                    | (4)            | (5)            | (6)        | (7)                    | (8)                        | (9)               | (10)                      | (11)                         | (12)              |
| NU 0.06           |                   |                        |                |                |            |                        |                            |                   |                           |                              |                   |
| 977,531           | 126,074           | 2,541,042              | 38,302         | 37,458         | 50,314     | 958,586                | 768,616                    | 768,634           | 1,492,357                 | 676,381                      | 372,304           |
| [7.18]            | [0.926]           | [18.7]                 | [0.281]        | [0.275]        | [0.370]    | [7.04]                 | [5.65]                     | [5.65]            | [11.0]                    | [4.97]                       | [2.73]            |
| NU 0.12           |                   |                        |                |                |            |                        |                            |                   |                           |                              |                   |
| 976,620           | 125,213           | 2,542,683              | 38,626         | 36,877         | 49,710     | 956,913                | 766,782                    | 773,083           | 1,499,201                 | 674,858                      | 368,624           |
| [7.12]            | [0.913]           | [18.5]                 | [0.282]        | [0.269]        | [0.362]    | [6.98]                 | [5.59]                     | [5.64]            | [10.9]                    | [4.92]                       | [2.69]            |
| NU 0.24           |                   |                        |                |                |            |                        |                            |                   |                           |                              |                   |
| 975,487           | 122,871           | 2,557,275              | 38,552         | 36,790         | 47,529     | 949,718                | 782,568                    | 787,095           | 1,516,806                 | 677,595                      | 362,874           |
| [6.98]            | [0.880]           | [18.3]                 | [0.276]        | [0.263]        | [0.340]    | [6.80]                 | [5.60]                     | [5.63]            | [10.9]                    | [4.85]                       | [2.60]            |
| NU 0.48           |                   |                        |                |                |            |                        |                            |                   |                           |                              |                   |
| 961,273           | 112,757           | 2,528,446              | 36,188         | 34,771         | 41,798     | 933,361                | 775,209                    | 784,477           | 1,526,328                 | 666,247                      | 335,871           |
| [6.66]            | [0.781]           | [17.5]                 | [0.251]        | [0.241]        | [0.290]    | [6.47]                 | [5.37]                     | [5.43]            | [10.6]                    | [4.61]                       | [2.33]            |

# Appendix C

## *Planck* cosmology

The plots included in this appendix are directly equivalent to Figures 3.1 to 3.12 (excluding Figure 3.4) of Chapter 3, differing in the fact that they present the results of analysis of the data carried out in the context of a *Planck* cosmology rather than WMAP-9.

In all cases, the results are qualitatively similar to those presented in Chapter 3.

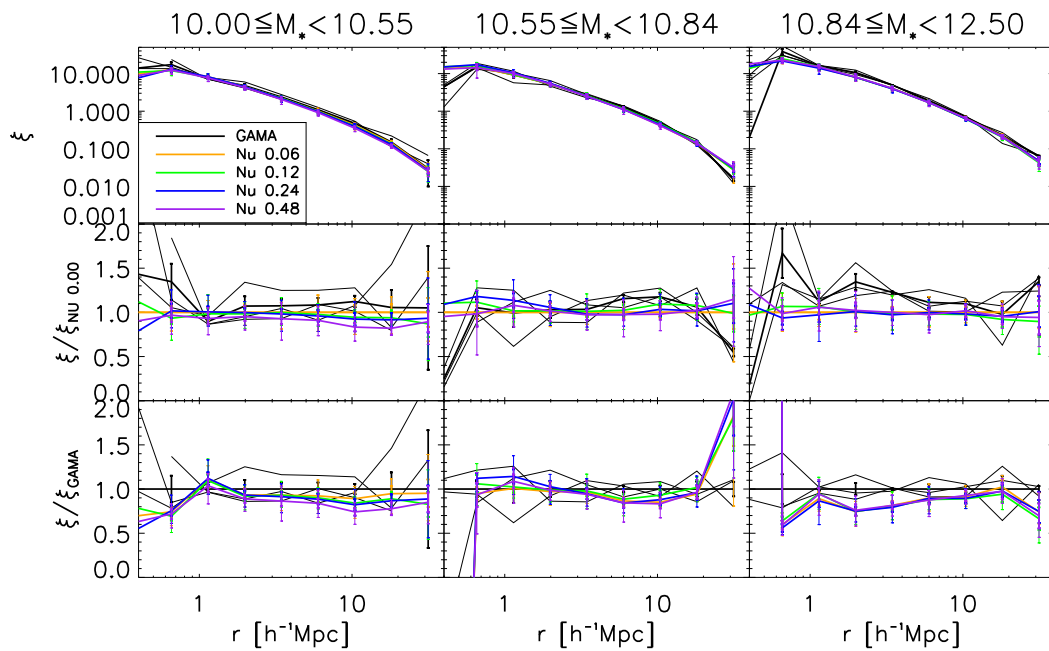


Figure C.1: As Figure 3.1, but in the context of a *Planck* cosmology. *Top*: The redshift-space 2-point galaxy group autocorrelation as a function of the inter-group separation for GAMA (black curve) and BAHAMAS (coloured curves) in equally populated bins of integrated stellar mass for a *Planck* cosmology. Groups have been identified by means of a FoF algorithm with a fixed linking length as described in section 3.3.2. For the BAHAMAS curves, thick error bars display the standard error on the mean and thin error bars show the 60th percentile of the cosmic variance. In the GAMA case, error bars show the standard error on the mean. *Middle*: The ratio of the autocorrelation function in each case to the BAHAMAS massless neutrino (“nu 0.00”) case. *Bottom*: The ratio of the autocorrelation function in each case to the GAMA case.

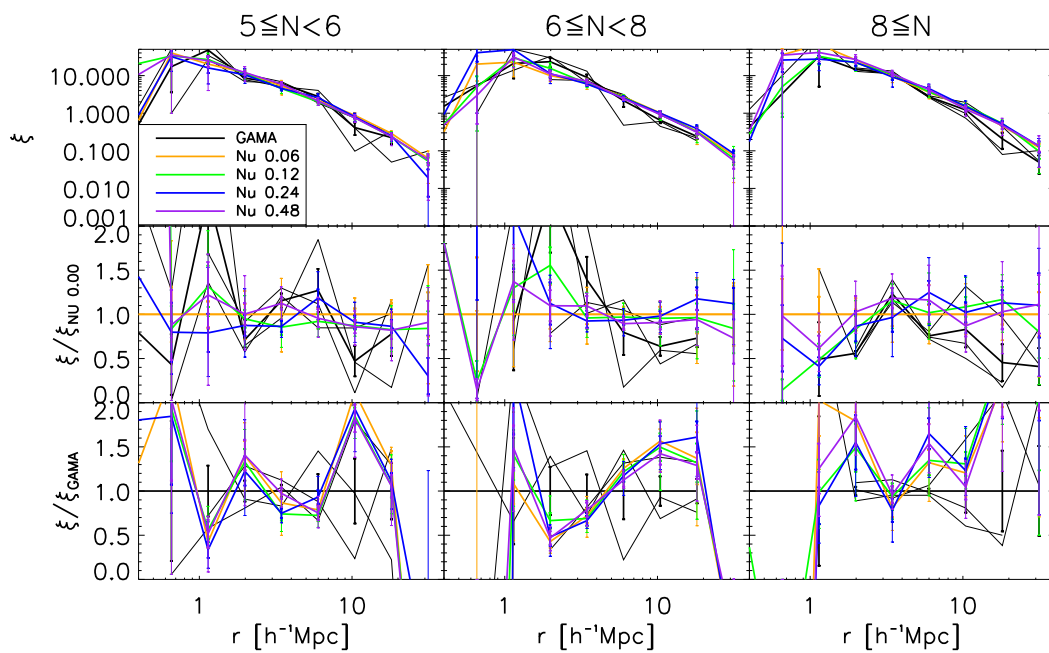


Figure C.2: The equivalent of Figure 3.2 but in the context of a *Planck* cosmology. *Top*: The redshift-space 2-point galaxy group autocorrelation as a function of the inter-group separation for GAMA (black curve) and BAHAMAS (coloured curves) in equally populated bins of multiplicity for a *Planck* cosmology. Groups have been identified by means of a FoF algorithm with a fixed linking length as described in section 3.3.2. For the BAHAMAS curves, thick error bars display the standard error on the mean and thin error bars show the 60th percentile of the cosmic variance. In the GAMA case, error bars show the standard error on the mean. *Middle*: The ratio of the autocorrelation function in each case to the BAHAMAS massless neutrino (“ $\nu$  0.00”) case. *Bottom*: The ratio of the autocorrelation function in each case to the GAMA case.

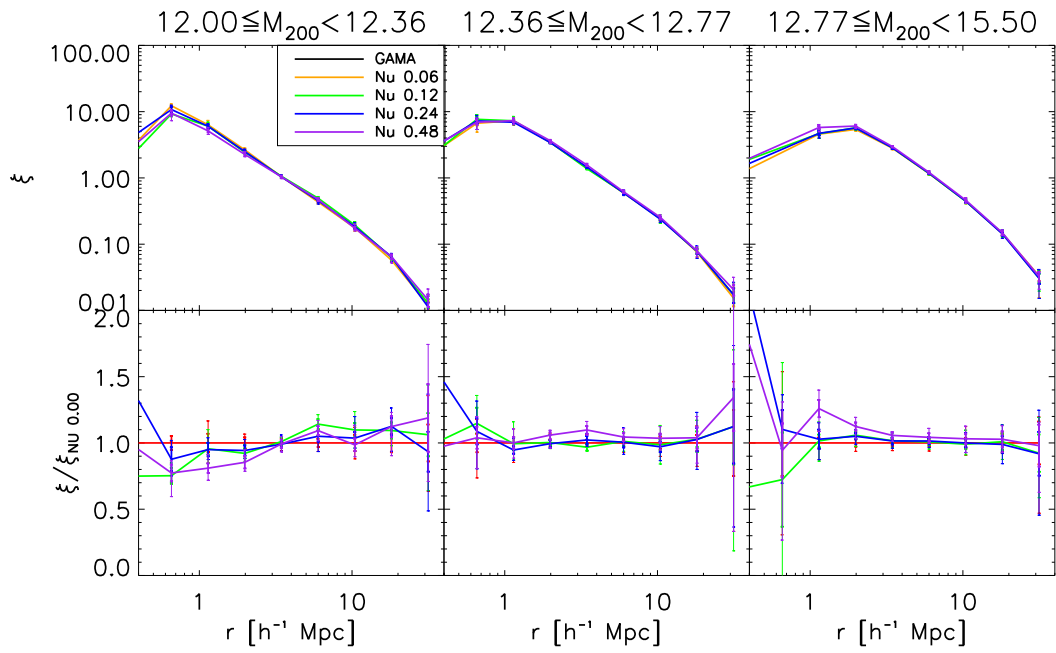


Figure C.3: As Figure 3.3, but in the context of a *Planck* cosmology. *Top*: Redshift-space 2-point autocorrelation functions for BAHAMAS galaxy groups in equally populated bins of halo mass  $M_{200,crit}$  in the *Planck* cosmology. As above, thick error bars display the standard error on the mean while thin error bars show the 60th percentile of the cosmic variance. *Bottom*: The autocorrelation function in each case normalised to the massless neutrino case. BAHAMAS runs with higher values for the summed neutrino mass show a higher amplitude for the galaxy group clustering than those with lower values. This effect is greatest in bins with higher halo mass.

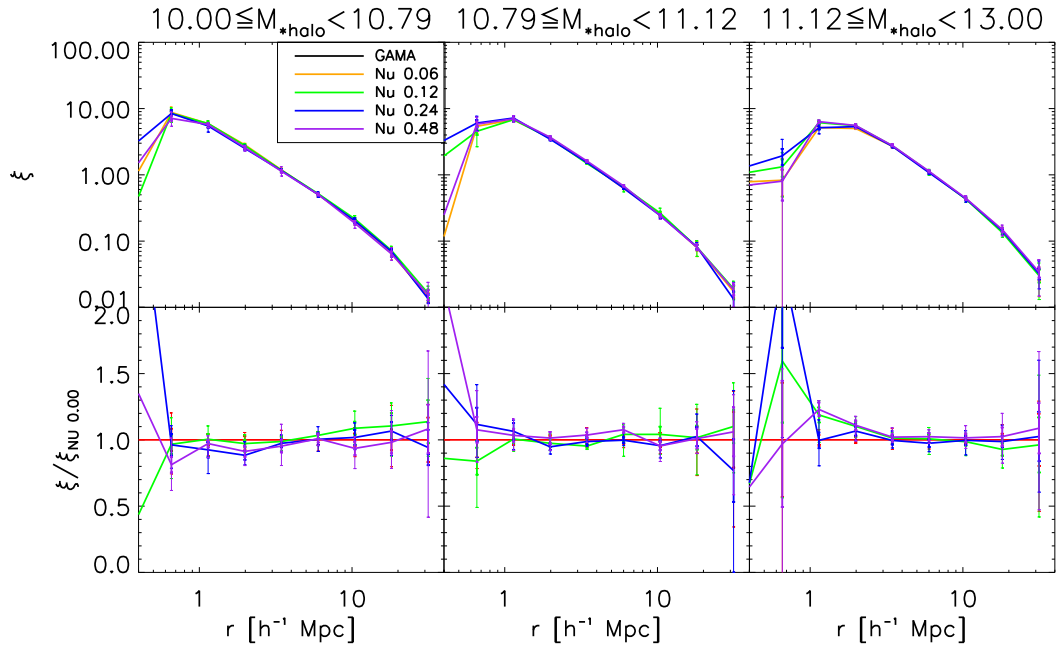


Figure C.4: As Figure 3.6, but for the *Planck* cosmology. *Top*: redshift-space 2-point autocorrelation functions for BAHAMAS haloes in equally populated bins of  $M_{*halo}$ , the 'true' stellar mass contained within  $M_{200,crit}$  in the *Planck* cosmology. Halo samples were identified by means of an on-the-fly FoF algorithm run on the BAHAMAS simulation particles. As above, thick error bars display the standard error on the mean while thin error bars show the 60th percentile of the cosmic variance. *Bottom*: The autocorrelation function in each case normalised to the massless neutrino case. BAHAMAS runs with higher values for the summed neutrino mass show a higher amplitude for the galaxy group clustering than those with lower values. This effect is greatest in bins with higher stellar mass.

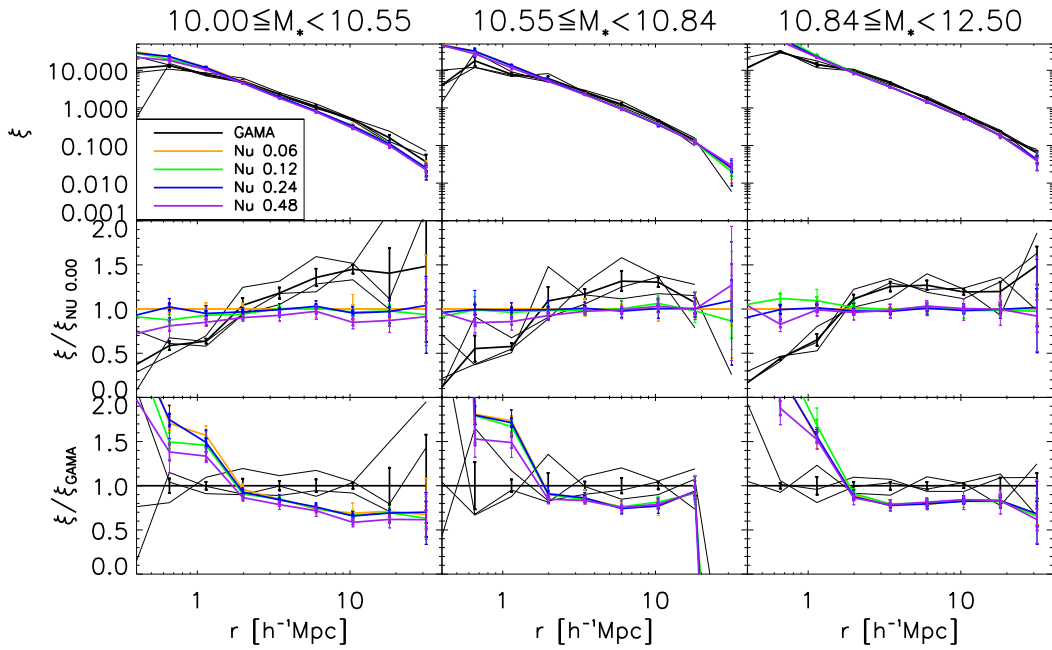


Figure C.5: *Top*: Redshift-space 2-point GGC autocorrelation as a function of the inter-group separation for GAMA (black curve) and BAHAMAS (coloured curves) in equally populated bins of integrated stellar mass. This is the equivalent of Figure 3.7, but in the context of the *Planck* cosmology. In contrast to Figure C.1, the redshift values used in the construction of these results for the simulated data do not include the contribution of the peculiar motions of galaxies and GGCs, i.e. only the Hubble redshift is considered. For the BAHAMAS curves, thick error bars display the standard error on the mean and thin error bars show the 60th percentile of the cosmic variance. In the GAMA case, error bars show the standard error on the mean. *Middle*: The ratio of the autocorrelation function in each case to the BAHAMAS massless neutrino (“nu 0.00”) case. *Bottom*: The ratio of the autocorrelation function in each case to the GAMA case. Since the peculiar motions cannot be excluded in the GAMA data, the agreement between GAMA and BAHAMAS is somewhat worsened in comparison to Figure 3.1. The exclusion of peculiar motions does not improve the sensitivity of this diagnostic to the neutrino mass.

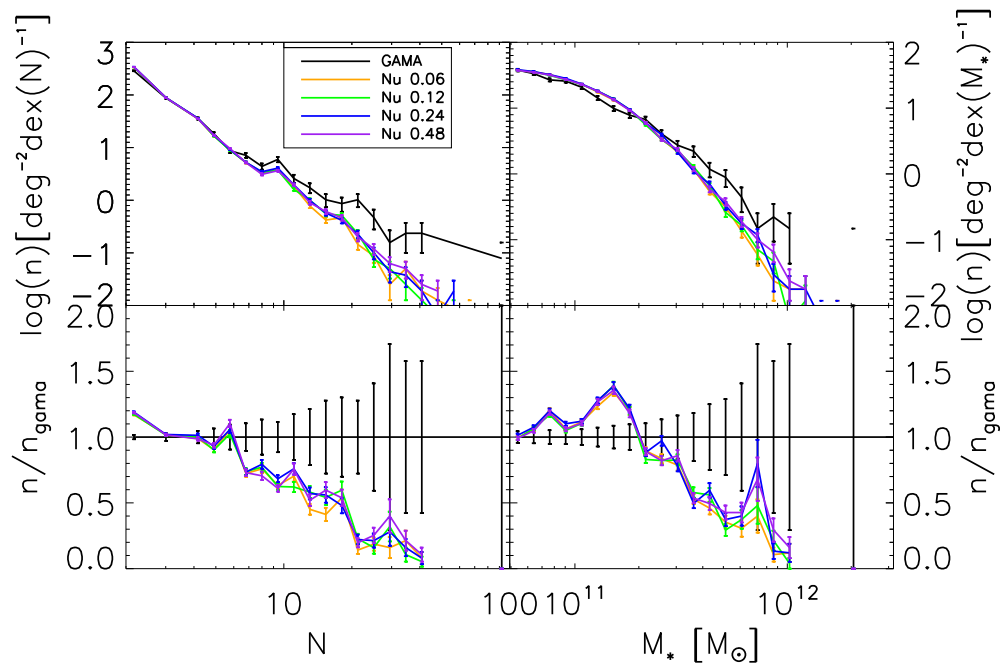


Figure C.6: The multiplicity and stellar mass functions of GAMA and BAHAMAS galaxy group samples identified using a FoF algorithm with a fixed value for the linking length. This Figure is the equivalent of Figure 3.8 in the context of a *Planck* cosmology. *Top Left*: the multiplicity functions of the GAMA fields and BAHAMAS runs. The black curve shows the stacked function for the G09, G12 and G15 GAMA fields. Coloured lines show the functions for the various BAHAMAS neutrino mass cases, stacked over all cones and cuts. Error bars are the poisson error on the count in each integrated stellar mass bin. *Bottom Left*: the ratio of the multiplicity function in each BAHAMAS case to the GAMA result. *Top Right*: the integrated stellar mass functions of the GAMA fields and BAHAMAS runs. The black curve shows the stacked function for the G09, G12 and G15 GAMA fields. Coloured lines show the functions for the various BAHAMAS neutrino mass cases, stacked over all cones and cuts. Error bars are the poisson error on the count in each integrated stellar mass bin. *Bottom Right*: the ratio of the stellar mass function in each BAHAMAS case to the GAMA result.

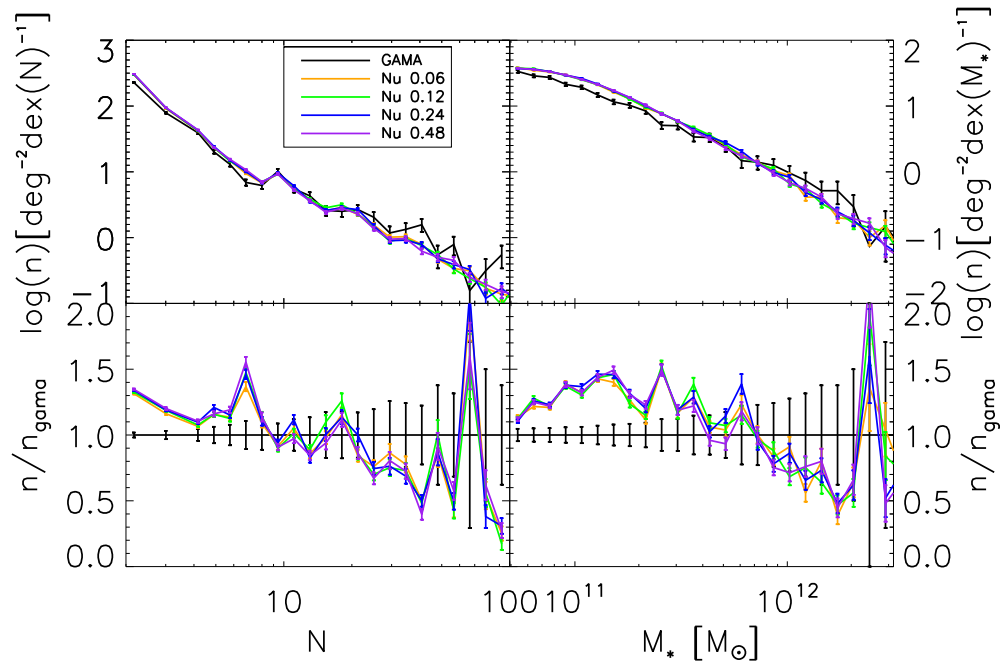


Figure C.7: The multiplicity and stellar mass functions of GAMA and BAHAMAS galaxy group samples in the context of a *Planck* cosmology. In contrast to figure C.6, galaxy group samples in this case are identified by means of a FoF algorithm with a *mass dependent* value for the linking length. This plot is the *Planck* equivalent of Figure 3.9. *Top Left:* the multiplicity functions of the GAMA fields and BAHAMAS runs. The black curve shows the stacked function for the G09, G12 and G15 GAMA fields. Coloured lines show the functions for the various BAHAMAS neutrino mass cases, stacked over all cones and cuts. Error bars are the poisson error on the count in each integrated stellar mass bin. *Bottom Left:* the ratio of the multiplicity function in each BAHAMAS case to the GAMA result. *Top Right:* the integrated stellar mass functions of the GAMA fields and BAHAMAS runs. The black curve shows the stacked function for the G09, G12 and G15 GAMA fields. Coloured lines show the functions for the various BAHAMAS neutrino mass cases, stacked over all cones and cuts. Error bars are the poisson error on the count in each integrated stellar mass bin. *Bottom Right:* the ratio of the stellar mass function in each BAHAMAS case to the GAMA result.

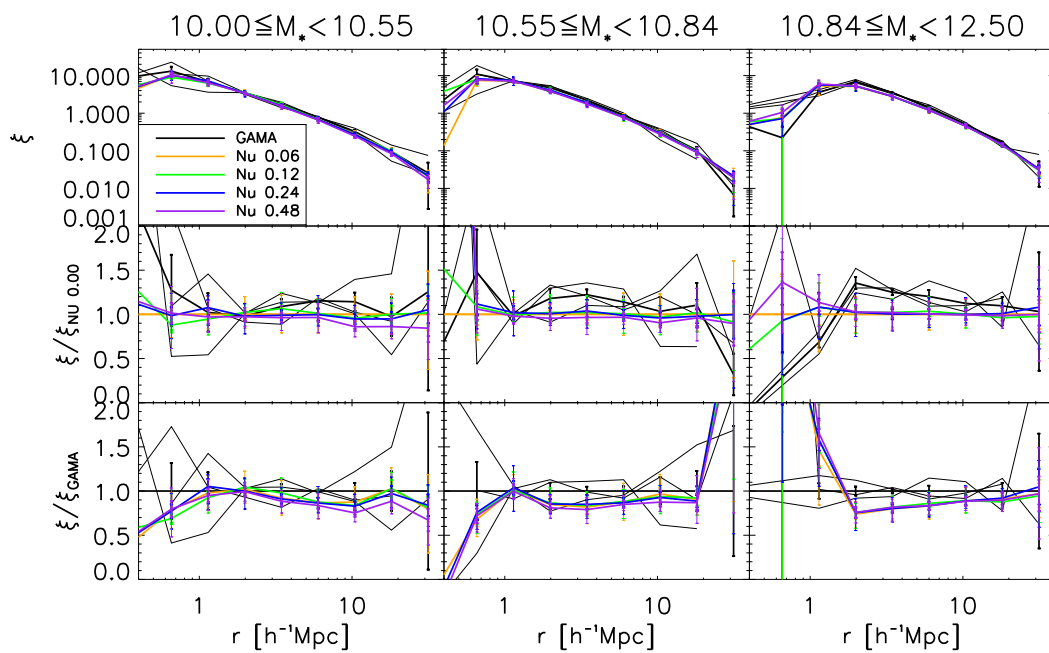


Figure C.8: The equivalent of Figure 3.10 *Top*: The redshift-space 2-point galaxy group autocorrelation as a function of the inter-group separation for GAMA (black curve) and BAHAMAS (coloured curves) in equally populated bins of integrated stellar mass for a *Planck* cosmology. In contrast to figure C.1, groups have been identified by means of a FoF algorithm with a *mass dependent* linking length as described in section 3.3.2. For the BAHAMAS curves, thick error bars display the standard error on the mean and thin error bars show the 60th percentile of the cosmic variance. In the GAMA case, error bars show the standard error on the mean. *Middle*: The ratio of the autocorrelation function in each case to the BAHAMAS massless neutrino (“nu 0.00”) case. *Bottom*: The ratio of the autocorrelation function in each case to the GAMA case.

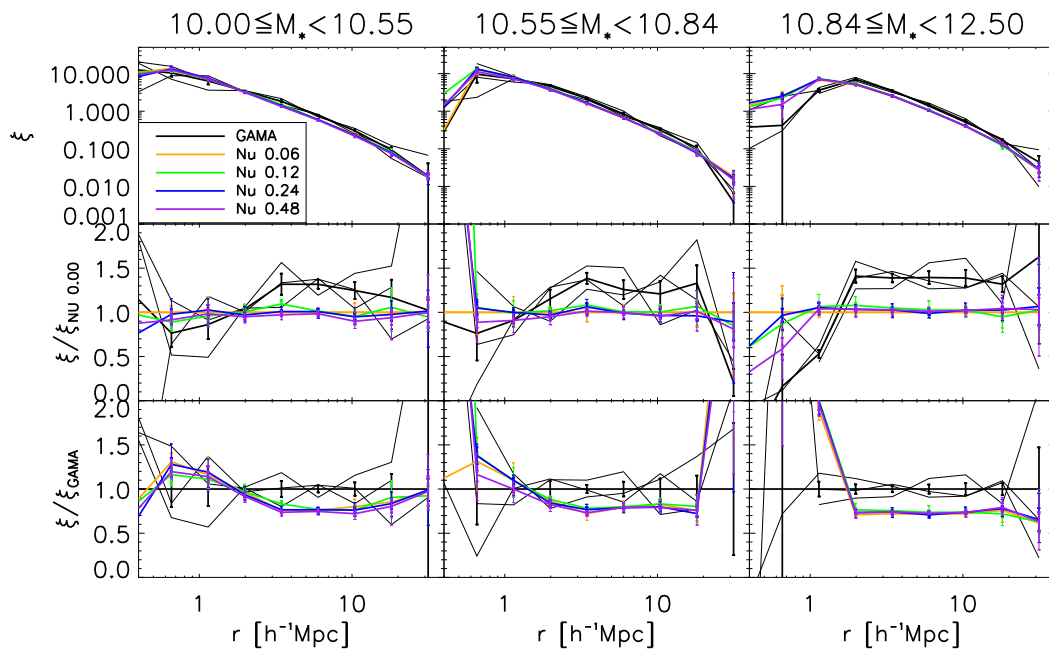


Figure C.9: As Figure 3.11, but in the context of a *Planck* rather than WMAP-9 cosmology. *Top*: Redshift-space 2-point GGC autocorrelation as a function of the inter-group separation for GAMA (black curve) and BAHAMAS (coloured curves) in equally populated bins of integrated stellar mass. In contrast to Figure C.5, GGCs have been identified by means of a FoF algorithm using a *mass-dependent* linking length. For the BAHAMAS curves, thick error bars display the standard error on the mean and thin error bars show the 60th percentile of the cosmic variance. In the GAMA case, error bars show the standard error on the mean. *Middle*: The ratio of the autocorrelation function in each case to the BAHAMAS massless neutrino (“nu 0.00”) case. *Bottom*: The ratio of the autocorrelation function in each case to the GAMA case.

# Bibliography

Aarseth, S. J.

1963. Dynamical evolution of clusters of galaxies, I. *MNRAS*, 126:223.

Ali-Haïmoud, Y. and S. Bird

2013. An efficient implementation of massive neutrinos in non-linear structure formation simulations. *MNRAS*, 428:3375–3389.

Allen, S. W., A. E. Evrard, and A. B. Mantz

2011. Cosmological Parameters from Observations of Galaxy Clusters. *ARA&A*, 49:409–470.

Andernach, H. and F. Zwicky

2017. English and Spanish Translation of Zwicky’s (1933) The Redshift of Extragalactic Nebulae. *ArXiv e-prints*.

Bagla, J. S. and S. Ray

2005. Comments on the size of the simulation box in cosmological N-body simulations. *MNRAS*, 358:1076–1082.

Baldry, I. K., J. Liske, M. J. I. Brown, A. S. G. Robotham, S. P. Driver, L. Dunne, M. Alpaslan, S. Brough, M. E. Cluver, E. Eardley, D. J. Farrow, C. Heymans, H. Hildebrandt, A. M. Hopkins, L. S. Kelvin, J. Loveday, A. J. Moffett, P. Norberg, M. S. Owers, E. N. Taylor, A. H. Wright, S. P. Bamford, J. Bland-Hawthorn, N. Bourne, M. N. Bremer, M. Colless, C. J. Conselice, S. M. Croom, L. J. M. Davies, C. Foster, M. W. Grootes, B. W. Holwerda, D. H. Jones, P. R. Kafle, K. Kuijken, M. A. Lara-Lopez, Á. R. López-Sánchez, M. J. Meyer, S. Phillipps, W. J. Suther-

- land, E. van Kampen, and S. M. Wilkins  
2018. Galaxy And Mass Assembly: the G02 field, Herschel-ATLAS target selection and data release 3. *MNRAS*, 474:3875–3888.
- Balogh, M. L., F. R. Pearce, R. G. Bower, and S. T. Kay  
2001. Revisiting the cosmic cooling crisis. *MNRAS*, 326:1228–1234.
- Bardeen, J. M., J. R. Bond, N. Kaiser, and A. S. Szalay  
1986. The statistics of peaks of Gaussian random fields. *ApJ*, 304:15–61.
- Bartelmann, M.  
2010. The dark universe. *Rev. Mod. Phys.*, 82:331–382.
- Battye, R. A. and A. Moss  
2014. Evidence for Massive Neutrinos from Cosmic Microwave Background and Lensing Observations. *Physical Review Letters*, 112(5):051303.
- Benson, A. J., R. G. Bower, C. S. Frenk, C. G. Lacey, C. M. Baugh, and S. Cole  
2003. What Shapes the Luminosity Function of Galaxies? *ApJ*, 599:38–49.
- Bird, S., M. Viel, and M. G. Haehnelt  
2012. Massive neutrinos and the non-linear matter power spectrum. *MNRAS*, 420:2551–2561.
- Bond, J. R., J. Centrella, A. S. Szalay, and J. R. Wilson  
1984. Dark matter and shocked pancakes. In *NATO Advanced Science Institutes (ASI) Series C*, J. Audouze and J. Tran Thanh Van, eds., volume 117 of *NATO Advanced Science Institutes (ASI) Series C*, Pp. 87–99.
- Bond, J. R. and G. Efstathiou  
1984. Cosmic background radiation anisotropies in universes dominated by non-baryonic dark matter. *ApJL*, 285:L45–L48.
- Bond, J. R., G. Efstathiou, and J. Silk  
1980. Massive neutrinos and the large-scale structure of the universe. *Physical Review Letters*, 45:1980–1984.

Booth, C. M. and J. Schaye

2009. Cosmological simulations of the growth of supermassive black holes and feedback from active galactic nuclei: method and tests. *MNRAS*, 398:53–74.

Borgani, S., K. Dolag, G. Murante, L.-M. Cheng, V. Springel, A. Diaferio, L. Moscardini, G. Tormen, L. Tornatore, and P. Tozzi

2006. Hot and cooled baryons in smoothed particle hydrodynamic simulations of galaxy clusters: physics and numerics. *MNRAS*, 367:1641–1654.

Borgani, S., A. Finoguenov, S. T. Kay, T. J. Ponman, V. Springel, P. Tozzi, and G. M. Voit

2005. Entropy amplification from energy feedback in simulated galaxy groups and clusters. *MNRAS*, 361:233–243.

Borgani, S. and A. Kravtsov

2011. Cosmological Simulations of Galaxy Clusters. *Advanced Science Letters*, 4:204–227.

Borgani, S., G. Murante, V. Springel, A. Diaferio, K. Dolag, L. Moscardini, G. Tormen, L. Tornatore, and P. Tozzi

2004. X-ray properties of galaxy clusters and groups from a cosmological hydrodynamical simulation. *MNRAS*, 348:1078–1096.

Bower, R. G., A. J. Benson, R. Malbon, J. C. Helly, C. S. Frenk, C. M. Baugh, S. Cole, and C. G. Lacey

2006. Breaking the hierarchy of galaxy formation. *MNRAS*, 370:645–655.

Brandbyge, J. and S. Hannestad

2009. Grid based linear neutrino perturbations in cosmological N-body simulations. *JCAP*, 5:2–+.

Brandbyge, J., S. Hannestad, T. Haugbølle, and B. Thomsen

2008. The effect of thermal neutrino motion on the non-linear cosmological matter power spectrum. *JCAP*, 8:20–+.

Bryan, G. L.

2000. Explaining the entropy excess in clusters and groups of galaxies without additional heating. *The Astrophysical Journal Letters*, 544(1):L1.

Bullock, J. S., T. S. Kolatt, Y. Sigad, R. S. Somerville, A. V. Kravtsov, A. A. Klypin, J. R. Primack, and A. Dekel

2001. Profiles of dark haloes: evolution, scatter and environment. *MNRAS*, 321:559–575.

Cleveland, B. T., T. Daily, R. Davis, Jr., J. R. Distel, K. Lande, C. K. Lee, P. S. Wildenhain, and J. Ullman

1998. Measurement of the Solar Electron Neutrino Flux with the Homestake Chlorine Detector. *ApJ*, 496:505–526.

Cohen, A. G., S. L. Glashow, and Z. Ligeti

2009. Disentangling neutrino oscillations. *Physics Letters B*, 678:191–196.

Collins, C. A., L. Guzzo, H. Böhringer, P. Schuecker, G. Chincarini, R. Cruddace, S. De Grandi, H. T. MacGillivray, D. M. Neumann, S. Schindler, P. Shaver, and W. Voges

2000. The ROSAT-ESO Flux-Limited X-ray (REFLEX) galaxy cluster survey - II. The spatial correlation function. *MNRAS*, 319:939–948.

Costanzi, M., F. Villaescusa-Navarro, M. Viel, J.-Q. Xia, S. Borgani, E. Castorina, and E. Sefusatti

2013. Cosmology with massive neutrinos III: the halo mass function and an application to galaxy clusters. *JCAP*, 12:012.

Cowan, Jr., C. L., F. Reines, F. B. Harrison, H. W. Kruse, and A. D. McGuire

1956. Detection of the Free Neutrino: A Confirmation. *Science*, 124:103–104.

Cowsik, R. and J. McClelland

1972. An Upper Limit on the Neutrino Rest Mass. *Physical Review Letters*, 29:669–670.

- Crain, R. A., J. Schaye, R. G. Bower, M. Furlong, M. Schaller, T. Theuns, C. Dalla Vecchia, C. S. Frenk, I. G. McCarthy, J. C. Helly, A. Jenkins, Y. M. Rosas-Guevara, S. D. M. White, and J. W. Trayford  
2015. The EAGLE simulations of galaxy formation: calibration of subgrid physics and model variations. *MNRAS*, 450:1937–1961.
- Croton, D. J.  
2013. Damn You, Little  $h$ ! (Or, Real-World Applications of the Hubble Constant Using Observed and Simulated Data). *PASA*, 30:e052.
- Cui, W., S. Borgani, and G. Murante  
2014. The effect of active galactic nuclei feedback on the halo mass function. *MNRAS*, 441:1769–1782.
- Cusworth, S. J., S. T. Kay, R. A. Battye, and P. A. Thomas  
2014. Impact of baryons on the cluster mass function and cosmological parameter determination. *MNRAS*, 439:2485–2493.
- Dalla Vecchia, C. and J. Schaye  
2008. Simulating galactic outflows with kinetic supernova feedback. *MNRAS*, 387:1431–1444.
- Danby, G., J.-M. Gaillard, K. Goulianos, L. M. Lederman, N. Mistry, M. Schwartz, and J. Steinberger  
1962. Observation of High-Energy Neutrino Reactions and the Existence of Two Kinds of Neutrinos. *Physical Review Letters*, 9:36–44.
- Davé, R., B. D. Oppenheimer, and S. Sivanandam  
2008. Enrichment and pre-heating in intragroup gas from galactic outflows. *MNRAS*, 391:110–123.
- Dav, R., N. Katz, and D. H. Weinberg  
2002. X-ray scaling relations of galaxy groups in a hydrodynamic cosmological simulation. *The Astrophysical Journal*, 579(1):23.

De Lucia, G. and J. Blaizot

2007. The hierarchical formation of the brightest cluster galaxies. *MNRAS*, 375:2–14.

Dicke, R. H., P. J. E. Peebles, P. G. Roll, and D. T. Wilkinson

1965. Cosmic Black-Body Radiation. *ApJ*, 142:414–419.

Dolag, K., S. Borgani, G. Murante, and V. Springel

2009. Substructures in hydrodynamical cluster simulations. *MNRAS*, 399:497–514.

DONUT Collaboration, K. Kodama, N. Ushida, C. Andreopoulos, N. Saoulidou, G. Tzanakos, P. Yager, B. Baller, D. Boehnlein, W. Freeman, B. Lundberg, J. Morfin, R. Rameika, J. C. Yun, J. S. Song, C. S. Yoon, S. H. Chung, P. Berghaus, M. Kubantsev, N. W. Reay, R. Sidwell, N. Stanton, S. Yoshida, S. Aoki, T. Hara, J. T. Rhee, D. Ciampa, C. Erickson, M. Graham, K. Heller, R. Rusack, R. Schwienhorst, J. Sielaff, J. Trammell, J. Wilcox, K. Hoshino, H. Jiko, M. Miyanishi, M. Komatsu, M. Nakamura, T. Nakano, K. Niwa, N. Nonaka, K. Okada, O. Sato, T. Akdogan, V. Paolone, C. Rosenfeld, A. Kulik, T. Kafka, W. Oliver, T. Patzak, and J. Schneps  
2001. Observation of tau neutrino interactions. *Physics Letters B*, 504:218–224.

Duffy, A. R., J. Schaye, S. T. Kay, and C. Dalla Vecchia

2008. Dark matter halo concentrations in the Wilkinson Microwave Anisotropy Probe year 5 cosmology. *MNRAS*, 390:L64–L68.

Duffy, A. R., J. Schaye, S. T. Kay, C. Dalla Vecchia, R. A. Battye, and C. M. Booth

2010. Impact of baryon physics on dark matter structures: a detailed simulation study of halo density profiles. *MNRAS*, 405:2161–2178.

Efstathiou, G., S. Moody, J. A. Peacock, W. J. Percival, C. Baugh, J. Bland-Hawthorn, T. Bridges, R. Cannon, S. Cole, M. Colless, C. Collins, W. Couch, G. Dalton, R. de Propris, S. P. Driver, R. S. Ellis, C. S. Frenk, K. Glazebrook, C. Jackson, O. Lahav, I. Lewis, S. Lumsden, S. Maddox, P. Norberg, B. A. Peterson, W. Sutherland, and K. Taylor

2002. Evidence for a non-zero  $\Lambda$  and a low matter density from a combined analysis

- of the 2dF Galaxy Redshift Survey and cosmic microwave background anisotropies. *MNRAS*, 330:L29–L35.
- Eifler, T., E. Krause, S. Dodelson, A. R. Zentner, A. P. Hearin, and N. Y. Gnedin  
2015. Accounting for baryonic effects in cosmic shear tomography: determining a minimal set of nuisance parameters using PCA. *MNRAS*, 454:2451–2471.
- Einstein, A.  
1915. Die Feldgleichungen der Gravitation. *Sitzungsberichte der Königlich Preussischen Akademie der Wissenschaften (Berlin)*, Seite 844-847.
- Einstein, A.  
1917. Kosmologische Betrachtungen zur allgemeinen Relativitätstheorie. *Sitzungsberichte der Königlich Preussischen Akademie der Wissenschaften (Berlin)*, Seite 142-152.
- Eisenstein, D. J. and W. Hu  
1999. Power Spectra for Cold Dark Matter and Its Variants. *ApJ*, 511:5–15.
- Eke, V. R., J. F. Navarro, and M. Steinmetz  
2001. The Power Spectrum Dependence of Dark Matter Halo Concentrations. *ApJ*, 554:114–125.
- Evrard, A. E. and J. P. Henry  
1991. Expectations for X-ray cluster observations by the ROSAT satellite. *ApJ*, 383:95–103.
- Fabian, A. C.  
2012. Observational Evidence of Active Galactic Nuclei Feedback. *ARA&A*, 50:455–489.
- Farahi, A., A. E. Evrard, I. McCarthy, D. J. Barnes, and S. T. Kay  
2018. Localized massive halo properties in BAHAMAS and MACSIS simulations: scalings, log-normality, and covariance. *MNRAS*.

Frenk, C. S., S. D. M. White, and M. Davis

1983. Nonlinear evolution of large-scale structure in the universe. *ApJ*, 271:417–430.

Friedmann, A.

1922. Über die Krümmung des Raumes. *Zeitschrift für Physik*, 10:377–386.

Fukuda, Y., T. Hayakawa, E. Ichihara, K. Inoue, K. Ishihara, H. Ishino, Y. Itow, T. Kajita, J. Kameda, S. Kasuga, K. Kobayashi, Y. Kobayashi, Y. Koshio, M. Miura, M. Nakahata, S. Nakayama, A. Okada, K. Okumura, N. Sakurai, M. Shiozawa, Y. Suzuki, Y. Takeuchi, Y. Totsuka, S. Yamada, M. Earl, A. Habig, E. Kearns, M. D. Messier, K. Scholberg, J. L. Stone, L. R. Sulak, C. W. Walter, M. Goldhaber, T. Barszczak, D. Casper, W. Gajewski, P. G. Halverson, J. Hsu, W. R. Kropp, L. R. Price, F. Reines, M. Smy, H. W. Sobel, M. R. Vagins, K. S. Ganezer, W. E. Keig, R. W. Ellsworth, S. Tasaka, J. W. Flanagan, A. Kibayashi, J. G. Learned, S. Matsuno, V. J. Stenger, D. Takemori, T. Ishii, J. Kanzaki, T. Kobayashi, S. Mine, K. Nakamura, K. Nishikawa, Y. Oyama, A. Sakai, M. Sakuda, O. Sasaki, S. Echigo, M. Kohama, A. T. Suzuki, T. J. Haines, E. Blaufuss, B. K. Kim, R. Sanford, R. Svoboda, M. L. Chen, Z. Conner, J. A. Goodman, G. W. Sullivan, J. Hill, C. K. Jung, K. Martens, C. Mauger, C. McGrew, E. Sharkey, B. Viren, C. Yanagisawa, W. Doki, K. Miyano, H. Okazawa, C. Saji, M. Takahata, Y. Nagashima, M. Takita, T. Yamaguchi, M. Yoshida, S. B. Kim, M. Etoh, K. Fujita, A. Hasegawa, T. Hasegawa, S. Hatakeyama, T. Iwamoto, M. Koga, T. Maruyama, H. Ogawa, J. Shirai, A. Suzuki, F. Tsushima, M. Koshiha, M. Nemoto, K. Nishijima, T. Futagami, Y. Hayato, Y. Kanaya, K. Kaneyuki, Y. Watanabe, D. Kielczewska, R. A. Doyle, J. S. George, A. L. Stachyra, L. L. Wai, R. J. Wilkes, and K. K. Young

1998. Evidence for Oscillation of Atmospheric Neutrinos. *Physical Review Letters*, 81:1562–1567.

Gao, L., J. F. Navarro, S. Cole, C. S. Frenk, S. D. M. White, V. Springel, A. Jenkins, and A. F. Neto

2008. The redshift dependence of the structure of massive  $\Lambda$  cold dark matter haloes. *MNRAS*, 387:536–544.

Haardt, F. and P. Madau

2001. Modelling the UV/X-ray cosmic background with CUBA. In *Clusters of Galaxies and the High Redshift Universe Observed in X-rays*, D. M. Neumann and J. T. V. Tran, eds.

Harnois-Déraps, J., L. van Waerbeke, M. Viola, and C. Heymans

2015. Baryons, neutrinos, feedback and weak gravitational lensing. *MNRAS*, 450:1212–1223.

Herschel, W.

1785. Xii. on the construction of the heavens. *Philosophical Transactions of the Royal Society of London*, 75:213–266.

Heymans, C., E. Grocutt, A. Heavens, M. Kilbinger, T. D. Kitching, F. Simpson, J. Benjamin, T. Erben, H. Hildebrandt, H. Hoekstra, Y. Mellier, L. Miller, L. Van Waerbeke, M. L. Brown, J. Coupon, L. Fu, J. Harnois-Déraps, M. J. Hudson, K. Kuijken, B. Rowe, T. Schrabback, E. Semboloni, S. Vafaei, and M. Velander

2013. CFHTLenS tomographic weak lensing cosmological parameter constraints: Mitigating the impact of intrinsic galaxy alignments. *MNRAS*, 432:2433–2453.

Hildebrandt, H., M. Viola, C. Heymans, S. Joudaki, K. Kuijken, C. Blake, T. Erben, B. Joachimi, D. Klaes, L. Miller, C. B. Morrison, R. Nakajima, G. Verdoes Kleijn, A. Amon, A. Choi, G. Covone, J. T. A. de Jong, A. Dvornik, I. Fenech Conti, A. Grado, J. Harnois-Déraps, R. Herbonnet, H. Hoekstra, F. Köhlinger, J. McFarland, A. Mead, J. Merten, N. Napolitano, J. A. Peacock, M. Radovich, P. Schneider, P. Simon, E. A. Valentijn, J. L. van den Busch, E. van Uitert, and L. Van Waerbeke

2017. KiDS-450: cosmological parameter constraints from tomographic weak gravitational lensing. *MNRAS*, 465:1454–1498.

Hinshaw, G., D. Larson, E. Komatsu, D. N. Spergel, C. L. Bennett, J. Dunkley, M. R. Nolta, M. Halpern, R. S. Hill, N. Odegard, L. Page, K. M. Smith, J. L. Weiland, B. Gold, N. Jarosik, A. Kogut, M. Limon, S. S. Meyer, G. S. Tucker, E. Wollack,

and E. L. Wright

2013. Nine-year Wilkinson Microwave Anisotropy Probe (WMAP) Observations: Cosmological Parameter Results. *ApJS*, 208:19.

Holmberg, E.

1941. On the Clustering Tendencies among the Nebulae. II. a Study of Encounters Between Laboratory Models of Stellar Systems by a New Integration Procedure. *ApJ*, 94:385.

Hubble, E. P.

1926. Extragalactic nebulae. *ApJ*, 64.

Jakobs, A., M. Viola, I. McCarthy, L. van Waerbeke, H. Hoekstra, A. Robotham, G. Hinshaw, A. Hojjati, H. Tanimura, T. Tröster, I. Baldry, C. Heymans, H. Hildebrandt, K. Kuijken, P. Norberg, J. Schaye, C. Sifon, E. van Uitert, E. Valentijn, G. Verdoes Kleijn, and L. Wang

2017. Multi-wavelength scaling relations in galaxy groups: a detailed comparison of GAMA and KiDS observations to BAHAMAS simulations. *ArXiv e-prints*.

Jenkins, A., C. S. Frenk, S. D. M. White, J. M. Colberg, S. Cole, A. E. Evrard, H. M. P. Couchman, and N. Yoshida

2001. The mass function of dark matter haloes. *MNRAS*, 321:372–384.

Kaiser, N.

1986. Evolution and clustering of rich clusters. *MNRAS*, 222:323–345.

Kaiser, N.

1991. Evolution of clusters of galaxies. *ApJ*, 383:104–111.

Kay, S. T., P. A. Thomas, A. Jenkins, and F. R. Pearce

2004. Cosmological simulations of the intracluster medium. *MNRAS*, 355:1091–1104.

Kerscher, M., I. Szapudi, and A. S. Szalay

2000. A Comparison of Estimators for the Two-Point Correlation Function. *ApJL*, 535:L13–L16.

King, A.

2003. Black Holes, Galaxy Formation, and the  $M_{BH}-\sigma$  Relation. *ApJL*, 596:L27–L29.

Kolb, E. W. and M. S. Turner

1990. *The early universe*.

Komatsu, E., K. M. Smith, J. Dunkley, C. L. Bennett, B. Gold, G. Hinshaw, N. Jarosik, D. Larson, M. R.olta, L. Page, D. N. Spergel, M. Halpern, et al.

2011. Seven-year Wilkinson Microwave Anisotropy Probe (WMAP) Observations: Cosmological Interpretation. *ApJS*, 192:18.

Kravtsov, A. V. and S. Borgani

2012. Formation of Galaxy Clusters. *ARA&A*, 50:353–409.

Kuijken, K., C. Heymans, H. Hildebrandt, R. Nakajima, T. Erben, J. T. A. de Jong, M. Viola, A. Choi, H. Hoekstra, L. Miller, E. van Uitert, A. Amon, C. Blake, M. Brouwer, A. Buddendiek, I. F. Conti, M. Eriksen, A. Grado, J. Harnois-Déraps, E. Helmich, R. Herbonnet, N. Irisarri, T. Kitching, D. Klaes, F. La Barbera, N. Napolitano, M. Radovich, P. Schneider, C. Sifón, G. Sikkema, P. Simon, A. Tudorica, E. Valentijn, G. Verdoes Kleijn, and L. van Waerbeke

2015. Gravitational lensing analysis of the Kilo-Degree Survey. *MNRAS*, 454:3500–3532.

Lachieze-Rey, M.

1995. *Cosmology - A First Course*. Cambridge University Press.

Landy, S. D. and A. S. Szalay

1993. Bias and variance of angular correlation functions. *ApJ*, 412:64–71.

Larson, R. B.

1969. A model for the formation of a spherical galaxy. *MNRAS*, 145:405.

Larson, R. B.

1974. Dynamical models for the formation and evolution of spherical galaxies. *MNRAS*, 166:585–616.

Le Brun, A. M. C., I. G. McCarthy, J. Schaye, and T. J. Ponman

2014. Towards a realistic population of simulated galaxy groups and clusters. *MNRAS*, 441:1270–1290.

Lemaître, G.

1927. Un Univers homogène de masse constante et de rayon croissant rendant compte de la vitesse radiale des nébuleuses extra-galactiques. *Annales de la Société Scientifique de Bruxelles*, 47:49–59.

Lemaître, G.

1931. Expansion of the universe, A homogeneous universe of constant mass and increasing radius accounting for the radial velocity of extra-galactic nebulae. *MNRAS*, 91:483–490.

Lesgourgues, J. and S. Pastor

2006. Massive neutrinos and cosmology. *Phys. Rep.*, 429:307–379.

Lesgourgues, J. and S. Pastor

2012. Neutrino mass from Cosmology. *ArXiv e-prints*.

Lesgourgues, J. and S. Pastor

2014. Neutrino cosmology and planck. *New Journal of Physics*, 16(6):065002.

Lewis, A., A. Challinor, and A. Lasenby

2000. Efficient Computation of Cosmic Microwave Background Anisotropies in Closed Friedmann-Robertson-Walker Models. *ApJ*, 538:473–476.

Limber, D. N.

1954. The Analysis of Counts of the Extragalactic Nebulae in Terms of a Fluctuating Density Field. II. *ApJ*, 119:655.

Lin, W. P., Y. P. Jing, S. Mao, L. Gao, and I. G. McCarthy

2006. The Influence of Baryons on the Mass Distribution of Dark Matter Halos. *ApJ*, 651:636–642.

- Ludlow, A. D., J. F. Navarro, R. E. Angulo, M. Boylan-Kolchin, V. Springel, C. Frenk, and S. D. M. White  
2014. The mass-concentration-redshift relation of cold dark matter haloes. *MNRAS*, 441:378–388.
- Lynds, R.  
1971. The Absorption-Line Spectrum of 4c 05.34. *ApJ*, 164:L73.
- Lynds, R. and V. Petrosian  
1986. Giant Luminous Arcs in Galaxy Clusters. In *Bulletin of the American Astronomical Society*, volume 18 of *BAAS*, P. 1014.
- Ma, C.-P.  
2000. Neutrinos and Dark Matter. In *Neutrinos in Physics and Astrophysics*, P. Langacker, ed., Pp. 504–523.
- Ma, C.-P. and E. Bertschinger  
1995. Cosmological Perturbation Theory in the Synchronous and Conformal Newtonian Gauges. *ApJ*, 455:7.
- MacCrann, N., J. Zuntz, S. Bridle, B. Jain, and M. R. Becker  
2015. Cosmic discordance: are Planck CMB and CFHTLenS weak lensing measurements out of tune? *MNRAS*, 451:2877–2888.
- Mandelbaum, R.  
2017. Weak lensing for precision cosmology. *ArXiv e-prints*.
- Mandelbaum, R., U. Seljak, and C. M. Hirata  
2008. A halo mass–concentration relation from weak lensing. *JCAP*, 8:006.
- Mantz, A., S. W. Allen, D. Rapetti, and H. Ebeling  
2010. The observed growth of massive galaxy clusters - I. Statistical methods and cosmological constraints. *MNRAS*, 406:1759–1772.
- McCarthy, I. G., M. L. Balogh, A. Babul, G. B. Poole, and D. J. Horner  
2004. Models of the intracluster medium with heating and cooling: Explaining

- the global and structural x-ray properties of clusters. *The Astrophysical Journal*, 613(2):811.
- McCarthy, I. G., S. Bird, J. Schaye, J. Harnois-Deraps, A. S. Font, and L. van Waerbeke  
2018. The BAHAMAS project: the CMB-large-scale structure tension and the roles of massive neutrinos and galaxy formation. *MNRAS*.
- McCarthy, I. G., A. M. C. Le Brun, J. Schaye, and G. P. Holder  
2014. The thermal Sunyaev-Zel'dovich effect power spectrum in light of Planck. *MNRAS*, 440:3645–3657.
- McCarthy, I. G., J. Schaye, S. Bird, and A. M. C. Le Brun  
2017. The BAHAMAS project: calibrated hydrodynamical simulations for large-scale structure cosmology. *MNRAS*, 465:2936–2965.
- McCarthy, I. G., J. Schaye, R. G. Bower, T. J. Ponman, C. M. Booth, C. Dalla Vecchia, and V. Springel  
2011. Gas expulsion by quasar-driven winds as a solution to the overcooling problem in galaxy groups and clusters. *MNRAS*, 412:1965–1984.
- McCarthy, I. G., J. Schaye, T. J. Ponman, R. G. Bower, C. M. Booth, C. Dalla Vecchia, R. A. Crain, V. Springel, T. Theuns, and R. P. C. Wiersma  
2010. The case for AGN feedback in galaxy groups. *MNRAS*, 406:822–839.
- McNamara, B. R. and P. E. J. Nulsen  
2007. Heating Hot Atmospheres with Active Galactic Nuclei. *ARA&A*, 45:117–175.
- Mead, A. J., C. Heymans, L. Lombriser, J. A. Peacock, O. I. Steele, and H. A. Winther  
2016. Accurate halo-model matter power spectra with dark energy, massive neutrinos and modified gravitational forces. *MNRAS*, 459:1468–1488.
- Mead, A. J., J. A. Peacock, C. Heymans, S. Joudaki, and A. F. Heavens  
2015. An accurate halo model for fitting non-linear cosmological power spectra and baryonic feedback models. *MNRAS*, 454:1958–1975.

Messier, C.

1784. *Catalogue des nebuleuses et des amas d'étoiles.*

Metzler, C. A. and A. E. Evrard

1994. A simulation of the intracluster medium with feedback from cluster galaxies. *ApJ*, 437:564–583.

Mummery, B. O., I. G. McCarthy, S. Bird, and J. Schaye

2017. The separate and combined effects of baryon physics and neutrino free streaming on large-scale structure. *MNRAS*, 471:227–242.

Navarro, J. F., C. S. Frenk, and S. D. M. White

1996. The Structure of Cold Dark Matter Halos. *ApJ*, 462:563.

Neto, A. F., L. Gao, P. Bett, S. Cole, J. F. Navarro, C. S. Frenk, S. D. M. White, V. Springel, and A. Jenkins

2007. The statistics of  $\Lambda$  CDM halo concentrations. *MNRAS*, 381:1450–1462.

Newman, A. B., T. Treu, R. S. Ellis, D. J. Sand, C. Nipoti, J. Richard, and E. Jullo

2013. The Density Profiles of Massive, Relaxed Galaxy Clusters. I. The Total Density Over Three Decades in Radius. *ApJ*, 765:24.

Oort, J. H.

1981. Superclusters and Lyman-Alpha Absorption Lines in Quasars. *A&A*, 94:359.

Pauli, W.

1994. *Writings on Physics and Philosophy.* Springer, Berlin, Heidelberg.

Peacock, J. A.

1998. *Cosmological Physics.* Cambridge University Press.

Pearce, F. R., A. Jenkins, C. S. Frenk, J. M. Colberg, S. D. M. White, P. A. Thomas, H. M. P. Couchman, J. A. Peacock, G. Efstathiou, and . V. Consortium)

1999. A Simulation of Galaxy Formation and Clustering. *ApJL*, 521:L99–L102.

Peebles, P. J. E.

1980. *The large-scale structure of the universe.*

Peebles, P. J. E.

1993. *Principles of Physical Cosmology*.

Penzias, A. A. and R. W. Wilson

1965. A Measurement of Excess Antenna Temperature at 4080 Mc/s. *ApJ*, 142:419–421.

Perl, M. L., G. S. Abrams, A. M. Boyarski, M. Breidenbach, D. D. Briggs, F. Bulos, W. Chinowsky, J. T. Dakin, G. J. Feldman, C. E. Friedberg, D. Fryberger, G. Goldhaber, G. Hanson, F. B. Heile, B. Jean-Marie, and et al.

1975. Evidence for anomalous lepton production in  $e^+e^-$  annihilation. *Physical Review Letters*, 35:1489–1492.

Perlmutter, S., G. Aldering, G. Goldhaber, R. A. Knop, P. Nugent, P. G. Castro, S. Deustua, S. Fabbro, A. Goobar, D. E. Groom, I. M. Hook, A. G. Kim, M. Y. Kim, J. C. Lee, N. J. Nunes, R. Pain, C. R. Pennypacker, R. Quimby, C. Lidman, R. S. Ellis, M. Irwin, R. G. McMahon, P. Ruiz-Lapuente, N. Walton, B. Schaefer, B. J. Boyle, A. V. Filippenko, T. Matheson, A. S. Fruchter, N. Panagia, H. J. M. Newberg, W. J. Couch, and T. S. C. Project

1999. Measurements of  $\Omega$  and  $\Lambda$  from 42 High-Redshift Supernovae. *ApJ*, 517:565–586.

Planck Collaboration, P. A. R. Ade, N. Aghanim, C. Armitage-Caplan, M. Arnaud, M. Ashdown, F. Atrio-Barandela, J. Aumont, C. Baccigalupi, A. J. Banday, and et al.

2014. Planck 2013 results. XX. Cosmology from Sunyaev-Zeldovich cluster counts. *A&A*, 571:A20.

Planck Collaboration, P. A. R. Ade, N. Aghanim, M. Arnaud, M. Ashdown, J. Aumont, C. Baccigalupi, A. J. Banday, R. B. Barreiro, J. G. Bartlett, and et al.

2016a. Planck 2015 results. XIII. Cosmological parameters. *A&A*, 594:A13.

Planck Collaboration, P. A. R. Ade, N. Aghanim, M. Arnaud, M. Ashdown, J. Aumont,

- C. Baccigalupi, A. J. Banday, R. B. Barreiro, J. G. Bartlett, and et al.  
2016b. Planck 2015 results. XXIV. Cosmology from Sunyaev-Zeldovich cluster counts. *ArXiv e-prints*, 594:A17.
- Ponman, T. J., D. B. Cannon, and J. F. Navarro  
1999. The thermal imprint of galaxy formation on X-ray clusters. *Nature*, 397:135–137.
- Press, W. H. and P. Schechter  
1974. Formation of Galaxies and Clusters of Galaxies by Self-Similar Gravitational Condensation. *ApJ*, 187:425–438.
- Qian, X. and P. Vogel  
2015. Neutrino mass hierarchy. *Progress in Particle and Nuclear Physics*, 83:1–30.
- Reid, B. A., W. J. Percival, D. J. Eisenstein, L. Verde, D. N. Spergel, R. A. Skibba, N. A. Bahcall, T. Budavari, J. A. Frieman, M. Fukugita, J. R. Gott, J. E. Gunn, Ž. Ivezić, G. R. Knapp, R. G. Kron, R. H. Lupton, T. A. McKay, A. Meiksin, R. C. Nichol, A. C. Pope, D. J. Schlegel, D. P. Schneider, C. Stoughton, M. A. Strauss, A. S. Szalay, M. Tegmark, M. S. Vogeley, D. H. Weinberg, D. G. York, and I. Zehavi  
2010a. Cosmological constraints from the clustering of the Sloan Digital Sky Survey DR7 luminous red galaxies. *MNRAS*, 404:60–85.
- Reid, B. A., L. Verde, R. Jimenez, and O. Mena  
2010b. Robust neutrino constraints by combining low redshift observations with the CMB. *JCAP*, 1:003.
- Riemer-Sørensen, S., C. Blake, D. Parkinson, T. M. Davis, S. Brough, M. Colless, C. Contreras, W. Couch, S. Croom, D. Croton, M. J. Drinkwater, K. Forster, D. Gilbank, M. Gladders, K. Glazebrook, B. Jelliffe, R. J. Jurek, I.-h. Li, B. Madore, D. C. Martin, K. Pimbblet, G. B. Poole, M. Pracy, R. Sharp, E. Wisnioski, D. Woods, T. K. Wyder, and H. K. C. Yee  
2012. WiggleZ Dark Energy Survey: Cosmological neutrino mass constraint from blue high-redshift galaxies. *Phys. Rev. D*, 85(8):081101.

- Riess, A. G., A. V. Filippenko, P. Challis, A. Clocchiatti, A. Diercks, P. M. Garnavich, R. L. Gilliland, C. J. Hogan, S. Jha, R. P. Kirshner, B. Leibundgut, M. M. Phillips, D. Reiss, B. P. Schmidt, R. A. Schommer, R. C. Smith, J. Spyromilio, C. Stubbs, N. B. Suntzeff, and J. Tonry  
1998. Observational Evidence from Supernovae for an Accelerating Universe and a Cosmological Constant. *AJ*, 116:1009–1038.
- Robotham, A. S. G., P. Norberg, S. P. Driver, I. K. Baldry, S. P. Bamford, A. M. Hopkins, J. Liske, J. Loveday, A. Merson, J. A. Peacock, S. Brough, E. Cameron, C. J. Conselice, S. M. Croom, C. S. Frenk, M. Gunawardhana, D. T. Hill, D. H. Jones, L. S. Kelvin, K. Kuijken, R. C. Nichol, H. R. Parkinson, K. A. Pimblet, S. Phillipps, C. C. Popescu, M. Prescott, R. G. Sharp, W. J. Sutherland, E. N. Taylor, D. Thomas, R. J. Tuffs, E. van Kampen, and D. Wijesinghe  
2011. Galaxy and Mass Assembly (GAMA): the GAMA galaxy group catalogue (G<sup>3</sup>Cv1). *MNRAS*, 416:2640–2668.
- Rodionov, S. A. and N. Y. Sotnikova  
2005. Optimal Choice of the Softening Length and Time Step in N-body Simulations. *Astronomy Reports*, 49:470–476.
- Rubin, V. C.  
1954. Fluctuations in the Space Distribution of the Galaxies. *Proceedings of the National Academy of Sciences of the United States of America*, 40:541–549.
- Sawala, T., C. S. Frenk, R. A. Crain, A. Jenkins, J. Schaye, T. Theuns, and J. Zavala  
2013. The abundance of (not just) dark matter haloes. *MNRAS*, 431:1366–1382.
- Schaller, M., C. S. Frenk, R. G. Bower, T. Theuns, A. Jenkins, J. Schaye, R. A. Crain, M. Furlong, C. Dalla Vecchia, and I. G. McCarthy  
2015. Baryon effects on the internal structure of  $\Lambda$ CDM haloes in the EAGLE simulations. *MNRAS*, 451:1247–1267.
- Schaye, J., R. A. Crain, R. G. Bower, M. Furlong, M. Schaller, T. Theuns, C. Dalla Vecchia, C. S. Frenk, I. G. McCarthy, J. C. Helly, A. Jenkins, Y. M. Rosas-Guevara,

- S. D. M. White, M. Baes, C. M. Booth, P. Camps, J. F. Navarro, Y. Qu, A. Rahmati, T. Sawala, P. A. Thomas, and J. Trayford  
2015. The EAGLE project: simulating the evolution and assembly of galaxies and their environments. *MNRAS*, 446:521–554.
- Schaye, J. and C. Dalla Vecchia  
2008a. On the relation between the Schmidt and Kennicutt-Schmidt star formation laws and its implications for numerical simulations. *MNRAS*, 383:1210–1222.
- Schaye, J. and C. Dalla Vecchia  
2008b. On the relation between the Schmidt and Kennicutt-Schmidt star formation laws and its implications for numerical simulations. *MNRAS*, 383:1210–1222.
- Schaye, J., C. Dalla Vecchia, C. M. Booth, R. P. C. Wiersma, T. Theuns, M. R. Haas, S. Bertone, A. R. Duffy, I. G. McCarthy, and F. van de Voort  
2010. The physics driving the cosmic star formation history. *MNRAS*, 402:1536–1560.
- Schmidt, M.  
1957. The distribution of mass in M 31. *Bull. Astron. Inst. Netherlands*, 14:17.
- Schneider, A. and R. Teyssier  
2015. A new method to quantify the effects of baryons on the matter power spectrum. *JCAP*, 12:049.
- Semboloni, E., H. Hoekstra, J. Schaye, M. P. van Daalen, and I. G. McCarthy  
2011. Quantifying the effect of baryon physics on weak lensing tomography. *MNRAS*, 417:2020–2035.
- Shapiro, P. R., C. Struck-Marcell, and A. L. Melott  
1983. Pancakes and the formation of galaxies in a neutrino-dominated universe. *ApJ*, 275:413–429.
- Sidharth, B. G. and R. Joseph  
2010. Different Routes to Multiverses and an Infinite Universe. *Journal of Cosmology*, 4:641–654.

Slipher, V. M.

1914. The Radial Velocity of the Andromeda Nebula. *Popular Astronomy*, 22:19–21.

Soucail, G., Y. Mellier, B. Fort, F. Hammer, and G. Mathez

1987. Further data on the blue ring-like structure in A 370. *A&A*, 184:L7–L9.

Springel, V.

2005. The cosmological simulation code GADGET-2. *MNRAS*, 364:1105–1134.

Springel, V., T. Di Matteo, and L. Hernquist

2005a. Modelling feedback from stars and black holes in galaxy mergers. *MNRAS*, 361:776–794.

Springel, V., S. D. M. White, A. Jenkins, C. S. Frenk, N. Yoshida, L. Gao, J. Navarro, R. Thacker, D. Croton, J. Helly, J. A. Peacock, S. Cole, P. Thomas, H. Couchman, A. Evrard, J. Colberg, and F. Pearce

2005b. Simulations of the formation, evolution and clustering of galaxies and quasars. *Nature*, 435:629–636.

Springel, V., S. D. M. White, G. Tormen, and G. Kauffmann

2001. Populating a cluster of galaxies - I. Results at  $z=0$ . *MNRAS*, 328:726–750.

Sun, M., G. M. Voit, M. Donahue, C. Jones, W. Forman, and A. Vikhlinin

2009. Chandra Studies of the X-Ray Gas Properties of Galaxy Groups. *ApJ*, 693:1142–1172.

Taylor, E. N., A. M. Hopkins, I. K. Baldry, M. J. I. Brown, S. P. Driver, L. S. Kelvin, D. T. Hill, A. S. G. Robotham, J. Bland-Hawthorn, D. H. Jones, R. G. Sharp, D. Thomas, J. Liske, J. Loveday, P. Norberg, J. A. Peacock, S. P. Bamford, S. Brough, M. Colless, E. Cameron, C. J. Conselice, S. M. Croom, C. S. Frenk, M. Gunawardhana, K. Kuijken, R. C. Nichol, H. R. Parkinson, S. Phillipps, K. A. Pimbblet, C. C. Popescu, M. Prescott, W. J. Sutherland, R. J. Tuffs, E. van Kampen,

- and D. Wijesinghe  
2011. Galaxy And Mass Assembly (GAMA): stellar mass estimates. *MNRAS*, 418:1587–1620.
- Tereno, I., C. Schimd, J.-P. Uzan, M. Kilbinger, F. H. Vincent, and L. Fu  
2009. CFHTLS weak-lensing constraints on the neutrino masses. *A&A*, 500:657–665.
- Thomas, S. A., F. B. Abdalla, and O. Lahav  
2010. Upper Bound of 0.28 eV on Neutrino Masses from the Largest Photometric Redshift Survey. *Physical Review Letters*, 105(3):031301.
- Tormen, G. and E. Bertschinger  
1996. Adding Long-Wavelength Modes to an N-Body Simulation. *ApJ*, 472:14.
- Turner, M. S.  
1999. Cosmological parameters. In *COSMO-98*, D. O. Caldwell, ed., volume 478 of *American Institute of Physics Conference Series*, Pp. 113–128.
- Tyson, J. A., F. Valdes, and R. A. Wenk  
1990. Detection of systematic gravitational lens galaxy image alignments - Mapping dark matter in galaxy clusters. *ApJL*, 349:L1–L4.
- van Daalen, M. P., J. Schaye, C. M. Booth, and C. Dalla Vecchia  
2011. The effects of galaxy formation on the matter power spectrum: a challenge for precision cosmology. *MNRAS*, 415:3649–3665.
- van Daalen, M. P., J. Schaye, I. G. McCarthy, C. M. Booth, and C. Dalla Vecchia  
2014. The impact of baryonic processes on the two-point correlation functions of galaxies, subhaloes and matter. *MNRAS*, 440:2997–3010.
- van de Hulst, H. C., E. Raimond, and H. van Woerden  
1957. Rotation and density distribution of the Andromeda nebula derived from observations of the 21-cm line. *Bull. Astron. Inst. Netherlands*, 14:1.

- Velliscig, M., M. P. van Daalen, J. Schaye, I. G. McCarthy, M. Cacciato, A. M. C. Le Brun, and C. Dalla Vecchia  
2014. The impact of galaxy formation on the total mass, mass profile and abundance of haloes. *MNRAS*, 442:2641–2658.
- Viel, M., M. G. Haehnelt, and V. Springel  
2010. The effect of neutrinos on the matter distribution as probed by the intergalactic medium. *JCAP*, 6:015.
- Vikhlinin, A., A. Kravtsov, W. Forman, C. Jones, M. Markevitch, S. S. Murray, and L. Van Speybroeck  
2005. Chandra Sample of Nearby Relaxed Galaxy Clusters: Mass, Gas Fraction, and Mass-Temperature Relation. *ApJ*, 640:691–709.
- Vogelsberger, M., S. Genel, V. Springel, P. Torrey, D. Sijacki, D. Xu, G. Snyder, D. Nelson, and L. Hernquist  
2014. Introducing the Illustris Project: simulating the coevolution of dark and visible matter in the Universe. *MNRAS*, 444:1518–1547.
- Voigt, L. M. and A. C. Fabian  
2006. Galaxy cluster mass profiles. *MNRAS*, 368:518–533.
- Voit, G. M.  
2005. Tracing cosmic evolution with clusters of galaxies. *Reviews of Modern Physics*, 77:207–258.
- Voit, G. M. and T. J. Ponman  
2003. Signatures of galaxy formation in the intracluster medium. *The Astrophysical Journal Letters*, 594(2):L75.
- von Hoerner, S.  
1960. Die numerische Integration des n-Körper-Problemes für Sternhaufen. I. *ZAp*, 50.

von Hoerner, S.

1963. Die numerische Integration des n-Körper-Problems für Sternhaufen, II. *ZAp*, 57.

Wechsler, R. H., J. S. Bullock, J. R. Primack, A. V. Kravtsov, and A. Dekel

2002. Concentrations of Dark Halos from Their Assembly Histories. *ApJ*, 568:52–70.

Weinberg, D. H., M. J. Mortonson, D. J. Eisenstein, C. Hirata, A. G. Riess, and E. Rozo

2013. Observational probes of cosmic acceleration. *Phys. Rep.*, 530:87–255.

White, S. D. M.

1986. *The evolution of large-scale structure*, Pp. 228–245.

White, S. D. M. and C. S. Frenk

1991. Galaxy formation through hierarchical clustering. *ApJ*, 379:52–79.

White, S. D. M. and M. J. Rees

1978. Core condensation in heavy halos - A two-stage theory for galaxy formation and clustering. *MNRAS*, 183:341–358.

Wiersma, R. P. C., J. Schaye, and B. D. Smith

2009a. The effect of photoionization on the cooling rates of enriched, astrophysical plasmas. *MNRAS*, 393:99–107.

Wiersma, R. P. C., J. Schaye, T. Theuns, C. Dalla Vecchia, and L. Tornatore

2009b. Chemical enrichment in cosmological, smoothed particle hydrodynamics simulations. *MNRAS*, 399:574–600.

Wright, E. L.

2006. A Cosmology Calculator for the World Wide Web. *PASP*, 118:1711–1715.

Wyman, M., D. H. Rudd, R. A. Vanderveld, and W. Hu

2014. Neutrinos Help Reconcile Planck Measurements with the Local Universe. *Physical Review Letters*, 112(5):051302.

Xia, J.-Q., B. R. Granett, M. Viel, S. Bird, L. Guzzo, M. G. Haehnelt, J. Coupon, H. J. McCracken, and Y. Mellier

2012. Constraints on massive neutrinos from the CFHTLS angular power spectrum. *JCAP*, 6:010.

Zwicky, F.

1933. Die Rotverschiebung von extragalaktischen Nebeln. *Helvetica Physica Acta*, 6:110–127.